Characterisation and Testing of Multifunctional Surfaces

Godi, Alessandro; De Chiffre, Leonardo; Hansen, Hans Nørgaard; Klit, Peder

Publication date:
2013

Document Version
Publisher's PDF, also known as Version of record

Characterisation and Testing of Multifunctional Surfaces

In partial fulfilment of the requirements for the degree of
Philosophiae Doctor

Alessandro Godi

Department of Mechanical Engineering
Technical University of Denmark

To my family,
extraordinary example of joy and strength through all the difficulties of life.
Keep smiling on.

Preface

This thesis is submitted in partial fulfilment of the requirements for obtaining the degree of Philosophiae Doctor at the Department of Mechanical Engineering of the Technical University of Denmark (DTU). The work is part of the project "Manufacture and characterisation of industrial multifunctional surfaces" co-funded by the Danish National Technology Foundation (Højteknologifonden) and has been carried out from May 2010 to April 2013 under the supervision of Prof. Leonardo De Chiffre, Prof. Peder Klit and Prof. Hans Nørgaard Hansen.

I would like to thank all my supervisors for their inspiration and contribution to my work. In particular I would like to express my gratitude to Prof. Leonardo De Chiffre for his great collaboration, his friendly attitude and most of all for believing strongly in my capacities. By continuously following his precious advices and enlightening guidelines I have certainly grown as academic researcher and learnt how to handle contacts with the industrial world apart from clearly having deepened my knowledge about metrology. Prof. Peder Klit is gratefully acknowledged for the fruitful discussions and for sharing with me his long experience in tribology and machine elements. Prof. Hans Nørgaard Hansen is acknowledged for his calmness, his brilliant advices and remarkable experience in handling the academic problems and to be always available to hear the ever appearing problems.

I would like to thank all project partners, in particular Dr. Anders Kühle from Image Metrology A/S and Dr. Jens Grønbæk from Strecon A/S for the continuous discussions on software implementation, test development and specimen production. Their willingness to hear the problems of a young researcher is astounding.

Moreover, during the project, two weeks were spent at the University of Valenciennes, France, for developing the numerical models. For this reason I would like to express my heartfelt gratitude to Assistant Prof. Cédric Hubert for his infinite patience and availability. It must have been hard to answer all those questions. Prof. Laurent Dubar is acknowledged for creating this connection along with Prof. Niels Bay. In particular, I would like to sincerely thank Prof. Bay, for sharing with me his astonishing

experience on tribology and metal forming and to be always available to listen to my problems. Always in relation with tribology and metal forming, I would like to thank Mr. Erik Madsen for his kindness and for permitting me to run some important production test at Grundfos A/S.
I would also like to thank a number of persons at DTU, in particular Mr. Jakob Rasmussen for performing a number of measurements especially with the CMM; Mr. Jan Frank Pedersen for performing promptly all workshop services I needed and Mr. Peter Sanderhoff for his help with the Strip Reduction Test. Besides them, two people are gratefully acknowledged: Dr. Kasper Storgaard Friis for his help with the implementation of robust filters and Dr. Kamran Mohaghegh for his help with the Axial Sliding Test. I have not forgotten you, René Sobiecki: mange mange tak for at stole på mig ved at bruge FTS'en og for at dele din utrolige erfaring med mig.
Now it comes to thank all my colleagues and friends at university for enduring this chaotic Italian: Pavel, Chris, Jais, Stefano and Lukáš. One person is on purpose left out, because has listened and experienced more than all others to all my problems: Ermanno. I do not thank you only for helping me with the Bending Under Tension or for our daily discussions, but I thank you for being a true friend ever since we shared that apartment in Christian X's Allé.
Now come the most important and heartfelt acknowledgements.
Gracias a mi amor Maricruz, por todo. Gracias por estar siempre a mi lado, por tu paciencia en estos meses en los cuales vi más a la pantalla de la compu que tus ojos maravillosos y porque tu sola presencia es suficiente para hacerme feliz. Tu sonrisa es mi esencia vital, no dejes de sonreir nunca.
Grazie alla mia fantastica famiglia per star sempre vicino a me in qualsiasi momento, buono o brutto, e per afforntarlo con una risata. Grazie per il vostro supporto in questi anni. La distanza è una cosa brutta, lo so, però più la distanza aumenta, più siete vicini al mio cuore. Siete fondamentali per me e vi adoro.
Un ultimo grazie a mia nonna. Grasie parché te me ghé ensegnà che se połe star ałegri in'tei momenti pì duri, fin 'n ultima, sempre.

Kongens Lyngby, April 2013

Alessandro Godi

Abstract

Surface texturing is considered an effective way for reducing friction losses and wear occurrence in mechanical systems. A large number of surfaces with textures artificially engineered has been proposed by researchers worldwide and among them lie a new developed typology: MUFU surfaces, where the acronym stands for multifunctional. Produced by hard-turning followed by a highly controllable Robot Assisted Polishing process, MUFU surfaces feature reservoirs for providing extra-lubrication between the contacting parts as well as uppermost flat regions for ensuring the bearing capability. The introduction of MUFU surfaces is however bound with a series of challenges constituting the topic of the present work. The exploration touches a number of disciplines encompassing metrology, tribology and modelling. The metrological investigation represents the core of the work as further researches are bound to a clear and comprehensive description of the surfaces analysed. Robust filtering methods are adopted, extended, coded and implemented in the commercial software SPIP^{TM}. These methods prove to be extremely suitable in handling the raw data coming out from a measuring instrument and yield a correctly filtered and aligned roughness profile that would be unrealistically distorted if current practice methods were used. Once an aligned profile is obtained, a further operation is introduced: feature separation. The surface features are separated with a newly developed algorithm and analysed independently according to their function. In the present case, the roughness of the plateaus is investigated independently from the valleys, which on their turn are described by the amount of lubricant they can contain.
These methods are applied throughout the whole experimental work in assessing the performances of MUFU surfaces in different applications. In machine elements, characterised by lower normal pressures, a new test rig is designed and developed studying the friction between bodies in pure sliding contact. Tests with this new device display how the employment of MUFU surfaces can reduce friction up to 50% compared to regularly machined surfaces. In metal forming tools, experimental tests are run in different processes. In deep drawing applications MUFU surfaces reduce the likelihood of galling occurrence compared to a highly polished surface.

The presence of the valley impede the galling propagation especially in real production conditions and test can run smoothly without failures. In ironing applications the severity of the conditions makes instead the texture being more harmful than useful and is therefore not advised.
Both analytical and numerical models are considered for studying the functionality of the surfaces. The analytical models, depending on the approach adopted, can give underestimations or overestimations of the results obtained with the same texture and an improvements and extension are needed in the future with the modification of the assumptions made. The road to be trodden seems though numerical modelling, whose implementation is still at an early stage. Numerical models are necessary for studying the functionality of MUFU surfaces in metal forming applications. Numerical models exist but they require ameliorations and extensions before they can be reliably used.

Resume

Overfladeteksturering betragtes som en effektiv måde til at reducere friktionstab og slidforekomst i mekaniske systemer. Et stort antal overflader med teksturer, som er kunstigt manipuleret er blevet foreslået af forskere fra hele verden, og blandt dem ligger en nyudviklet typologi: MUFU overflader hvor forkortelsen står for multifunktionel. Produceret ved hård drejning efterfulgt af en meget styrbar Robot Assisted Polishing proces, har MUFU overflader reservoirer for at levere ekstra smøring mellem berørende delene samt plateau områder for at sikre bæreevnen. Indførelsen af MUFU overflader er dog forbundet med en række udfordringer, der udgør emnet med dette arbejde. Forskningen involverer en række discipliner, der omfatter metrologi, tribologi og modellering. Den metrologiske undersøgelse repræsenterer kernen af arbejdet, og yderligere undersøgelser er bundet til en klar og omfattende beskrivelse af de analyserede overflader. Robuste filtreringsmetoder er udvalgt, udvidet, kodet og implementeret i det kommercielle software SPIP^{TM}. Disse metoder viser sig at være særdeles velegnede i håndtering af de rå data, der kommer ud af instrumentet og giver en korrekt filtreret og justeret ruhedsprofil, som ville være urealistisk fordrejet, hvis gældende metoder blev anvendt. Efter profilopretning, bliver yderligere en operation indført: *feature separation*. Overfladens features adskilles med en nyudviklet algoritme og analyseres uafhængigt i henhold til deres funktion. I det foreliggende tilfælde er ruhed på plateauer undersøgt uafhængigt af dalene, som i stedet er beskrevet af den mængde smøremiddel, de kan indeholde.
Disse metoder anvendes i hele det eksperimentelle arbejde ved at vurdere præstationer af MUFU overflader i forskellige applikationer. I maskinelementer, karakteriseret ved lavere normaltryk, er en ny prøvestand designet og udviklet for at studere friktionen mellem dele i glidende kontakt. Tests med dette nye apparat viser, at anvendelsen af MUFU overflader kan reducere friktion på op til 50% i forhold til konventionelt bearbejdede overflader. I metalformgivningsapplikationer er der kørt eksperimentelle tests for forskellige processer. I dybtrækningsoperationer reducerer indførelsen af MUFU overflader sandsynligheden for rivningsforekomst sammenlignet med en højglanspoleret overflade. Tilstedeværelsen af dale

hindrer rivningsdannelse især under virkelige produktionsforhold og tests kan køre gnidningsløst uden fejl. I strækningsreduktionsapplikationer er teksturen derimod mere skadelig end nyttig på grund af sværhedsgraden af betingelserne, og MUFU-teksturering er derfor ikke anbefalet.
Både analytiske og numeriske modeller er udviklet for at studere funktionaliteten af overfladerne. De analytiske modeller, afhængigt af den valgte tilgang, kan give undervurdering eller overvurdering af de opnåede resultater med den samme tekstur, og der er behov for en forbedring og udvidelse i fremtiden med ændring af de opstillede forudsætninger. Vejen, der skal trædes synes at være numerisk modellering, hvor gennemførelse er stadigvæk i en tidlig fase. Numeriske modeller er nødvendige for at studere funktionaliteten af MUFU overflader i metalformgivningsapplikationer. Numeriske modeller findes, men de kræver forbedringer og udvidelser, før de kan anvendes pålideligt.

List of publications

International journal papers

1. A. Godi, K. Mohaghegh, J. Grønbæk, P. Klit, L. De Chiffre, Testing of newly developed functional surfaces under pure sliding conditions, Tribology Letters (2013). DOI 10.1007/s11249-013-0162-6.

2. A. Godi, J. Grønbæk, K. Mohaghegh, P. Klit, L. De Chiffre, A New Rig for Testing Textured Surfaces in Pure Sliding Conditions, Tribology Letters 50 (3) (2013) 397-405.

3. K.S. Friis, A. Godi, L. De Chiffre, Characterization and robust filtering of multifunctional surfaces using ISO standards, Measurement Science and Technology 22 (2011) 125101.

Submitted to international journals

1. A. Godi, A. Kühle, L. De Chiffre, A plateau-valley separation method for textured surfaces with a deterministic pattern, Precision Engineering (2013) under revision.

2. A. Godi, A. Kühle, L. De Chiffre, A new procedure for characterizing textured surfaces with a deterministic pattern of valley features, Measurement Science and Technology (2013) under revision.

Peer reviewed international conference papers

1. A. Godi, J. Grønbæk, K. Mohaghegh, P. Klit, L. De Chiffre, An Axial Sliding Test for machine elements surfaces, in: Proceedings of the 15th Nordic Symposium on Tribology, Trondheim, Norway, 2012, ISBN 978-82-14-05270-1.

2. A. Godi, A. Kühle, L. De Chiffre, A plateau-valley separation method for multifunctional surfaces characterization, in: Proceedings of the 12th eu**spen** International Conference, Stockholm, Sweden, 2012, pp.190-193.

3. A. Godi, K.S. Friis, L. De Chiffre, Characterization of multifunctional surfaces during fabrication, in: Proceedings of the 11th eu**spen** International Conference, Como, Italy, 2011, pp.92-95.

4. K.S. Friis, A. Godi, L. De Chiffre, Characterisation of multifunctional surfaces with robust filters, in: Proceedings of the 4th International Swedish Production Symposium, Lund, Sweden, 2011, pp. 525-532.

Posters

1. A. Kühle, J.F. Jørgensen, A. Godi, L. De Chiffre, J. Grønbæk, Feature separation, robust filtering and multiple profile roughness in SPIP™. Poster for the NanoScale Seminar, Paris, France, 2013.

2. A. Godi, A. Kühle, L. De Chiffre, A plateau-valley separation method for multifunctional surfaces characterization. Poster for the 12th eu**spen** International Conference, Stockholm, Sweden, 2012.

3. A. Godi, K.S. Friis, L. De Chiffre, Characterization of multifunctional surfaces during fabrication. Poster for the 11th eu**spen** International Conference, Como, Italy, 2011.

Invited Contributions

1. A. Godi, L. De Chiffre, Functional surfaces in mechanical systems: Classification, Fabrication and Characterisation, in: L. Santo, J.P. Davim (Eds.), Surface Engineering Techniques and Applications: Research Advancements, IGI Global, 2013.

2. A. Godi, New tests for multifunctional surfaces for machine elements, invited speaker at the Conference on Functional Surfaces in Mechanical System, Kongens Lyngby, Denmark, 2011.

Contents

Nomenclature for Chapter 6

α_1	contact area ratio of smaller scale asperities	[-]
α	Contact area ratio	[-]
β	Asperity radius	[µm]
δ	Tool travel	[µm]
δ'	Normalized tool travel	[-]
η	Lubricant dynamic viscosity	[Pa s]
γ_1	Small scale asperity angle	[°]
γ_{max}	Maximum asperity angle	[°]
γ	Asperity angle	[°]
κ	Coefficient of the first term of $g_l(\cdot)$ function	[µm^{-2}]
μ	Friction coefficient	[-]
ν	Poisson ratio	[-]
$\phi(\cdot)$	Height distribution	[-]
$\phi(\cdot)^*$	Normalized height distribution	[-]
σ_0	Yield strength of a material	[MPa]
τ_n	Friction stress	[MPa]
τ_n'	Friction stress at proportionality limit	[MPa]
θ	Centre angle for turned surfaces	[°]
ξ	Coefficient of $a_i(\delta_i)$ function	[µm^{1-t}]
ζ	Coefficient of the second term of $g_l(\cdot)$ function	[µm^{-1}]

a_i	Linear local area of contact	[mm]
A_{Nl}	Linear nominal area of contact	[mm]
A_N	Nominal area of contact	[mm^2]
A_{Rl}	Linear real area of contact	[mm]
A_R	Real area of contact	[mm^2]
b	Bearing segment	[mm]
BA	Plateau bearing area of a MUFU surface	[-]
C	Coefficient describing the texture geometry	[-]
d	Distance between tool and reference line	[µm]
d'	Normalized distance between tool and reference line	[-]
E	Elastic module of a material	[MPa]
E^*	Equivalent elastic module	[MPa]
F	Feed rate	[mm]
f	Friction factor	[-]
F_a	Adhesive friction force	[N]
F_d	Deformation friction force	[N]
F_f	Total friction force	[N]
$g(\cdot)$	Load for deforming one asperity	[N]
$g_l(\cdot)$	Load per unit length for deforming one asperity	[N/m]
h	Max height of an ideal MUFU profile	[µm]
K	Lubricant bulk modulus	[MPa]
k	Yield stress in pure shear	[MPa]
K_0	Coefficient of lubricant modulus of 0$^{\text{th}}$ order	[MPa]
K_1	Coefficient of lubricant modulus of 1$^{\text{st}}$ order	[-]
$m(\cdot)$	Contact area of a deformed asperity	[µm^2]
N	Total number of peaks	[-]

n	Number of penetrated peaks	[-]
p	Normal pressure acting on the real area of contact	[MPa]
p_f	Hydrostatic pressure	[MPa]
q	Nominal normal pressure	[MPa]
q'	Nominal normal pressure at proportionality limit	[MPa]
q_{dry}	Nominal normal pressure without trapped lubricant	[MPa]
q_{pl}	Normal pressure on plateaus	[MPa]
R	Turning tool nose radius	[mm]
Rq_{eq}	Equivalent root mean square roughness	[µm]
Rq_t	Tool root mean square roughness	[µm]
Rq_{wp}	Workpiece root mean square roughness	[µm]
Rz	Max height of a (turned) profile	[µm]
Rz_{tri}	Max height of a triangular turned profile	[µm]
$S_i(\cdot)$	Integral of the Gaussian distribution of the i$^{\text{th}}$ order	[-]
t	Exponent of $a_i(\delta_i)$ function	[-]
U	Relative speed	[mm/s]
V_0	Initial pocket volume (per unit length)	[mm^2]
V	Trapped lubricant volume (per unit length)	[mm^2]
W	Normal load	[N]
W_i	Load (per unit length) on an asperity	[N/m]
W_i'	Non-dimensional load on an asperity	[-]
W_l	Load per unit length	[N/m]
x	Horizontal distance	[mm]
y	Lubricant film thickness	[µm]
y_m	Minimum lubricant film thickness	[µm]
z_s	Local peak height	[µm]
z_s'	Normalized local peak height	[-]

Chapter 1

Introduction

1.1 Surface texture

Surfaces play a decisive role in governing the functional behaviour of a product [1]. On them take in fact place the most important physical phenomena involving energy exchanges [2] and it is thus not surprising that the 90% of all engineering failures are surface initiated [3]. What is, then, a surface? The answer to this question, though simple it may seem, is not straightforward. A possible definition is given in the ISO 25178-2 standard [4]:"*A set of features which physically exist and separate the entire workpiece from the surrounding medium*". This definition considers therefore a surface as a boundary separating the object from the environment and, most interestingly, as a *set of features*. With this definition, the concept of surface texture is automatically introduced. A perfectly flat surface does not exist in nature [5]. All surfaces have their texture [6], a set of ridges, valleys and other features which can be as complex and varying as the morphology of the Earth, as shown in figure 1.1.

The assessment, intended as the measurement and the quantification of surface texture, is a relatively early matter. The first instruments were in fact introduced in the late 20s / early 30s of the 20^{th} century by Schmalz [8] and Abbot and Firestone [9] in order to replace the previous qualitative approach consisting in running a fingernail across the surface [3, 5]. Their instruments followed the principles of a gramophone [5, 10]: a sharp tip scanning over the small asperities of a surface picking up height information to be quantified. Thus began the development of the branch of engineering that goes under the name of "Surface Metrology", area whose importance has been growing together with the technological improvements and boosted especially by the advent of digital techniques [11]. Over the last few decades the interest of industry and researchers spread and brought into being a "rush towards miniaturization" [2] envisaged by Feynman in

(a) The Sahara Desert. (b) Grinding wheel [7].

Figure 1.1: *Surfaces of the Sahara Desert and of a grinding wheel.*

his famous talk "There's plenty of room at the bottom" [12]. Many surface measuring instruments (topic that will be dealt with in Chapter 2) have been invented since then permitting accurate explorations at nanometer level and thus facilitating in a decisive manner the worldwide expansion of micro/nano manufacturing technologies [13]. Among their many merits, these innovations have greatly contributed at enriching and expanding the knowledge about surfaces [14], progress quantified by Thomas [15] in a tenfold increment of the number of publications within the subject during the last two decades of the 20^{th} century. In particular, with developed ultra-precision technologies, the manufacture and control of dedicated features on a surface [2] was made possible, allowing hence the attainment of *textured surfaces*.

1.2 From surface texture to textured surfaces

Surface texture is defined as the deviation from the nominal or "perfect" shape of a surface [16]. This viewpoint provides implicitly a negative nuance to the meaning of surface texture, considering it as an unavoidable error originating from the manufacturing process. Whitehouse [17] remarks that in industry, especially among designers, it is widespread the wrong belief that regards these deviations as "irritant" and that a good surface is as smooth as possible. Fortunately nature disproves them. In the natural world, in fact, there exist numerous examples of non-smooth surfaces presenting structures giving to the animal or plant featuring them particular properties. Renowned are the cases of the gecko pads and the lotus leaf (figure 1.2). The gecko pads have hair-like nano-structures giving it extraordinary capacities of adhesion to nearly every material [18];

(a) Gecko pad. (b) Lotus leaf.

Figure 1.2: *Examples of structured surfaces in the natural world.*

conversely the lotus leaves have micro-relieves (figure 1.2(b)) minimizing adhesion forces and bestowing superhydrophobic properties known as "the lotus effect" [19]. Only recently, and thanks to the technological developments, has emerged the interest of industry in trying to imitate Nature and shape surfaces with structures able to achieve a particular function. The properties sought after in a surface can be numerous depending on the application field and include optical, mechanical, wetting, aesthetic properties among others [2]. Lists of possible applications are given by [1, 2, 6] encompassing micro-optic systems as Fresnel lenses (figure 1.3(a)), abrasive tools (figure 1.3(b)), self-cleaning surfaces (figure 1.3(c)), biomedical systems (figure 1.3(d)) among many others.

The manufacturing methods are also extremely various. Bruzzone et al. [2] have classified them in three main categories: *adding*, *removing* and *moving* material technologies. Adding material techniques involve all the technologies creating patterns by physically or chemically depositing material onto the surface. The obtained features appear as small relieves added to the surface. Removing material techniques, instead, refer to all the processes in which the material is mechanically cut away, chemically dissolved or melted. The features will eventually appear are small areas of depression on the surface. Finally, with moving material techniques, the change in the surface structure is attributable to plastic deformation and redistribution of material from some parts of the surface to others. In table 1.1 some texturing methods are classified in the proposed categories.

Given these great diversities of properties, application fields and manufacturing methods, it is unfortunately not surprising that there is no uniform and unambiguous way to refer to these kind of surfaces. "Textured" surfaces, the name used so far, is just one of the many. In literature terms as "structured", "functional" and "engineered" surfaces are easily found, as for example in [1–3, 6, 14, 23, 24]. It is therefore absolutely paramount to provide an accurate classification and nomenclature of the several surface types in order to avoid later confusions.

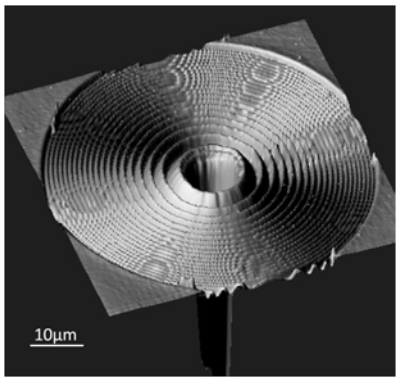

(a) AFM topography of a Fresnel lens [20].

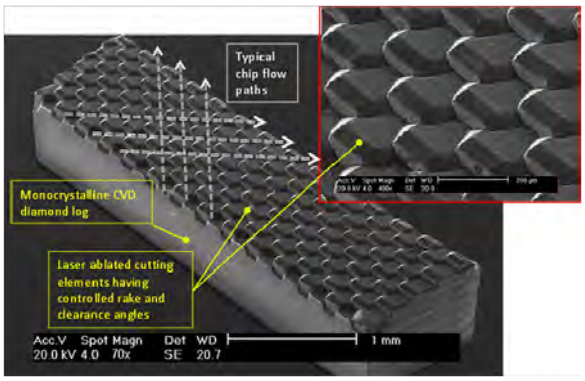

(b) Structured diamond grinding pad [21].

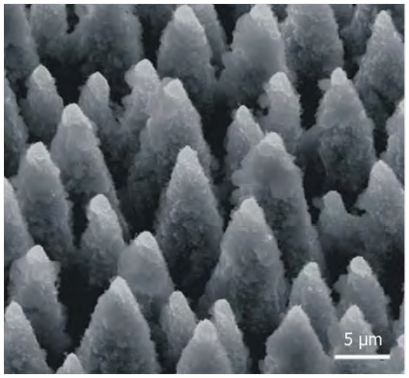

(c) SEM image of a laser-structured superhydophobic surface [22].

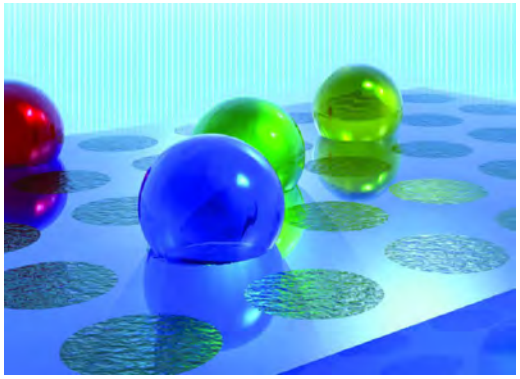

(d) BioMEMS with selective texture for droplet generation, shown with permission by [1].

Figure 1.3: *Examples of applications for structured surfaces.*

1.2.1 Surface classification: a path to multifunctionality

Evans and Bryan provide in [6] some definitions to differentiate textured, structured and engineered surfaces, but it is with Stout and Blunt [25] that a comprehensive classification is made. The one illustrated in figure 1.4 is based highly on theirs.

Considering from now on only industrial surfaces, i.e. surfaces produced by means of any manufacturing process, two big groups are detected: engineered and non-engineered surfaces. Non-engineered surfaces are by far the most common. Their functionality is not deemed as important and their texture is a direct consequence of the manufacturing process chosen with the only aim of providing a final geometry to the workpiece. A collection of textures resulting from typical manufacturing processes is found in [26]. These surfaces can present a deterministic, periodically

Table 1.1: Classification of textured surfaces manufacturing methods (summarized from [2]).

Adding Material Technologies	
Chemical processes	Chemical conversion coatings Chemical deposition coatings
Physical depostion	Patterned physical vapour deposition Deposition of micro- or nanoparticles
Removing Material Technologies	
High temperatures	Laser methods Electric discharge machining (EDM)
Chemical Etching	Masking methods Non-masking methods
Mechanical	Microcutting Grinding, polishing
Moving Material Technologies	
Mechanical	Shot blasting Embossing
Chemical	Molecular migration UV contraction

patterned texture or a random (Gaussian) one. The difference lies on the nature of the manufacturing process utilized. Typically, single-point machining such as turning or milling will generate regular, deterministic surfaces (figure 1.5(a)). Abrasive processes such as grinding, lapping and polishing have instead a high number of randomly distributed cutting grains that operate simultaneously [17, 27]. The generated surfaces will therefore be random [17], see figure 1.5(b).

On the left-hand side of figure 1.4 are presented all the surfaces created with the specific intention of providing or improving a certain function. They are the *functional* or *engineered* surfaces. In this work they are treated as synonyms, since their difference in name lies on which part of the definition the focus is set on. Functional surfaces set focus on their aim, providing a certain function; Engineered surfaces set focus on the way

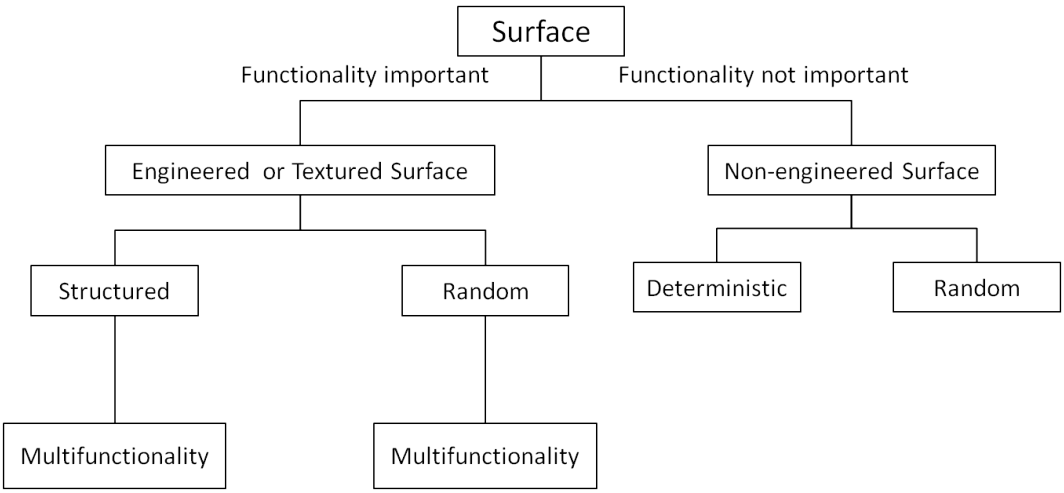

Figure 1.4: *Surface classification (based on [25]).*

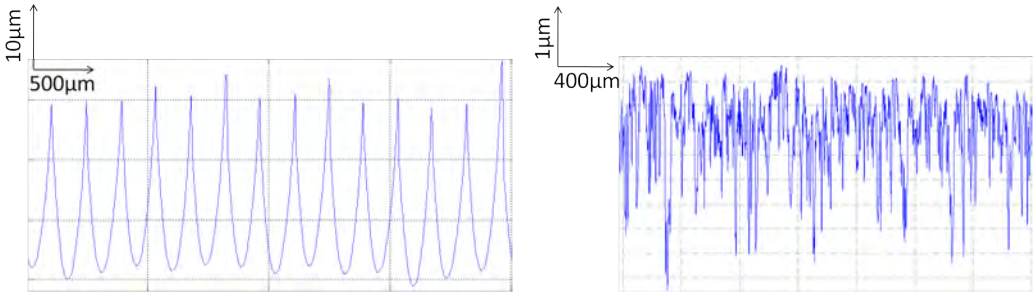

(a) Turned surface profile. (b) Ground surface profile.

Figure 1.5: *Examples of determistic (a) and random textures (b).*

they are produced, that is by deliberately altering surface and sub-surface layers [25]. The usage of the word "textured" is dissuaded by [6], but here it is maintained as direct synonym of "engineered" since it is nowadays still world-wide utilized [2, 28–35]. Structured surfaces, instead are not treated as synonyms of functional surfaces, but rather as a sub-category of them. The definition by [6] is followed, where structured surfaces are considered those functional surfaces with a *deterministic* pattern (of usually high aspect ratio) geometric features. Thus, alike non-engineered surfaces, also functional surfaces can then be divided into deterministic (or structured) and random textures. In figure 1.3(b) is shown an example of the first category: a newly developed grinding pad with regularly arrayed diamond cutters, whose employment has shown encouraging results in terms of surface finish, reduction of cutting forces and introduction of unrestricted chip paths thanks to the arrangement and the geometry (rake angles) of the

diamond cutters [21]. Furthermore, in all typologies of functional surfaces there are those featuring *multifunctionality*. Multifunctionality means that a surface provides more than one function at the time and an example of those is given in figure 1.3(d). It represents a biomedical system (BioMEMS) produced by the German laboratory Advalytix AG which is now incorporated to Beckman Coulter [36]. Their BioMEMS consist of a surface which is chemically functionalized with tracks shaped by lithography that can feature at need both hydrophobicity and hydrophilicity [1].
In this work, the focus is set on newly developed multifunctional surfaces, called **MUFU** surfaces (acronym for **Mu**lti-**Fu**nctional). These surfaces are designed for improving the *tribological* properties of the mechanical systems employing them. In the following section 1.3 a literature review of functional surfaces implemented or experimented in tribo-system is provided before concentrating on MUFU surfaces, whose study represents the core of the present work.

1.3 Textured surfaces for improved tribological performances

Tribology, which derives from the Greek *tribo* (to rub) and *logy* (knowledge of) is the science studying contacting surfaces in relative motion and covers disciplines as friction, lubrication and wear [37]. Though studies on friction trace back to Leonardo da Vinci's times, it is not until 1966 that the word tribology was adopted unifying the three disciplines and acknowledging the high economical relevance of the newly named science [37, 38]. It is in fact estimated that around 30% of the world energy consumption is used to overcome friction [39] and the costs associated with wear is in the order of percentage units (as high as 5%) of Gross Domestic Product of developed countries [40–42]. Friction is of vital importance in the everyday life (a person would not be able to walk in a frictionless world), but it is mostly an unwanted occurrence in the industrial world. Tribo-systems, i.e. mechanical systems constituted of contacting parts in relative movement, displaying high friction losses would lead to premature failures due to severe wear of the components. Therefore, in industry, lubricants (greases, oils, etc.) are widely employed to separate the two counterparts. When the applied lubrication works properly, the two surfaces are completely separated by a lubricant film: it is the so-called hydrodynamic regime and corresponds to the lowest friction conditions, see figure 1.6. Sometimes, though, the oil film thickness becomes so low that the asperities of the surfaces enter into contact. It is the dreaded mixed-lubrication regime, wherein the friction forces steeply increase leading

to energy consumption, wear and, ultimately, failure. Research within the field has worked hardly to avoid this occurrence. Better performing lubricants have been produced, but often the most effective are also the most hazardous for the environment and current regulations have become increasingly strict within the topic [43]. Certainly, studies on improving the lubrication conditions do not only pertain lubricants. The mixed-lubrication regime occurs at a surface level, and by handling, modifying and treating the surface texture, improved tribological conditions can be achieved. This work focuses its interest on this latter aspect.

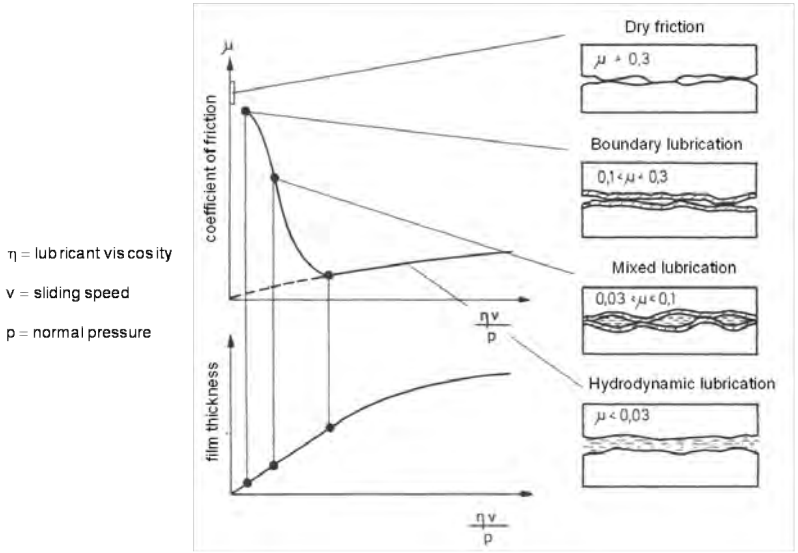

Figure 1.6: *Stribeck curve (adapted from [44]).*

When talking about functional surfaces for improved tribological conditions, the first example that pops in the mind is usually represented by plateau-honed surfaces. Plateau honing is a process that have been widely utilized in the automotive industry since the 70s in their strive for improving the tribological performances in cylinder liners of internal combustion engines. In plateau-honing a coarse honing operation is initially performed providing a rough texture; followed by a second, much finer honing operation truncating the original texture [45, 46]. This double honing process generates a flat uppermost area without main outwards peaks though crossed by deep scratches, see figure 1.7. These two regions give a series of advantages, making plateau-honed surfaces de facto (random) multifunctional surfaces. The flat area, in fact, gives good bearing properties to the surface and reduces drastically the so-called run-in period, in which the peaks of the surface are eliminated by attrition produced by the reciprocating action of the piston [47]. On the other hand, the scratches, residuals of the coarse honing process, provide the

surface with good lubricant retentions properties and offer a location for debris storage. The employment of plateau-honed surfaces proffers the great advantages of reducing wear phenomena and oil consumption and it is thus not surprising that this manufacturing process was taken up with enthusiasm by car manufacturers already in the early years after its introduction [47].

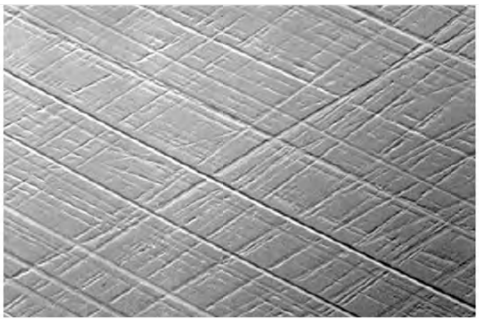

Figure 1.7: *Plateau honed surface [48].*

Due to the novelty it represented and its widespread utilization, plateau-honing has been widely studied in its different aspects, encompassing chracterisation issues [46, 47, 49] which lead to the publishing of the dedicated ISO 13565 [50–52], surface modelling [53, 54] and even the development by Rosén et al. of an expert system (ISM, interactive support modelling system) supporting the manufacturing decisions regarding the texture design [53–56]. Of course, the crossed texture of plateau-honed surfaces is not the only one known to improve tribological performances. Sticking to the field of machine elements, Holmberg [57] tested the effect of a number of different texture shapes on the mechanisms of lubrication in low speed rolling contacts. Grooves, dents and herringbone patterns were investigated and all displayed lower friction coefficients especially at higher rolling speeds compared to reference smooth rollers. In another study carried out some years later by [28], real hydraulic motor components are used for studying the sliding contact between a roller and a textured piston with grooves or meshed patterns applied by an embossing technique. The textured piston displayed lower and more stable coefficient of frictions compared to the original tumbled surface. Improved frictional performances in sliding conditions were also demonstrated by [58], which applied dimples by laser ablation to a highly polished steel sample. The effect of dimples size and distribution was investigated by [29], which demonstrated significant improvements in wearing resistance compared to a surface without dimples. In [30] other geometries besides dimples apt to promote hydrodynamic lubrication in reciprocating sliding conditions were examined and the study showed that chevron pockets were the most

effective in increasing the lubricant film thickness. In [31] the effect of texturing in sliding contacts is also studied, but applied to cast-iron surfaces. By using a pin-on-block tribo-tester, they achieved lower and more stable friction coefficients compared to a reference flat surface like [28]. A similar study was carried out by [59], which used a pin-on-disk tribo tester and textured the stainless steel pin by means of a micro-casting technique. They report friction reduction as high as 80% when using the textured surface with respect to the untextured case. Both pure rolling and rolling/sliding conditions were investigated by [32] in a rolling contact fatigue (RCF) apparatus. The texture produced by a Rockwell indenter could in some cases improve significantly the RCF life.
Surface texturing is well known improving the tribological performances also in metal forming applications. Traditionally, textures in the form of pockets have been applied to the softer workpiece in order to entrap lubricant therein. During the forming operation, the lubricant pressure increasing and the pocket volume compression cause the escape of oil from the pocket and the subsequent feeding of the contact with extra-lubrication. This phenomenon was dubbed *micro-plasto-hydrodynamic* lubrication (MPHL) by Mizuno and Okamoto [60] and experimentally verified by Azushima et al. [61]. DTU actively contributed in the research within the topic as Bech et al. [62, 63] and Sørensen et al. [64] further studied the phenomenon by employing strips with texture created by coining. The textured strip was drawn through converging dies, one of which transparent for allowing the visualization of the escape phenomenon. Their studies investigated the influence of process parameters, lubricant and pockets geometry and density on the escape onset. The escape was explained theoretically and linked to local friction forces drops. The field of application mainly exploiting the advantages of strip texturing is the automotive industry, representing the 55% of total users [3].
Recently, the application of textures has also involved the tool side. Laser technologies were utilized by [65] and by [66] for producing micro textures on cold-forging tools. This operation resulted in a significant increasing of tool life, as high as the 180% of the life of the untextured tool. Strip drawing experiments similar to the ones above described were carried out by [67], but applying the texture to the converging dies by photochemical texturing. Their experiments displayed friction forces considerably reduced when the dies feature grooves transversal to the strip movement compared to when the original polished dies are employed.
The examples here cited demonstrated how the application of surface texturing can lead to significant improvements in the performances of tribo-systems which is also the goal of MUFU surfaces are targeted at. The MUFU concept is finally introduced in the following section 1.4.

1.4 MUFU surfaces

MUFU surfaces are the answer given by the Danish company Strecon A/S [68] to the question: *"How is it possible to use environmental friendly lubricants in deep drawing without experiencing galling?"*. MUFU surfaces are therefore also known as "Strecon" surfaces, and are comparable to plateau-honed ones, since they are produced through a two-step process and pursue the same functions. They feature, in fact, an uppermost flat region (the *plateau region*) able to bear loads and deep channels (the *valley region*) for lubricant retention and debris storage. The difference between MUFU and plateau-honed surfaces lies on the manufacturing processes employed, and, consequently, on the final texture achieved. The first operation is hard-machining, typically hard-turning or hard-milling, which yields a deterministic texture later constituting the lubricant channels. The second operation is Robot Assisted Polishing (RAP), a highly controlled finishing technique invented by Strecon and presented in [69] and investigated in [70, 71] which makes use of a robot arm for performing the polishing operation rather than skilled craftsmen. In figure 1.8, the processes utilized for producing MUFU surfaces and the desired texture are depicted.

After being turned (or milled), the surface is mounted in a rotating chuck (or

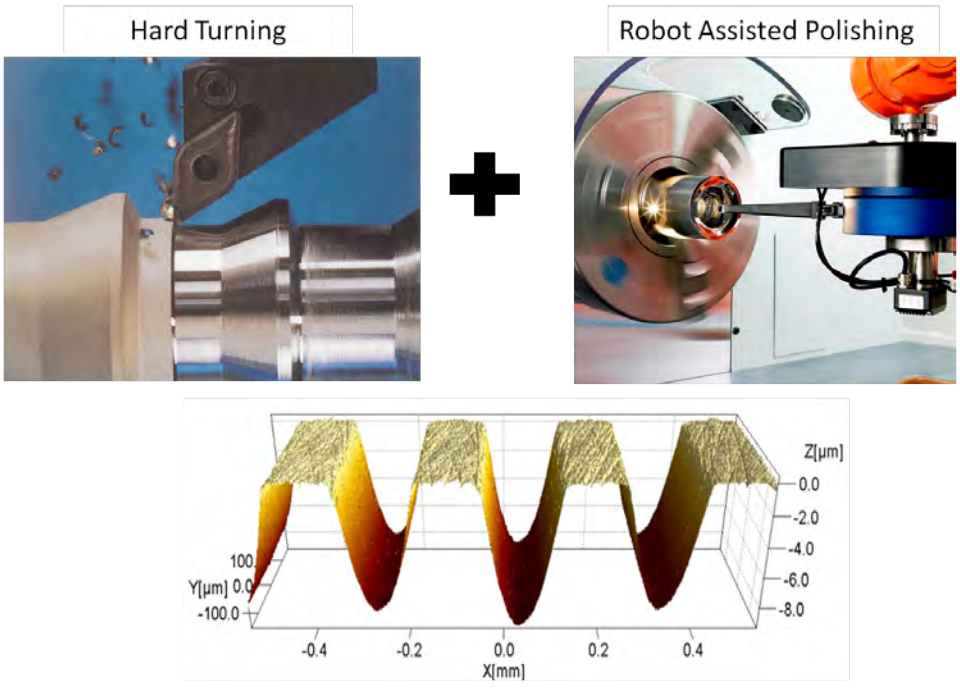

Figure 1.8: *Generation of MUFU surfaces and desired texture (lathe image taken from [72]); RAP image courtesy of Strecon [68].*

spindle) embedded in the RAP machine. A robot arm carrying a grinding stone or a felt-pad with diamond paste approaches the surface and, once in contact, performs the polishing operation. Whilst the workpiece rotates, the stone advances pulsating over the surface and removes thus material. In this way, the cusps, natural outcome of the first machining operation, are gradually scraped off creating the sought plateau regions (figure 1.9). In principle, by carefully controlling the RAP parameters, any value of the plateau bearing area comprised between 0% (original turned surface) to 100% (mirror polished surface) is achievable. The control of the RAP parameters is not a trivial task, because the parameters involved in the process are numerous, including spindle speed, choice of grinding stone, pulsation frequency and amplitude, and cutting speed.

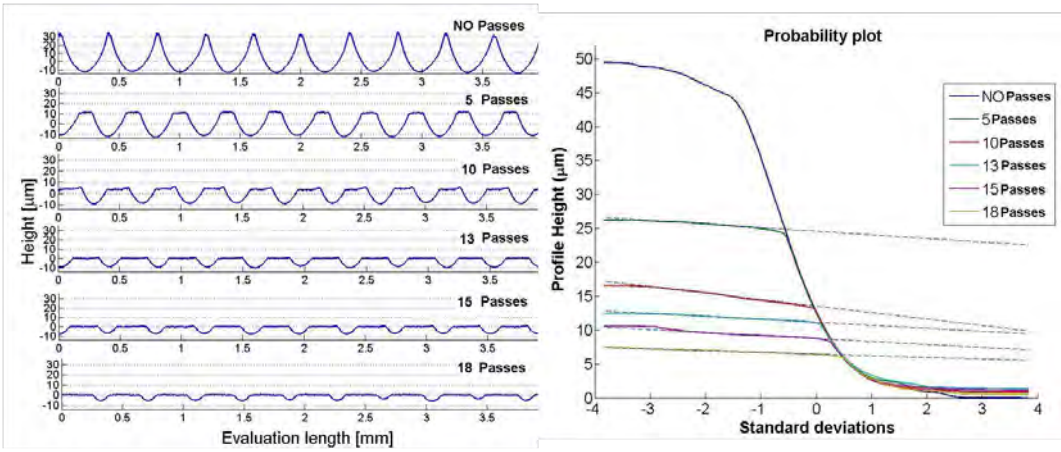

Figure 1.9: *Evolution of surface topography and bearing area as a function of the number of polishing passes.*

In a study by the author [73] the influence of the polishing parameters is assessed in the fabrication of MUFU surface from alloyed steel cylinders turned at different feed rates. The results from that investigation showed how some parameters as spindle speed (especially at low feed rates) and the choice of the stone can have a strong influence in the removal process (figure 1.10) and can lead to a fast increase of the bearing area. This occurrence is certainly non-desirable when cautiously trying to attain a targeted bearing area. Irremediable errors can take place, hence the selection of the polishing parameters must be very accurate according to the scope.
Nevertheless, though interesting, the selection of the polishing parameters and procedures to obtain specific MUFU surfaces is not the topic of the present work.
Rather, the attention here goes back to the introductory question, reformulated in: "Do MUFU surfaces improve the tribological performances of the

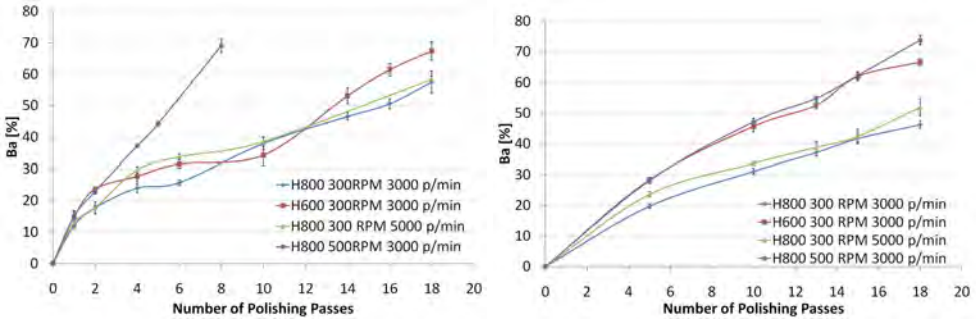

(a) Feed rate = 0.2 mm/rev. (b) Feed rate = 0.4 mm/rev

Figure 1.10: *Bearing area evolution of the cylindrical specimens [73].*

mechanical systems employing them?", which is naturally connected to a second, fundamental question: "How can MUFU surfaces be described?". The focus of the work lies here on **characterisation** and **testing** of MUFU surfaces, including their geometrical and functional modelling.

1.4.1 The MUFU project

This work represents a central and fundamental part in the so-called MUFU project (Manufacture and characterisation of industrial multifunctional surfaces). In figure 1.11 the MUFU project participants and their role is outlined.
The project, running from March 2010 till March 2014, has been supported by the Danish National Technology Foundation (Højteknologifonden) and has involved three partners: Strecon A/S, Image Metrology A/S and the Technical University of Denmark (DTU).
Strecon [68], the inventor of MUFU surfaces, was involved in the design and had the task of generating all the parts, test apparatuses and especially the MUFU specimens utilized developing polishing procedures for realizing them. Image Metrology [74] is a Danish company producing the metrological software SPIP^{TM}, image processor for analysing surface measurements. Image Metrology was in charge of managing the MUFU project as well as providing the software and implementing the methods and algorithms for the characterisation of MUFU surfaces. Part of the work done by DTU is summarized in this thesis, which pertains the research done in relation to characterisation and testing. In particular, the task was to provide the metrological and tribological expertise to the project, including the development of mathematical methods and algorithms for the characterisation of MUFU surfaces, to perform traceable measurements and to identify and run functional tests for proving the surface efficacy in

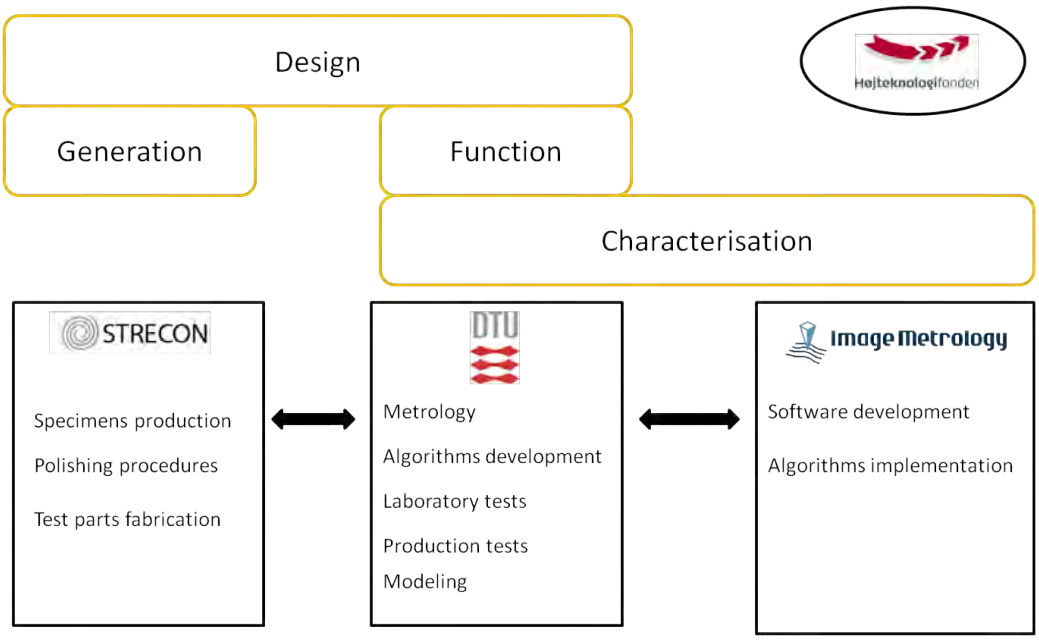

Figure 1.11: *MUFU project participants.*

two fields of applications detected: **machine elements** and **metal forming tools**. Moreover, another task was also to devise geometrical and functional models for MUFU surfaces and disseminate the knowledge obtained by producing a number of scientific publications. All these tasks represent the motivations for this Ph.D. project.

1.5 Structure of the work

In this last section of chapter 1, the detailed structure of this thesis work is outlined. Including this introductory chapter, the thesis is divided in 8 chapters plus the appendices, in this manner subdivided:

Chapter 1 (the present one) is an introduction to this thesis starting from the basis of surface texture to the particular case of textured surfaces for improving the tribological conditions. MUFU surfaces have been introduced, the study of which represents the aim of this thesis.

Chapter 2 is a review of existing characterisation methods, describing nowadays utilized characterisation procedures for both engineered and non-engineered surfaces. The review includes descriptions of measuring instruments, filtering methods and parameter calculations according to the standards. Newly standardised, advanced character-

isation methods are also dealt with. Eventually, traceability issues are covered.

Chapter 3, instead, concerns the characterisation of MUFU surfaces, illustrating the limitations of existing methods and providing an innovative solution based on robust filtering and feature detection and separation.

Chapter 4 concerns the testing of MUFU surfaces for machine elements applications. A wholly new test rig was devised and fabricated for the scope and a number of tests comparing the friction performances of MUFU surfaces with the ones of classically machined surfaces were carried out.

Chapter 5 concerns the testing of MUFU surfaces for metal forming tools. Simulative laboratory tests exploring mild and severe tribological conditions were performed as well as full-scale tests in a production environment.

Chapter 6 is a theoretical chapter on geometrical and functional modelling of MUFU surfaces. The model described is analytical and consider the case of a soft MUFU surface when in contact with a hard flat one in lubricated conditions.

Chapter 7 introduces numerical modelling of MUFU surfaces, suitable for the case of textured metal forming tools. The chapter represents a starting point for future studies on multifunctional surfaces, introducing FEM modelling for examining the lubricant escape at a roughness level.

Chapter 8 concludes the thesis work summarizing what achieved in the project and provides a list of proposals for future work.

Chapter 2

Surface Characterisation

This chapter deals with surface metrology, which is the science involving the techniques and methods useful for the measurement and the description (i.e. characterisation) of a surface. Surface characterisation is a powerful tool which has a central importance in the design and generation of a surface in relation to its function, as depicted in figure 2.1.

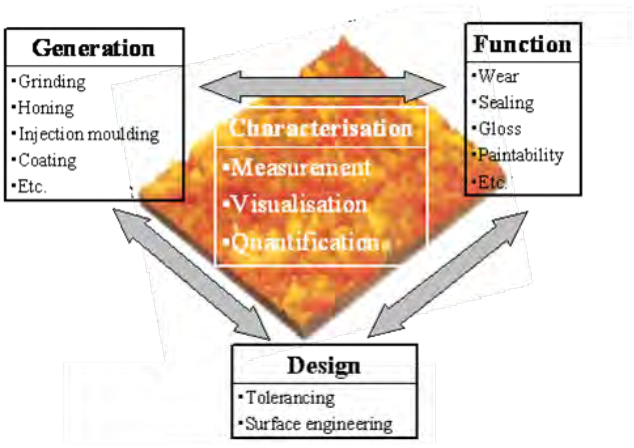

Figure 2.1: *Surface characterisation links design, generation and function [75].*

The first step of surface characterisation is the physical measurement. The most appropriate instrument must be chosen for assessing the surface depending on its characteristics and the size of the features to be measured.

2.1 Instruments for measuring surface texture

2.1.1 Stylus instruments

By far the most common and widespread instrument for measuring surface texture is the stylus, otherwise called profilometer, which works on the same principle of the primeval instruments built in the 30s, and represents their natural evolution. In modern instruments the tip scanning over the surface is made of diamond and has a conical shape with cone angles of 60°-90° and tip radius in the order of the micrometer (1-10 µm, with typical values 2, 5 or 10 µm) [5, 75, 76]. The tip is physically connected to a pick-up and to a transducer, generally piezoelectric, inductive or laser interferometric, detecting the vertical difference between the stylus and a reference, and converting it into an electric signal. The signal is then amplified by the electronic systems of the machine, digitized and sent to a computer for further data processing (figure 2.2).

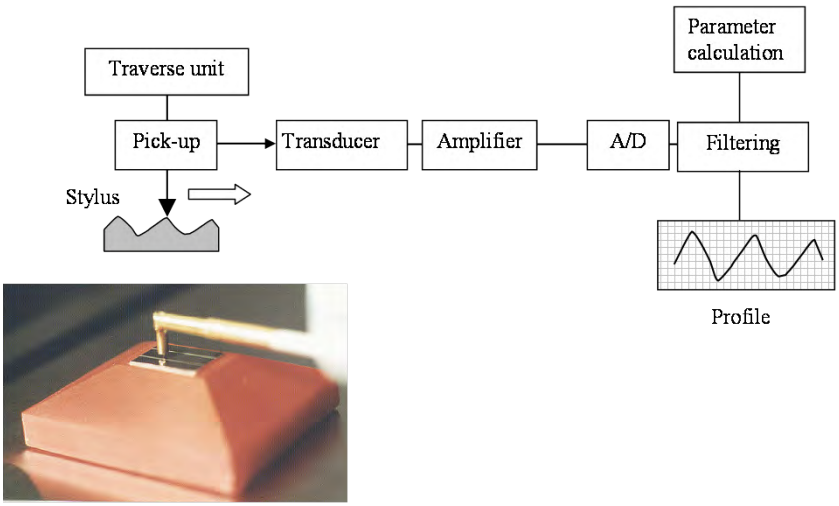

Figure 2.2: *Scheme of a stylus profilometer (A/D stands for analog-to-digital converter) [75].*

Normally, stylus instruments can be divided in two classes depending on the reference datum they use: intrinsic or independent datum (figure 2.3). In independent datum instruments the reference is separate from the surface to be measured; in intrinsic datum instruments the reference is the test surface itself [17]. Practically speaking, intrinsic datum instruments are the ones having a skid attached to the pick-up; independent datum instruments do not have any skid, but use a superfinished bar with straight or curved cross section and characterised by a high degree of straightness

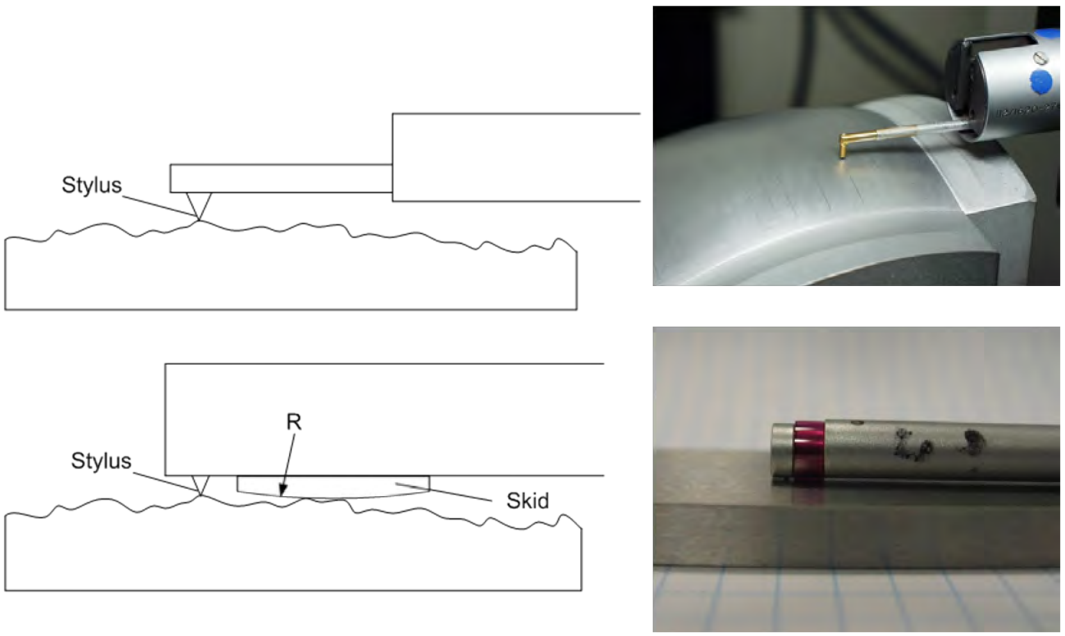

Figure 2.3: *Independent datum (top) and instrinsic datum (bottom) systems, from [16].*

(0.5µm over 120 mm) [16, 17].
Skid instruments have the advantage that they do not need long and tedious levelling and setting up time [5] and have been used since the early days of the introduction of the instrument. They are nowadays still very common especially in the industrial world, being extremely compact and in many cases portable. They are though less precise than independent datum instruments, since the presence of the skid can in some cases generate distortions [17] and their utilization is not recommended by ISO [76]. Moreover, the skid acts as a mechanical filter, removing surface higher wavelengths and leaving out only the small deviations constituting the roughness, concept introduced in section 2.2. The mechanical filtering could have decisive effects on the measurement [17], therefore the skid radius has a minimum dimension of at least 50 times the cut-off (other concept introduced in section 2.2) used. Besides being not able to measure all the surface components, skid instruments are not suitable for 3D measurements since a two orthogonal axes reference (a plane) is needed for this task [11]. For these scopes, independent datum instruments are rather utilized. Those instruments, more delicate and usually kept in environmentally controlled laboratories, are also used for calibration purposes, but suffer the drawbacks of having limited versatility and of requiring sometimes long time for properly aligning the specimens.
Generally speaking, vertical resolutions at a nanometer level and spatial resolutions at a sub-micrometer level can be achieved by the instrument's

transducers. The probing of the stylus, though, is greatly affected by its geometry and the slopes and heights in the neighbourhood of the point of contact [75]. Because of its finite dimensions, the tip cannot in fact reach the bottom of deep and narrow furrows, while steep features will appear bulkier than they actually are (figure 2.4). This mechanical filtration generates a measured profile which is in practice an envelope of the real one. This occurrence makes the instrument not suitable for measuring surface features below 1 µm, which will be treated as "noise" and discarded.

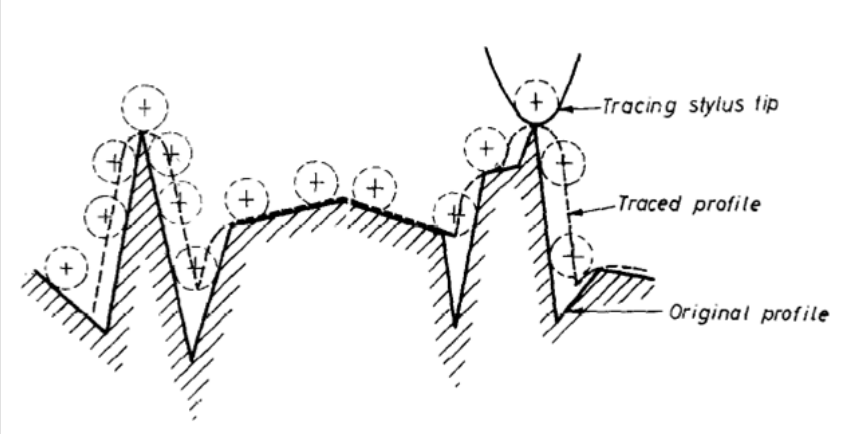

Figure 2.4: *The effect of stylus radius on the profile traced [77].*

Another limitation of stylus instruments concern their contact with the examined surfaces. The diamond tip loads the surface with a force of generally 0.75 mN, which can in some cases generate plastic deformations [75]. This instrument is therefore inapplicable to soft samples or to samples where even light scratches cannot be accepted [75].
3D topographies can be acquired by stylus instruments by means of multiple scans taken in a raster fashion. Besides the need of a reference plane, the acquisition time is usually long and for that purpose optical instruments are in many cases preferable.

2.1.2 Optical instruments

The development of optical instruments for surface texture measurement followed closely the one of stylus instruments [78], of which they represent the followers and compared to which they have a number of advantages as well as limitations. Reviews and discussions on optical instruments are widely discussed in literature, for example in [5, 17, 78, 79]. There are various kinds of optical techniques, of which the most important ones are optical profilometers, confocal microscopes and interferometers(figure 2.5).

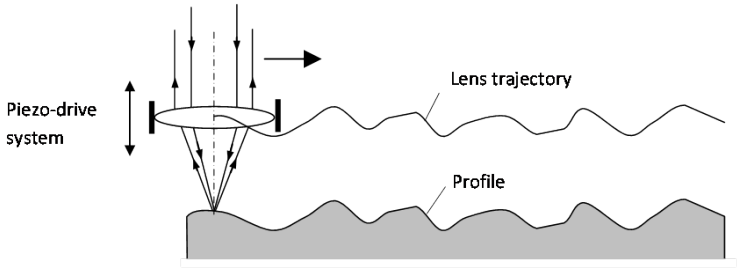

(a) Autofocusing method operating principle.

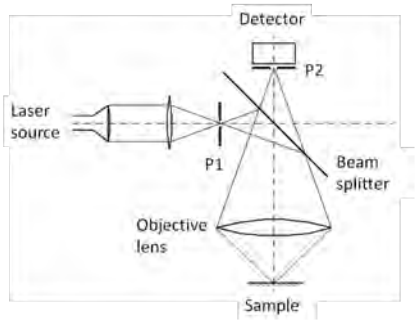

(b) Confocal principle.

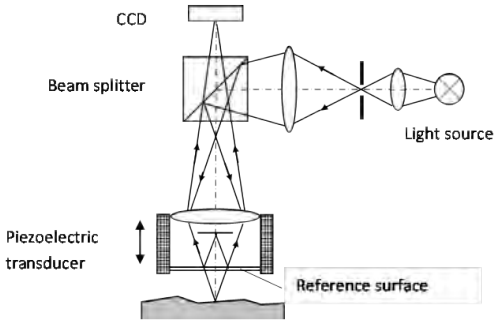

(c) Interferometric measuring system.

Figure 2.5: *Schemes of the principal optical instruments, pictures taken from Lonardo [79].*

Optical profilometers (figure 2.5(a)) operate in a way similarly to conventional styli, scanning over a surface although not contacting it. They are based on the autofocusing signal of a laser beam detector. The laser beam, which has a spot diameter of about 1 µm, is focused onto the surface through a lens. The same lens collects afterwards the scattered light on a focus detector operating on its turn a control system. As the detector moves horizontally, the lens adjusts the distance from the surface to keep the beam focused. Its trajectory describes therefore the surface profile. Vertical resolutions achievable are approximately 5 nm. Confocal microscopes (figure 2.5(b)) are based on the focus detection principle, where both the light source pinhole P1 and the detector pinhole P2 are focused on the specimen. One surface element (pixel) is imaged at the time; recording a number of vertical optical sections and considering only the ones in focus (usually bright) for the final reconstructions. This technique has the disadvantage of being slow in recording areal topographies. Interference microscopy (figure 2.5(c)) combines an optical microscope and an interferometer objective into a single instrument. A beam is sent onto the surface by a light source. Part of the beam is reflected back by a reference surface interfering with the beams reflected from the sample. A piezoelectric transducer moves the objective causing fringe modulation from which the

initial phase at each point can be calculated and hence the corresponding height. The instrument is characterized by great speed and high vertical resolutions, being capable of measuring surfaces with roughnesses down to 0.1 nm.
A fourth technique which has been recently introduced in the field of surface metrology is represented by focus variation instruments [80, 81] and here mentioned because the optical instrument utilized in this work belongs (Alicona Infinite Focus®, figure 2.6(a)) to this category. In focus variation instruments, white light is emitted from a source and transmitted through the semi-transparent mirror and the objective lens to the specimen (figure 2.6(b)). Depending on the topography of the specimen, the light is reflected in different direction [80, 81]. The reflected light is partly collected by the objective and projected to the CCD sensor [81]. Due to the small depth of field of the optics, only small regions of the object are sharply imaged; therefore, in order to completely detect surface information, the optical arrangement is moved along the vertical direction while continuously capturing data [80]. Every region of the object is thus sharply focused. Eventually, algorithms convert the acquired data into 3D topographies by analysing the variation of focus along the vertical axis [80].

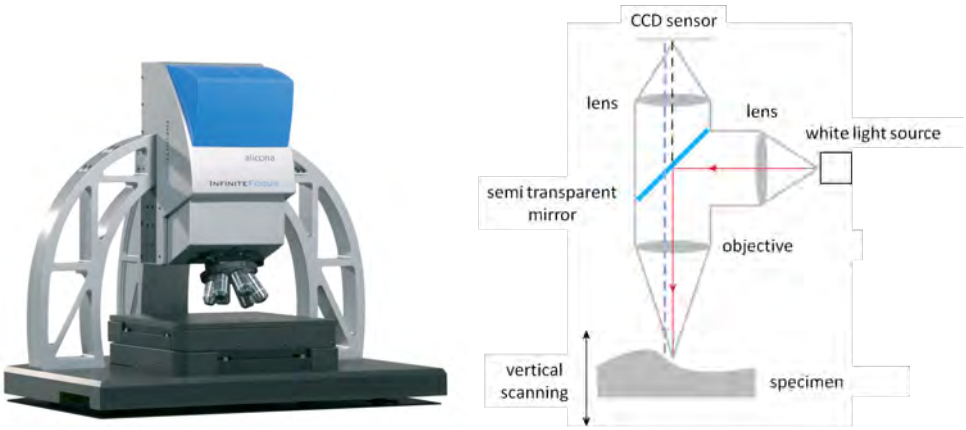

(a) Alicona Infinite Focus® [82]. (b) Focus variation principle [80].

Figure 2.6: *Focus variation instrument and operating principle.*

Optical instruments are acknowledged having two advantages with respect to stylus instruments: they are generally faster (except for optical profilometers that are as slow as styli), especially in areal acquisitions (a 3D topography can take many minutes or even hours with a profilometer, while sometimes only seconds with an optical instrument [80]); and the non-contacting nature allow the study of delicate and soft samples.
On the other hand, being not in mechanical contact with the surface has also

some drawbacks, due to the fact that a "real" picture of the situation (i.e. mechanical surface [3, 4]) is not given and properties such as reflectivity can play an important role. Peak height overestimation [75, 79] and creation of non-existing spikes [81] are for example problems connected with high-reflectivity or transparency of the sample surface making it at times impossible to measure. The numerical aperture of the objective represents another limitation for optical instruments, which can lead to speckle noise [83], and most importantly reduces the range of measurable asperity slopes. Autofocusing and interferometry methods are usually connected with low measurable slopes (15° - 30°), while confocal methods can go up to 75° [75]. Focus variation techniques, instead, are not limited by the numerical aperture of the objective and can measure slopes above 80° [80]. Unfortunately these instruments suffer the major drawbacks of having relatively poor vertical (tens of nanometers) and lateral resolutions (microns) as well as being incapable of imaging surfaces where the focus does not sufficiently (flat surfaces such as polished ones).

2.1.3 Scanning Probe Microscopy

Scanning Probe Microscopy (SPM) encompasses a number of measuring techniques allowing sub-nanometric investigations. SPMs (together with Scanning Electron Microscopy) are nearly the only instruments capable of detecting surface features in that range. They include atomic force microscopes (AFM) and scanning tunneling microscopes (STM) among others listed by [17, 84], and, at the time of their invention in the mid 80s, they represented a major breakthrough in the field of surface metrology and resulted in the awarding to one of their inventors, Gerd Binnig, of the Nobel Prize in Physics in 1986. Alike profilometers (but one order of magnitude smaller), their measuring modality consists of a sharp tip with radius comprised between 5 and 20 nm [75] scanning over the surface in a raster fashion. The philosophy behind the measurement, instead, is completely different and so are the actuation and control mechanisms. In SPMs, and particularly in the case of AFM, the tip is not in a real physical contact with the surface; rather its vertical position is affected but the forces exerting at the atomic level. With reference to figure 2.7, when the tip approaches the surface, the atomic forces make the cantilever (to which the tip is attached) bend and to this movement is associated a change in position of the laser beam (1) reflection onto the photodector (2). A signal proportional to the bending of the cantilever is issued by the photodetector (3) and compared to a pre-fixed set point value (4)in order to generate an error signal (5). Eventually, the correct position of the tip is restored by a PID feedback control which provides a voltage (6) to a piezoelectric crystal

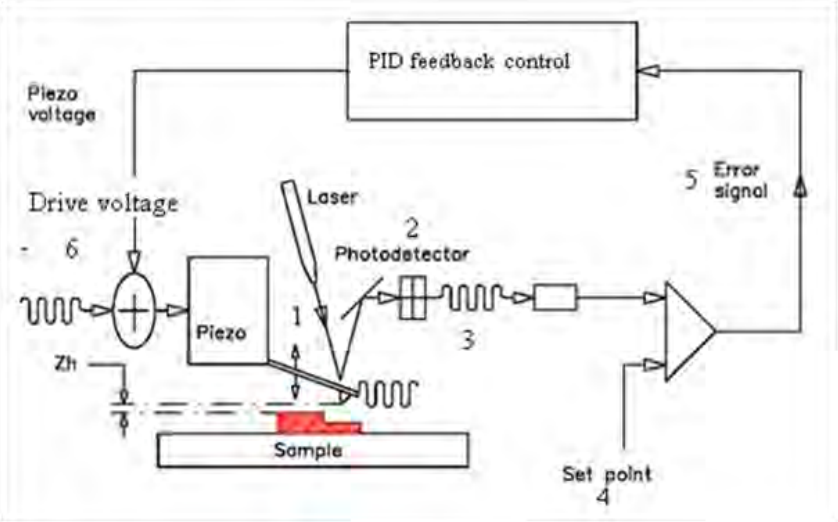

Figure 2.7: *Scheme of the major components of a AFM [85].*

that expands or contracts accordingly. The vertical displacement is therefore thus acquired.
The advantages connected with SPMs are numerous: extremely high resolutions both in vertical and lateral directions; nanometric or in some cases sub-nanometric uncertainties of the measurements; contacting conditions that do not harm the specimens involved (polymers can be analysed without risks of damaging them). There are unfortunately also drawbacks with these techniques. The major flaw of SPMs is the limited scan range. In commercial instruments the horizontal range is usually less than 100 µm, typically with values around 70 µm. Also in the vertical direction the range is limited by the piezoelectric capacity of extension, which is generally few microns. There exists only few instruments that can scan over bigger areas and are usually confined in national metrological laboratories, such as the AFM present at the German Physikalisch-Technische Bundesanstalt (PTB) which has a scanning range of 25 mm x 25 mm x 5 mm [86]. Another limitation of SPMs is their slowness: a single 3D topography can even take days if the scanning range is particularly broad.

2.1.4 Instrument comparison

Given advantages and disadvantages of each technique, the selection of the most appropriate instrument must be done in relation to the surface typology and the overall size of the features to be analysed. With reference to figure 2.8, when the features of interest are in the nanometric order, SPMs represent practically the only choice, being those feature either impossible

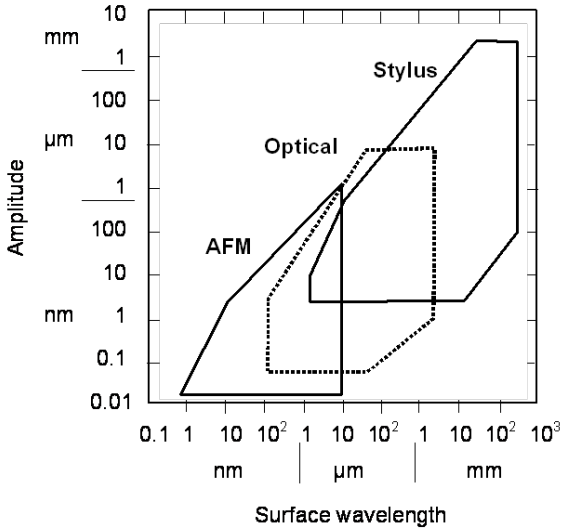

Figure 2.8: *Resolution ranges for styli, optical instruments and AFMs, after Stedman [87].*

to be detected or captured with relatively high uncertainties by other instruments. Optical and stylus instruments performances overlap. The choice between them depends on the characteristics of the available instruments such as resolution, surface characteristics (hardness, transparency, reflectivity, etc.), feature characteristics (steepness, depth or height) and time available. Stylus instruments are usually preferable in the case of shiny or hard metals or when time is not crucial; optical instruments in the case of opaque polymers or when the measuring time is of primary importance .

2.2 Procedure for surface data analysis

After the measurement is taken, the second step in surface characterisation is visualisation. It is extremely important to know how a surface looks like before choosing the most suitable procedure for correctly quantifying it keeping in mind the horizontal-vertical scale relation and the feature distribution. The choice does not only pertain the selection of the most proper parameter among the many that exist, but also of the filtering procedure employed to arrive at the calculation of those parameters. Once a measurement is taken by means of any instrument, a profile or an areal topography is the outcome. This is still in a "raw state", containing instrument noise and all the wavelength components constituting a surface. It is in fact acknowledged [5, 11, 16, 17] that a surface consists of three main components: *form*, *waviness* and *roughness*. In particular, form represents

the nominal shape of a surface; roughness comprises all small deviations and marks typical of the machining process employed [17]; while waviness refers to larger wavelength deviations due to unexpected vibrations occurred during the fabrication process [17] (figure 2.9). Generally only the last two components constitute what it has been referred to as surface texture, but some may also include in the texture errors of form, much larger waves caused by errors in the slideways or thermal distortions [17].
The profile (the same reasoning goes for areal topographies) yielded by a measurement operation is called total profile and it is a discrete array of points representing the sampled surface heights. This profile needs to be "cleaned" of all the not-interesting components in order to obtain the profile of interest, which in most cases is the roughness profile. The "cleaning" is done by accurately choosing a sequence of low-pass and high-pass filters. Depending on whether the surface functionality is deemed as important or not, it is possible to extract from ISO standards indications on how to perform the filters selection. In figure 2.10 the characterisation procedure for the two cases is shown, highlighting the filtering sequence. In particular, the red path of figure 2.10 illustrates the filtering procedure for non-engineered surfaces, summary of the indications given in ISO 3274 [76] and preparatory for the quantifications according to the parameters described in ISO 4287 [88]. Conversely, the blue path of figure 2.10 depicts the procedure for functional surfaces according to ISO 13565 guidelines [50–52]. ISO 13565 is actually designed for surfaces with "stratified functional properties", which is in practice another way for indicating multifunctionality and therefore represents the standardised method for analysing MUFU surfaces.
Starting then from the total profile, the first step for both procedures is the removal of the geometrical form of the object under investigation by typically applying a least-square polynomial fitting. At the same time, the extremely high frequency representing the noise of the instrument (and therefore not truly belonging to the surface) are removed by operating a first filtering operation, called λs filtering. The filter most widely used in

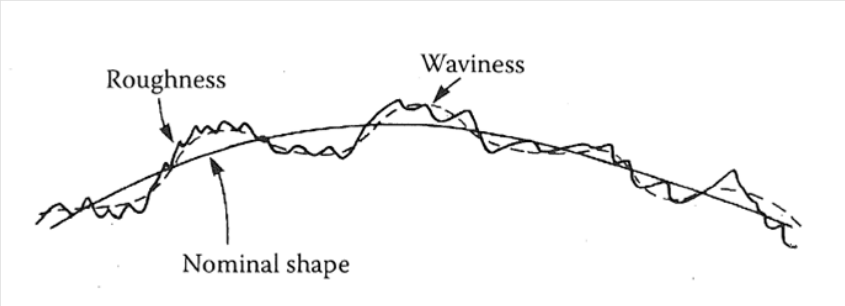

Figure 2.9: *Geometric deviations from intended shape [17].*

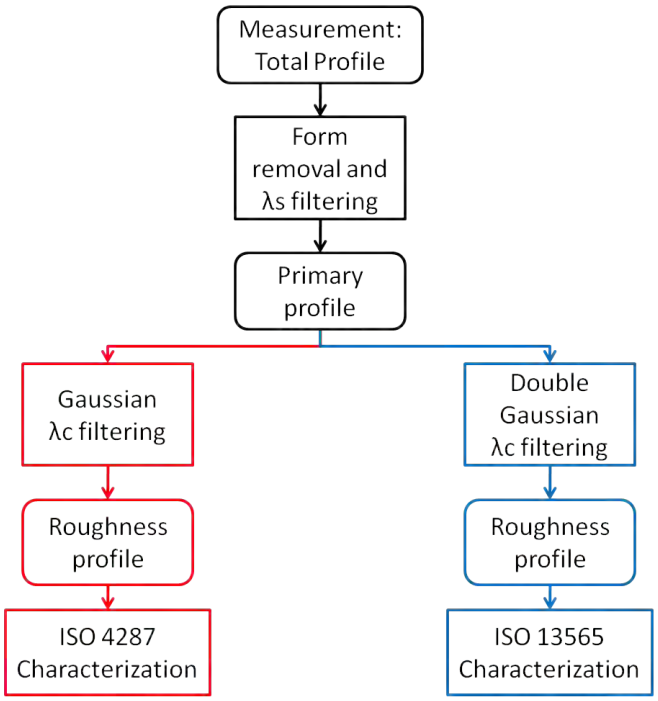

Figure 2.10: *Standardised characterisation procedures. Red path: classical characterisation procedure; blue path: characterisation procedure for stratified functional surfaces.*

this as well as in the following operations is the phase-corrected Gaussian filter. This and other filter typologies will be discussed in section 2.3. A λs filter is a low-pass filter, meaning that it damps all wavelengths beneath the targeted one and lets the wavelengths above it passing almost unaltered. A typical value for the λs filter is 2.5 µm, case of a stylus profilometer with tip radius equal to 2 µm [76]. After the λs filtering operation (noise removal), the primary profile comprising waviness (medium wavelengths) and roughness (shorter wavelengths) is obtained. The distinction between the two components is given by λc, **cut-off** wavelength. All the wavelengths below λc are included in the roughness profile; whereas all the wavelengths above it are included in the wavelength profile. The choice of the cut-off wavelength is purely arbitrary, as there are not distinctive definitions of the boundaries between waviness and roughness [5, 16]. Standards can provide guidelines: ISO 4288 [89], for example, suggests the cut-off wavelength to be applied in the case of tolerance verification. By far the most common value for λc is 0.8 mm. The λc filtering operation generates the final profile to be quantified, usually the roughness profile. The parameters describing the surface are calculated according to ISO 4287 [88], which gives alike definitions for roughness parameters (R-parameters),

waviness parameters (W-parameters) and even primary profile parameters (P-parameters) depending on which profile is retained for quantification. As it will be explained in section 2.3.5, though, this three-groups division is currently being surpassed and set aside by the technological shifts that surface metrology is undergoing [7].
In the case of surfaces with stratified functional properties, instead, a simple Gaussian filtering operation is not suitable for separating the roughness and waviness components as it can generate distortions (see sections 2.3.2 and 2.3.3). ISO 13565 [50] starts then from the assumption that the surface has a very small waviness and suggests to apply a double-step Gaussian filtering operation in order to obtain an undistorted roughness profile ready for quantification. Since the surface hos to provide specific functional properties, conventional parameters of ISO 4287 are not suitable for its description. Therefore ISO 13565 part 2 [51] and 3 [52] suggest two separate ways for tackling the quantification procedure based on German and American approaches [10]. These methods will be discussed in section 2.4.

2.3 Surface filtering

In the previous section it was mentioned how filtering is a decisive operation in surface characterisation. Gaussian filters represent the current practice adopted for obtaining roughness profiles, but other techniques exist, some surpassed and some being recently introduced. The purpose of this section is to review the existing filtering techniques.

2.3.1 2RC filters

The 2RC filter was probably the earliest filter used for surface analysis [90]. It was introduced before the advent of the digital age and consists of two resistor (R)-capacitor (C) circuits inserted directly in the transducer circuit [5, 17]. It was also the first internationally agreed filter [5], so that the transmission characteristics at the cut-off value was a result of a compromise [17]: the value of 75% was chosen as approximate average between the British 80% and the American 70.7%. This filter has the advantage of eliminating well all the electrical signals sourcing from the circuits of the instrument which could affect the resulting profile. Nevertheless, compared to modern filters, it has a number of disadvantages. The major problem lies in the introduction of phase distortions in the filtered profile (figure 2.11) due to the filter's asymmetrical weighing function [5, 90]. Moreover, profile distortions are also present also at the edges of the profile (end effects), see figure 2.11. In addition the transmission rate at 75% implies that it is not

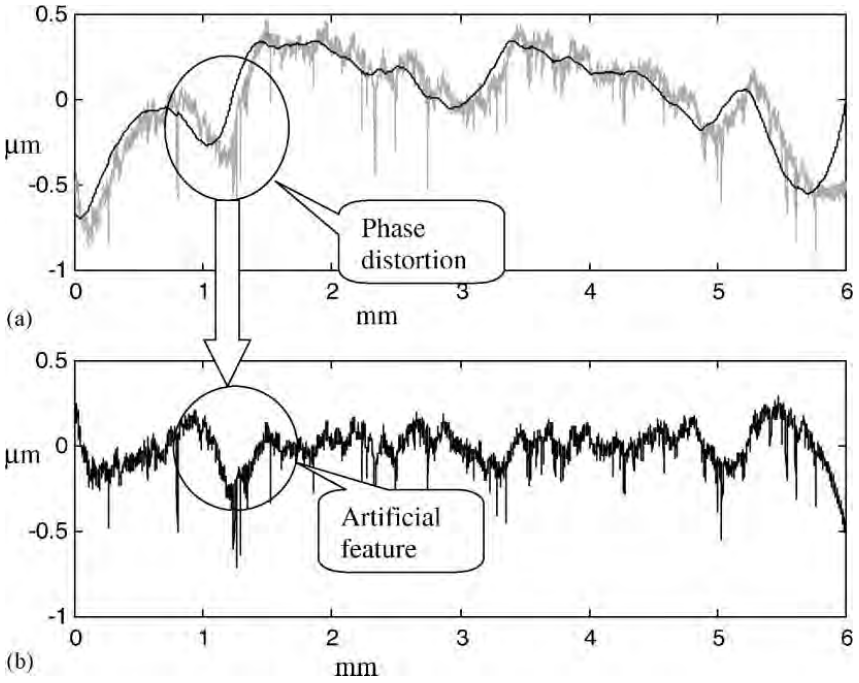

Figure 2.11: *Profile and 2RC mean line (not waviness profile) (a); roughness profile (b), from Raja [90].*

possible to get the waviness profile by simply subtracting the roughness profile from the primary profile [90].
To overcome the phase distortions, the usage of a phase corrected filter was proposed by Whitehouse some 45 years ago [91]. This could be done by using filters with symmetrical weighing functions, such as Gaussian filters, whose implementation has become practical since the advent of ceapt digital processing [5].

2.3.2 Gaussian filters

The Gaussian filter is nowadays the filter technique most widely utilised for surface characterisation and it is standardised in ISO 16610 part 21 [92] (previously ISO 11562). The Gaussian filter is phase corrected meaning that does not cause any phase-distortion of the final profile. The weighing function $s(x)$ of the filter is symmetrical and has the characteristics of the Gaussian distribution (equation 2.1):

$$s(x) = \frac{1}{\alpha\lambda_c} \cdot \exp\left[-\pi\left(\frac{x}{\alpha\lambda_c}\right)^2\right] \tag{2.1}$$

where λc is the cut-off wavelength and α is constant equal to 0.4697 [5, 92].

Given this weighing function the filter is described by the solution of the following minimisation problem [93] (equation 2.2):

$$\int_0^l (z(\xi) - w(x))^2 \cdot s(\xi - x)\mathrm{d}\xi \Rightarrow \min_{w(x)} \tag{2.2}$$

where $z(\cdot)$ is the measured profile, $w(\cdot)$ is the mean line and l is the profile length.
The solution to the minimisation problem, is given in equation 2.3

$$w(x) = \int_0^l z(\xi) \cdot s(\xi - x)\mathrm{d}\xi = z(x) \otimes s(x) \tag{2.3}$$

where $\otimes$ is the operator of convolution [93].
The Gaussian filtration can be therefore seen as the convolution of the measured profile with the Gaussian weighing function. In figure 2.12, the operation is illustrated.

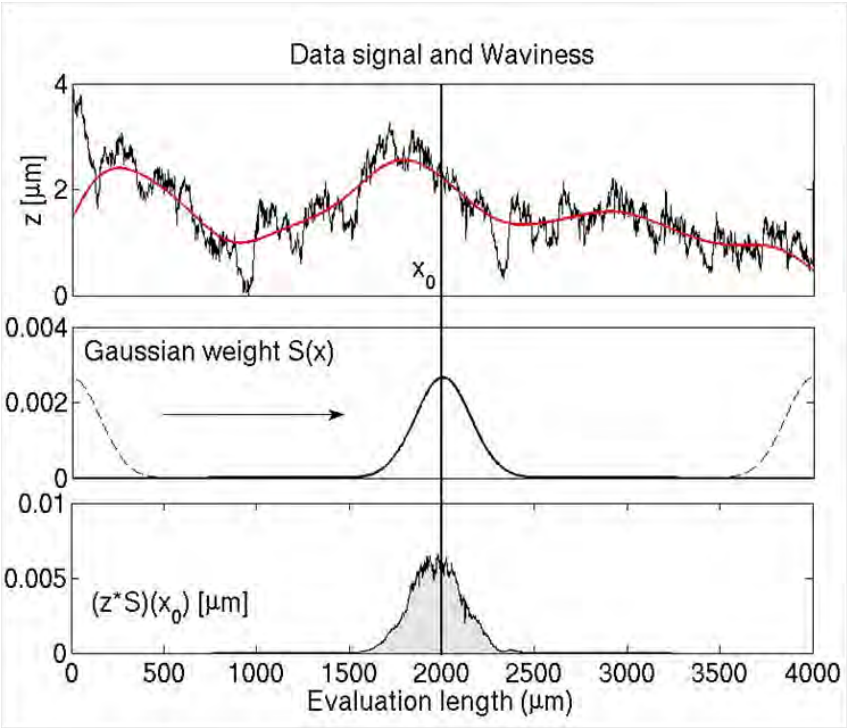

Figure 2.12: *Principles of the Gaussian convolution filter.*

The weighing function "slides" over the x-axis keeping the same shape over each data point. For every point x_0 the profile and the weighing function are multiplied; then the integral is calculated giving the estimate $w(x_0)$; the array of all the points thus calculated constitutes the mean line.

By decreasing the cut-off wavelength, the Gaussian weighing function will become narrower thereby limiting the number of points in the vicinity of x_0 that are included in the calculation of the waviness component. The transmission characteristics of a Gaussian filter are illustrated in figure 2.13. Differently from the 2RC filters, the transmission at the cut-off wavelength is equal to 50%, meaning that the mean line corresponds to the actual waviness profile.

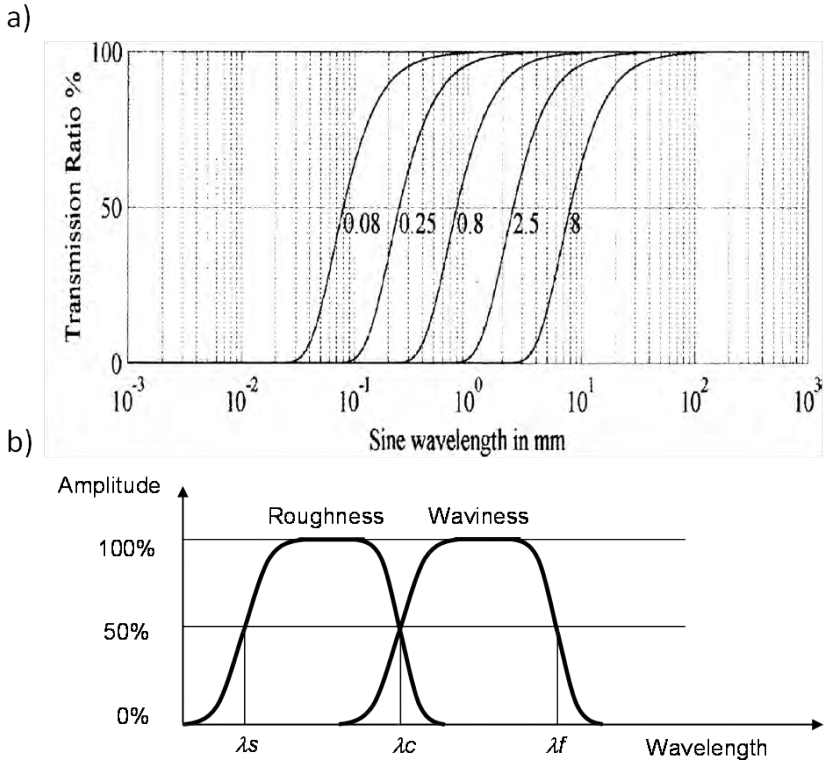

Figure 2.13: *Transmission characteristics of the Gaussian filter (a), from [90]; detection of roughness and waviness bandwidths (b), from [89].*

The phase-corrected Gaussian filter solves then many problems of the 2RC filters eliminating the phase shifting distortions, but it suffers still of some weaknesses: first of all it is very very sensitive to outliers (see section 2.3.3); furthermore it also suffers of end effects due to the non-changing nature of the weighing function.

2.3.3 Double-step Gaussian filters

The double-step Gaussian filtering is standardised in ISO 13565 part 1 [50] and known also as R_k filtering [17, 90] or two-stage filtering [23]. The filter

is an empirical technique representing an evolution of the Gaussian filter conceived for eliminating the sensitivity to outliers when filtering profiles of plateau-honed surfaces. The deep scratches of the first honing process, in fact, generate a measurement problem detected by Whitehouse in [47]: the mean line is "pulled down" generating overshoots or "ghost peaks" [7], more evident with 2RC filters, but detectable also with Gaussian filters. The solution proposed by ISO recommends therefore that the Gaussian filtering is applied twice, as illustrated in figure 2.14.

At the beginning a normal Gaussian filtering operation is performed (a) and the valleys have an evident influence on the mean line position. Therefore, the profile is "cut" and all the points beneath the mean line are substituted by the mean line itself (b). The Gaussian filtering operation is then done

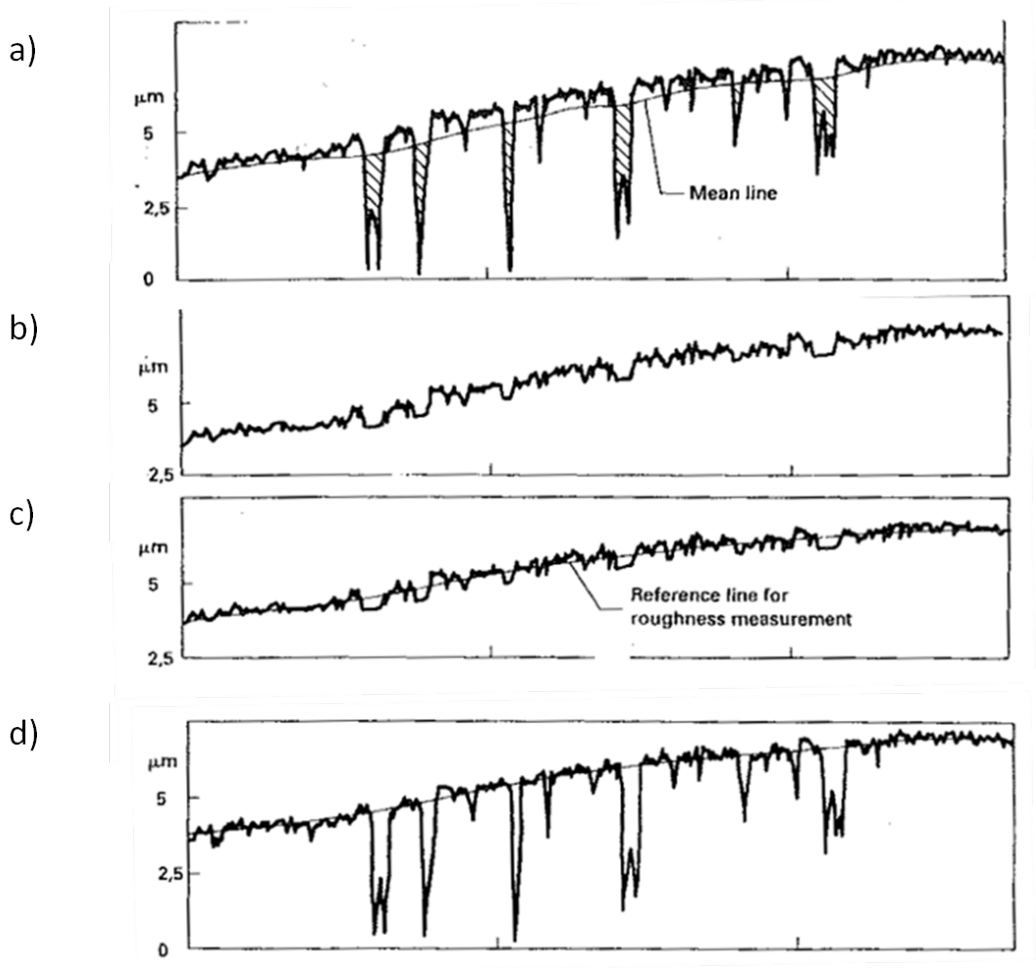

Figure 2.14: *Double-step Gaussian filtering procedure according to ISO 13565 part 1 [50].*

again on this artificial new profile (c) which eventually results in the attainment of the final mean line (d). This empirical procedure ensures thus the elimination of the aforementioned distortions and represents the current practice in the characterisation of functional surfaces..

2.3.4 Advanced filtering

The research on surface filtration, though, did not stop at double-step Gaussian filtering, and in the last decade a number of advanced solution have been explored and eventually collected and standardised in ISO 16610 [94–99]. In this section some of these techniques are reviewed.

Gaussian Regression filters

Gaussian Regression (GR) filters represent an improvement of linear Gaussian filters. Developed in the last ten years by German researchers such as Brinkmann et al. [100], GR filters solve the problem of end-effect distortions affecting regular Gaussian filtering operations. The solution consists in utilising a weighing function that could vary in proximity of the ends keeping the enclosed volume constant. Equation 2.2 would now appear like that:

$$\int_0^l (z(\xi) - w(x))^2 \cdot \tilde{s}(\xi - x)\mathrm{d}\xi \Rightarrow \min_{w(x)} \tag{2.4}$$

where:

$$\tilde{s}(\xi - x) = \frac{s(\xi - x)}{\int_0^l s(\xi - x)\mathrm{d}\xi} \tag{2.5}$$

The local variant weighing function $\tilde{s}(x)$ conforms then for every x position the volume condition [100]:

$$\int_0^l \tilde{s}(\xi - x)\mathrm{d}\xi = 1 \tag{2.6}$$

The minimisation problem is solved like before just substituting $s(x)$ with $\tilde{s}(x)$.
Practically speaking the weighing function is exactly a Gaussian bell far from the profile edges, whereas it varies locally at the edges proximity (figure 2.15).
Thanks to the changing weighing function, then, edge effect distortions are eliminated. This, however, is not the only advantage achievable with GR filters. The one that has been just presented, in fact, is the most basic GR filter, called 0^{th} order Gaussian Regression filter (GR0) because

Figure 2.15: *Weighing function of a GR filter [101].*

in equations 2.2 and 2.4 to each measured point is subtracted a constant value represented by the mean line $w(x)$ itself. This can generate distortions when strong form components are present in the profile to be filtered and end-effect can present themselves again, as shown in figure 2.16.

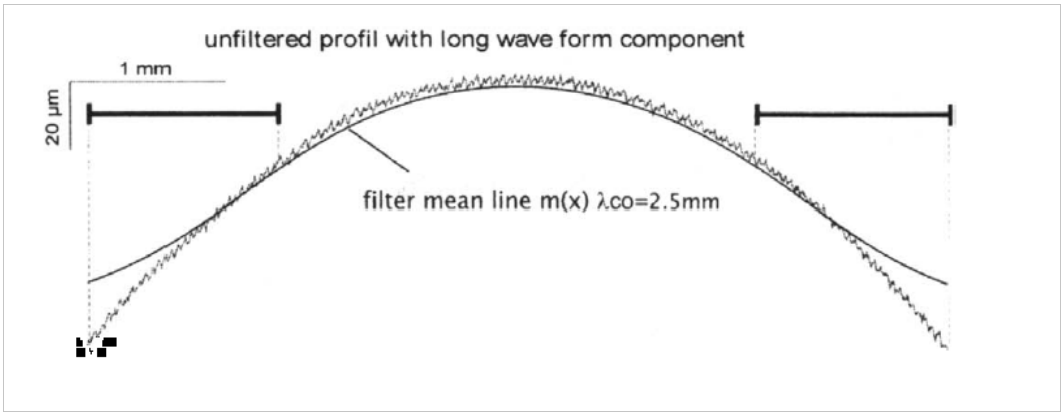

Figure 2.16: *GR0 filter behaviour in presence of strong form components [101].*

This problem has always been bypassed by removing the form component through polynomial fitting before performing any filtering operation, as depicted in figure 2.10.
Higher order GR filters, however, may make this operation not necessary anymore. Instead of a constant value, in fact, a polynomial of the first or second order can be subtracted from the measured data (equation 2.7). In this way, the form component in the neighbourhood of a random point x can be approximated by a polynomial curve within the measured length [23, 93, 102].

$$\int_0^l [z(\xi)-(w(x)+\beta_1(x)(\xi-x)+\beta_2(x)(\xi-x)^2]^2 \cdot s(\xi-x)\mathrm{d}\xi \Rightarrow \min_{w(x),\beta_1(x),\beta_2(x)} \tag{2.7}$$

By zeroing the partial derivatives in the directions of w, β_1 and β_2 a system of linear equations shown in [23, 93, 100–103] and in a more general form in section 3.2 is obtained delivering the mean line of the higher order Gaussian Regression filter [101].

$$w(x) = \int_0^l z(\xi) \cdot s_2(\xi - x) \mathrm{d}\xi \tag{2.8}$$

with $s_2(\xi) = (k_0(x) + k_1(x) \cdot \xi + k_2(x) \cdot \xi^2) \cdot s(\xi)$, where the new scaling functions from $k_0(x)$ to $k_2(x)$ are obtained from the inverted matrix of the linear equation system [101]. The new weighing function differs slightly from the GR0 case and so do its transmission characteristics, steeper but always equal to 50% at the cut-off wavelength, see figure 2.17.

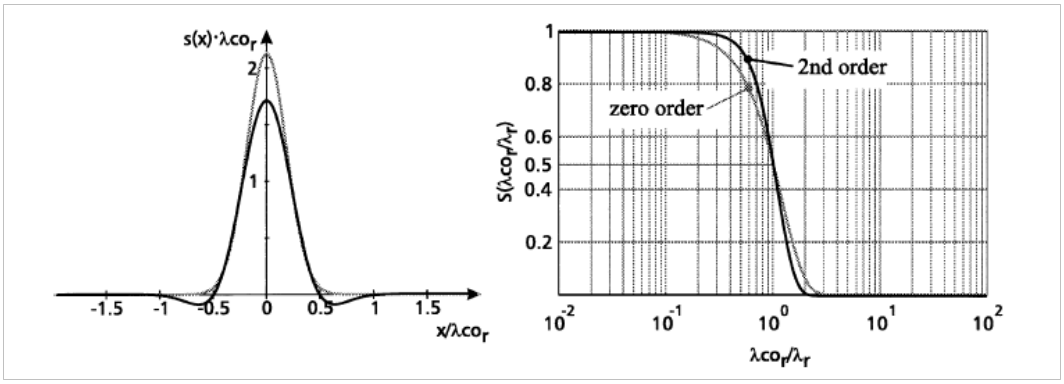

Figure 2.17: *GR2 weighing function and transmission characteristics comparison with the 0^{th} order (grey) case [100].*

The filter is now able to handle large form component without presenting distortions [101] (figure 2.18).
This, however, is not the "definitive" filter because it still suffers the drawback of all Gaussian filters: sensitivity to outliers such as deep scratches. It is not then suitable for handling surfaces for stratified functional properties. For that purpose a further evolution is represented by **Robust Gaussian**

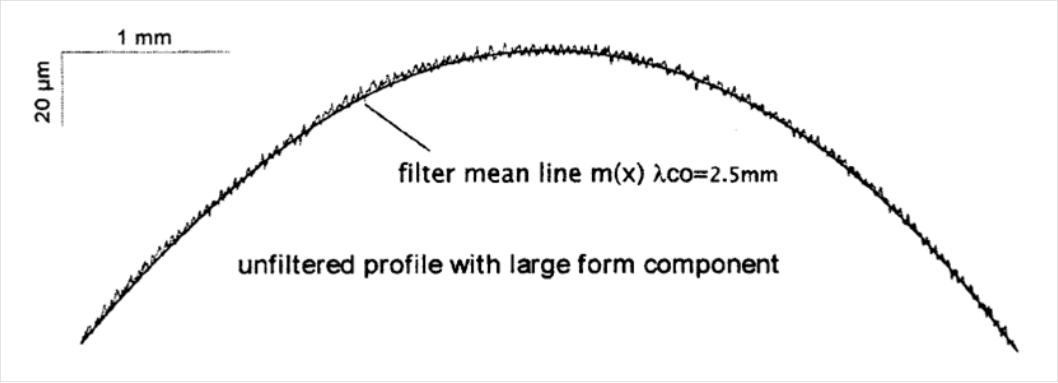

Figure 2.18: *GR2 filter behaviour in presence of strong form components [101].*

Regression filters. Robust filters cluster the advantages of both Double-step Gaussian filters and GR filters. They will be explained in chapter 3 as part of the solution chosen for the characterisation of MUFU surfaces.

Spline filters

Spline filters described in ISO 16610 part 22 [94] is a more recent linear filtering technique developed by Krystek [104, 105]. The development of these filters has been motivated by the desire to overcome some or all of the drawbacks of the linear Gaussian filter, such as end-effects and distortions due to large form-components. A spline is a linear combination of piecewise polynomials with a smooth fit between the pieces [94]. The degree of the spline relates to the highest degree of the polynomials, e.g. a cubic spline is made of third order polynomials. Unfortunately, the weighing function of the filter can not be given by a simple closed formula [94]. Therefore, a filter equation is often used to describe the filter [94]:

$$[1 + \beta\alpha^2\mathbf{P} + (1-\beta)\alpha^4\mathbf{Q}]w = z \tag{2.9}$$

being **P** and **Q** the n x n diagonal symmetric matrices:

$$P = \begin{bmatrix} 1 & -1 & & & & & \\ -1 & 2 & -1 & & & & \\ & -1 & 2 & -1 & & & \\ & & \ddots & \ddots & \ddots & & \\ & & -1 & 2 & -1 & & \\ & & & -1 & 2 & -1 & \\ & & & & -1 & 1 & \end{bmatrix} \quad Q = \begin{bmatrix} 1 & -2 & 1 & & & & \\ -2 & 5 & -4 & 1 & & & \\ 1 & -4 & 6 & -4 & 1 & & \\ & \ddots & \ddots & \ddots & \ddots & \ddots & \\ & & 1 & -4 & 6 & -4 & 1 \\ & & & 1 & -4 & 5 & -2 \\ & & & & 1 & -2 & 1 \end{bmatrix}$$

and $\alpha = \frac{1}{2\sin(\frac{\pi\Delta x}{\lambda_c})}$; β the tension parameter comprised between 0 and 1 controlling how tightly the spline fits through the data points; z the vector of measured data and w the vector of filtered data [94].
Spline filters have the same advantages of Gaussian Regression filters, which were developed approximately at the same time, with very much reduced boundary effect and good form-following properties [7].

Wavelet based filters

Wavelet based filters extend the traditional approach of subdividing the surface components into roughness, waviness and form components. The new approach consists in recognising that the topography of a surface can be broken into a multitude of textures from different sources and

having different scales [7]. Wavelet based filters represent the tool able to carry out this multi-scale analysis. Described in ISO 16610-29 [95], wavelet filters decompose the profile into a series of wavelets (equation 2.10, where $g(x)$ is the mother wavelet, a is the dilatation parameter and b is the translation parameter), scaled and shifted version of a mother wavelet (figure 2.19) rather than breaking the profile into a series of sine waves (Fourier transform).

$$g_{a,b}(x) = a^{-0.5} \cdot g(\frac{x-b}{a}) \tag{2.10}$$

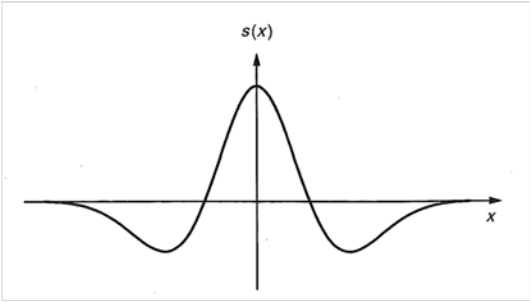

Figure 2.19: *Example of mother wavelet [95].*

The great advantage of this operation is the retention of spatial information besides frequency information. The signal is therefore broken into a series of scale-frequency components instead of the classical roughness-waviness-form division. This operation can be thought as ladder having multiple smoothing steps. The original profile S_0 is the first rung. For each step a smoother approximation of the previous rung is calculated together with the difference between the previous and the new rung (figure 2.20).

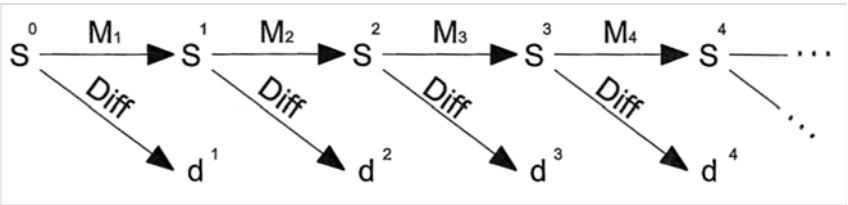

Figure 2.20: *Multiresolution separation using wavelet transform [95].*

An example of practical application of a wavelet filter using a cubic spline wavelet (as suggested by ISO 16610-29) is shown in figure 2.21.
Another difference with the Fourier transform lies indeed in the fact that many typologies of wavelet transforms can be devised enhancing the flexibility of this technique. First generations wavelet filters had problems in

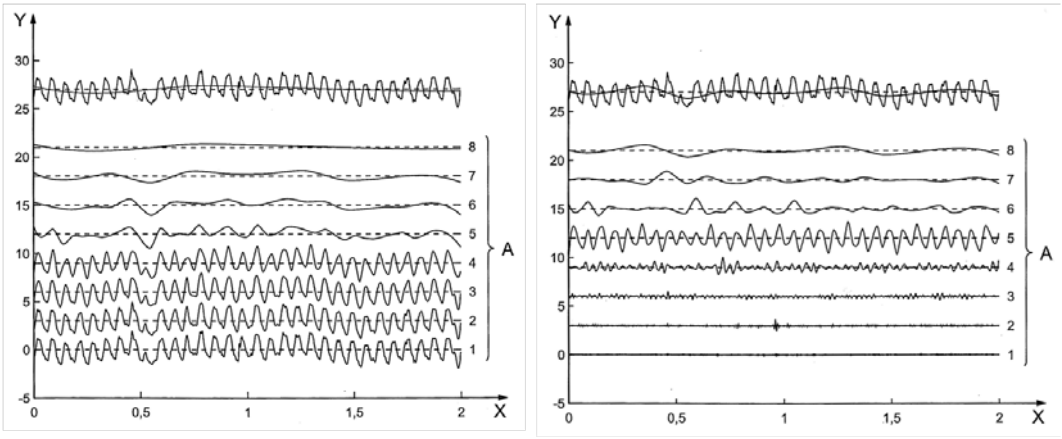

Figure 2.21: *Milled profile successively smoothed and differences between the multi scale profiles [95].*

extracting morphological features such as deep scratches in plateau honed surfaces [106, 107], therefore now techniques as complex wavelets have been recently developed by Jiang et al. [106, 107] eliminating the distortions.

Morphological filters

Morphological filters are quite different from the ones presented so far and more intuitive. Proposed in the 50s by Von Weingraber [108], morphological filters do not calculate a mean line of the measured profile during the filtering operation, as filters of the so-called M-system do; rather they provide an envelope of the profile and they belong therefore to the E-system [17]. Since the days of its introduction the envelope was represented by the locus of the center of a ball rolling over the surface corrected by the ball radius (figure 2.22); the roughness profile was obtained by subtracting the measured profile with the envelope [7].

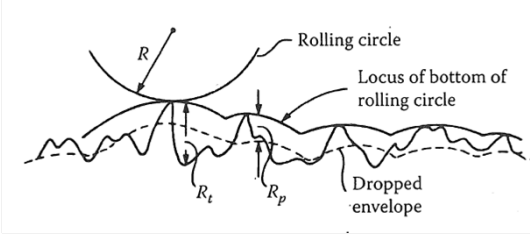

Figure 2.22: *Enveloper generate from rolling a circle over the profile, from [17].*

Nowadays, morphological filters have been standardized in ISO 16610 part 40 and 41 [98, 99] and the morphological operations defined. With reference

to figure 2.23, *dilation* is a morphological operation that expands an input set (the measured profile) by means of another (the structuring element), and corresponds to a Minkowski addition [98]. *Erosion* is another morphological operation which shrinks the measured profile by means of the structuring element, and corresponds to a Minkowski subtraction [98]. By combining these two operations, morphological filters are obtained, namely *opening* (erosion followed by dilation) and *closing* (dilation followed by erosion). Typical typologies of structuring elements are circular elements and simple segments [99].

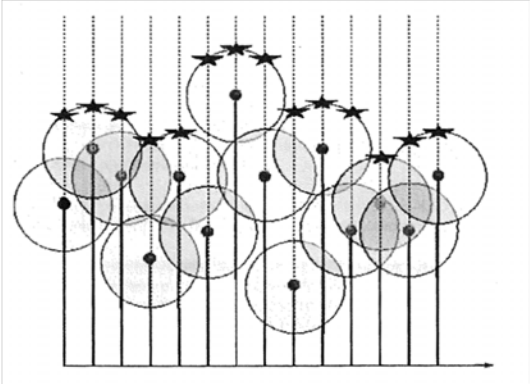

Figure 2.23: *Dilation with a circular element from [99].*

The radius of the circle or the length of the segment determine the level of filtration to be obtained. It is not a straightforward task the structuring element dimension and Whitehouse [17] affirms that suggested radii span from 3.2 mm to 25 mm. ISO [99] suggests to choose this dimension from a logarithmic series of scale values (1 µm, 2 µm, 5 µm, 10 µm, 20 µm, 50 µm, ...).
The major drawback of this technique is the long computation time and the size of the memory required for running the morphological operation, especially in the case of large data sets and large structuring elements [7]. Recently Lou, Jiang and Scott [109] have developed a fast algorithm for performing morphological filtering based on the calculation of the alpha shape through Delaunay triangulation. The fast algorithm proved more effective than naive algorithms especially when large data sets and large elements are involved.

2.3.5 Areal considerations

In areal analyses, instead of having a simple array, the measured data are represented by a matrix of surface heights $z(x, y)$. The y-direction must be taken now into account when handling the data and the filters extended

accordingly. In the case of the Gaussian filter, for example, equations 2.1 and 2.3 are respectively modified in this way:

$$s(x,y) = \frac{1}{\alpha\lambda_{cx}\alpha\lambda_{cy}} \cdot \exp\left[-\pi\left(\frac{x}{\alpha\lambda_{cx}}\right)^2 - \pi\left(\frac{y}{\alpha\lambda_{cy}}\right)^2 \right] = s(x) \cdot s(y) \quad (2.11)$$

$$w(x,y) = \int_0^{l_x}\int_0^{l_y} z(\xi,\eta) \cdot s(\xi - x, \eta - y)\mathrm{d}\xi\mathrm{d}\eta = z(x,y) \otimes s(x,y) \quad (2.12)$$

The convolution with the measured data is therefore done with a bell-shaped surface, three-dimensional version of the Gaussian curve rotated around its axis. Thanks to the separability of the Gaussian weighing function the filtration for an areal surface can be seen as the profile filtration in the x-direction followed by the profile filtration in the y-direction or vice versa [93]. Starting from these considerations, Gaussian Regression areal filters can be easily implemented. As in the profile case, the modified weighing function will maintain an enclosed volume equal to 1 (figure 2.24).

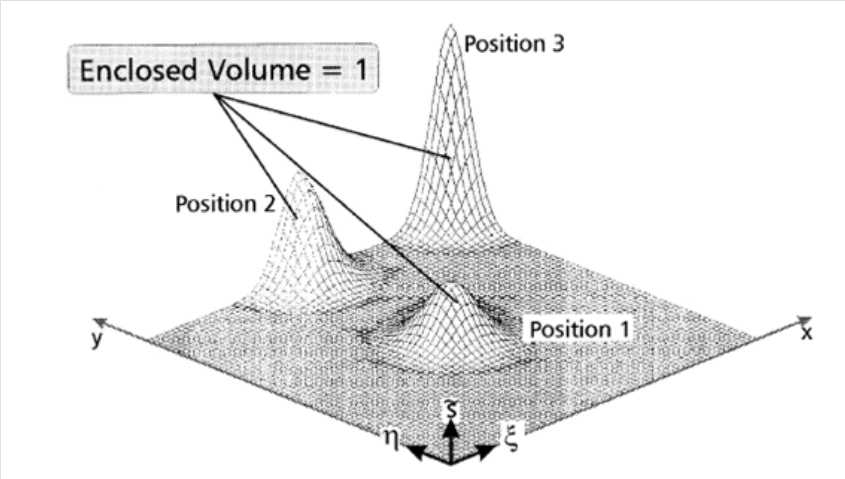

Figure 2.24: *Weighing function of an areal GR filter [100].*

Similarly, the other advanced filters can also be extended to the third dimension quite straightforwardly, as indicated by Krystek [110, 111] both in the case of spline and of morphological filters and by Jiang et al. [112] in the case of wavelet-based filters. The problem with surface filtering lies often in the slowness of the algorithms employed, hence research in improving this aspect is unrelentingly proceeding: Zeng, Jiang and Scott [93], for example, proposed an algorithm for improving the GR (and robust GR) filtering operations by means of a fast Fourier transform

(FFT); the already mentioned fast algorithm devised by Lou, Jiang and Scott [109] is particularly effective in the morphological filtration of areal measurements; etc.
While the operative implementation of surface filters did not present a major issue, the philosophy behind the areal filtering operation is quite revolutionary and Jiang and Whitehouse [7] consider it an important shift in surface metrology. ISO 25178-2 [4] introduces in fact the concept of *scale-limited* surface (figure 2.24), which puts aside the traditional approach differentiating among primary, waviness and roughness profiles.

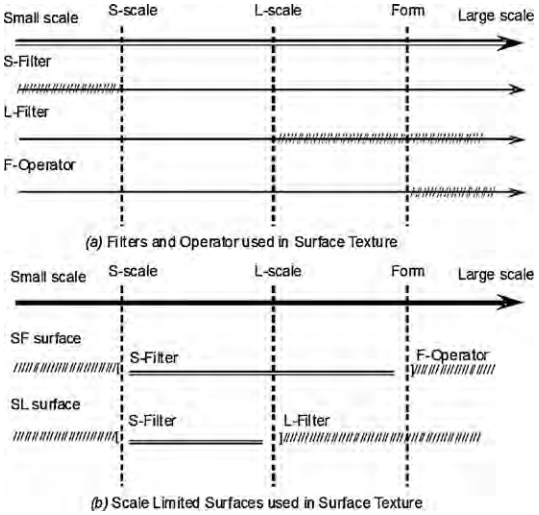

Figure 2.25: *Filters (S-filter or L-filter), operator (F-operator) and Scale-limited surfaces (SF or SL surface) [7].*

A SF surface is a surface obtained using a S-filter and a F-operator; practically a primary surface. The usage of a L-filter on a SF surface yields a SL surface, or roughness surface [7]. Both SF and SL surfaces are scale-limited surfaces [4].
According to ISO 25178-2, in areal surface characterisation only **one** group of parameters is defined (rather than three) depending on the scale-limited surface chosen, i.e. on the filter or operator employed [7].

2.4 Surface quantification

Once the filtering operation produced the roughness profile or the scale-limited surface, the last step of surface characterisation is quantification. Quantification implies extracting from the vector or the matrix of filtered data the statistical parameter that can describe best the surface. There exists a huge number of parameters, whereof the classical *Ra*, *Rq* and

Rz represent maybe the most known instances. Most of parameters for linear profiles are collected in ISO 4287 [88], but others are also defined in ISO 12085 [113] (motif parameters) and ISO 13565 [51, 52] (material bearing curve and probability plot parameters). As said above, there are three groups of parameters with alike definitions and to be used depending on the profile of interest, whereas there is instead only one group of areal parameters. The development of areal parameters is attributed to the research group commissioned by the European Community and coordinated by prof. Stout [11], which proposed 14 parameters dubbed the "Birmingham 14 parameters" [3]. The work started by Stout et al. was taken up by the following project "SURFSTAND" which revisited the parameter definitions, proposed appropriate changes and even introduced new parameters [3]. The outcome of that project eventually lay the basis for the development of ISO 25178-2 [4], the standard presenting all the parameters for surface analyses. Many of the areal parameters are simple extensions of profile parameters, but some of them are novelties. The standard differentiates between two sets, S-parameters and V-parameters according to the indications resulting from the SURFSTAND project [3]. The first set can be itself divided into different typologies encompassing height, spatial, hybrid and miscellaneous parameters [3], whereas the second set is dedicated to functional analyses by assessing the material volume and void volume [3, 7]. Moreover, ISO 25178-2 introduces fractal methods (not treated here) and, most importantly, provides the guidelines for feature characterisation, which represents another critical change in surface texture analysis allowing the assessment of structured surfaces [7].
Starting from height parameters, in table 2.1 the definitions as given in the several ISO standards are presented.
The height parameters are defined by the following equations (R-parameters are considered, the areal one are a simple extension to the third dimension of the definitions):

Arithmetical mean height

$$Ra = \frac{1}{l}\int_0^l |z(x)|\mathrm{d}x \tag{2.13}$$

Root mean square height

$$Rq = \sqrt{\frac{1}{l}\int_0^l z^2(x)\mathrm{d}x} \tag{2.14}$$

Table 2.1: Profile and areal height parameters as indicated in ISO standards [4, 88]).

Primary	**Waviness**	**Roughness**	**Areal**	**Meaning**
Pa	Wa	Ra	Sa	Arithmetical mean height
Pq	Wq	Rq	Sq	Root mean square height
Pp	Wp	Rp	Sp	Maximum peak height
Pv	Wv	Rv	Sv	Maximum valley depth
Pz	Wz	Rz	Sz	Maximum profile/surface height
Psk	Wsk	Rsk	Ssk	Skewness
Pku	Wku	Rku	Sku	Kurtosis
Pt	Wt	Rt	-	Total profile height
Pc	Wc	Rc	-	Mean height of profile elements

Skewness Rsk measures the asymmetry of the heights probability density function.

$$Rsk = \frac{1}{Rq^3}\left[\frac{1}{l}\int_0^l z^3(x)\mathrm{d}x\right] \tag{2.15}$$

Kurtosis Rku measures the sharpness of the heights probability density function.

$$Rsk = \frac{1}{Rq^4}\left[\frac{1}{l}\int_0^l z^4(x)\mathrm{d}x\right] \tag{2.16}$$

where l in this case is the sampling length, equal to the cut-off wavelength. Typically the profile length (evaluation length) is a multiple (usually 5 times) of the sampling length.
Rp and Rv are maxima positives and negatives respectively within l. Rz is the sum of the two terms. Rt, instead is the maximum peak and deepest valley vertical distance within the whole evaluation length. Areal analysis surpasses this differentiation being the sampling area the actual evaluation area. Rc is the mean height of the profile element (peak and adjacent valley). It requires spacing discrimination [88]. Its usage has been abandoned by ISO 25178-2.
Spatial parameters are listed in table 2.2

Table 2.2: Profile and areal spatial parameters as indicated in ISO standards [4, 88]).

Primary	**Waviness**	**Roughness**	**Areal**	**Meaning**
Psm	Wsm	Rsm	-	Mean width of the profile element
-	-	-	Sal	Auto correlation length
-	-	-	Str	Texture aspect ratio

As it can be seen from table 2.2, profile and areal spatial parameters definitions differ.
Similarly to Rc, Rsm considers each profile element composed by a peak (portion of the profile above the mean line) and a valley (portion of the profile below the mean line) and calculates its width. The average width within a sampling length is equal to Rsm. Areal parameters are less straightforward and are defined in this manner by ISO 25178-:

Autocorrelation length *Sal* is defined as the horizontal distance of the auto-correlation function ACF(tx, ty) which has the fastest decay to a specified value *s*, with $0 \leq s < 1$.

$$Sal = \min_{tx,ty \in R} \sqrt{tx^2 + ty^2} \tag{2.17}$$

where $R = \{(tx, ty) : ACF(tx, ty) \leq s\}$

Texture Aspect Ratio *Str* is derived from *Sal*. In fact it is defined as the "ratio of the horizontal distance of the ACF(tx, ty) which has the fastest decay to a specified value *s* to of the horizontal distance of the ACF(tx, ty) which has the slowest decay to *s*, with $0 \leq s < 1$".

$$Str = \frac{\min_{tx,ty \in R} \sqrt{tx^2 + ty^2}}{\max_{tx,ty \in Q} \sqrt{tx^2 + ty^2}} \tag{2.18}$$

where $R = \{(tx, ty) : ACF(tx, ty) \leq s\}$ and $Q = \{(tx, ty) : ACF(tx, ty) \geq s\}$
Stout [11] interprets the parameter in this way: for *Str* values higher than 0.5 the texture has stronger uniform aspect in all directions, while *Str* values lower than 0.3 indicate stronger long-crestness.
Hybrid and miscellaneous parameters are listed in table 2.3

Table 2.3: Profile and areal hybrid and miscellaneous parameters as indicated in ISO standards [4, 88]).

Primary	**Waviness**	**Roughness**	**Areal**	**Meaning**
PΔq	WΔq	RΔq	Sdq	Root mean square slope
Pmr(c)	Wmr(c)	Rmr(c)	Smr(c)	Material ratio of the profile/area
-	-	-	Sdr	Developed interfacial area ratio
-	-	-	Std	Texture direction (misc.)

Areal hybrid parameters are approximately the same as the profiles ones, with the addition of Sdr. They are thus defined:

Root Mean Square slope

$$R\Delta q = \sqrt{\frac{1}{l}\int_0^l \left(\frac{\partial z(x)}{\partial x}\right)^2 \mathrm{d}x} \tag{2.19}$$

Material ratio of the profile *Rmr(c)* is defined as the material length of the profile elements $Ml(c)$ at a given level c divided by the evaluation length [88]

$$Rmr(c) = \frac{Ml(c)}{ln} \tag{2.20}$$

Developed interfacial area ratio *Sdr* is defined as "the ratio of the increment of the interfacial area of the scale limited surface within the definition area over the definition area" [4]. The interfacial area is the surface area comprised within the definition area, that is of course bigger than the latter due to the roughness. *Sdr* can be thought as the ratio between the difference of the surface area and the definition area over the definition area. A large value of this parameter indicates significance of either the amplitude or the spacing or both [11].

$$Sdr = \frac{1}{A}\left[\int\int_A \left(\sqrt{\left[1 + \left(\frac{\partial z(x,y)}{\partial x}\right)^2 + \left(\frac{\partial z(x,y)}{\partial y}\right)^2\right]} - 1\right)\mathrm{d}x\mathrm{d}y\right] \tag{2.21}$$

Texture direction of the scale limited surface *Std* is a miscellaneous parameters representing the angle of the absolute maximum value of the angular power spectrum with respect to a specified direction θ.

The second set of parameters treated is the so-called V-set. The profile parameters corresponding to the areal V-set are defined in ISO 13565-2 [51] and ISO 13565-3 [52]. They are listed in table 2.4. Note that there are not parameter describing the waviness profile: the listed parameters are destined to surfaces with stratified functional properties, filtered with the double-step Gaussian filter under the hypothesis that the waviness is small [50].

Table 2.4: Profile and areal hybrid parameters as indicated in ISO standards [4, 51, 52]).

Primary	**Waviness**	**Roughness**	**Areal**	**Meaning**
Pk	-	Rk	Sk	Core depth
Ppk	-	Rpk	Spk	Reduced peak height
Pvk	-	Rvk	Svk	Reduced valley depth
Pmr1	-	Rmr1	Smr1	Peak material ratio
Pmr2	-	Rmr2	Smr2	Valley material ratio
Ppq	-	Rpq	Spq	Plateau root mean square deviation
Pvq	-	Rvq	Svq	Valley root mean square deviation
Pmq	-	Rmq	Smq	Relative material ration
-	-	-	Vvv	Valley void volume
-	-	-	Vvc	Core void volume
-	-	-	Vmp	Peak material volume
-	-	-	Vmc	Core material volume
-	-	-	Sxp	Peak extreme height

In the first five rows of table 2.4 are placed the parameters developed by the German automotive industry [10] and explained in ISO 13565-2. They are based on Abbot and Firestone's material ratio curve and their meaning is illustrated in figure 2.26.

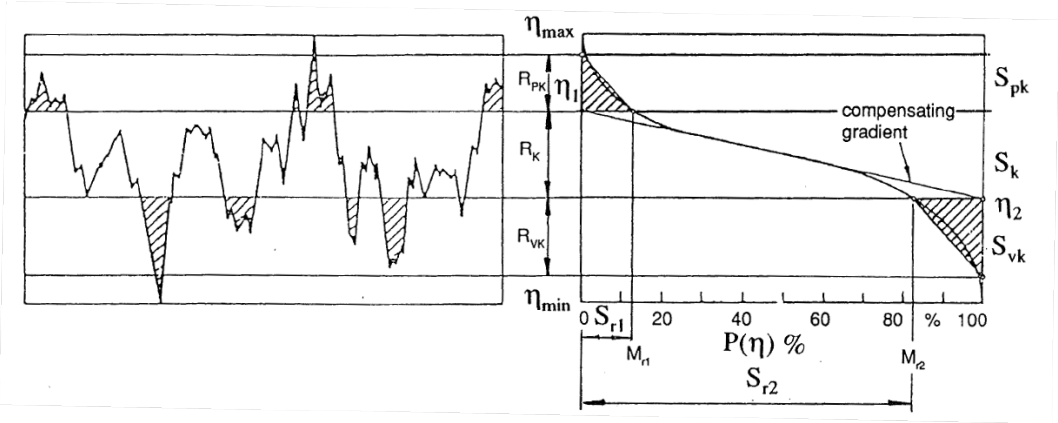

Figure 2.26: *Calculation of material ratio curve parameters [11].*

The procedure for calculating the German parameters starts from the detection of the 40%-line with the minimum slope. This line is prolonged till the vertical axes and at the intersections two points are detected. The material ratios at the two points' heights are respectively $Rmr1$ and $Rmr2$. The height difference between the two points is equal to Rk. Rpk and Rvk are respectively the heights of the triangles equivalent to the highlighted "peak" and "valley" areas and having as bases the segments connecting namely intersection point 1 - $Rmr1$ and intersection point 2 - $Rmr2$.
In the rows between 6 and 8 of table 2.4 the parameters proposed by the American automotive industry can be found. They are based on the material probability plot (figure 2.27): from the intersection of a line fitting the plateau region and one fitting the valley region Rmq is extrapolated, while Rpq and Rvq are the slopes of such lines. They are equivalent of the Rq values of the plateau roughness and valley roughness respectively [52].

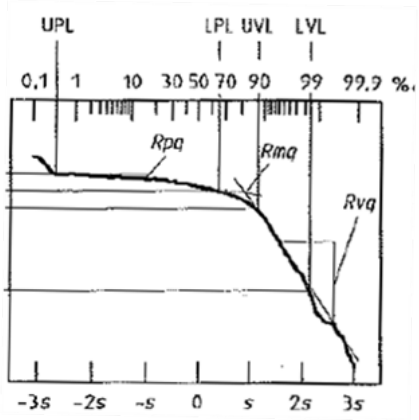

Figure 2.27: *Calculation of material probability plot parameters [52].*

The last five rows correspond to areal parameters. Four of the last five rows are related to material volume and void volume, concepts illustrated by figure 2.28.

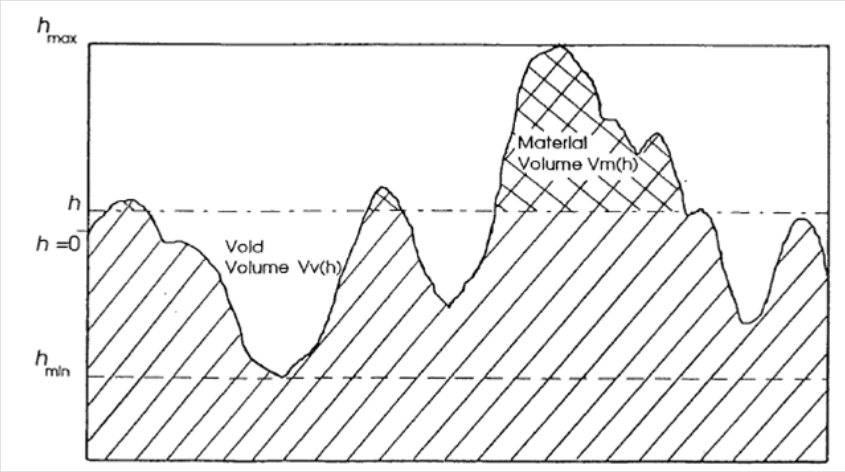

Figure 2.28: *Material volume and void volume [11].*

The void volume is "the air volume enclosed between a truncation plane at a given level parallel to the mean plane and the material beneath the plane" [11]. Conversely, the material volume is the volume of the material per unit area at a given material ratio calculated from the areal material ratio curve [4]. The remaining parameters are described by the following formulas:

Void volume

$$Vv(mr) = \frac{K}{100 \quad [\%]} \int_{mr}^{100\%} [Sdc(mr) - Sdc(q)]dq \tag{2.22}$$

where *Sdc(mr)* is the inverse material ratio and *K* is a constant to convert milliliters per meters square.
The dale and core void volume are therefore defined as $Vvv = Vv(80\%)$ and $Vvc = Vv(10\%) - Vv(80\%)$.

Material volume

$$Vm(mr) = \frac{K}{100 \quad [\%]} \int_{0}^{mr} [Sdc(q) - Sdc(mr)]dq \tag{2.23}$$

The peak and core material volume are defined as $Vmp = Vm(10\%)$ and $Vmc = Vm(80\%) - Vm(10\%)$.

Peak extreme height

$$Sxp = Smr(p\%) - Smr(q\%) \tag{2.24}$$

where $p = 97.5\%$ and $q = 50\%$.

There are still a number of parameters which have not been treated yet. Those are the profile parameters called motif parameters which have been developed by French car industry [10] and described in ISO 12085 [113]. Differently from the parameters presented so far, which are mostly dependent on the mean line, motif analysis requires an envelope of the profile (E-system). The envelope is obtained first by opportunely merging the peaks into few significant features and then by connecting the tops of those together. The parameters are then calculated directly from the primary profile and the envelope. They are listed in table 2.5. Though being of secondary importance within this framework (and therefore not further discussed), motif analysis makes use of a merging operation for detecting significant features which is of fundamental importance in areal feature characterisation, see section 2.4.1.

Table 2.5: Profile and areal hybrid parameters as indicated in ISO standards [4, 113]).

Primary	**Waviness**	**Roughness**	**Areal**	**Meaning**
-	AW	AR	-	Motifs mean spacing
-	W	R	-	Motifs mean depth
-	Wx	Rx	-	Motifs maximum depth
-	Wte	-	-	Motifs waviness total depth

2.4.1 Areal feature characterisation

The last section of ISO 25178-2 concerns areal feature characterisation, a novel approach studied at the end of the 90s by Scott [114] and by the French researchers Bleau and Leon [115] and Barré and Lopez [116]. The method described by the standard is actually based on a much older work (from some hundred and forty years ago) carried out by Maxwell [117] introducing a methodology for dividing the landscape. According to Maxwell, the territory is divided in regions named hills and dales: a Maxwellian hill is an upward region culminating in a peak; a dale is a

downward region culminating in a pit. The boundaries between subsequent hills are lines named "course lines" (watercourses); whereas the boundaries between subsequent dales are lines named "ridge lines" (watershed lines). Moreover "saddle" points are defined as the crossing of course and ridge lines. This method represented a good starting point for feature recognition and identification, but is not satisfactory if taken "as it is". The surface would in fact result over-segmented and divided into a large quantity of insignificant tiny dales rather than few significant large dales. The insignificant peaks and dales must therefore be merged into significant ones in an operation equivalent to motif combination (the dale is the areal equivalent of a profile motif [114]) before further analyses can be carried out. A correct merging operation will result in few critical peaks, pits and saddle points as well as few critical ridge and course lines, as illustrated in the contour map of figure 2.29.

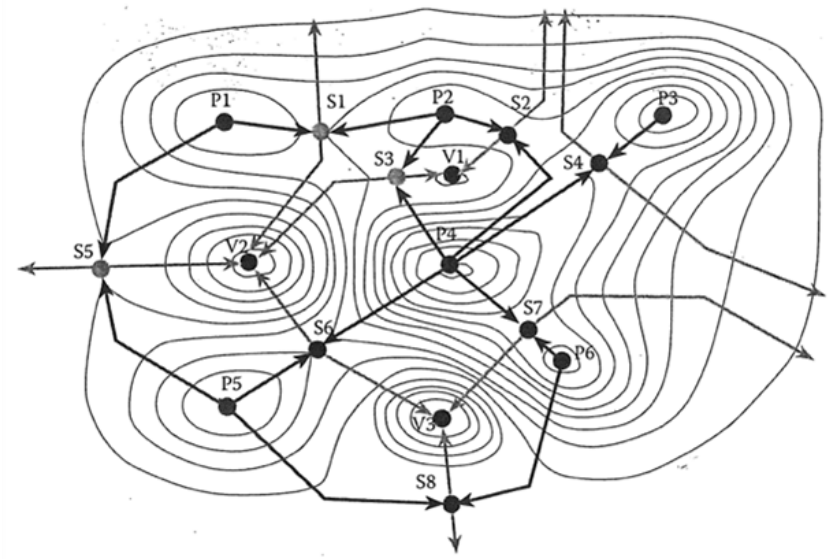

Figure 2.29: *Contour map showing critical lines and points (peaks P, pits V and saddles S) [4, 24].*

The first step for merging surface features is to organise them in an orderly way so it is easier to visualise them. This can be done by calculating the so-called "full change tree", a graph connecting all peaks and pits of the surface by means of saddle points 2.30(a).
After this fundamental operation, the actual merging operation is carried out. It consists of simplifying the change tree by eliminating the insignificant small features and unifying into bigger, significant ones. This operation is called "Wolf pruning". The assumption is that the set of significant peaks or pits remains the same after each merging. A threshold is initially stated,

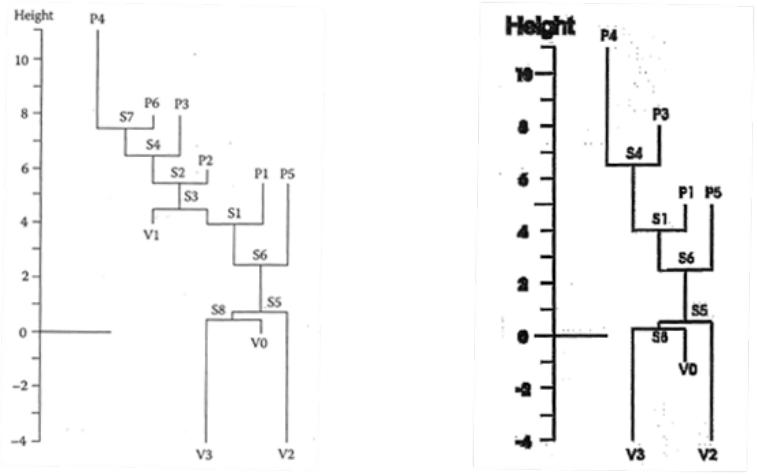

(a) Full change tree.

(b) Wolf-pruned change tree

Figure 2.30: *Full and Wolf-pruned change trees [4].*

setting the condition that must be obeyed for a point to be considered significant for the pruning operation. The condition can be for example a percentage of the total areal height (Wolf pruning percentage). The vertical distance between each peak (pit) and the adjacent saddle point is calculated, and if the smallest does not comply with the condition, the peak (pit) is eliminated and the adjacent peak connected to another saddle point. The process continues until all points comply with the condition thus obtaining the wolf pruned change tree (figure 2.30(b)). Once completed this operation, the surface is ready for quantification: a number of parameter can thence be calculated, listed in the following paragraphs as defined by ISO 25178-2 [4].

Density of peaks *Spd* This parameter counts the number of significant peaks per unit area. It is defined as follows:

$$Spd = \text{FC; H; Wolfprune:X\%; All; Count; Density} \tag{2.25}$$

FC means feature characterization; H refers to hill; *Wolfprune:X%* is the criterial of size for segmentation, in this case are considered significant all the hills above a certain percentage x% of the Sz. If not specified this percentage is 5%. *All* refers to both open hills (connected to the edge) and closed hills (not connected to the edge). *Count* means that every attribute fulfilling the parameters has a value of 1. *Density* is the sum of all attribute values divided by the definition area.
This way of presenting the parameters is common for every feature parameter.

Arithmetic mean peak curvature *Spc* It is the arithmetic mean of the principle curvatures of peaks within a definition area:

$$Spc = \text{FC; P; Wolfprune:X\%; All; Curvature; Mean} \tag{2.26}$$

Where *P* refers to Peak, and *Curvature* is the local curvature at critical point.

Ten Point Height of surface *S10z* Average value of the heights of the five peaks with largest global peak height added to the average value of the heights of the five pits with largest global pit height, within the definition area.

$$S10z = S5p + S5v \tag{2.27}$$

where S5p and S5v are mathematically defined as follows:

$$S5p = \text{FC; H; Wolfprune:X\%; Top:5; lpvh; Mean} \tag{2.28}$$

$$S5v = \text{FC; D; Wolfprune:X\%; Bot:5; lpvh; Mean} \tag{2.29}$$

Top:5 and *Bot:5* mean that only the highest five peaks and lowest 5 pits are considered significant. *lpvh* refers to peak or pit height.

Closed Dale Area *Sda(c)* ands Closed Hill Area *Sha(c)* It's the average area of dales connected to the edge at height *(c)*

$$Sda(c) = \text{FC; D; Wolfprune:X\%; Open:c; Area; Mean} \tag{2.30}$$

The same goes for the hills connected to the edge:

$$Sha(c) = \text{FC; H; Wolfprune:X\%; Open:c; Area; Mean} \tag{2.31}$$

Closed Dale Volume *Sdv(c)* ands Closed Hill Volume *Shv(c).* It's the average volume of dales connected to the edge at height *(c)*

$$Sdv(c) = \text{FC; D; Wolfprune:X\%; Open:c; VolE; Mean} \tag{2.32}$$

The same goes for the hills connected to the edge:

$$Shv(c) = \text{FC; H; Wolfprune:X\%; Open:c; VolE; Mean} \tag{2.33}$$

2.5 Traceability of surface measurements

Traceability of surface measurements is a matter that can be easily overlooked, but is actually of paramount importance. Traceability is defined by the ISO International Vocabulary of Metrology (VIM) as [118]:

> "property of a measurement result whereby the result can be related to a reference through a documented unbroken chain of calibrations, each contributing to the measurement uncertainty."

Simply speaking, the characterisation of a surface ultimately yields a value (or a set of values) quantitatively describing the surface itself. This value, as definitive it may seem, has little importance if it cannot be compared nationally and internationally and thereby accepted worldwide. In order to achieve this, the value must be associated to an **uncertainty**, which is a non-negative parameter characterising the dispersion of the values being attributed to the measurand [118]. A result consists of the value (or indication) and its uncertainty. The uncertainty of the result must contain the one of the measuring system, which must be **calibrated** by measuring some kind of reference standard and by providing on its turn an uncertainty to such measurement. This uncertainty must include the uncertainty carried by the standard itself which had been previously measured by other means carrying on their turn a (lower) uncertainty and so on up to the meter definition. This is the so-called traceability chain: in figure 2.31 is illustrated how roughness measurements performed at DTU are traceable to the meter through standards developed at PTB.
In the case of texture measurements the standards to be used for calibration are defined in ISO 5436-1 [119] in the profile case and in ISO 25178-701 [120] in the areal case. There are several types of surface texture calibration standard, summarized in table 2.6. In figure 2.32 a roughness measurement standard is shown similar to the ones present at DTU-CGM (Center for Geometrical Metrology) for the calibration of the styli instruments there present.
Thanks to these standards the surface texture measurement can be made traceable to the meter if a proper uncertainty budget is performed and associated to the measured values. Assessing the uncertainty of a measurement is not an easy task. The uncertainty assessment guidelines are provided by the "Guide to the expression of uncertainty in measurement", universally known as (GUM) [121]. The first step in assessing the uncertainty is to recognise all the errors that can affect a measurement, differentiating between *systematic* and *random* errors. A **systematic** error is a "component of measurement error that in replicate measurements remains constant or varies in a predictable manner", whereas a **random** error is a "component

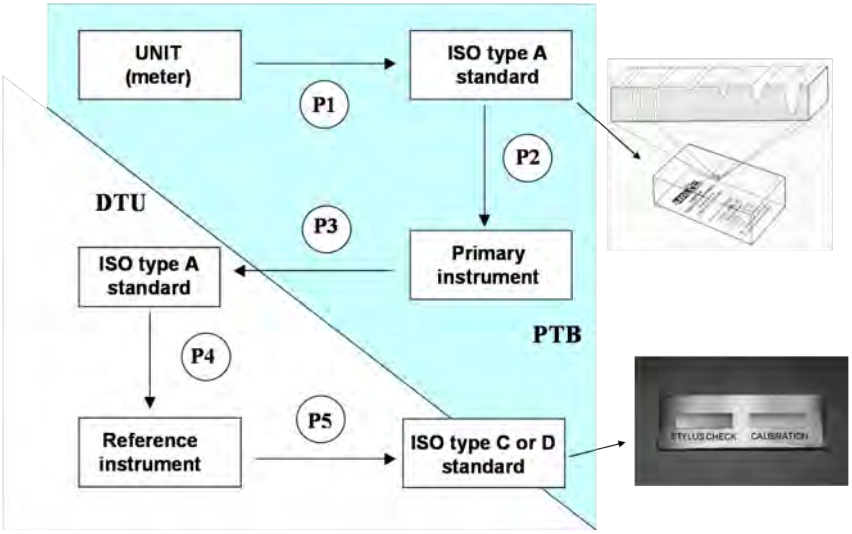

Figure 2.31: *Roughness traceability chain. DTU is traceable to the meter through PTB [16].*

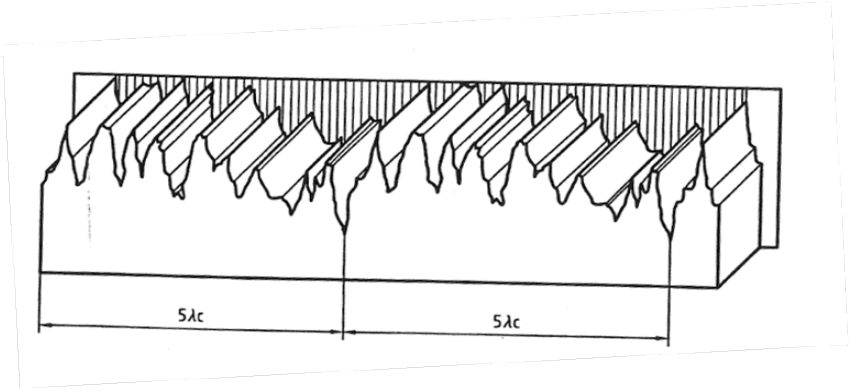

Figure 2.32: *Roughness measurement standard [119].*

of measurement error that in replicate measurements varies in an unpredictable manner" [118]. According to GUM, every effort must be made in order to identify the systematic components and correct them whenever possible. Once the value resulting for a measurement has been thus corrected, the uncertainty evaluation can start by identifying all its possible contributions sourcing mostly from the random errors. A measurement can be modelled in the generic way:

$$Y = f(X_1, \ldots, X_n) \tag{2.34}$$

where X_i are the input quantities sources of uncertainty. These can be the very various including the operator, the repetition of the procedure, the

Table 2.6: Type of surface texture measurement standards [119, 120]).

Type	Name
A	Depth measurement standard
B	Tip condition measurement standard
C	Spacing measurement standard
D	Roughness measurement standard
E	Profile coordinate measurement standard
ER1	Measurement standard with two parallel grooves
ER2	Measurement standard with four grooves forming a rectangle
ER3	Measurement standard with a circular groove
ES	Measurement standard with a sphere/plane intersection
CS	Measurement standard with a contour profile
CG	Crossed-grating measurement standard

environment, the instrument and, of course, the calibration standard. The input contributions can be divided in two groups: *group A* and *group B*. **Group A** contributions are estimated by statistical analysis usually by repeated measurements; **group B** contributions are calculated from assigned probability distributions (normal, triangular, rectangular, U-shaped, etc.) from past measurement experiences, calibrated certificates, etc.
Once the different sources of uncertainty are estimated the *combined standard uncertainty* is calculated, described by equation 2.35:

$$u_c(y) = \sqrt{\sum_{i=1}^{N} \left(\frac{\partial f}{\partial x_i}\right)^2 \cdot u^2(x_i) + 2\sum_{i=1}^{N-1}\sum_{j=i+1}^{N} \frac{\partial f}{\partial x_i}\frac{\partial f}{\partial x_j} u(x_i, x_j)} \tag{2.35}$$

where the second term under the square root is used in case of correlated input quantities. In most cases the function describing the measurement is linear and the input quantities are uncorrelated, so that the second term is equal to 0.
The expanded uncertainty U is equal to $U = k \cdot u_c$, where k is a coverage factor chosen on the desired level of confidence, see table 2.7.
By far, the most common coverage factor used is $k = 2$. The final result of a measurement is therefore given by the equation 2.36:

Table 2.7: Coverage factor k corresponding to different levels of confidence [122]).

Level of confidence p%	68.27	90	95	95.45	99	99.73
Coverage factor k	1	1.645	1.96	2	2.576	3

$$y \pm U = y \pm (k \cdot u_c) \tag{2.36}$$

These equations are valid generally for all types of dimensional measurement. In the particular case of roughness measurements, the final value of a measurement is equal to:

$$R = \bar{R} \pm U \tag{2.37}$$

where U is calculated by equation 2.35 reduced in this way [16]:

$$U = 2\sqrt{u_{inst}^2 + u_s^2} = 2\sqrt{u_n^2 + u_r^2 + u_b^2 + u_s^2} \tag{2.38}$$

where u_s is the uncertainty caused by variations in the roughness of the specimen in different locations $u_s = \frac{STD_s}{\sqrt{n}}$, being n the number of measurements carried out on the specimen and *STD* the standard deviation; and u_{inst} is the uncertainty of the calibrated instrument, composed by three contributions u_n,u_r and u_b. In particular, u_n is the uncertainty of the roughness calibration standard taken from a certificate ($u_n = \frac{U_n}{2}$); u_r is the repeatability of the instrument in measuring the standard ($u_r = \frac{STD_r}{\sqrt{n}}$); u_b is the uncertainty contribution due to the background noise $Rx0$ by measuring an optical flat and assuming a rectangular distribution ($u_b = \frac{1}{2} \cdot \frac{Rx0}{\sqrt{3}}$) [16].
The calibration certificate for the instrument mostly used in this project, an independent datum Form TalySurf (FTS) with maximum traversing length equal to 50 mm (figure 2.33), is attached in appendix A.

2.6 Summary

In this chapter the current approach to surface characterisation has been presented. Acknowledging its central role among generation, design and function, surface characterisation is composed by measurement, visualisation and quantification. The most common measuring instruments have been listed and described. Afterwards, visualising the results obtained by the measurement and knowing the type of surface which is dealt with, the most suitable filtering procedure and technique must be chosen in order to properly adjust and treat the raw data. Finally, from the filtered data,

Figure 2.33: *Form TalySurf 50 Inductive.*

a parameter quantifying the surface in analysis must be selected always keeping in mind its relevance in relation to the surface function. The filtering techniques and parameters defined in the standards have been here described. The last section of the chapter dealt with the traceability of a measurement, fundamental issue for accepting a measurement result worldwide. Traceability is indissolubly linked to measurement uncertainty. The theory of uncertainty calculation has been briefly exposed with eventually discussing the case of uncertainty calculation in roughness measurements.

Chapter 3

Characterisation of MUFU surfaces

This chapter deals with the characterisation of MUFU surfaces, one of the main challenges of the present work. The basis to start is the state-of-the-art approach to characterisation described in chapter 2. The current practice is investigated highlighting its limitations in this task and solutions are proposed [123–126]. The starting point in characterising MUFU surfaces is to utilise current standards. From now onwards, the profile case is considered. In chapter 1 it has been noted how MUFU surfaces can be compared to plateau-honed surfaces: both surface typologies are produced through a two-steps manufacturing process, both have a uppermost flat region and deep valleys, both have stratified functional properties. Given these similarities, the procedure will naturally follow the blue path of figure 2.10 for the primary assessment of MUFU surface profiles.

3.1 Filtration of MUFU surfaces with ISO 13565-1

After attaining the primary profile, the procedure indicates the usage of the double-step Gaussian filter standardised in ISO 13565-1 [50] for obtaining the roughness profile in order to proceed with the quantification. The assumption in using this filter is to have small or negligible waviness. The same assumption is made in this case and will be generally valid in the following.
The mean line position calculated after filtering a primary MUFU profile through a double step Gaussian filter is shown in figure 3.1. The filter used had a cut-off length λ_c equal to 0.8 mm. Unless otherwise specified, all the profile visualisations, data filtering and parameter calculations herein presented are done by means of the software SPIP^{TM} developed by Image Metrology [74].
As it can be seen from figure 3.1, the double step Gaussian filter fails in its attempt to fit a line through the plateau region. Differently from

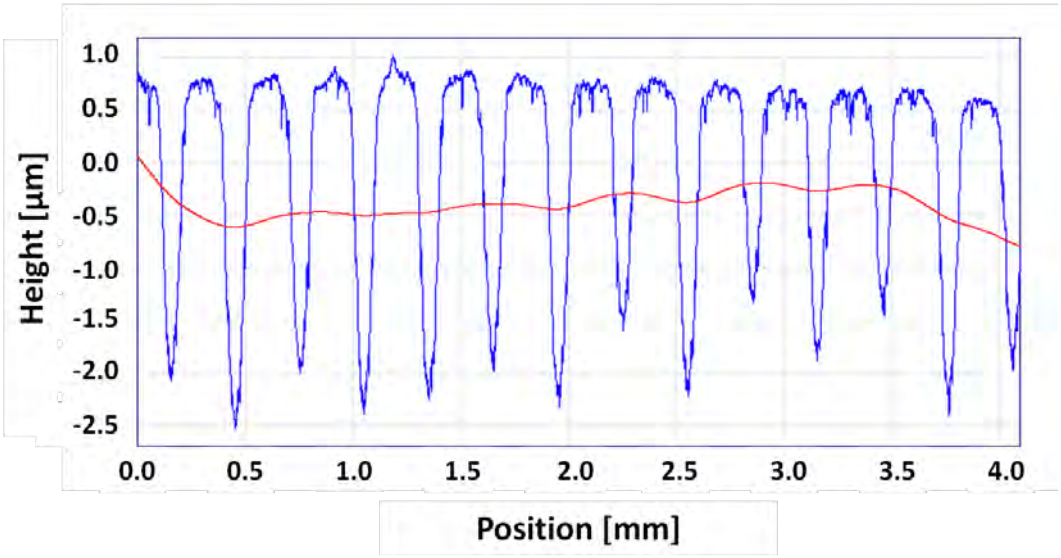

Figure 3.1: *Mean line position after double step Gaussian filtering of a MUFU profile.*

plateau-honed surfaces which feature narrow furrows, MUFU surfaces have in fact broader valleys containing many more sampled points. The first Gaussian operation fits therefore a line in the center of these valleys, at a too low level for the second operation to rise the mean line to the plateau level. Moreover, the deterministic nature of these surfaces and the amount of sample points at a valley level generate a "ondulate" mean line causing distortions as "ghost peaks". It is therefore conspicuous that the characterisation by means of ISO 13565 cannot take place at these conditions. Before starting with the quantification, the first challenge is thus to find a method for producing a sound mean line (or better said, reference line) passing through the plateau region without inducing distortions. A solution can be performing iterative Gaussian filtering operations rising at each iteration the level of the mean line until it fits through the plateaus. This approach based on an iterative procedure is taken up and refined by more sophisticated **Robust Gaussian Regression (RGR)** filters, briefly mentioned in chapter 2.

3.2 Robust Filtering

The Robust Gaussian Regression filtering technique is a further evolution of the Gaussian filter, which has been described by Jiang, Brinkmanm, Seewig et al. [23, 93, 100–103] as well as in ISO 16610-31 [96]. Precisely, RGR filters are an evolution of Gaussian Regression filters picking up their peculiarities of eliminating end effects and of following carefully the form of the object

if a 2nd order Gaussian Regression is utilised. The problem with GR filters as well as of other linear filters is that they are extremely sensitive against outliers such as deep scores or jutting out peaks [93, 100, 101, 103]. The RGR technique provides an iterative and robust solution to the problem calculating a profile reference line with less or zero weight given to the outliers depending on their magnitude. The filter equations must be therefore changed in order to achieve this. Equation 2.7 can be generalised in the following way:

$$\int_0^l \rho[z(\xi) - (w(x) + \beta_1(x)(\xi - x) + \beta_2(x)(\xi - x)^2] \cdot s(\xi - x)\mathrm{d}\xi \Rightarrow \min_{w(x),\beta_1(x),\beta_2(x)} \tag{3.1}$$

where $\rho(\cdot)$ is the error metric function used for the *m-estimation*. A $\rho(x) = x^2$ represents the already discussed GR filter of the 2nd order (GR2), but in the pursuit of robust properties, another *m-estimator* different from the least square one must be used. Several other functions can be instead defined and, among those, the Beaton function or Tukey estimator is the one commonly used for functional surfaces [23, 93, 100–103]. The Beaton function is illustrated by figure 3.2.

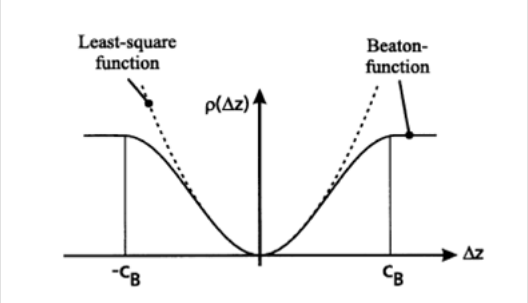

Figure 3.2: *Least-square function and Beaton function [100].*

The difference between the least square function and Beaton function depicted in figure 3.2 is explanatory of their behaviour. In presence of outliers, i.e. deep scores, the residual Δz enters the minimisation problem with great impact, hence the attraction of the mean line towards the valleys. Differently, the Beaton function follows the least-square one only up till a certain threshold c_B, after which the residual enters the minimisation problem with a constant value [100]. The utilisation of the Beaton function leads to the modification of the minimisation problem introducing an additional re-weighing function $\delta(\cdot)$ (equation 3.2) [100, 101]:

$$\int_0^l [z(\xi)-(w(x)+\beta_1(x)(\xi-x)+\beta_2(x)(\xi-x)^2]^2\cdot\delta(\xi)\cdot s(\xi-x)\mathrm{d}\xi \Rightarrow \min_{w(x),\beta_1(x),\beta_2(x)} \tag{3.2}$$

which is solved as for GR filters by zeroing the partial derivatives in the directions of w, β_1 and β_2 [102]. The equation system is a more general case than the one for GR2 filters and has the following form [102]:

$$\begin{bmatrix} A & B & C \\ B & C & D \\ C & D & E \end{bmatrix} \cdot \begin{bmatrix} w(x) \\ \beta_1(x) \\ \beta_2(x) \end{bmatrix} = \begin{bmatrix} F0 \\ F1 \\ F2 \end{bmatrix} \tag{3.3}$$

where:

$A(x) = \int_0^l \delta(\xi)s(\xi-x)\mathrm{d}\xi$; $B(x) = \int_0^l \delta(\xi)(\xi-x)s(\xi-x)\mathrm{d}\xi$;
$C(x) = \int_0^l \delta(\xi)(\xi-x)^2s(\xi-x)\mathrm{d}\xi$; $D(x) = \int_0^l \delta(\xi)(\xi-x)^3s(\xi-x)\mathrm{d}\xi$;
$E(x) = \int_0^l \delta(\xi)(\xi-x)^4s(\xi-x)\mathrm{d}\xi$; $F0(x) = \int_0^l \delta(\xi)z(\xi)s(\xi-x)\mathrm{d}\xi$;
$F1(x) = \int_0^l \delta(\xi)z(\xi)(\xi-x)s(\xi-x)\mathrm{d}\xi$; $F2(x) = \int_0^l \delta(\xi)z(\xi)(\xi-x)^2s(\xi-x)\mathrm{d}\xi$.

The re-weighing function $\delta(\cdot)$ is defined as:

$$\delta(x) = \begin{cases} \left(1-\left(\dfrac{\Delta z}{c_B}\right)^2\right)^2 & \text{for} \quad \left|\dfrac{\Delta z}{c_B}\right| < 1 \\ 0 & \text{otherwise} \end{cases} \tag{3.4}$$

The threshold value c_B is most commonly calculated using the median absolute deviation (MAD):

$$c_B = 4.4\text{median}(|z(x)-w(x)|) \tag{3.5}$$

For a normal distribution, it approximately holds that the standard deviation σ equals 1.483MAD. The threshold value c_B is often estimated as three times the standard deviation of the profile distribution, resulting in equation 3.5 [127]. This definition of c_B intrinsically implies the iterative nature of the robust filter. Starting from a first-guess reference line, the threshold is calculated, hence the re-weighing function and again the reference line. The cycle then starts again until a certain convergence condition is met, e.g. small difference between two consecutive thresholds. The iterations flowchart is shown in figure 3.3 as presented by [100].
Usually, the initial threshold c_B is equal to infinite, meaning that all the profile points are considered in the calculation of the first-guess reference line which is the result of a normal Gaussian filtering operation. As the iterations proceed, the outliers are given zero weight and the reference line is elevated supposedly at a plateau level (figure 3.4).

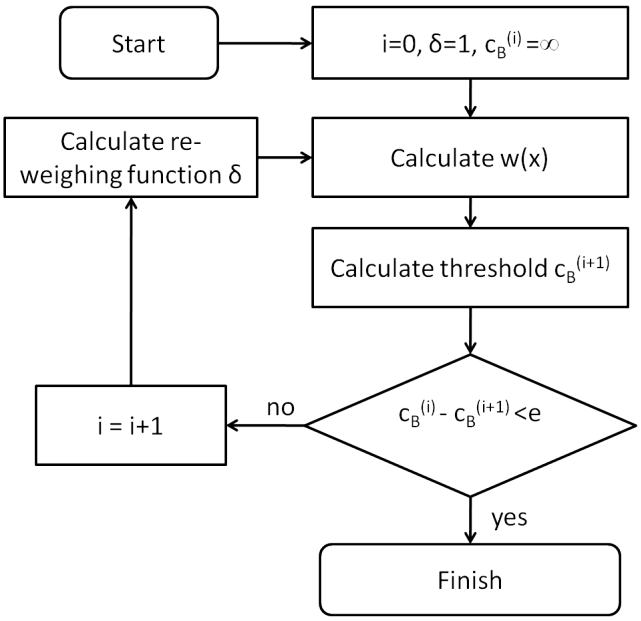

Figure 3.3: *Flowchart of the robust filtering algorithm [100].*

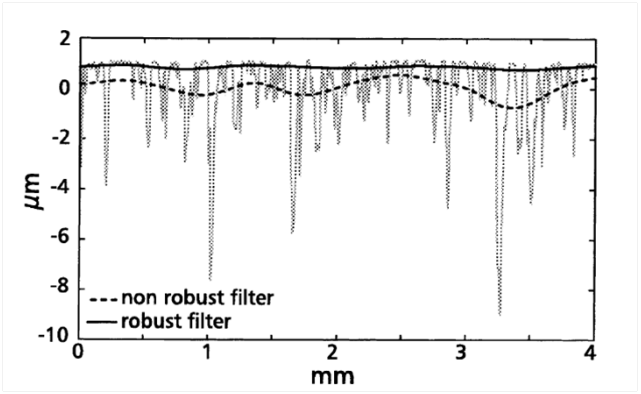

Figure 3.4: *Profile extraction of a plateau honed surface with a non robust and robust filter line [100].*

The iterative algorithm, though, can be extremely time consuming and inefficient. For this reason Zeng et al. [93, 102] developed a fast algorithm based on the Fast Fourier Transform (FFT) to speed the calculation time up. In the fast algorithm, the functions of the system 3.3 are defined as follows, being $FT(\cdot)$ and $IFT(\cdot)$ the forward and inverse Fourier transforms respectively [93, 102]:

$A(x) = IFT(FT(\delta(x))FT(s(x)))$; $B(x) = IFT(FT(\delta(x))FT(xs(x)))$;
$C(x) = IFT(FT(\delta(x))FT(x^2s(x)))$; $D(x) = IFT(FT(\delta(x))FT(x^3s(x)))$;

$E(x) = IFT(FT(\delta(x))FT(x^4 s(x)))$; $F0(x) = IFT(FT(\delta(x)z(x))FT(s(x)))$;
$F1(x) = IFT(FT(\delta(x)z(x))FT(xs(x)))$; $F2(x) = IFT(FT(\delta(x)z(x))FT(x^2 s(x)))$.

Since the opportunity of performing robust filtering of profiles was not implemented in SPIP™, within this work the filter algorithms of the 0th and 2nd order have been scripted in Matlab 7 according to the indications of ISO 16610-31 [96] and of Jiang, Brinkmann, Seewig et al. [23, 93, 100–103] both in the "standard" and "fast" ways. The Matlab code is presented in appendix B as well as a verification against the filters implemented in the commercial software MountainsMap® 6.1 Premium by Digital Surf [128]. Afterwards, the filter codes have been utilised in creating a SPIP™ plug-in allowing the robust filtering of MUFU surfaces.

3.2.1 Robust Filtering of MUFU surfaces

The profile of figure 3.1 is taken up again and filtered with a RGR of the 2nd order (RGR2). The starting point is not the primary profile, but the total profile after noise removal, because of the form-following properties of this filter typology. The reference line thus calculated is shown in figure 3.5 together with the double step Gaussian mean line for the sake of comparison.

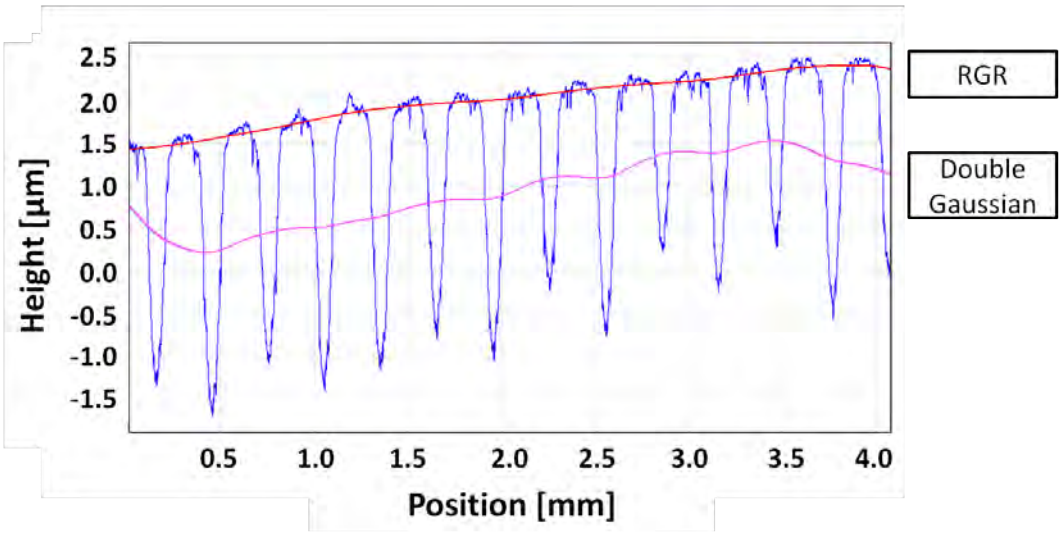

Figure 3.5: *Reference line position after Robust Gaussian Regression filtering of a MUFU profile.*

The filter behaviour is correct and the reference line crosses only the plateaus without being affected from the valleys or presenting the boundary distortions. Unfortunately, the method works correctly only for plateau

bearing areas (BA) sufficiently high: the shown profile had bearing area of approximately 60%.
For lower bearing areas (50% or less), the robust estimator fails in its scope and the reference line becomes highly affected by the valleys (figure 3.6). The reason is that robust techniques are capable of removing the effect of gross outliers as long as a suitable measure of scale is used for detecting them. The MAD statistics is a very robust measure of scale with a breakdown point of 50%. Therefore, the reason for the poor performance of the RGR filter is due to the fact that the surface profile, has more than 50% "outliers". Or, in other words, more than 50% of the profile belongs valleys, which shall be disregarded in the filtering process. In the present case, the MAD statistics proves to be unstable and becomes no longer a robust estimator. Moreover, there is another aspect that can result problematic: the choice of the m-estimator. The Tukey function is re-descending and may not have a unique solution, which depends on the initial guess or 0-iteration step [127]. For most engineered surfaces the RGR filter will normally converge to a single solution regardless of the starting point. But for MUFU surfaces with low ($\leq$ 50%) bearing area, the iteration starting point can influence the solution. The risk is that with a first-guess mean line well under the plateau level, the plateau themselves can be excluded from the calculation and the iterations may converge in the valleys!

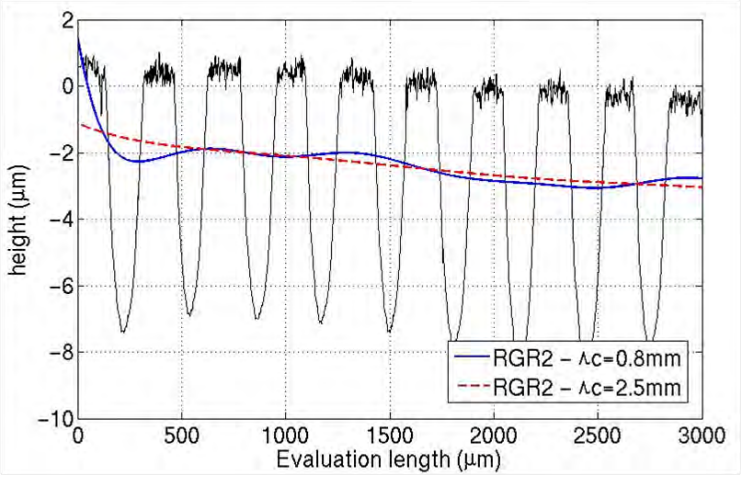

Figure 3.6: *Reference line position Robust Gaussian Regression filtering of a MUFU profile with approximately 50% bearing area (Matlab visualisation).*

A number of solutions have been proposed to these problems in [123]. First of all, the outlier detection problem has been tackled. Modifying equation 3.5 by setting a tighter threshold can represent a solution to the problem. Rather than having a threshold at 3σ, a c_B value diminished to 1σ is supposed to improve greatly the convergence. In figure 3.7, an example

of the effect of reducing the outlier threshold value to $c_B = 1.483$MAD is shown. The mean line fits suitably through the plateau region, as only a minor part of the valleys will be given any weight in the filter. However, reducing the threshold alone does not resolve the convergence problems, which, instead, risk to be accentuated and it is thus not a general solution method.

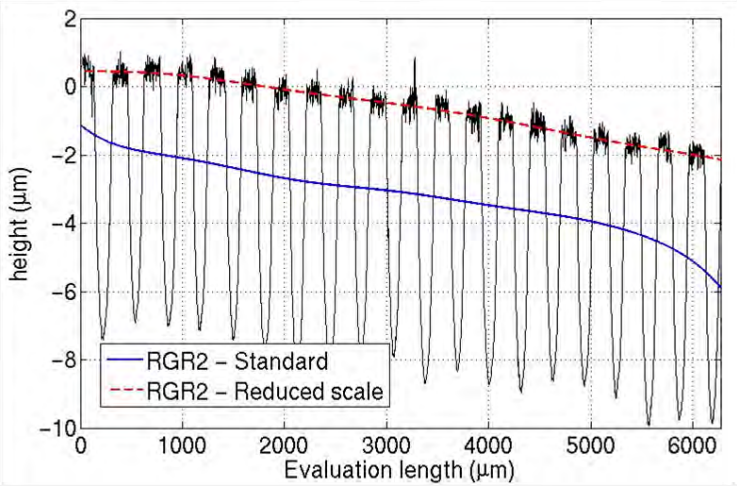

Figure 3.7: *Effect of reducing the threshold value by decreasing the scale factor to 1σ (Matlab visualisation).*

A second solution consists in utilising another estimate of scale instead of the MAD estimator. Again, equation 3.5 can be modified by using the the 25% quartile (or first quartile) operator Q_{25} of the absolute value of the residuals.

$$c_B = 4.4\mathrm{Q}_{25}(|z(x) - w(x)|) \tag{3.6}$$

If A MUFU surface has low bearing area and the initial guess is close to the plateau level, the 25% quartile value of the residuals will be a good representative of the scale of the plateau region, because the majority of the residuals related to the valleys. The two solutions (quartile estimator and single standard deviation) reduce both the threshold value and the be used concurrently resulting in a particularly tight condition to be met for the residuals to have any weight. Nevertheless, it is important that for the initial guess to be close enough to the plateau region or, even better, an upper bound of it ensuring thereby that the residuals are larger in the valley region. A simple Gaussian filtering operation will for this reason most likely provide an inappropriate first-guess, as shown in figure 3.8: neither the "classical" RGR nor a RGR with a first quartile estimator could reach the plateau level and converge just above the first-guess.

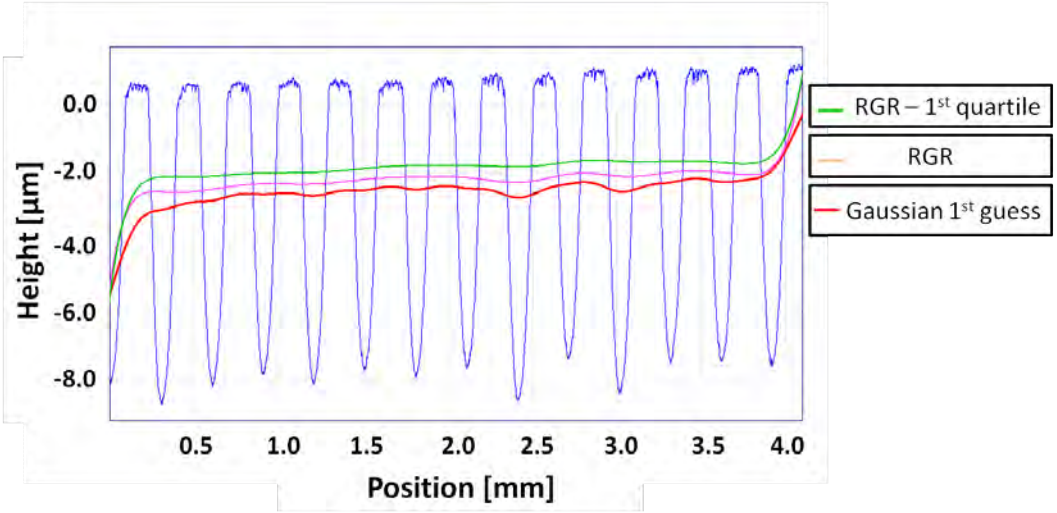

Figure 3.8: *Effect of using a first quartile estimator when employing a Gaussian first guess.*

The solution to this problem is to modify the RGR algorithm in order to calculate separately a first-guess line from which the first threshold and re-weighing functions are obtained. Unbinding the first-guess from the RGR calculation gives the possibility of choosing freely any kind of filtering method for this operation. The filtering technique must provide an upper bound of the targeted profile, therefore a filter belonging to the E-system has to be selected. The choice falls on morphological filters described in section 2.3.4. The first loop of the algorithm of figure 3.3 is substituted by the algorithm proposed in figure 3.9 before proceeding normally with the iterations. The morphological filter is utterly independent from the RGR filter and so is the nesting index (cut-off). The likelihood of excluding the valleys is higher with a larger structuring element.

Neither profile morphological filters were offered by SPIP™, therefore a "naive" algorithm was implemented again in Matlab following the indications given by ISO 16610-40 and ISO 16610-41 [98, 99]. Also the morphological filter codes are present in appendix B. The morphological operation chosen is the closing operation and a disk as structuring element. Due to large memory requirements, the Matlab algorithm could perform the morphological filtering only on profiles with reduced length. Nevertheless, the algorithm was taken up and improved by Image Metrology allowing the filtering of longer profiles as well as the selection of the kernel size for the disk used.

The profile of figure 3.8 is analysed again with a modified RGR (modRGR) filter presenting a morphological closing operation as first guess. A 0.8 mm disk radius is chosen. The result is shown in figure 3.10. The first-

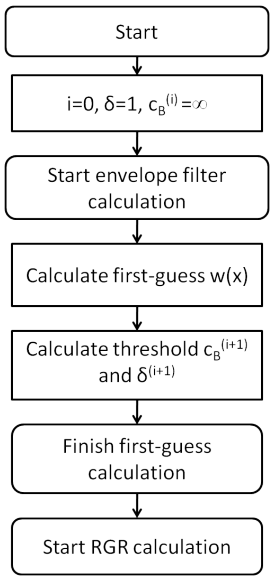

Figure 3.9: *First guess calculation algorithm in the modified RGR.*

guess envelopes the profile, passing closely above the plateau tops and descending in the valleys down to approximately half their depth. Such first-guess will make the RGR calculate a sound reference line passing through the plateau zone. The roughness profile will result undistorted with the zero at the plateau level.

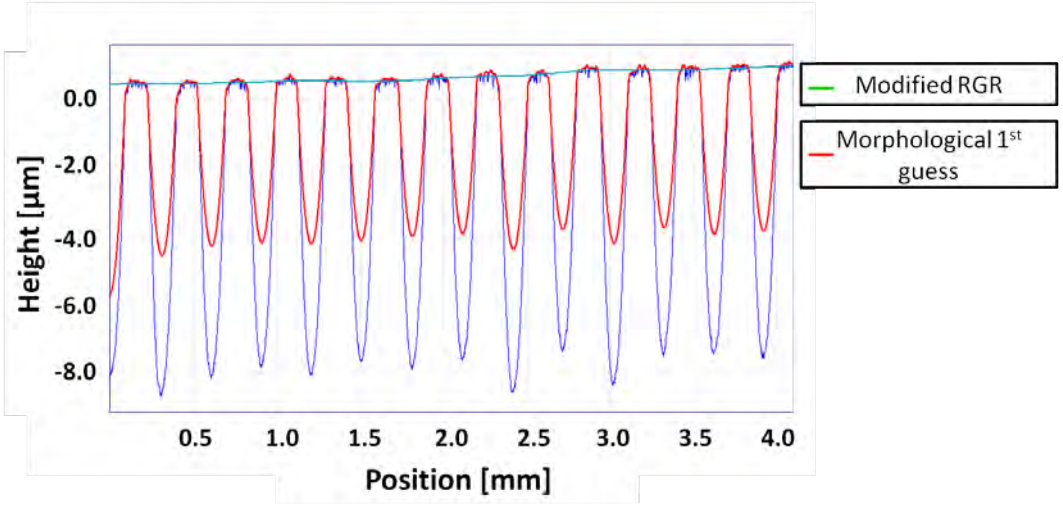

Figure 3.10: *Effect of using a modified RGR with morphological first guess.*

The solutions above proposed (single standard deviation, first quartile estimator and morphological first guess) are independent from each other and can be implemented at the same time. The first two solutions should

reduce the valley effect, while the third one should help the convergence at a plateau level. The final roughness profile results therefore aligned and undistorted even in the case of a MUFU surface with relatively low plateau bearing area. The analysis can now proceed to quantification.

3.3 Quantification of MUFU surfaces with ISO 13565 parameters

Now that the roughness profile is properly aligned, ISO 13565 is looked at again for calculating the parameters described in section 2.4 apt for functional analyses.

3.3.1 ISO 13565-2

In figure 3.11 a MUFU profile treated with robust filtering is displayed along with its material ratio curve. Due to the deterministic pattern of lubricant reservoirs with the same height provided by the turning operation, the material ratio curve presents two major bends highlighted by the red circles. The presence of the second bend highly affects the mathematical calculation of the material ratio curve parameters. In the given profile, for example, the total height $Rt = 9.01\mu m$, while the valley depth $Rvk = 9.97\mu m$, meaning that the valleys of the profile would be higher than the profile itself, which is physically impossible.

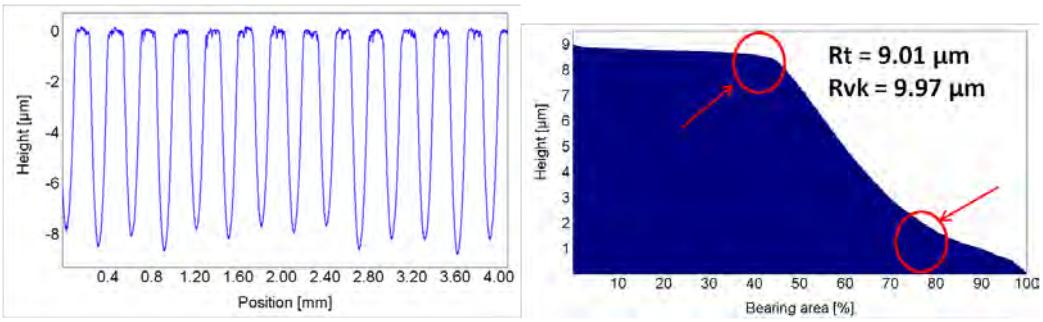

(a) (b)

Figure 3.11: *a) MUFU roughness profile and (b) material ratio curve.*

The reason of this occurrence is explained in figure 3.12. The material ratio curve of a turned multifunctional surface profile has in the valley zone a change of concavity compared to the one showed in figure 2.26, therefore the triangle, whose height is Rvk, must reach a height level lower than the minimum profile height in order to satisfy the equivalence condition.

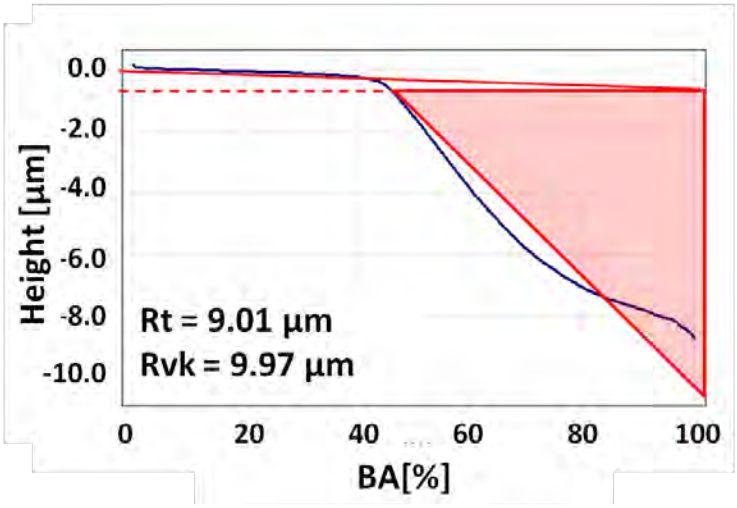

Figure 3.12: *Rvk calculation on a MUFU profile.*

Moreover, MUFU surfaces with plateau bearing area less than 40% risk having zero Rpk value. The least-slope 40% segment would in fact start from the first point of the bearing curve and end already in the valley region. Starting from the first point of the bearing curve would result in an equivalent triangle with null area, thus $Rpk = 0\mu m$.
The method described by ISO 13565-2 proves then not to be generally suitable in MUFU profiles characterisation.

3.3.2 ISO 13565-3

The profile of figure 3.11 is analysed also according to the guidelines provided by ISO 13565-3. The probability plot is calculated and shown in figure 3.13. The concavity change in the valley zone is even more pronounced impeding the calculation of ISO 15365-3 parameters since a proper line-fitting through the valley zone is not possible with the current methods.
Standard ISO 13565-3 was in fact conceived for and destined to plateau-honed surfaces, or anyhow surfaces with both plateaus and valleys presenting a Gaussian distribution of heights. A perfectly random distribution appears as a straight line in a material probability plot [52]. Therefore in plateau-honed surfaces, the heights in the material probability plot are arranged in two distinct regions through which it is easy to fit lines and hence calculate the parameters. In MUFU surfaces, instead, only through the plateau region is possible to properly fit a line, but not through the valleys. It is therefore theoretically possible to calculate only plateau parameters, but not in the way outlined by the standard, since both the

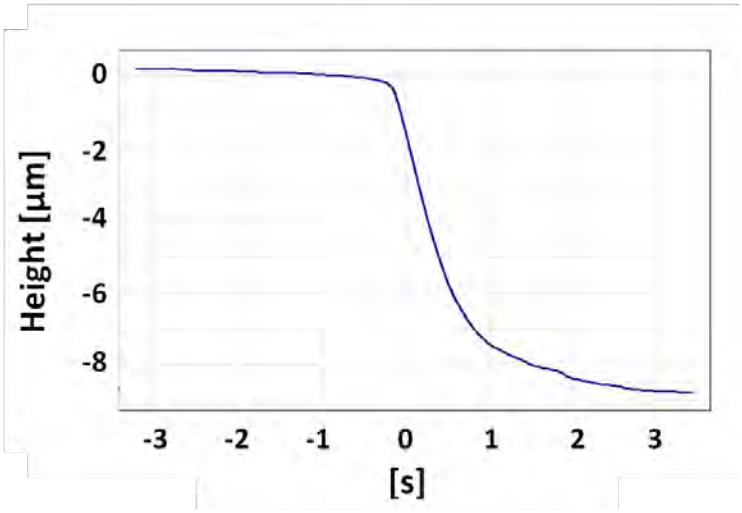

Figure 3.13: *Material probability plot of a MUFU profile.*

plateau and valley fit are required for the parameters calculation. A similar problem was faced by Grabon et al. [129] while characterizing surfaces having oil pockets applied by a burnishing technique. This texturing technique creates circular pockets deterministically patterned: the resulting material probability curve will present the same shape as a MUFU one. In order to retrieve information from the curve, they developed an empirical method for determining the transition point between random and deterministic zone, i.e. between plateaus and valleys. With reference to figure 3.14, their method consists in: calculating the material probability curve of the profile; tracing the line passing through plus and minus 4 standard deviations and determining its slope ψ (a); rotating the probability plot by ψ anticlockwise (b); calculating the point of highest ordinate of the rotated plot and thus determining the transition point through which the regression is performed (c).
By means of their method (which they applied only to the primary profile), plateau information can be retrieved such as the root mean square height Ppq and the abscissa transition point Pmq. Unfortunately, the method lacks of information provided since the valley analysis is disregarded.
Neither the method described by ISO 13565-3 proves then to be suitable for analysing MUFU profiles. Other characterisation modalities need thus to be sought.

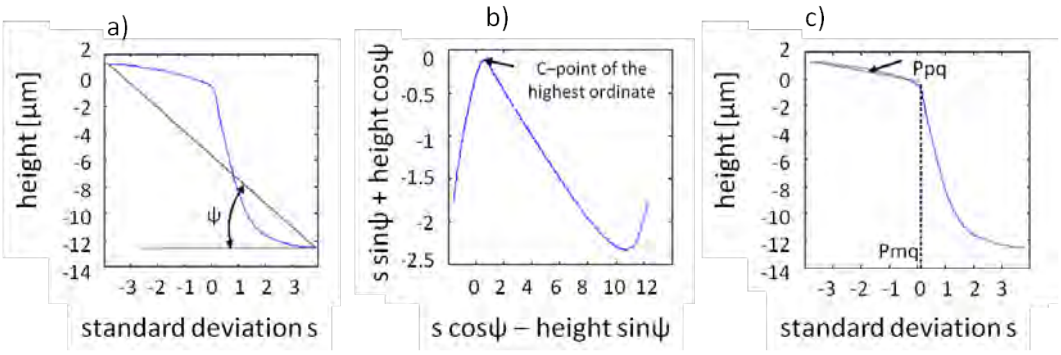

Figure 3.14: *Transition point determination by rotating the surface probability curve, adapted from Grabon et al. [129].*

3.4 A new feature separation method

The procedure followed by Grabon et al. [129] is here adopted as initial step of a further operation in the characterisation of MUFU profile: identification and separation of profile features [124, 125]. While areal feature characterisation methods have been proposed and even standardised as explained in section 2.4.1, surprisingly enough, the profile counterpart has not been studied yet. Similar to the areal one, the method proposed in this section does not perceive the profile anymore as a whole, but composed of a number of features or, better said, feature sets, each pursuing separately a specific function. MUFU profiles are composed of two main feature sets: "plateaus" and "valleys". Grabon's method above described represents a good starting point in the recognition and separation of the feature sets since it provides the transition point between plateaus and valleys in profiles similar to MUFU ones. Inspired by Grabon's approach, then, the probability plot of the MUFU profile is taken, but, instead of rotating the curve, the method herein adopted calculates the largest perpendicular distance between the line and the curve, see figure 3.15.
The plateau-valley threshold is therefore found, but rather than calculating parameters from the material probability curve, the transition point is used directly on the profile for separating the plateau and the valleys. The operation would result in two different profiles representing each a different feature set which can be analysed independently. Nevertheless, caution must be used in saying that whatever above the threshold belongs to the plateaus and whatever below it belongs to the valleys. In case of particularly rough plateaus, some of the plateau roughness could lay below the threshold point and therefore being included erroneously in the valleys (figure 3.16).
Hence, blindly clipping the profile at the threshold level, though being a

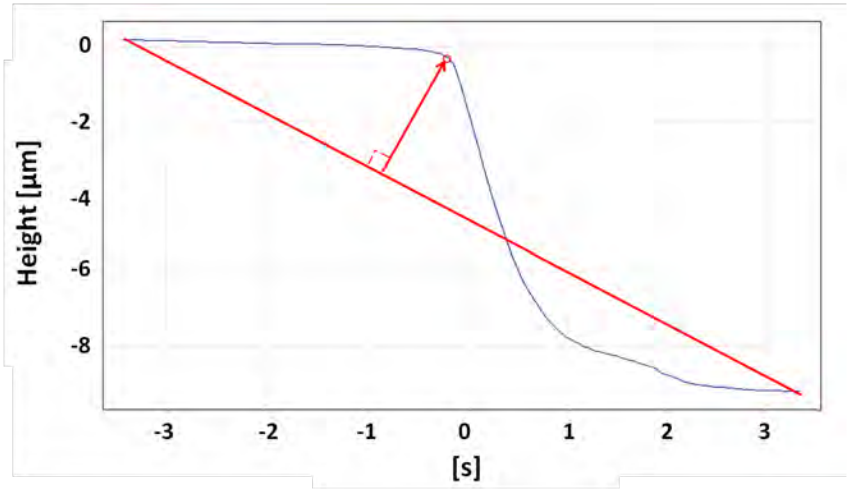

Figure 3.15: *Transition point determination by calculating the largest perpendicular distance.*

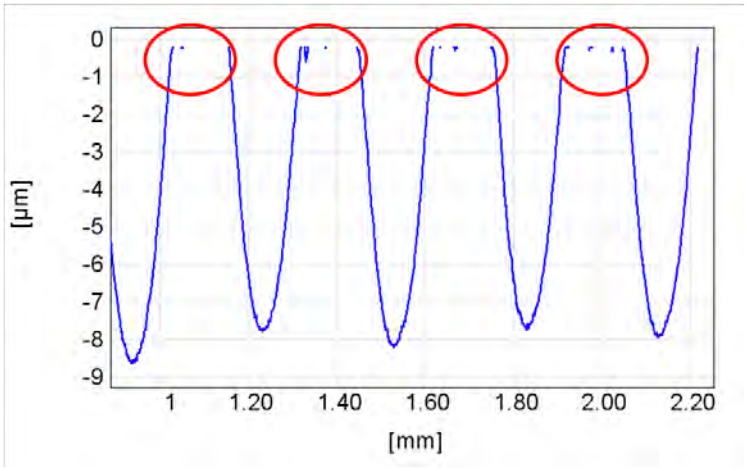

Figure 3.16: *Separation problem by direct clipping of the profile at the threshold level.*

fast solution, may not have satisfactory outcomes. A further algorithm has therefore been implemented able to recognize the starting and ending point of each plateau and leaving the plateau roughness untouched during the separation operation. The algorithm relies on the deterministic nature of the valleys and assumes the plateau roughness height considerably smaller than the valley height. The assumption is generally valid, since a typical finishing operation generates surfaces with Rz values of approximately 0.1-0.2 µm, while pockets depth can reach depths of 10-20 µm. The algorithm flowchart is shown in figure 3.17, with illustrations enlightening the most crucial steps. After determining the higher threshold, a lower threshold is set, typically at 25-50% of the total profile height from the bottom. Because

of their deterministic height distribution, the lower threshold will pass through all the valleys. The first sampled points above the lower threshold (x_i, where $i = 1, \ldots, n$) are thus detected and the ones below discarded. Afterwards all the points between the several x_i and the last below the upper threshold are eliminated, meaning all the points following x_i if the gradient is positive or all the points preceding x_i if the gradient is negative. The plateau profile is then obtained; the valley profile can be derived by subtracting the plateaus from the roughness profile.

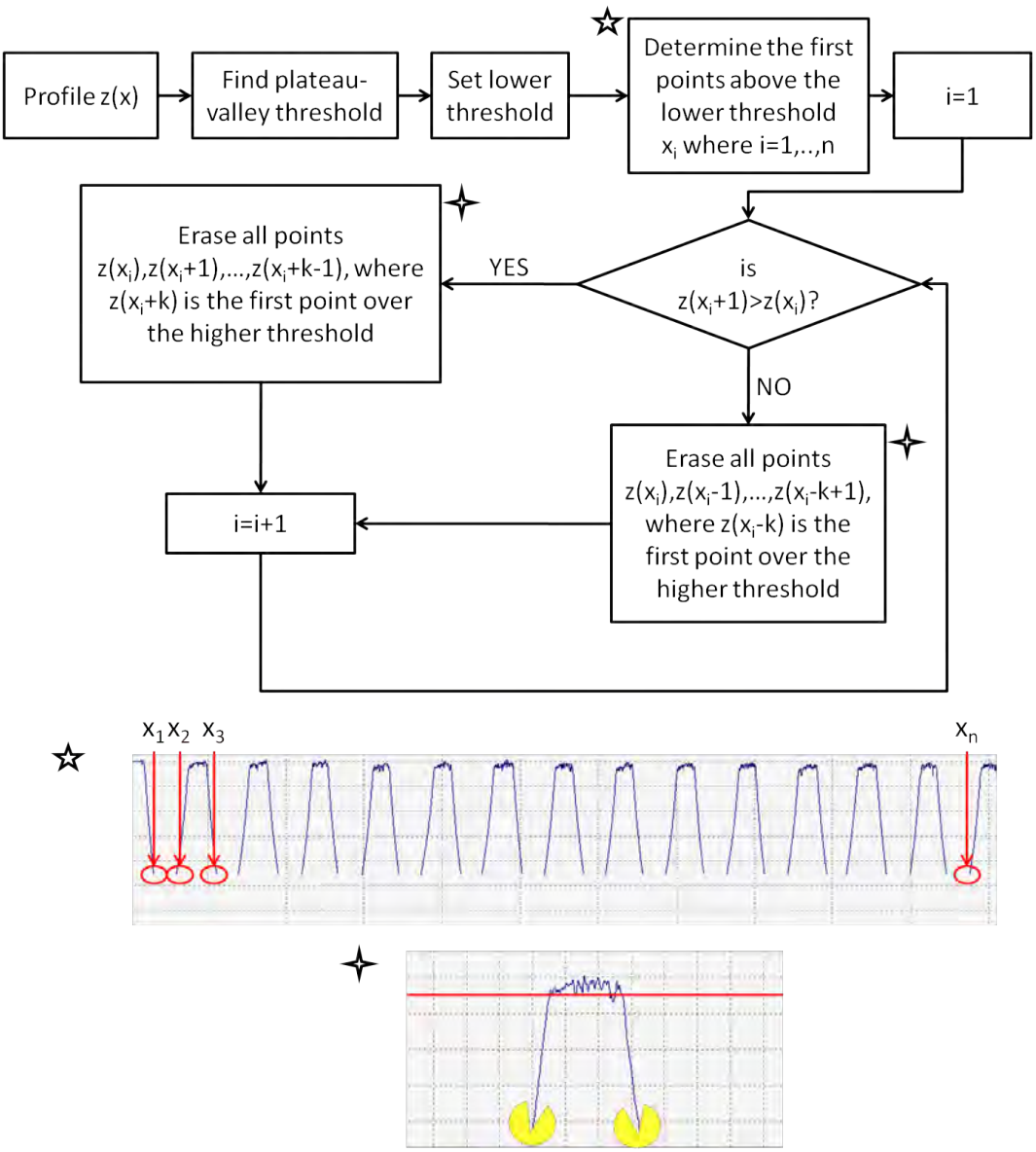

Figure 3.17: *Illustrated algorithm for separating plateaus and valleys without affecting the plateau roughness.*

A correct plateau-valley separation performed on a MUFU profile is shown in figure 3.18. Rougher plateaus as the zoomed one are not anymore clipped and included in the valley profile. Functional analyses can now be carried out independently.

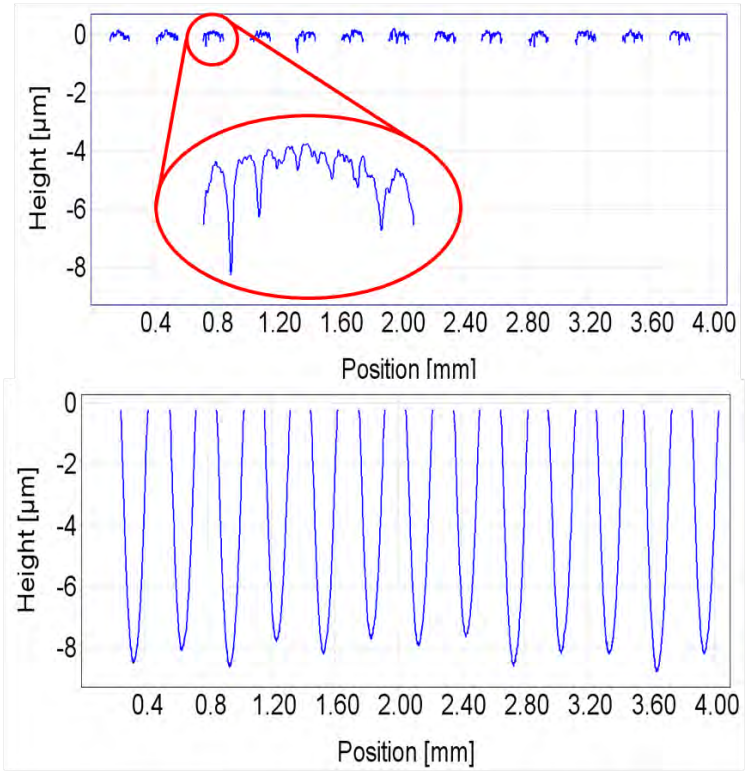

Figure 3.18: *Correct separation of plateaus and valleys of a MUFU profile.*

3.5 A new characterisation procedure

From the reasoning done in this chapter and the solutions proposed, a whole new and more complicated characterisation procedure than the ones depicted in figure 2.10 can be derived [126]. The new procedure is summarized in figure 3.19.
The starting point is the total profile to which is applied the λs filter. Now, the employment of a RGR of the 2nd order would not require in principle any form removal, so that the λc filtering operation can be performed at once. Practically, however, when extremely large form components are present, though the reference line seems following the plateaus well, due to the large shape of the valleys some distortions can occur especially at profile ends, see figure 3.20. Therefore, in particular cases, the form must

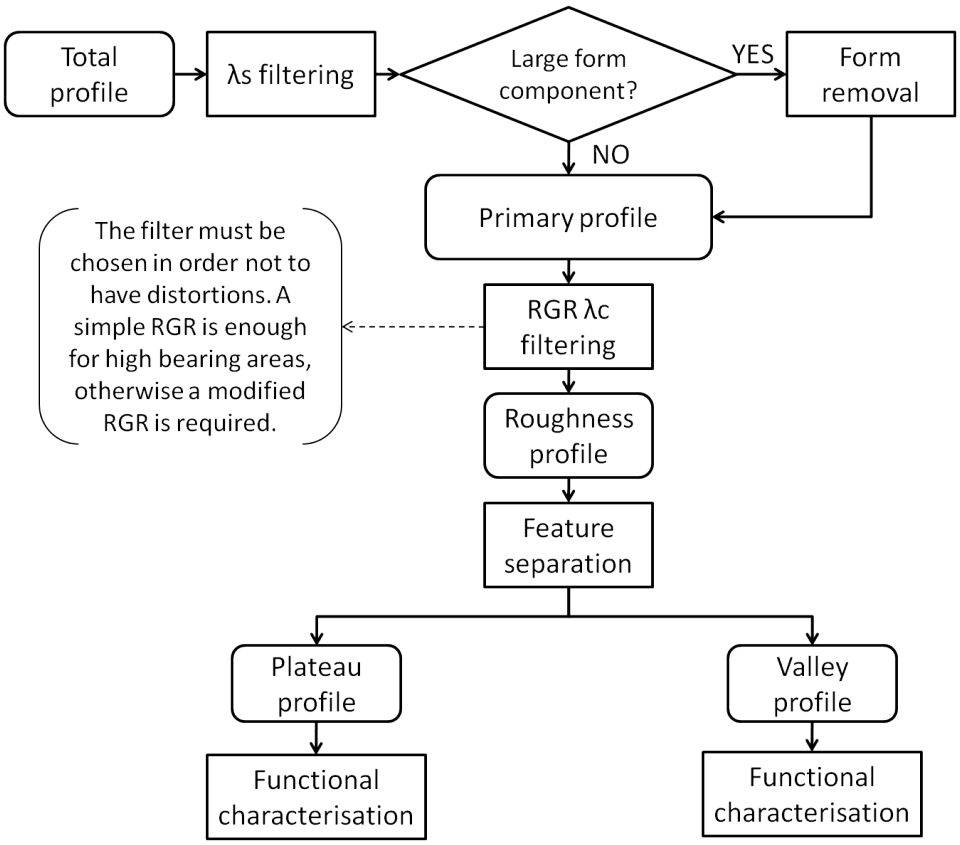

Figure 3.19: *New characterisation procedure for MUFU surfaces.*

be removed beforehand, though in most cases it is not necessary. Once obtained the primary profile, the robust filtering operation is carried out. As the note in figure 3.19 says, the filter must be chosen properly for not having distortions. A "classical" robust filter is enough for high bearing areas of the plateaus, otherwise a modified RGR is necessary. The employment of a morphological first guess with high radius can generally solve any problem, but might have high computational requirements. The choice of a proper filter can be done with a careful visualisation of the profile once the measurement is taken. Once an undistorted roughness profile is obtained, the next step is the separation of the surface features in order to attain two distinct profiles for carrying out independent functional characterisations.

In the next section a MUFU profile is characterised following the new procedure.

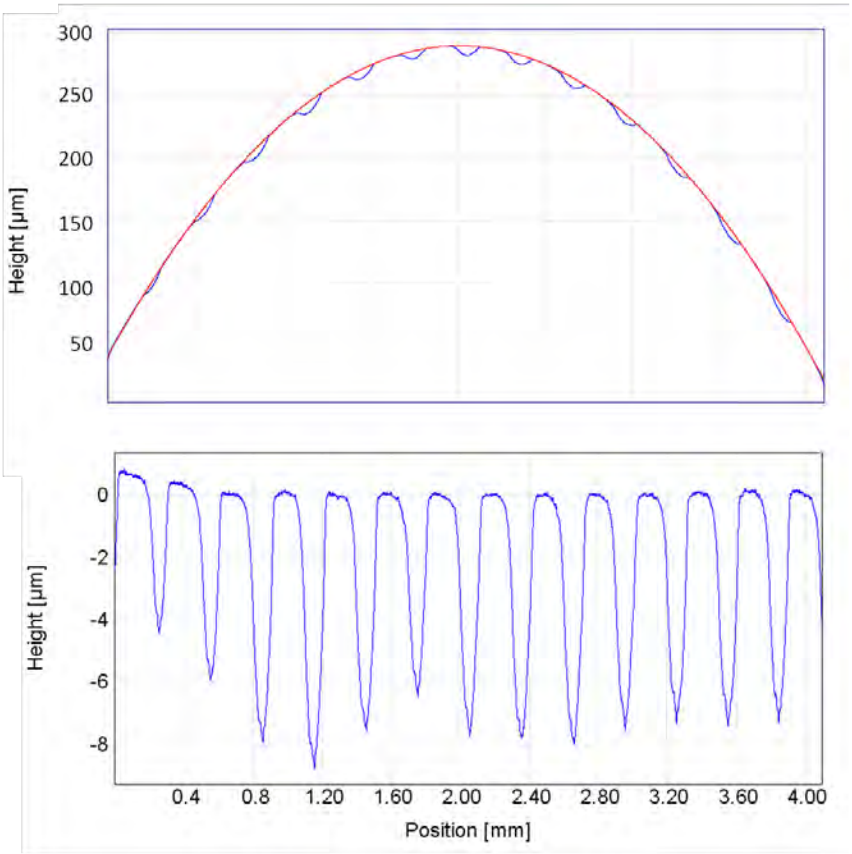

Figure 3.20: *MUFU profile with a large form component and consequent distortion that may occur.*

3.5.1 Characterisation of a MUFU profile using the new procedure

The profile of figure 3.10 (to which the noise had already been removed) is now analysed emphasising the difference of using the standardised RGR method and the modified RGR. With reference to the upper part of figure 3.21 the RGR filtering operation yielded a distorted roughness profile, being the first and last peaks unnaturally "pulled" up or down. Moreover the other plateaus are not aligned either, effect of the weight given to the valleys during the calculations. In the lower part of figure 3.21, the roughness profile resulting after RGR filtering with morphological first guess is displayed. The profile is correctly aligned and the zero line crosses the plateaus, as already noted when figure 3.10 was explained.

The feature separation algorithm is hence run, resulting in a correct separation (figure 3.22).

The great advantage of this technique is that it gives the possibility of

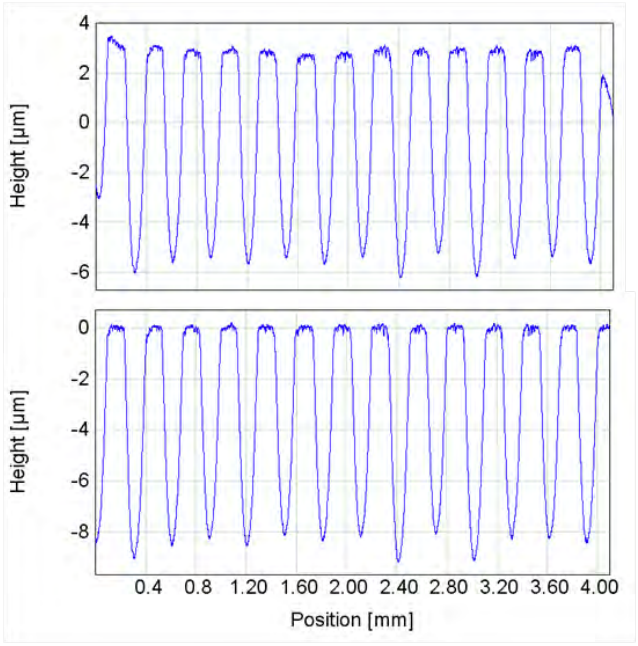

Figure 3.21: *Roughness profile using a classical RGR filter (above) and a modified RGR filter with a closing morphological first-guess (below).*

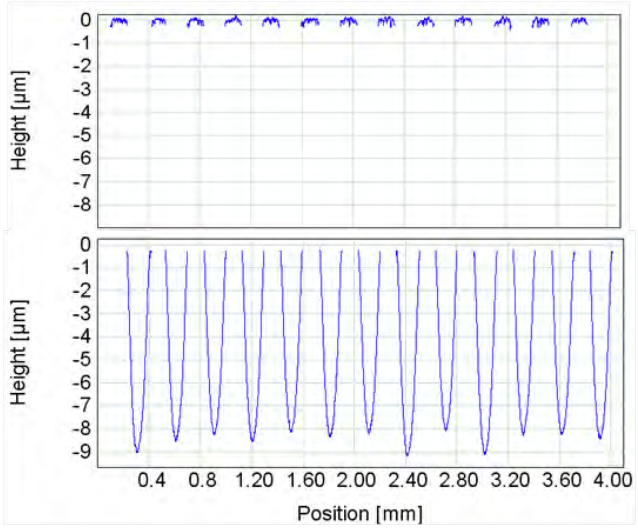

Figure 3.22: *Feature separation of the profile of figure 3.10.*

various and thorough analyses and the calculation of the majority of parameters from the obtained profiles. It is hence more flexible than ISO 13565 methods, which allowed the calculation of only one or few parameters for each feature type. Anyhow, the quantification must be done in relation to the function and it is likely that only one or few parameters

are enough for the purpose. The proposed method gives the freedom of selecting the parameter the user thinks is most suitable. In particular, the plateaus of this kind of surfaces have the function of bearing loads and are in tribological contact with a matching surface. Therefore they can be described by a field parameter as Ra or Rq. The plateaus Ra and Rq are estimated being respectively 0.073 µm and 0.095 µm, but, in this case are not reliable due to a detected local roundness (figure 3.23). A parabolic fit is applied to each plateau for removing this roundness and therefore estimate more appropriately the roughness from the finishing process. The plateau roughness thus obtained is $Ra = 0.056\mu m$ and $Rq = 0.073\mu m$.

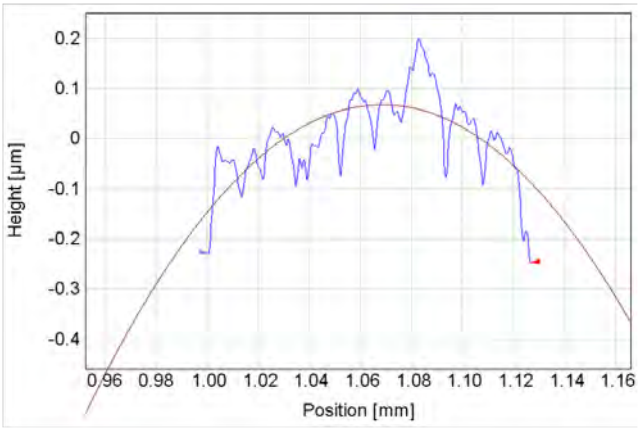

Figure 3.23: *Plateau roundness.*

The valleys, instead, are described by the amount of lubrication they can contain. A suitable parameter for this scope is the "equivalent film thickness" (EQF) that is the total volume of lubricant contained in the valleys divided by a reduced profile length (figure 3.24). The profile length is reduced in a way that the calculation considers only the valleys belonging to complete periods of the MUFU profile. The parameter, which ideally represents the height of the film separating two flat surfaces if all the trapped lubricant was used, is therefore independent from the profile length. For the given profile $EQF = 5.633\mu m$.

3.5.2 Limitations of the procedure

It must be remarked that this procedure and the methods adopted work generally well for the great majority of MUFU profiles analysed within this framework. Nonetheless, it is not always infallible and has some limitations.
The modified robust filtering allows the attainment of undistorted roughness profiles unachievable with standardised methods. However, the

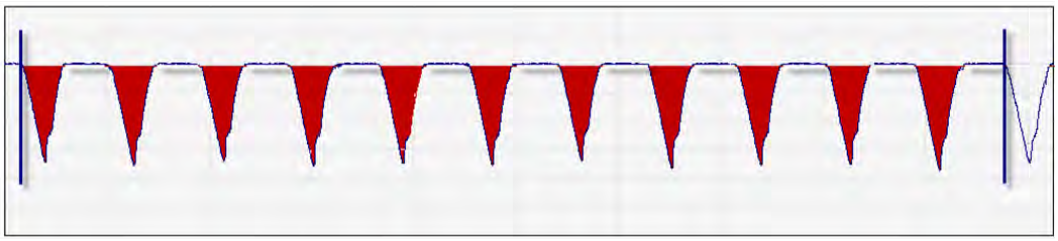

Figure 3.24: *Valleys considered in the EQF calculation.*

smaller the plateau bearing area becomes, the higher is the likelihood that points belonging to the valleys enter the filtering calculation with non-zero weights and influence therefore the reference line position. This problem can be again handled by setting an even tighter threshold c_B. In any case, when the plateau bearing area tends to zero (for instance in the case of a turned surface), only few points will constitute the "plateau" and the mean line will cross the cusps at a height somewhere between the small plateau and the mean line obtained with a regular Gaussian filtering operation.
In some cases when a profile starts or end in a deep valley and the number of sampled points is high therein, it may happen that the reference line tends to follow the profile causing boundary distortions. These boundary distortions are not due to the filter definition (weighing function, etc.), but to the surface itself. A solution can be to increase the size of the structuring element, although there is the limitation of the computer capacity. A "rough" solution is to eliminate the valley by manually reducing the profile length down till the vicinity of the nearby plateau threshold. In this way, no distortions will be detected. In most cases it is an acceptable solution also because the profile length is usually longer than 5 times the cut-off values (i.e. 4 mm in most of the cases here considered) due to run-in and run-out of the stylus actuator.
The separation method works well as long as the valleys have a deterministic height distribution. The lower threshold relies highly on this aspect. Sometimes it can happen that, due to manufacturing errors of the primary machining process, it can be detected the presence of a shallower valley which is not crossed by the lower threshold. This valley will enter the plateau profile biasing both plateau and valley parameters calculations. This, however, is not a limitation of the methodology itself.
The parabolic fits to each plateaus can not be optimal and lead to some nano-scale end distortions. The method is quite rudimentary and could be improved as for example by using wavelet filters at a plateau scale.

3.6 Further considerations

3.6.1 Areal considerations

In this chapter, only profile methods have been presented, with little heed to areal analyses. It can be argued that MUFU surfaces have overall a 2D structure [13] which is projected to the third dimension; but it is not particularly true for the plateau nano-roughness, which exhibits the imprints of the RAP process (figure 3.25).

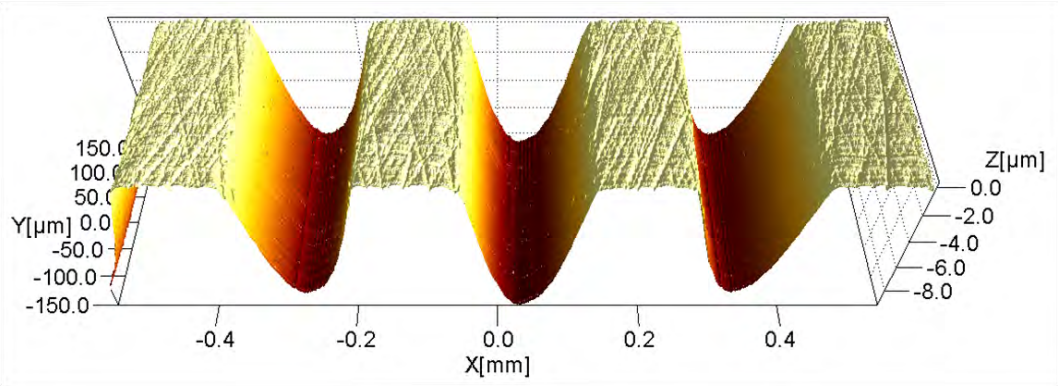

Figure 3.25: *Areal measurement of a MUFU surface: the RAP traces are evident on the plateaus.*

However, the presented method can utterly be extended to the third dimension without any major complications, except for the computing requirements and the algorithms coding complexity and speed. The areal robust filtering has been described Jiang and Brinkmann [93, 100, 101] and implies an extension of the minimisation problem of equation 2.7 and consequently of the systems 3.3. In this case the contribution of the Fast algorithm developed by Zeng, Jiang and Scott [93] can be decisive. The modifications suggested do not depend on the fact that it is a linear or an areal measurement unless a morphological first guess is adopted. Nevertheless, a morphological filter can on its turn be extended quite easily to the areal domain by considering a ball instead of a disk [130]. The naive algorithm can be extremely slow in this task and more efficient algorithms should be taken into account as the Alpha-shape method described by Lou, Jiang and Scott [109] or others listed in [130]. Once an undistorted SL surface is obtained, the feature separation method can work as it is here defined, i.e. no extensions are required. The threshold can be calculated from a probability curve alike the profile one; the separation algorithm can also work if each profile is analysed independently and the valley distribution height does not change drastically. In particular, if along the

Y-direction there are, say m profiles, each x_{ij} where $j = 1, \ldots, m$ and $i = 1, \ldots, n$ represents abscissa of the first point above the lower threshold. The following operation is to erase the points between the two thresholds. In appendix B a pseudocode is suggested, whose basic difference with the two dimensional one is the introduction of a further cycle *for* for taking into account the Y-direction. This separation method is an alternative to the standardised feature characterisation outlined in section 2.4.1. The two methodologies can be used independently from each other or even simultaneously. The "watershed" technique is however not yet available in SPIP^{TM}. As a demonstration on how such an analysis would look like on a MUFU surface, prof. Liam Blunt kindly analysed an areal measurement by means of the SurfStand software(figure 3.26).

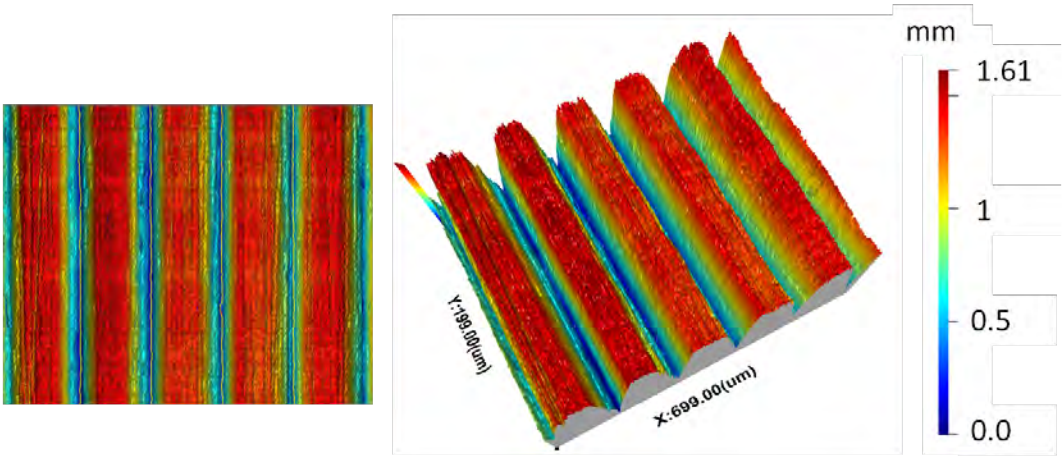

Name	Value	Unit	Explain
Spd	35.945099	Pts/mm^2	FC;H;Wolfprune:5.00%;All;Count;Density
Ssc	11366.962891	1/mm	FC;P;Wolfprune:5.00%;All;Curvature;Mean
S10z	0.000000	mm	FC;S;Wolfprune:5.00%;Top:5;Ipvh;Mean
S5p	0.000000	mm	FC;P;Wolfprune:5.00%;Top:5;Ipvh;Mean
S5v	0.000000	mm	FC;V;Wolfprune:5.00%;Bot:5;Ipvh;Mean
Sda	0.012029	mm^2	FC;D;Wolfprune:5.00%;Open:40.0%;Area;Mean
Sha	0.007000	mm^2	FC;H;Wolfprune:5.00%;Open:25.0%;Area;Mean
Sdv	5891423744.000000	mm^3	FC;D;Wolfprune:5.00%;Open:40.0%;VolE;Mean
Shv	433739968.000000	mm^3	FC;H;Wolfprune:5.00%;Open:25.0%;VolE;Mean

Figure 3.26: *Analysis of an areal measurement of a MUFU surface using the standardised watershed methodology.*

Areal analyses will not be treated any further in this framework, unless for visualisation purposes. The implementation of areal methodologies for analysing MUFU surfaces represents a future work.

3.6.2 Traceability considerations

The calibration certificate shown in appendix A regards the stylus instrument used for most of the measurements done on MUFU surfaces, which are the only measurements from which parameters are calculated. In particular the calibration was made on a roughness standard and pertains height parameters such as Ra. The certificate provides a calibration factor for adjusting the instrument indication. It is a systematic error, so that the calculated parameters are multiplied by this factor for achieving a "correct" result. The question now is whether or not the plateau and valley results can be corrected by this factor and the certificate can be used for providing traceability to the measurements. The answer is *yes*. Looking at the definition of Ra (equation 2.13), applying the correction factor to Ra is in fact equivalent to correcting each sampled height point $z(x_i)$. Therefore, in order to have a corrected value of the plateaus Ra and assuming that the reference line crosses correctly through them, it is sufficient to multiply the Ra (or alternatively each plateau point) by the calibration factor. Given these equivalences, the uncertainty calculation can be then carried out according to equations 2.37 and 2.38. The same reasoning goes for the valley parameter EQF. Although being it a parameter introduced within this framework which cannot be compared with any other elsewhere so that, strictly speaking, the traceability issue does not stand to reason *yet*, the traceability can be achieved likewise. Its definition is indeed very similar in a way to the one of Ra, being the void area of the valleys divided by a length. EQF is itself a field parameter and the correction by the calibration factor holds still. The uncertainty calculation is carried out as above considering the two main contributions: the first from the instrument u_{inst} for measurements yielding field parameters and the second u_s from repeated measurements.
Another consideration regards the calibration factor itself: in the certificate the software used for the parameter evaluation is Sursam74, developed by DTU. Here the evaluations are made using the commercial SPIP™. The raw data from the calibration are therefore analysed with SPIP™ following the same procedure described in the certificate in order to find the new factor, see table 3.1. The calibration factors for the different height ranges of the SPIP™ software are the same as the Sursam ones indicating good agreement between the two programs.
A last issue concerns a parameter that will afterwards introduced: BA, indicating the bearing area at the separation level, which is extremely similar to the bearing area of the plateaus (it is a little lower due to the small plateau dips below the upper threshold). Presently, the software does not provide the height at which the separation is performed, but does it automatically. The calculation is therefore performed "manually"

Table 3.1: Analysis of calibration data with SPIP™.

Reference value			
Ra [µm]	0.229	0.604	1.706
Measurement number	**Ra [µm]**	**Ra [µm]**	**Ra [µm]**
1	0.230	0.600	1.689
2	0.232	0.600	1.692
3	0.232	0.600	1.683
4	0.231	0.601	1.680
5	0.231	0.600	1.694
6	0.227	0.601	1.696
7	0.227	0.604	1.688
8	0.230	0.606	1.690
9	0.227	0.602	1.715
10	0.230	0.606	1.707
11	0.233	0.610	1.709
12	0.229	0.603	1.702
Average [µm]	**0.230**	**0.603**	**1.695**
Calibration factor	**0.996**	**1.002**	**1.006**

detecting the ordinate of the highest point of the valley profile (which is closed to the separation threshold), transferring this height to the profile histogram (in order to have a overall height independent to the position of the zero line) and eventually estimating the bearing area from the material ratio value at the found height. This complicated (and time-consuming) procedure suffers positioning uncertainty contributions at each step and the uncertainty calculation due to this lack of automatisms would not be as straightforward as for the other parameters. Moreover, as for EQF, the BA parameter has no match with external work. For these reasons a thorough uncertainty calculation is not performed within this work and the BA is accompanied by its standard deviation (or 2 times the standard deviation)

for comparison or orientation purposes. Presently, the automatic calculation of BA is being developed by Image Metrology.

3.7 Summary and Conclusions

In this chapter the problems related to the metrological analysis of MUFU surfaces have been presented. The usage of current practice standards has been attempted, but demonstrated soon being not suitable both concerning the filtering and the quantification operations. Advanced Robust Gaussian Regression filters have been studied and coded, proving being the correct path towards the characterisation of MUFU surfaces. Not always, though, the filters have proven apt for the task, and modifications such as tighter thresholds and the utilisation of a separate first guess belonging to the E-system were needed in order to eventually obtain an undistorted roughness profile. The "modified" RGR can now filter successfully the majority of MUFU surfaces. Moreover, profile feature characterisation was introduced whose method can first find the plateau-valley threshold and afterwards perform a correct separation. This operation results in two independent profiles that can be analysed thoroughly according to the features functions. One field parameters is deemed enough for the plateaus and one parameter (EQF) is defined for describing the valleys. The parameters have been demonstrated traceable as it was a regular roughness measurement. A summarizing procedure, generally valid for all MUFU surfaces, has been derived from the amount of operations performed and its limitations discussed. The areal case was not (and will not) be considered, but the proposed methods are utterly extendible to the third dimension.

Chapter 4

Testing of MUFU surfaces for machine element applications

This chapter is the first of the two dealing with the testing of MUFU surfaces. The division of the two chapters is based on the detected fields of application for MUFU surfaces as indicated in section 1.4.1, namely **machine elements** and **metal forming tools**. The present chapter concerns the former, hence testing of MUFU surfaces for machine elements applications. For achieving this task, a whole new test apparatus has been devised, designed and developed by the project participants in particular by the joint efforts of Strecon and DTU [131, 132]. A comprehensive explanation of the apparatus including a description of the several components is hereby presented, together with an account of the tests performed and an analysis and a discussion of the results obtained, which can be found also in [133].

4.1 A new test rig

There exists a large number of tests for machine elements as there exists a huge variety of machine elements. In section 1.3 a number of tests for evaluating textured surfaces in machine elements have been presented [28–32, 57–59] which can simulate two possible kinds of tribological contacts: rolling contact and sliding contact, being the latter the most severe. The cited experiments include "standardised", well-established methods as well as "tailored", personalised methods. Among the most famous well-established methods lie rolling contact fatigue (RCF) tests and pin-on-disk tests.
Rolling contact fatigue encompasses a series of wear phenomena occurring to surfaces in prolonged rolling contact conditions such as ball bearings [134, 135]. The test principle for determining rolling contact fatigue occurrence is to load a rolling element, typically a sphere or a cylinder,

against a moving counterpart, typically a disk. In RCF tests both pure rolling, and rolling with a percentage of sliding conditions, can be investigated. A large variety of different set-ups have been developed during the years [136], including the method used by [32] consisting of two disks loaded and running against cylindrical test specimens.
In pin-on-disk tests, friction and wear under pure sliding conditions are analysed by loading a stationary pin over a rotating disk [137]. The friction coefficient is determined by dividing the measured frictional force by the load applied to the pin, while the wear can be determined by estimating the variation of geometry (shortening) of the pin. Usually the pin is rounded, but [59], e.g., utilised instead a flat pin for examining the effect of surface texturing.
Other famous test rigs for machine elements were developed during the last 50 years by Plint (father and son) and Cameron, the list of which can be found in [138].
Although the usage of well-established test-methods was proposed at the beginning of the project, the final decision veered on the *ex novo* development of a tailored, general-purpose apparatus making use of established Strecon technologies and, most importantly, permitting a relatively easy manufacturing of MUFU specimens. The **Axial Sliding Test** (**AST**) was hence created [131, 132]. The test idea is sketched in figure 4.1: an enveloping body will convert a horizontal force to a vertical normal pressure applied to a cylindrical object which, in the meantime, slides back and forth.

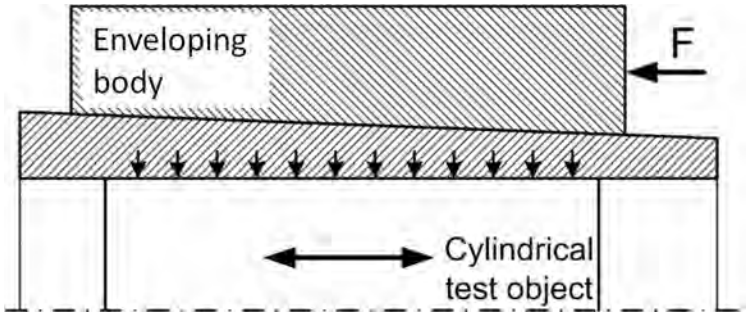

Figure 4.1: *Axial Sliding Test sketch.*

The AST can simulate any machine element presenting an axial movement between two counterparts under pure sliding conditions, such as a piston ring sliding in a cylinder liner. It represents therefore an alternative to well-established test rigs examining sliding contacts, such as the aforementioned pin-on-disk apparatus or the Cameron-Plint tester [138, 139], with the advantage of achieving at once high areas of contact. Although being conceived to evaluate the effectiveness of MUFU surfaces, it can be

actually used for other purposes as for instance lubricants testing. In the next section the AST apparatus is described in detail.

4.1.1 Axial Sliding Test apparatus description

The test rig consists of four major components (one more compared to the sketch of figure 4.1): a stripwound Strecon® container, a conical housing, a rod and a sleeve (figure 4.2). The technical drawing of the entire assembly is shown in figure 4.4. During the experiments the only parts in relative motion with respect to each other are the rod and the sleeve, to which the tested surfaces are applied. The rod is a cylinder: in the studied cases the rods were made of chromium-molybdenum-vanadium alloyed steel (Vanadis 6® [140]) with a hardness of 62 HRC, Ø38 mm diameter and length equal to 135 mm. The sleeve is a 60 mm long hollow cylinder made of the same material, but slightly harder (64 HRC). Its inner diameter is nominally 50 µm larger than the rod outer diameter, while the sleeve outer diameter is Ø58 mm. The sleeve is placed inside the housing (left-hand side of figure 4.3), which is cylindrical on the inside and slightly conical (1°) on the outside. The fourth major component, the Strecon® container, envelops the conical housing and has the crucial function of keeping the normal pressure on the housing-sleeve system uniform.

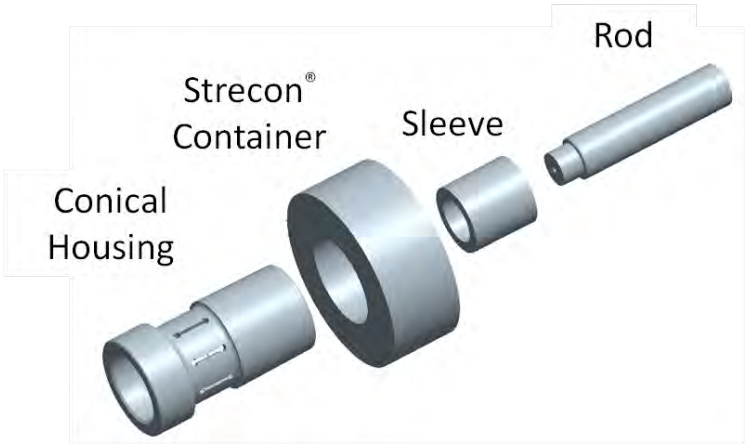

Figure 4.2: *Axial Sliding Test major components.*

Stripwound container

In order to guarantee the keeping of a constant pressure, a special production process has been used to realize the Strecon® container: the stripwinding technique. Developed over the last thirty years [141, 142], the

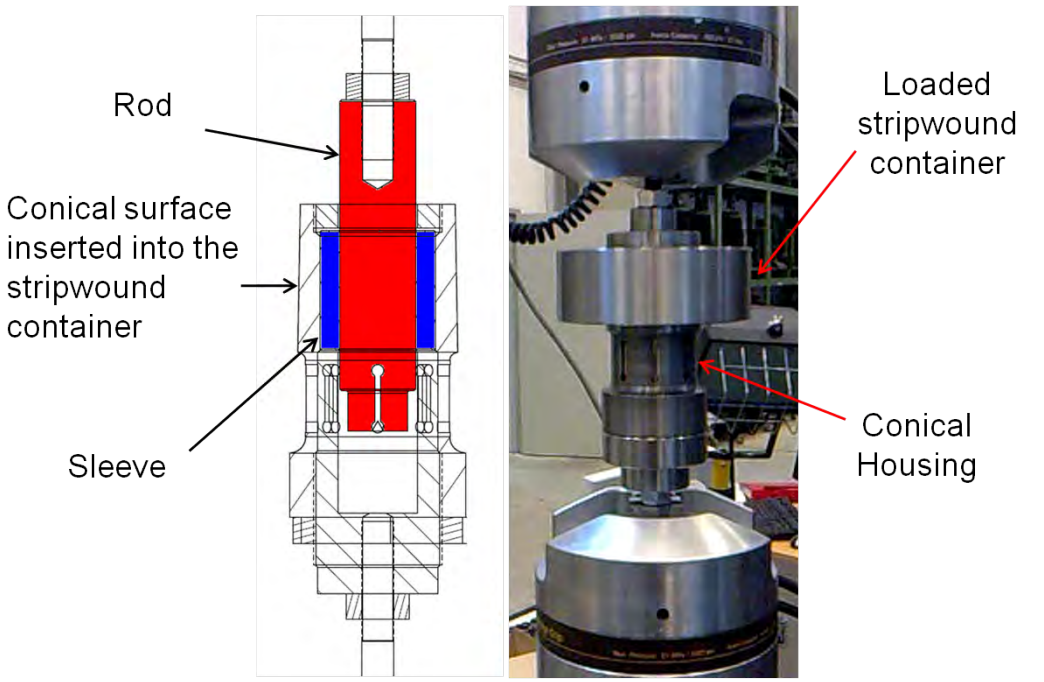

Figure 4.3: *Axial section of the assembled AST rig without stripwound container (left); the apparatus mounted in a tensile machine (right).*

stripwinding process consists in a 0.1 mm thick high-strength strip wound around a hardened core of high-alloyed tool steel (figure 4.5(a)) [68, 143]. During the winding process the strip material is loaded with a controlled back tension: varying it from layer to layer provides an optimal stress distribution (figure 4.5(b)) [68, 143]. The equivalent stress is distributed over hundreds of layers, thus avoiding stress concentrations [68]. As a result, the peak stresses in stripwound containers lie within the elastic limits: no plastic deformation and pressure losses are observed [68, 143]. The inner surface of the container used for the Axial Sliding Test has been ground to the same angle (1°) as the housing. The low cone angle keeps the container self-locking on the housing and thus the maintaining of a constant pressure is achieved.

4.1.2 Axial Sliding Test set-up

In order to be performed, the axial sliding test needs two machines: a hydraulic press and a tensile test machine.

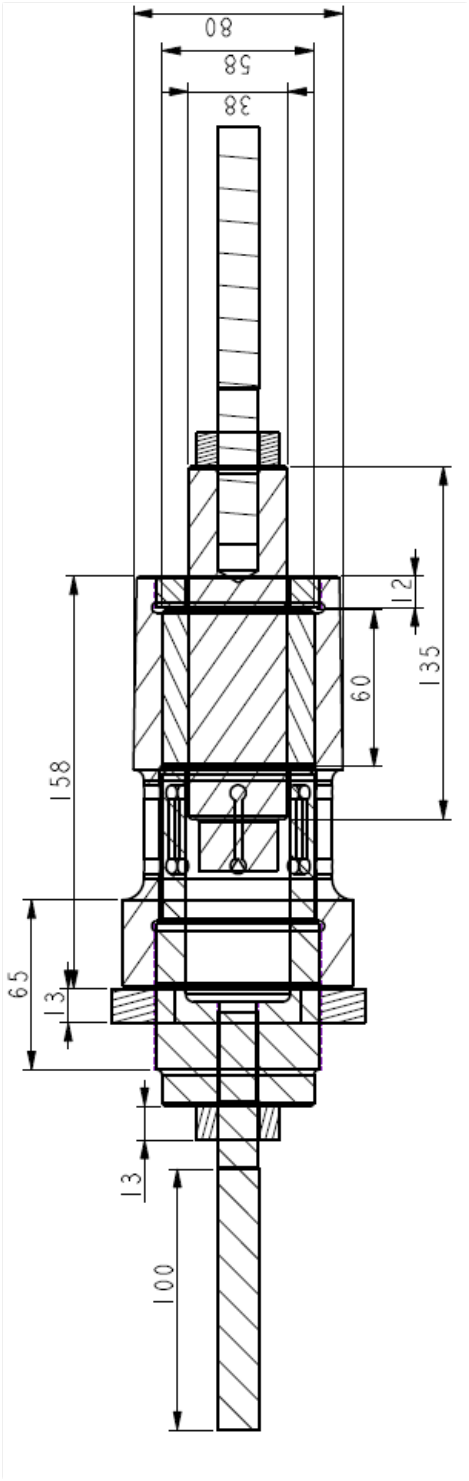

Figure 4.4: *AST technical drawing.*

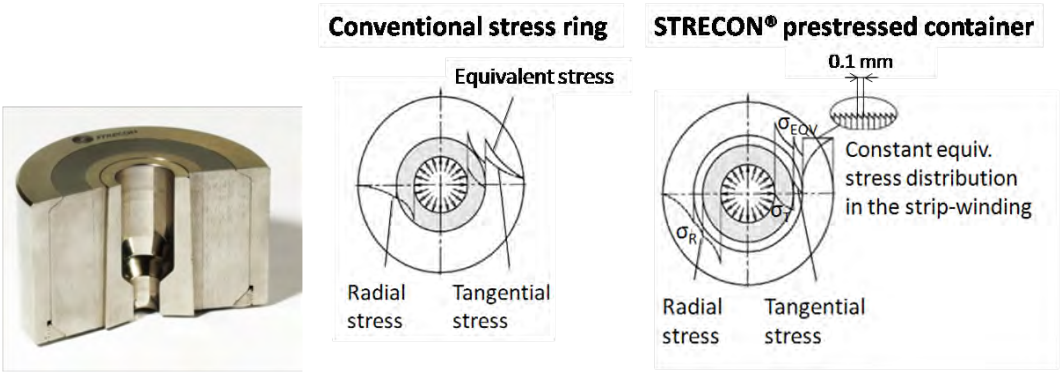

(a) (b)

Figure 4.5: *Stripwound container section (a): the AST one presents the inner surface with the same degree of conicity as the housing; Stress distribution in a conventional stress ring and in a stripwound container (b) [68].*

Pressing operation

The first operation to be performed is to load the AST apparatus. The assembled test rig is placed in the hydraulic press and the container is pressed down the housing increasing the normal pressure at a constant rate with its advance. The incremental advance of the container at every press stroke is known thanks to a series of pressure rings with calibrated heights beforehand arrayed around the housing. A mathematical model based on the theory of multiple shrink fitted rings [144] developed and utilised for many years at Strecon has been used in order to correlate container advance, sleeve inner diameter shrinkage and normal pressure. In order to verify and calibrate the model, the sleeve shrinkage as a function of the container progress is determined experimentally by a series of pressing operations (figure 4.6). In the first experiment the rod is not assembled in the test rig. The loading operation is repeated several times and before each stroke the sleeve inner diameter was measured with a three-point internal micrometer at different axial positions. When the sleeve and the housing come to full contact, the sleeve diameter reduces proportionally with the container advancement (figure 4.6). The reduction is estimated being 13 µm every mm of progress of the stripwound container. The experiment is then repeated with a hollow rod (Ø26 mm inner diameter) assembled with the sleeve. The reduction is now estimated being 9 µm every mm of progress of the container.

The verification and calibration of the model and the calculation of the normal pressure as a function of the container advance are shown in appendix C. From the calibration of the model, the normal pressure increase

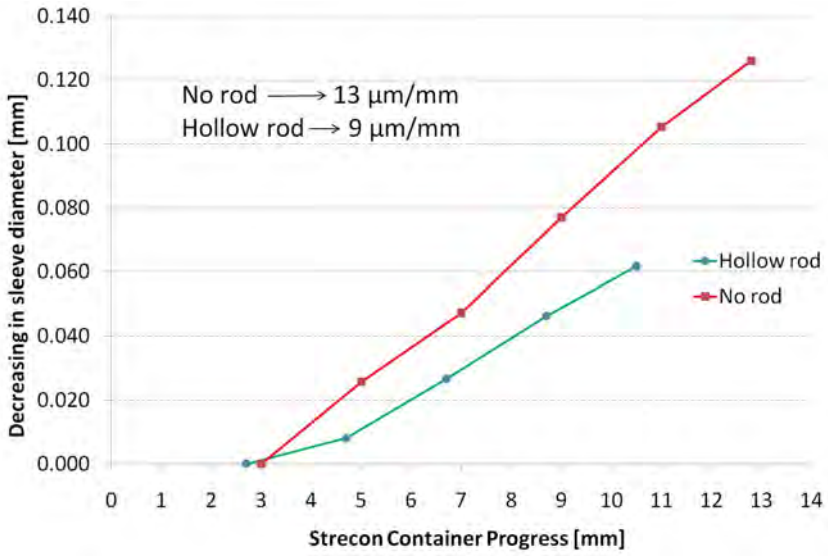

Figure 4.6: *Sleeve inner diameter reduction as a function of the container progress: the "no rod" and "hollow rod" configurations.*

is deemed being **34 MPa every mm** the stripwound container slides down the housing when a full rod is mounted in the apparatus.
This is the typical case examined: a full rod with a known texture is lubricated and inserted; the pressing operation performed and the normal pressure increment determined from the known container advancement provided by the press. Once this first operation is completed, the whole apparatus is transferred to the second station, the tensile test machine.

Tensile machine

The loaded apparatus is mounted in a tensile test machine with a load capacity of 100 kN both in tension and in compression (figure 4.3, right-hand side). The test is at last carried out making the rod sliding back and forth inside the sleeve according to a predefined program. Throughout the test, the force necessary to keep the set frequency (or speed) constant is measured by a calibrated load cell. In figure 4.7 are shown load and position results of an Axial Sliding Test performed following a sinusoidal movement: 10 cycles with a frequency of 0.2 Hz and a sampling frequency of 10 points/s. The rod is slid 15 mm back and forth, meaning that the sliding speed varies between 0 mm/s (dead centers) and approximately 19 mm/s at the center of the stroke. In the presented example, the load is comprised between 1.5 and -1.5 kN.

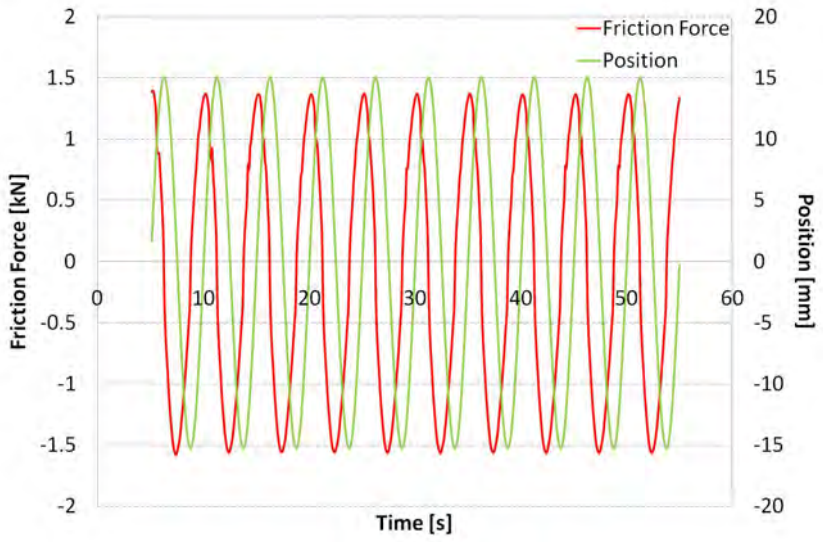

Figure 4.7: *Load and position results of an Axial Sliding Test following a sinusoidal movement.*

4.2 Preliminary and repeatability tests

In this section the very first tests run with the AST apparatus are presented. The preliminary tests were performed in order to gain knowledge on the machineries functioning, to refine the testing procedures and to have a qualitative assessment of the MUFU surfaces performances before a more comprehensive test campaign. After, repeatability tests are carried out in order to evaluate how reliable are the results obtained.

4.2.1 Preliminary tests

For the preliminary tests three specimens were realized, namely a mirror-polished sleeve with roughness Ra < 0.02 µm, a rod turned with a feed rate of 0.1 mm/rev (finely turned) and a MUFU rod turned with a feed-rate of 0.3 mm/rev and polished to a bearing area of the plateaus equal to 40% (figure 4.9). Both rods were turned using a tool nose radius of 0.4 mm. The roughness was measured with the afore mentioned independent datum inductive profilometer FTS along the axial direction. The characterisation details (FTS settings and filtering procedures) are provided in section 4.3.1. The results from the measurements are displayed in table 4.1. Every result is the average corrected by the calibration factor of 12 measurements done in 4 different locations 90° apart. The expanded uncertainty is calculated as explained in section 2.5: the instrument uncertainty can be found in the certificate of appendix A, while the u_s contribution corresponds to

the standard deviation of the 12 measurements divided by the square root of 12. The uncertainties refer to a factor $k = 2$ corresponding to a confidence level of approximately 95%. All expanded uncertainties calculated in the following will refer to this confidence level. The relatively high uncertainty connected with the sleeve measurements will also be discussed in section 4.3.1.

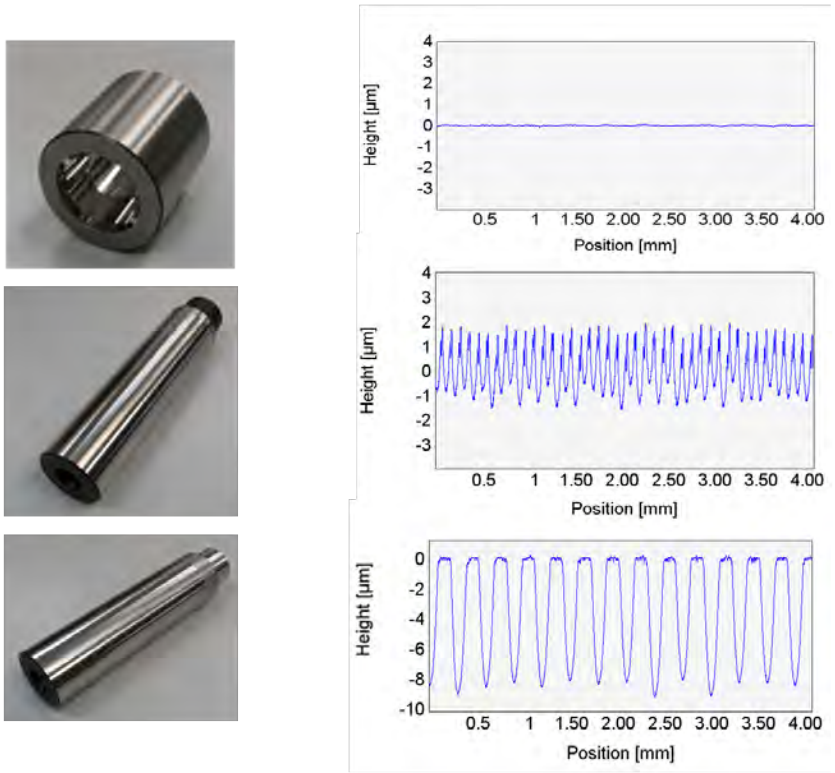

Figure 4.8: *Specimens used for the preliminary tests and their roughness profiles: a mirror polished sleeve (top), a fine turned rod (center) and a MUFU rod (bottom). The profiles were taken along the axial direction.*

The specimens were then lubricated with high-viscosity synthetic grease based on perfluorinated polyether oil (BARRIERTA® L55/3) [145]. The tests were carried out as previously described, since figure 4.7 is taken from a test performed with the MUFU rod. 30 mm constant-speed ramps (not shown in the figure) preceded and followed the sinusoidal movement in order to utilise the central zone of the rod. A number of tests were performed at different normal pressures, i.e. at different advances of the stripwound container. Precisely, the friction forces were recorded each 0.2 mm advance of the container. In order to start the experiments, a reference point (a reference pressure ring combination) is needed. Initially, the ring combination which would not allow a manual movement of the rod after

Table 4.1: Characterisation of the specimens.

Specimen	**Ra [µm]**		**Rt [µm]**		**Ra pl. [µm]**		**EQF [µm]**	
	Aver.	**U**	**Aver.**	**U**	**Aver.**	**U**	**Aver.**	**U**
Sleeve	0.013	0.009	0.183	0.029	-	-	-	-
Fine Turned Rod	0.746	0.024	3.584	0.130	-	-	-	-
MUFU 40% Rod	-	-	8.873	0.279	0.054	0.009	2.813	0.143

the pressing operation was chosen as reference point. It is a subjective method and therefore not an ideal one, but it allows the screening out of loose combinations. For each test the positive friction forces when the rod is at its maximum speed (rod position equal to 0 according to figure 4.7) were taken and averaged. The test results are plotted in figure 4.9. The ordinate axis displays the friction stresses obtained dividing the measured forces by the nominal area of contact. The abscissas, instead, represent the normal pressure increase relatively to a zero point. This zero point is not the manually determined reference; rather it is the first combination which requires loads higher than 0.5 kN. This artificial reference, which corresponds to still low friction stresses, has the advantage of being based on a specific number rather than a subjective feeling. Moreover, by discarding the results at extremely low loads, it helps to pair otherwise offset curves. The error bars shown in figure 4.9 represent the standard deviation calculated from the 10 results each test provides.

Discussion

With reference to figure 4.9, the artificial reference couples very well the two curves, being the friction stress 0.136 MPa and 0.127 MPa for the MUFU and the fine turned rod respectively. The two curves show to increase coherently for the first 15 MPa of normal pressure increase from the zero point, to eventually diverge after that limit. Due to the high lubricant viscosity it is possible that a thin film separating the two surfaces is still maintained until the pressure is 15 MPa, hence the similar behavior. After the limit, asperity contact begins to occur and the system enters in a mixed lubrication regime. The friction force appears to increase more rapidly for the combination fine turned rod - polished sleeve than the MUFU rod – polished sleeve one. By fitting a line through the observed data, the friction coefficient μ can be estimated as the slope of the line (more on friction theory in chapter 6). For the combination involving the fine turned rod µ= 0.044, while for the one

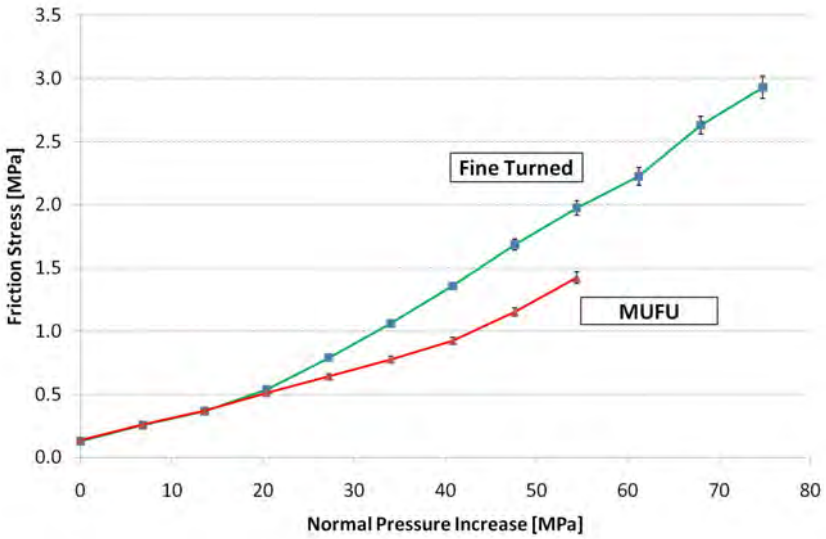

Figure 4.9: *Friction stresses comparison between a fine turned and a multifunctional rod loaded with a polished sleeve.*

involving the MUFU rod μ= 0.026. The MUFU surface seems to assure a better friction reduction than the fine turned one. Nevertheless, the results obtained with these preliminary tests must not be taken as definitive. These tests were in fact performed mainly with the purpose of improving the understanding of the AST apparatus and the machineries involved. The high viscosity lubricant, for example, was chosen to protect the surfaces for future usage (no wear marks were indeed detected in the post-test examination). The results could have hence been partly biased by the high lubricant performances. Only a qualitative assessment of the MUFU surfaces effectiveness can be given after these tests, and their initial good performance must be confirmed by a more comprehensive test campaign. The campaign is presented in section 4.3, where the definitive assessment on MUFU surface functionality is provided.

4.2.2 Repeatability tests

When a new test rig is introduced, it is important to assess the reliability of the results achieved. That can be done by testing whether or not the device provides the same results if repeatedly tested under the same conditions. For this purpose the fine turned rod was tested again. A less effective lubricant Texaco Multifak® EP2 with a viscosity of 173 cSt at 40°C [146] was used, which is more suitable for experimental purposes. The reciprocating program was also changed from a sinusoidal wave to square wave ensuring a constant speed throughout the stroke. The speed was set to 1 mm/s along

a 30 mm stroke. At the end of the stroke, a waiting time was observed, initially set to 10 s, later reduced to 2 s to shorten the test duration. The test was performed in two different days. The first day, 10 cycles at a 27 MPa were performed (figure 4.10) and afterwards, the rig was disassembled.

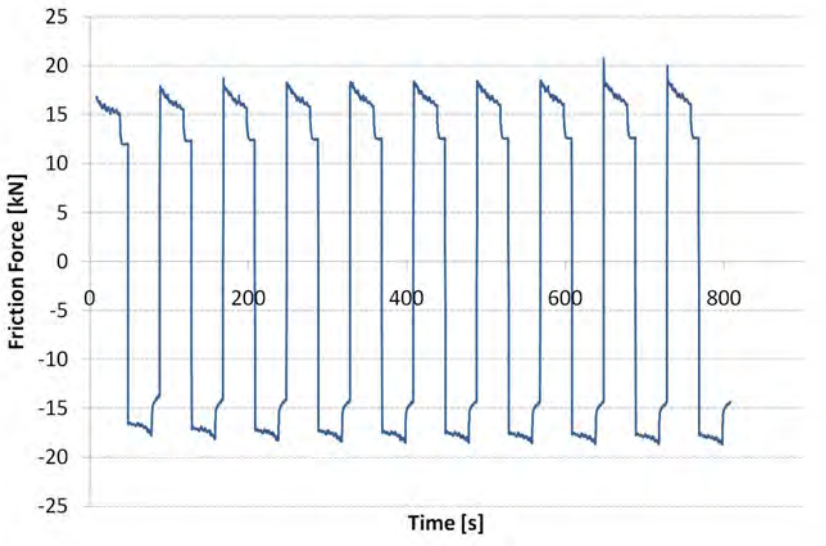

Figure 4.10: *Fine-turned rod tested at 27 MPa on the first day.*

The obtained 17 kN of friction force (average of the five last positive periods) lead to 2.8 MPa of friction stresses, more than three times higher than the ones obtained with the previous lubricant. The second day, the 10 cycles at 27 MPa were repeated 10 times consecutively without disassembling the rig between each test (figures 4.11 and 4.12).
Looking at figure 4.11, both the shape and the values of the friction forces are in agreement to what measured on the first day. The repeatability of the results is confirmed by the temporal alignment of the measured friction forces of figure 4.12. In figure 4.13 the average friction forces, calculated on the last five periods of each repetition are plotted.
The red column represents the test on the first day, the others the 10 repetitions of the second day. The error bars represent the average range between the max and min forces measured during the stroke (this systematic contribution will be explained in section 4.3.2). The range was chosen due to the systematic nature of the force trends. The test showed a slightly increasing trend in the first 5 repetitions and then stabilizing afterwards. The increment can be explained by a redistribution of the grease on the surface of the rod. This hypothesis is supported by a reduction in the force ranges and by force values similar to the ones measured the first day. In the first day, in fact, some tests had already been carried out at lower

pressures distributing the lubricant more uniformly. Generally speaking the test showed an extremely satisfactory repeatability, both in terms of force trends, all descending, and values, all comprised between 16 kN and 17 kN and all well within the error bars.

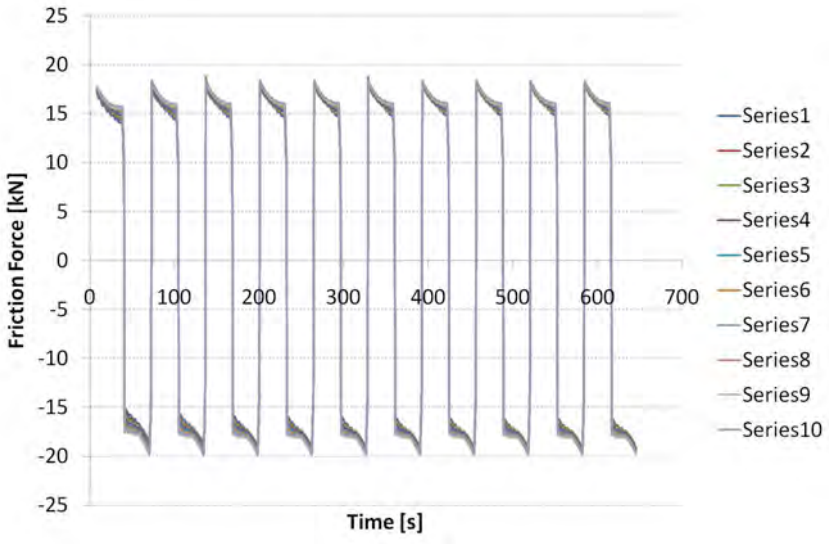

Figure 4.11: *Superimposition of the 10 repetitions at 27 MPa performed with a fine-turned rod.*

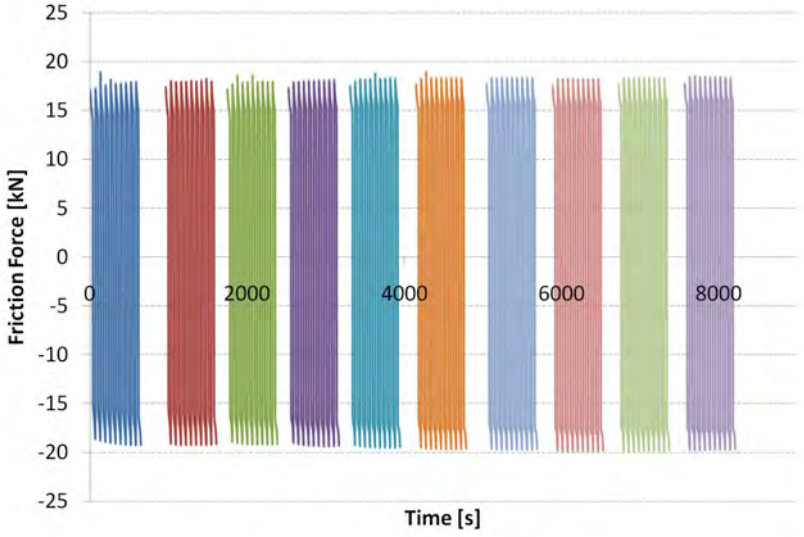

Figure 4.12: *Alignment of the 10 repetitions at 27 MPa performed with a fine-turned rod.*

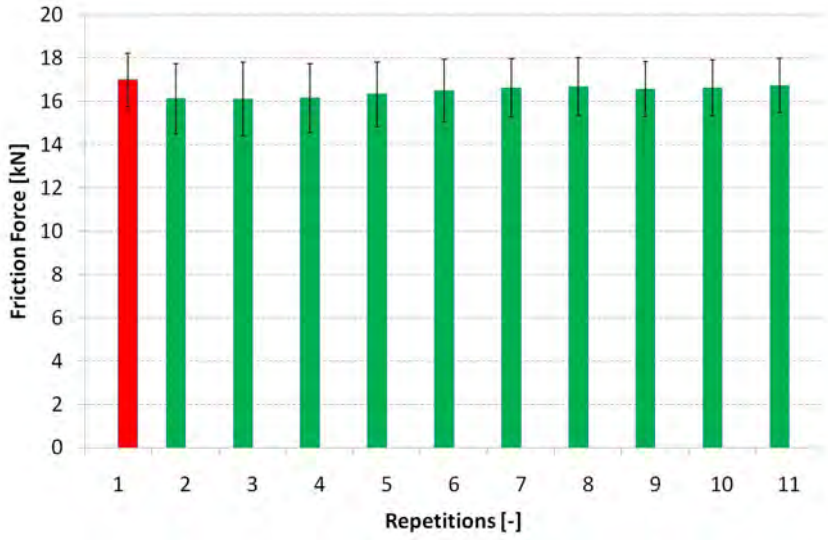

Figure 4.13: *Average friction forces during the repeatability tests.*

4.3 Axial Sliding Test campaign

In this section the test campaign for quantitatively assessing the performances of MUFU surfaces is presented. The section consists of two main parts: the specimens characterisation and the test results together with form considerations and discussion.

4.3.1 Specimens characterisation

In order to decrease the degrees of freedom of the test, it was decided that only the rods would have texture applied. The case under study is therefore the one of a nominally flat surface in contact with a non-flat one, i.e. the sleeve roughness should be at least one order of magnitude smaller than the rods'. The same mirror-polished sleeve used in the preliminary tests is here employed. Six rods were instead realized, three using classical manufacturing methods and three MUFU. In particular, the regularly machined rods were respectively one fine-turned with feed rate 0.1 mm/rev (the same used in the preliminary tests), one ground and one polished. The three MUFU rods were hard-turned with feed rate 0.3 mm/rev but polished at a different level of plateau bearing area. The rods are labelled respectively MUFU20%, MUFU40% and MUFU55%, where the percentage represents the nominal bearing area of the plateaus. All rods which underwent a turning operation were turned with a tool nose radius of 0.4 mm. All the specimens were characterised using the FTS. As before, for each specimen 12 profiles were taken in four different positions

90° apart. The roughness was measured before and after testing. Each profile has an evaluation length of 4 mm and was filtered in order to remove form and waviness components. The measurements were carried out with a stylus speed of 0.5 mm/s and with a probe tip radius of 2 µm. The "traditionally" machined surfaces were filtered beforehand with a λs filter of 2.5 µm and afterwards with a 2nd order Gaussian Regression filter using a cut-off length of 0.8 mm. No form removal was applied due to the excellent form following properties of the 2nd order regression. The measured profiles are shown in figures 4.14 and 4.15 alongside 1 mm x 0.3 mm 3D topographies taken for visualization purposes. The range of visualization (8 µm) was chosen for comparing the textures scales at the same axes values. The choice was based on the Rt of the MUFU40% rod. All the specimens textures but MUFU20%'s can be represented within 8 µm. Choosing MUFU20% would have cause difficulties in visualizing the texture of the traditionally machined specimens.

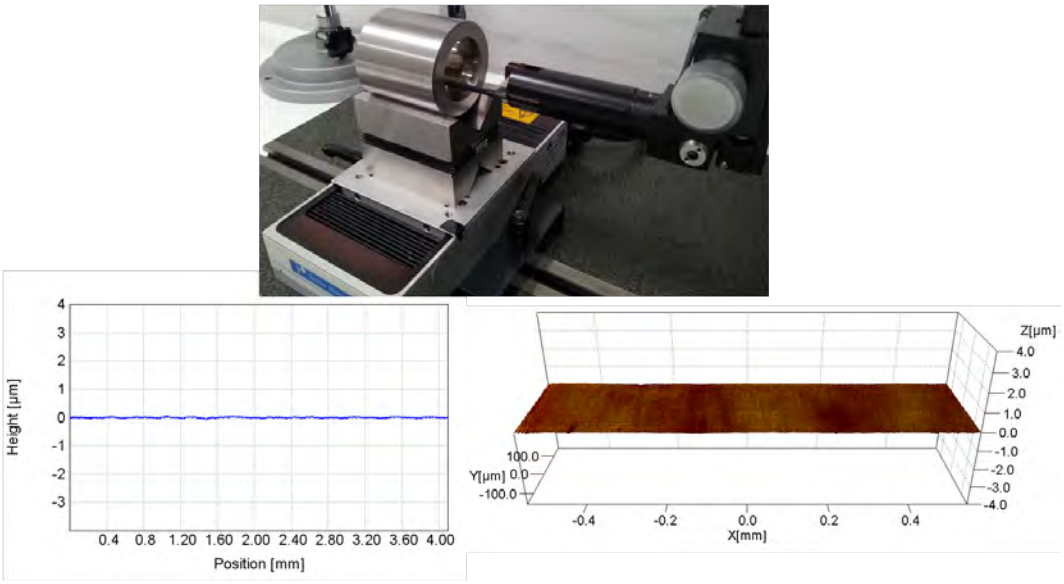

Figure 4.14: *Mirror-polished sleeve: measurement set-up, profile and 3D topography.*

The Ra and Rt values of the obtained profiles together with their expanded uncertainties were calculated and listed in table 4.2. The uncertainty calculations ware carried out as before explained.
The MUFU rods, conversely, were characterised using the procedure of figure 4.15. They were filtered using Robust Gaussian Regression filters with 0.8 mm cut-off length as a basis. Only MUFU55% was characterised with a "normal" RGR of the 2nd order, while for the other two rods, a modified RGR was required. The initial closing operation was performed with a disk radius equal to 0.8 mm and the Robust filtering used a first

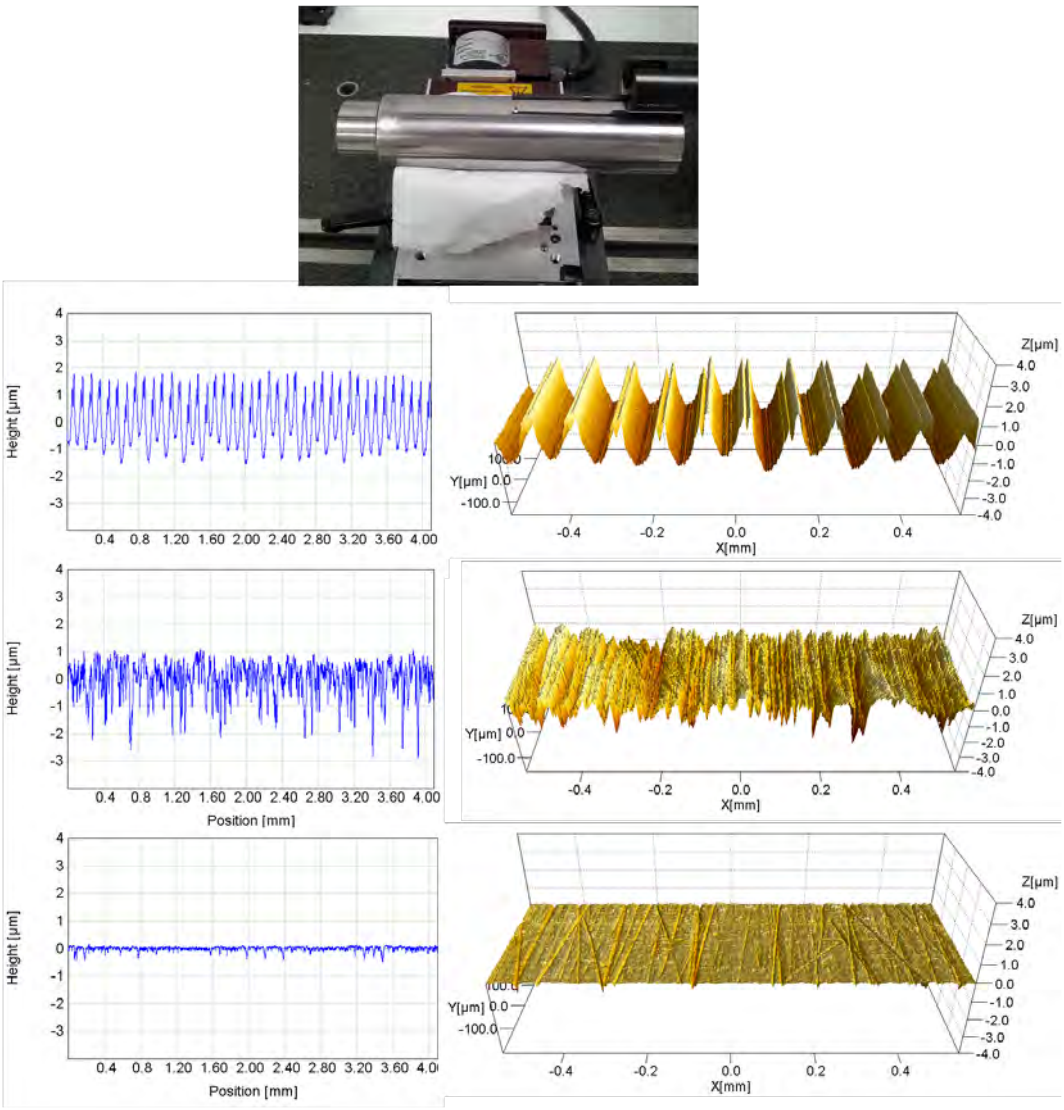

Figure 4.15: *Regularly machined rods: measurement set-up, profiles and 3D topographies.*

quartile estimator. In the filtering of MUFU20% only 1σ was used, whereas 3σ were used in the case of MUFU40%. The profiles as well as the 3D topographies are displayed in figure 4.16. It can be seen that the filters choices produced sound reference lines which caused no distortion in the resulting roughness profile. For the quantification, three parameters are extracted:the plateaus Ra; EQF and the Rt of the entire profile for comparison with the other surfaces. They are collected in table 4.3 along with their expanded uncertainty. Moreover, as an indication, the bearing area of the plateaus BA is presented together with its standard deviation as

Table 4.2: Characterisation of the regularly machined specimens.

Specimen	**Ra [µm]**		**Rt [µm]**	
	Average	**U**	**Average**	**U**
Sleeve	0.013	0.009	0.146	0.026
Fine Turned Rod	0.752	0.024	3.615	0.136
Ground Rod	0.512	0.027	4.526	0.214
Polished Rod	0.047	0.009	0.848	0.062

explained in section 3.6.2.

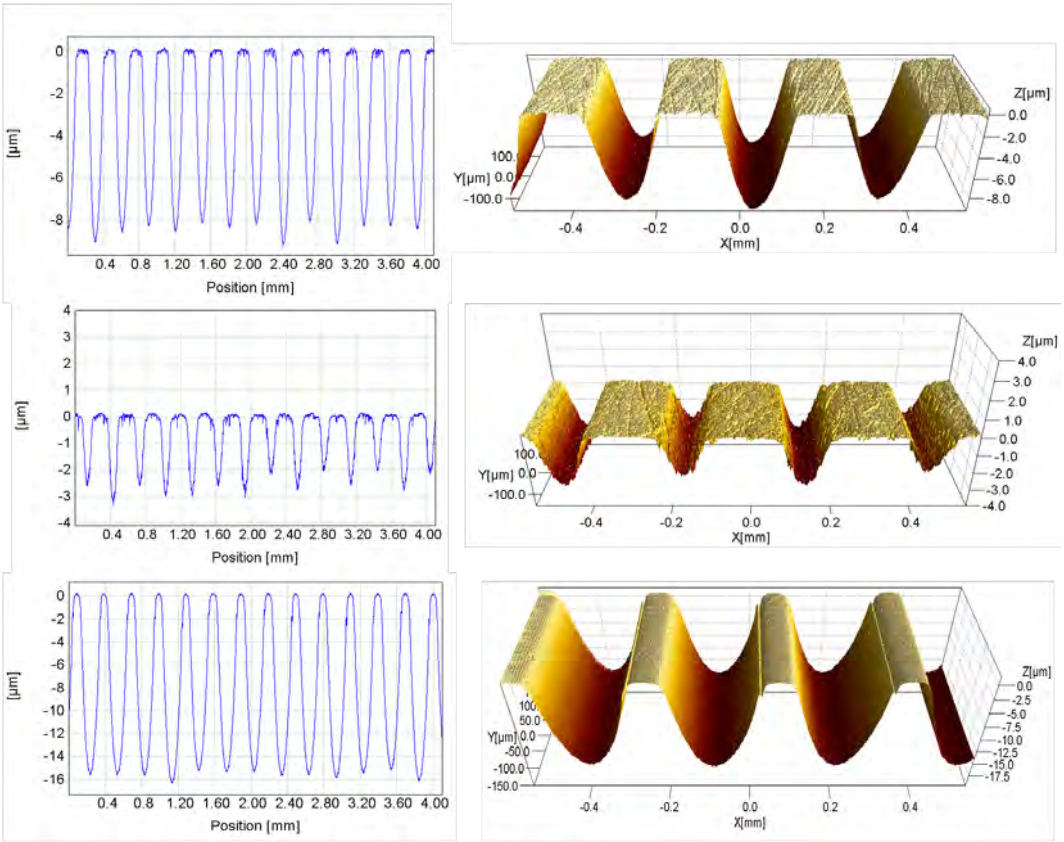

Figure 4.16: *MUFU rods: measurement set-up, profiles and 3D topographies.*

Table 4.3: Characterisation of the MUFU rods.

Specimen	**Rt [µm]**		**Ra pl. [µm]**		**EQF [µm]**		**BA [%]**	
	Aver.	**U**	**Aver.**	**U**	**Aver.**	**U**	**Aver.**	σ
MUFU 20%	16.910	0.197	0.022	0.009	7.870	0.099	20.3	0.7
MUFU 40%	9.234	0.173	0.055	0.009	2.948	0.108	41.9	1.3
MUFU 55%	3.619	0.168	0.037	0.009	0.619	0.027	54.4	1.5

Discussion

The sleeve is characterised by a roughness which nearly reaches the noise of the instrument, hence the relatively high uncertainty. The measurements on the optical flat revealed a background noise of 0.008 µm (see appendix A) which represents the major contribution to the instrument uncertainty when fine surfaces are measured. The measurements on the sleeve are not then extremely reliable, even though they were very repeatable, being the standard deviation just 0.001 µm. For having less uncertain results, instruments with higher resolutions and less noise should be used, but they would face the non-trivial problem of accessing such internal features without destroying the specimen (figure 4.14): the FTS was the only instrument available capable of such measurements. However, it is safe to assume that the roughness of the sleeve is lower than 0.02 µm, where the average value of 0.013 µm represents a good estimate. The sleeve has therefore a roughness of at least 1 order of magnitude lower than all the other surfaces, except the polished rod. This was however polished rougher than the sleeve and its Ra equal to 0.047 well comply with its uncertainty. The fine-turned and the ground rods have similar roughness: the turned one has slightly higher Ra, the ground one slightly higher Rt. It is anyhow evident from figure 4.15 the deterministic nature of the turned process in contrast with the stochastic nature of the ground one. The Rt value of the fine-turned rod and the MUFU55% are similar, with the MUFU one presenting broader valleys due to the higher feed-rate employed. The other MUFU rods have much higher Rt. These three rods were manufactured with the same feed-rate and tool nose radius, meaning that an increasing bearing area of the plateaus corresponds to a lower amount of lubrication stored in the valleys. MUFU55% has therefore a much lower EQF than MUFU20%. Finally, the roughness of the plateaus is comparable with the one of the polished rod, especially in the case of the MUFU40% rod. That was expected since they are produced by using the same RAP process. Moreover, looking at the 3D plots of figures 4.15 and 4.16 (which is the

same as in figure 1.8), the similarities are highlighted. The polished rod presents transversal scratches, remainders from the pre-machining process, and crossed scratches from the RAP polishing. The same crossed scratches can be detected in the plateaus of the multifunctional rod. These two surfaces will thus present a similar tribological contact with the sleeve.

4.3.2 Test results

The tests were performed with the same settings and lubricant as the repeatability tests. More specifically, the "square wave" implies that the movement follows a trapezoidal position curve. The movement was reciprocating, meaning that the rod travelled back and forth 30 mm each stroke. Ten cycles were run. Before and after the first and last 30 mm stroke, 8 mm run-in and run-outs were observed. The idle periods were kept, initially equal to 10 s, then reduced to 2 s for speeding the experiments up. The function of the idle period was to monitor the response of the acquisition system with respect to the rod movement. The travel speed was chosen deliberately low so that no hydrodynamic effect occurs during the test and the most severe tribological conditions for machine elements are achieved. Friction forces were measured throughout the test by the calibrated load cell embedded into the machine at a frequency of 5 points/s.

Form considerations

With these settings the friction forces curve against time would ideally have the shape of a square wave, with constant friction forces during the constant speed stroke. In figure 4.17 are plotted the position and the forces of a test run with the fine-turned rod.
Positive and negative forces differ slightly in absolute value: this may be due to different tribological contact pairs along the two directions. Considering only the positive forces, they are to some extent decreasing during the stroke. The same trend was found when testing the ground and the polished rod. The multifunctional rods exhibited instead different behaviors: MUFU20% rod had initially constant forces decreasing in the end, MUFU40% rod showed increasing forces, whereas the MUFU55% showed a more various trend. The trends are summarized in figure 4.18.
A first explanation found in literature could be attributed to hysteretic frictional behaviour that can occur during large-scale motion in pure sliding [147, 148]. This, however, seems not to be the case, since in [147, 148] the pure sliding was performed using an oscillatory, sinusoidal movement where the speed was varying during the stroke. Here, instead, the movement was set to a constant speed (1 mm/s), much slower than the

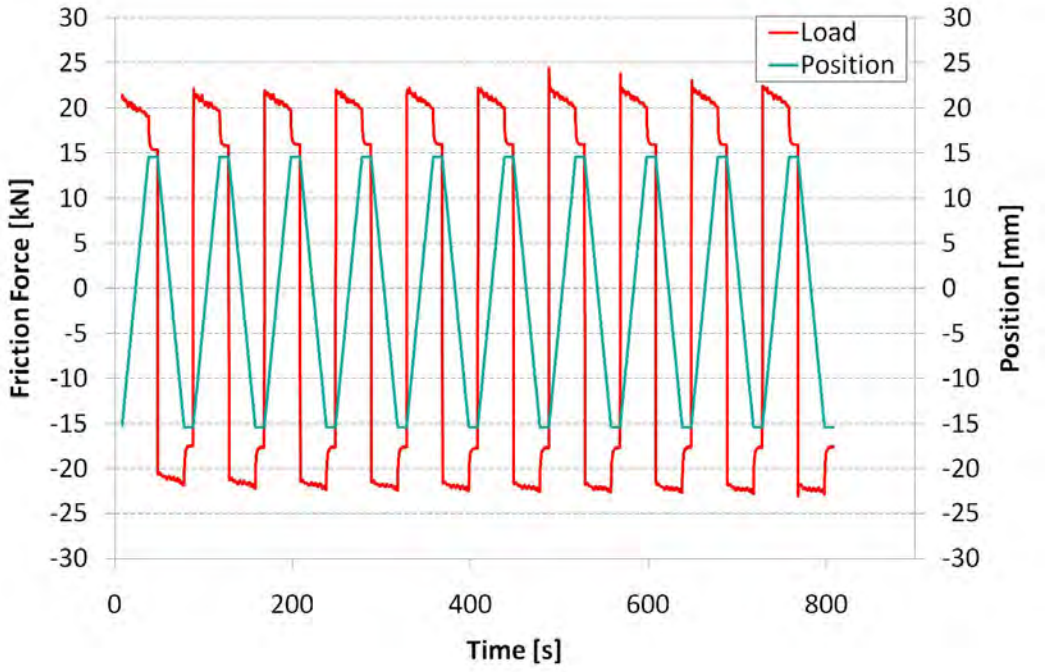

Figure 4.17: *Example of position and friction force measurements while testing the fine-turned rod.*

experiments of [147]. The acceleration/deceleration period was limited to tens of a second (thus tens of mm) at the beginning and at the end of the stroke. Hence, if any hysteresis had occurred, it would have had a much smaller effect on the force trends compared to the observed ones. Other explanations for such behaviours must be sought and one can be found by studying the rod geometries, hitherto considered as perfect cylinders. If, instead, the rods present form errors, fewer points will be in contact displaying higher local pressures. The hypothesis is that, a decreasing trend, for instance, means that some points at higher pressure will be drawn out of the loaded zone releasing lightly the rod. Similar geometries will therefore have similar force trends. In order to prove the hypothesis, the form errors must be found and compared to friction force trends. Diameter measurements were then performed every 10 mm using a CMM (figure 4.19) and the diameter results were plotted in the test zone, i.e. the zone of the rod nominally contacting the sleeve during one ramp.

In figure 4.20(a) the two most similar rods in terms of geometry are compared: the ground and the polished ones. Although the polished rod has slightly higher diameter than the ground one, their trends are extremely similar, with 5 µm difference between the first and the last diameter in both cases. In order to confirm the hypothesis the force trends of the two rods

should also be similar. Figure 4.20(b) displays the friction forces results of the seventh cycle at their respective highest normal load. The friction forces exhibit alike tendencies, slightly descendent (positive forces) as the rod runs, confirming thus the hypothesis.

A comment must be done on the force trends of the rod MUFU55% which change suddenly shape at higher forces (figure 4.18(f)). This is due to the fact that in this analysis the sleeve shape was considered perfectly cylindrical. Measurements done with a three-points internal micrometer at

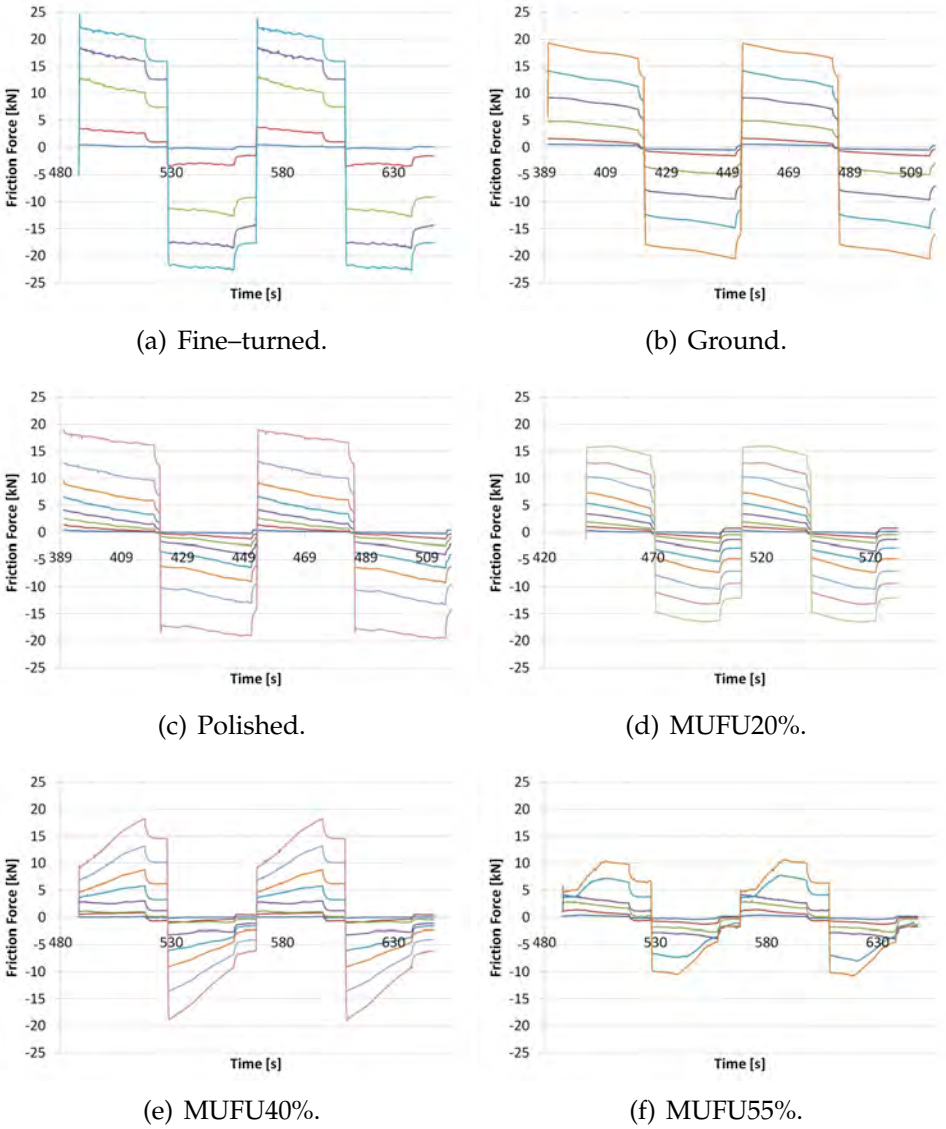

(a) Fine–turned.

(b) Ground.

(c) Polished.

(d) MUFU20%.

(e) MUFU40%.

(f) MUFU55%.

Figure 4.18: *Force trends during the entire test campaign of the several rods taken at cycles 7 and 8.*

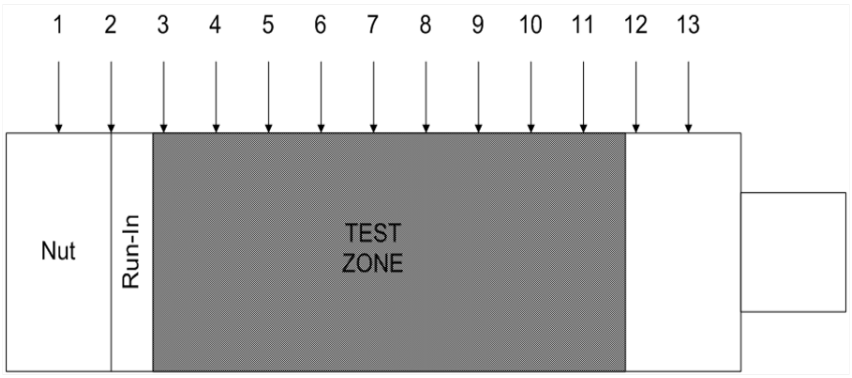

Figure 4.19: *CMM measurement position with the test zone highlighted.*

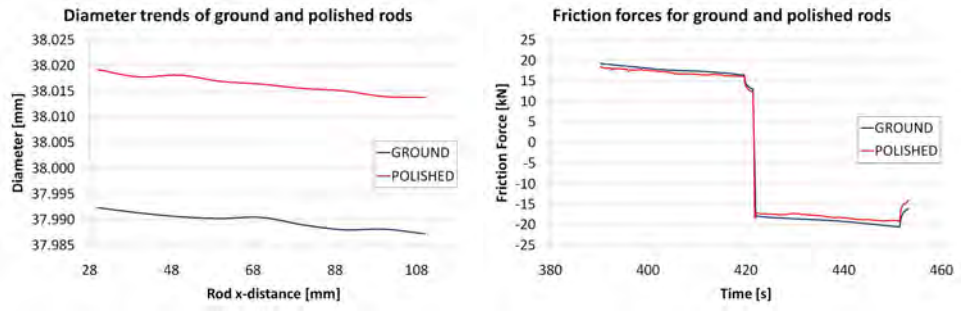

(a) (b)

Figure 4.20: *Comparison between the ground and polished rods geometries and friction forces.*

different pressures confirmed this hypothesis, with the exception of when the stripwound container reached the end of the conical housing: there the sleeve was becoming conical on its innermost end. The MUFU55% rod had the lowest diameter of all rods and had to be tested until the end of the container. The CMM measurements on the MUFU55% rod confirmed that the geometry of the rod follows the force trend: the conicity of the sleeve only enhanced the rod form error since a "bottleneck" was created causing higher local pressures.

Data analysis

Acknowledging therefore the presence of form errors affecting the force shape, the analysis of data was performed as follows: for each experiment the last 5 cycles, (the more stable) were considered; the average value of each positive cycle is taken and plotted; the range is utilized as measure of data variation. The reason for using the range rather than the standard deviation

is the systematic trends of the force within a period. In figure 4.21 the resulting friction stresses are plotted against the normal pressure increase. The friction stresses were calculated by dividing the measured forces by the internal area of the sleeve. The normal pressure increase represents the increment of normal pressure from an artificially chosen "zero-point". Starting from loose assembly conditions, the stripwound container was made gradually advancing with steps of 0.2 mm (i.e. 6.8 MPa of normal pressure increase). The zero-point corresponds to the last assembly conditions leading to friction forces lower than 1 kN. From the zero-point the forces were considered relevant (mixed-lubrication regime) and recorded keeping the same advancing step.

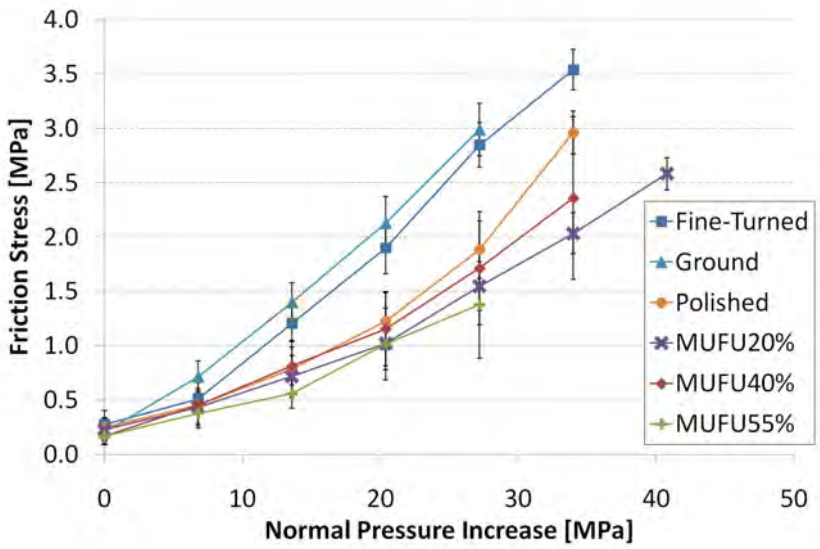

Figure 4.21: *Resulting friction stresses of the tested surfaces vs. normal pressure increase. The intervals covered by the error bars represent the ranges of force variation.*

Moreover, the Coulomb friction coefficients (μ, see chapter 6) are estimated. This is done by fitting a third order polynomial curve to each line and calculating the first order derivative at specific normal pressures. For each rod, five friction coefficients are calculated in the range 15-25 MPa. The results are shown in figure 4.22. The error bars indicate the variability of the friction coefficients due to the imperfect form of the specimens and their calculation is explained in the following. Similarly to what done for the friction stresses, also for the friction coefficients the range was selected as a measure of deviation. The ranges are calculated by creating two plots similar to the one of figure 4.21: in the first one are plotted the maximum friction stresses; in the second one the minimum friction stresses. Afterwards the polynomial fitting is performed again in these two plots yielding the maximum and minimum friction coefficients and thus

the ranges. These can be considered as rectangular distributions with limits plus and minus half range. According to [121], if a half range is divided by $\sqrt{3}$, the uncertainty contribution corresponding to a singular standard deviation is eventually found. The error bars of figure 4.22 represent indeed this contribution.

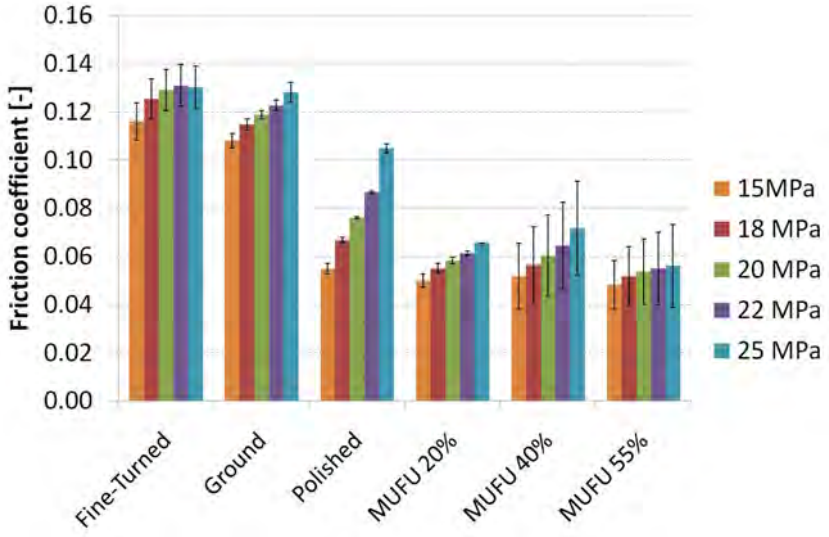

Figure 4.22: *Friction coefficients comparison at different normal pressure increments. The error bars indicate the variability of friction coefficients as explained in the text.*

Discussion

From figure 4.21 it is evident that the ground and the fine-turned rod displayed higher friction stresses compared to the other rods. The polished rod follows initially the MUFU40% one, but it increases steeply at higher pressures. Generally, the MUFU rods displayed lower friction forces than the ordinarily manufactured rods. Although the MUFU40% presented high variations making its assessment governed by high uncertainty, it is safe to conclude that all the MUFU rods caused less friction forces than the turned and the ground rod. Moreover the MUFU55% and the MUFU20% rods presented lower friction forces with respect also to the polished rod. As particular instance, it is observed that the friction stresses associated with the MUFU55% rod at 27 MPa of normal pressure increase were half the ones of the fine-turned rod (1.4 MPa against 2.8 MPa). Figure 4.22 confirms the analysis made with the friction stresses: the fine-turned and the ground rod exhibit the highest friction coefficients, with μ average values comprised between 0.11 and 0.135. On the other hand, the three MUFU rods showed average friction coefficients of approximately 0.05-0.06, slightly increasing

with the normal pressure. MUFU55%, in spite of the high force variations within a stroke due to higher local normal pressure experienced, maintains a rather stable average friction coefficient at increasing pressures. The highest average friction coefficient ($\mu = 0.072$) detected on the MUFU rods is reached by MUFU40% at a pressure increase of 25 MPa, which is well below the level of the fine-turned and ground ones despite the high variations. The polished rod showed low initial friction coefficients (comparable to the MUFU rods ones), though steeply increasing till reaching $\mu = 0.1$ at the highest pressure increment considered. The polished rod is therefore extremely sensitive to normal pressure changes, which is not favourable in practical applications. The comparison demonstrates how the MUFU surfaces lead to improved performances in terms of both friction forces and coefficients under pure sliding conditions compared to traditionally machined surfaces. The phenomenon can be explained by the particular conformation of the MUFU texture. The load is withstood by polished plateaus spaced out by large pockets for lubricant storage in which a hydrostatic pressure is built up. The effect of hydrostatic pressure build-up helps the surface to bear the load and is more important as the normal load increases. Generally speaking, smaller pockets, corresponding to lower equivalent film thicknesses, experience higher build-ups and are therefore particularly effective at high normal loads. As a matter of fact, the rod with lowest equivalent film thickness, MUFU55%, displayed the lowest friction stresses and coefficients at high normal pressures. The result of MUFU55% would have been probably even better if the non-symmetrical shrinking of the sleeve had not occurred: the "bottleneck" effect caused in fact an abrupt increase of the friction stresses (figure 4.21). However, at low normal pressure the hydrostatic pressure build-up seems not to be important, so that the friction coefficients of the MUFU rods and even the polished rod are alike. At those pressures the nano-scale plateau roughness is of predominant importance: at similar roughness correspond similar behaviours. The comparison between the polished rod and the MUFU40% one is enlightening in this matter. The two rods displayed similar roughness (the Ra values are respectively 0.047 µm and 0.055 µm and both have transversal polishing tracks) and superimposing friction forces trends and coefficients at low normal pressures. At higher pressures, instead, the absence of pressurized reservoirs in the polished rod caused an abrupt increase in contact and thus of friction forces and coefficients. The obtained results are in agreement on what found in the cited previous research within the topic. In their tests, [28] displayed how parallel, transversal grooves reduce the sliding friction between a roller and piston in hydraulic motors compared to the original tumbled surface. Moreover, their tests show similarities between the friction coefficient of the textured surface and a

well-polished one. Furthermore, [59] demonstrate how a textured pin for pin-on-disk testing can result in high degrees of friction reduction compared to the untextured case (up to 80% reduction).

4.3.3 Post-test inspection

The surface roughness was measured again after each test using the same strategy as before. The aim was to observe any possible difference with the original texture caused by wear occurred during the testing process. No wear was visible by simply visually inspecting the rods and the roughness measurements, summarized in table 4.4, confirmed the impression.

Table 4.4: Characterisation of the specimens after testing.

Specimen	**Ra [µm]**		**Rt [µm]**		**Ra pl. [µm]**		**EQF [µm]**	
	Aver.	**U**	**Aver.**	**U**	**Aver.**	**U**	**Aver.**	**U**
Fine Turned Rod	0.748	0.024	3.771	0.242	-	-	-	-
Ground	0.507	0.032	4.464	0.330	-	-	-	-
Polished	0.042	0.009	0.698	0.038	-	-	-	-
MUFU 20% Rod	-	-	16.765	0.176	0.022	0.009	7.866	0.096
MUFU 40% Rod	-	-	8.953	0.202	0.055	0.009	2.799	0.1173
MUFU 55% Rod	-	-	3.675	0.094	0.032	0.009	0.698	0.031

Generally speaking, the rod roughness results were extremely close to the initial one and no plastic deformation of the asperities occurred. Only the polished rod presented a slight decrease in roughness both in Ra and Rt. The decrease in Ra is within the uncertainty limits of the previous measurement and therefore not significant, whereas the decrease in Rt seems more significant in relation to the uncertainty. This can be due to the relatively high loads and the metal-to-metal contact causing the steep increase in friction. Anyhow this is just an hypothesis, since no wear was detected on the specimens, which was an expected result as the rods underwent less than 100 sliding cycles each. The sleeve, instead, underwent all the cycles and was measured after each rod had been tested. Looking at table 4.5, the Ra value is almost unchanged with respect to the original one, but the Rt values are higher with higher uncertainties due to larger deviations.

Table 4.5: Characterisation of the mirror-polished sleeve after each test (results in µm).

	Fine-Turned		**Ground**		**Polished**		**MUFU20%**		**MUFU40%**		**MUFU55%**	
	AV	**U**	**AV**	**U**	**AV**	**U**	**AV**	**U**	**AV**	**U**	**AV**	**U**
Ra	0.015	0.009	0.013	0.009	0.015	0.009	0.013	0.009	0.015	0.009	0.015	0.009
Rt	0.239	0.046	0.193	0.056	0.184	0.020	0.215	0.049	0.223	0.061	0.210	0.053

The Rt value, being the max peak-to-valley distance in the profile, is extremely sensitive to outliers, but, in this case, it can give information on occasional scratches accidentally probed by the stylus. By visually inspecting the sleeve, some scratches along the axial direction were detected. The higher Rt values together with higher deviations confirmed the hypothesis: some scratches were probed and influenced the results. In order to estimate the scratches depth, a replica of the sleeve inner surface was taken with a low viscosity casting silicone (AccuTrans® [149]), which [122] states being the best choice available for a faithful replication of surface texture. The replica was measured using the focus variation microscope of figure 2.6(a) with a 20X magnification. In figure 4.23, left-hand side, the top view of the 3D measurement is shown.

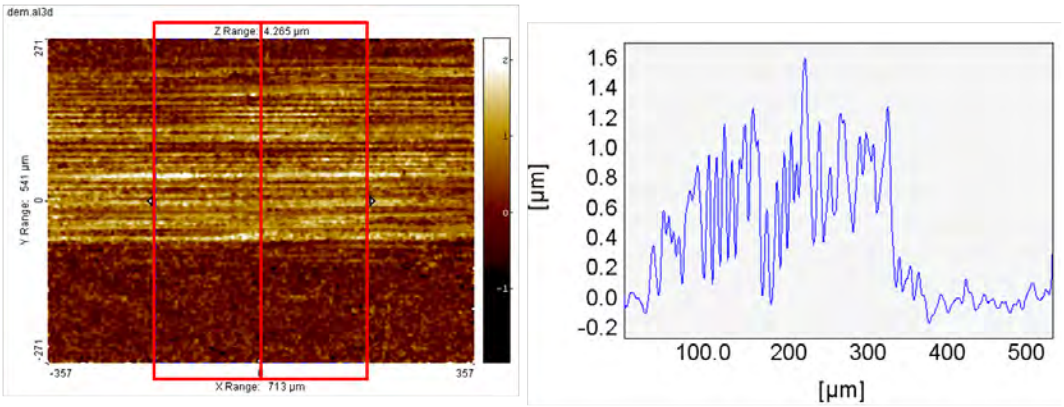

Figure 4.23: *Optical measurement on replica of the inner surface of the sleeve and transversal average profile.*

The presence of a much rougher scratch is evident, highlighted by the transversal profile at the right-hand side of figure 4.23 which is the average of the profiles contained in the red area: the scratched zone has a Ra =0.271µm, while the unworn zone has Ra =0.041µm. Ploughing wear (a wear typology that includes the relocation of material of the surface forming peaks and leaving valleys [150]) seems therefore to occur on the mirror-polished surface of the sleeve after being tested for a high number of cycles

at high loads and under mixed lubrication conditions.

4.4 Summary and Conclusions

In this chapter the testing of MUFU surfaces for machine elements applications has been presented. A new test rig, named Axial Sliding Test, has been devised and developed for simulating pure sliding conditions between two counterparts: the rod and the sleeve. The stripwinding technique was employed for keeping the normal pressure constant throughout the experiments. For performing the test, two machines are needed: a press to load the system and a tensile test machine for ensuring the rod-sleeve relative movement. The test is calibrated so that the normal pressure increase for every mm of advance of the stripwound container is known. This is equal to 34 MPa/mm. At first preliminary tests are carried out for improving the test knowledge and refine the test procedures. A fine-turned rod and a MUFU one were utilized against a mirror-polished sleeve. These initial tests prove qualitatively that a multifunctional surface can be a valid candidate for reducing friction forces in machine elements subjected to pure sliding. Afterwards, repeatability tests were carried out using again the fine-turned rod displaying an extremely satisfactory repeatability both in terms of average force values and curve shape. Eventually, the comprehensive test campaign was carried out. Six rods with different textures were selected for the experiments as well as a single mirror-polished sleeve. The specimens were characterised before testing with the techniques before presented. The specimens were then tested under the same conditions, i.e. lubrication, temperature, reciprocating movement settings, etc. Moreover, the tests were all carried out in the same range of normal pressure increments; therefore the recorded friction forces and the extrapolated friction coefficients could be compared. In particular, the tests have shown that:

- Systematic force trends were detected during the stroke and linked to form errors by means of force-geometry comparisons;

- MUFU surfaces showed clearly lower friction forces and coefficients compared to ground or turned surfaces (up to 50% reduction);

- The polished surface displayed similar friction forces and coefficients with respect to the MUFU rods at low normal pressure, but presented an abrupt force increment at high normal pressures due to the absence of lubricant reservoirs;

- The presence of lubricant reservoirs is effective at high normal pressures due to the hydrostatic pressure increase of the trapped lubricant:

in this particular case lower EQF were related to higher pressure increases;

- No wear was detected on the rods, whereas the sleeve showed initial signs of ploughing wear due to repeated cycles under high pressure in a mixed-lubrication regime.

The introduction of the new test rig opens up a number of possibilities for further work. It would be interesting to confirm or compare the results obtained with full-scale tests in a production environment, but that was not possible within this framework. Keeping confined to the AST itself, the investigation of new surface combinations as the texturing of the sleeve rather than of the rods represents another appealing basis for future work. Moreover, it must be reminded that the AST is not limited to surface texture assessment but can be also used as a mean, for example, for lubricant testing. The research possibilities that the test rig offers, then, are not limited to the borders of this project, but are much larger. The test is indeed a general purpose test for machine elements under sliding conditions.

Chapter 5

Testing of MUFU surfaces for metal forming tools

This chapter deals with the testing of MUFU surfaces on metal forming applications, in particular sheet metal forming. There exists a large variety of sheet metal forming processes (see [27, 38]), whereof the one deemed being positively affected by the introduction of MUFU surfaces is **deep drawing**. Deep drawing is a process in which a blank is drawn into the gap between a punch and a die in order to form a cup-shape part [38], as shown in figure 5.1. Usually the process is carried out without reducing the thickness of the blank, but in some cases the process is used in combination with another sheet metal forming operation, **ironing**, which reduces the sheet thickness without changing its inner diameter [38] achieving therefore greater height-to-diameter ratios.
In sheet metal forming applications, when it is employed, texturing has

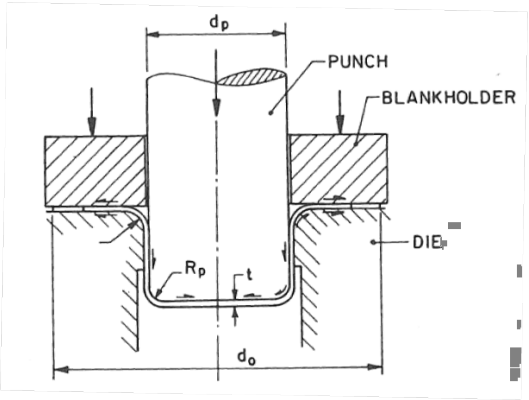

Figure 5.1: *Deep drawing of a cylindrical cup: d_p punch diameter; R_p punch radius; d_0 blank diameter; t blank thickness. Half arrows indicate frictional shear stresses acting on partially formed cup. Picture taken from [38].*

traditionally regarded the workpiece side. As explained in section 1.3, recent studies by [65–67] have though collected their attention on the tool side, more suitable for the application of MUFU surfaces. The aim of the investigations presented in this chapter is therefore to assess the tribological performances of dies featuring MUFU surfaces compared to the ones of more classical untextured dies. The first step to be done is to identify simulative tests which can give relevant indications on MUFU surfaces functionality under controlled laboratory conditions. In the following section 5.1 the simulative tests selection is carried out and their description is presented.

5.1 Simulative tests identification

Simulative tests are tests modelling the tribological conditions in metal forming processes with the attempt to study friction and/or lubrication in a specially controlled way [151]. An overview of the most frequently applied simulative tests for sheet metal forming is shown in figure 5.2 [151]. These tests simulates the possible tribological situations that can occur in metal forming processes: three tests (number 1-3) regard the flange region; two (4-5) simulate the conditions on the die curvature; one (6) simulates ironing in a conical die and the last two (7-8) represent stretching over the punch radius of curvature and under the punch nose [151].

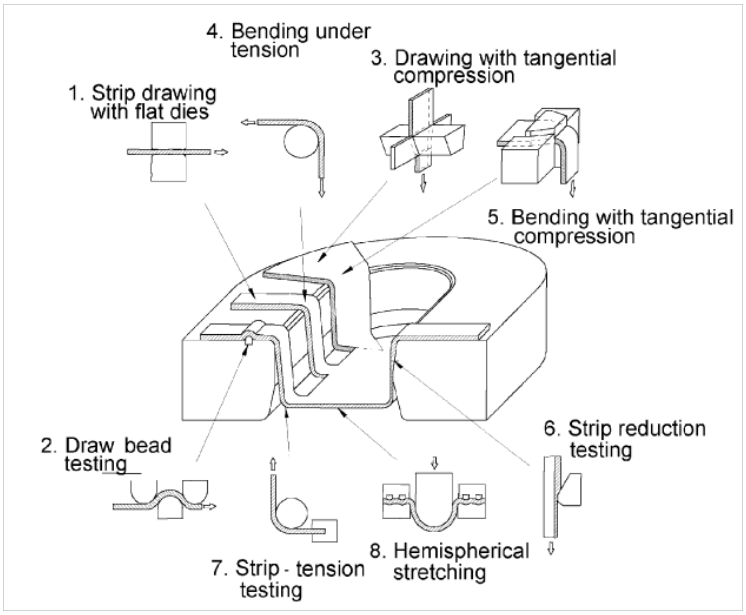

Figure 5.2: *Schematic illustration of simulative tests for sheet metal forming [151].*

DTU has been extremely active throughout the years in the development of simulative tests for sheet metal forming especially in the work by Andreasen et al. [152–156] with the purpose of evaluating the performances of environmental friendly lubricants against the ones of effective but hazardous chlorinated paraffin oils [43, 151]. Among those tests, two were chosen for the testing of MUFU surfaces, namely the Bending Under Tension (BUT) test and the Strip Reduction Test (SRT). These tests are respectively number 4 and number 6 in figure 5.2 and they will be described in the two following sections.

5.1.1 Bending Under Tension test

The Bending Under Tension is a test which faithfully represents deep-drawing operations in the zone where most likely lubricant breakdown will occur: the die entry [155]. Compared to other simulative tests, however, the BUT represents mild tribological conditions with medium normal pressure, low sliding length, no surface expansion [151]. Simply speaking the test consists of a plane strip drawn over a die shoulder with a superimposed back tension (see illustration 4 in figure 5.2) [155]. Several BUT set-ups were developed worldwide in the last 40 years with two basic differences: the tool pin (the die shoulder) can be freely rotating (no sliding) or it can be fixed (stationary) [155]. The test developed at DTU adopts the second set-up. An exploded view of the test components is given in figure 5.3. During a test, the front and back tension as well as the torque around the pin are measured by means of a transducer. The knowledge of these three parameters helps in determining the friction stresses and the normal pressure acting on the tool pin [155]. Other two parameters are required in these calculations and concern the tool geometry, which is displayed in the technical drawing of figure 5.4.
If the tool pin was round, the diameter would be Ø10 mm implying a die radius R = 5 mm. Smaller die radius can be achieved (down to 1 mm): the tool pin will present flat faces with a curvature equal to the die radius. The distance between two parallel flat faces is still 10 mm. Moreover, the test offers the possibility of pre-heating the tools, but this feature was not be used during the present investigation. The other test parameters will be listed in section 5.2 when the campaign is described. The relevance of BUT tests in connection with MUFU surfaces is deemed high, since it is the test that best simulates the chosen field of application: deep drawing. The tests will represent a novelty: while normally the tool is ground (or polished) to a roughness $Ra < 0.1$ µm and the performances of lubricants are screened; now the tool will present a texture that is coarser to the eye, but actually thought and designed to improve the tribological properties. Therefore

instead of verify the lubricant performances, the surface performances are analysed keeping the lubrication constant. The aim of the test is however still to detect, when present, the breakage of the lubricant film. Breaking the lubricant film, in fact, causes the pick-up of workpiece material on the tool surface and the subsequent scoring of the workpiece surface, named *galling* [154]. With constant process parameters, the later or no occurrence of galling implies a better surface.
For the tests a newly developed machine was used: an universal sheet tribo-tester (figure 5.5) which can perform strip reduction test and draw bead test beside BUT.

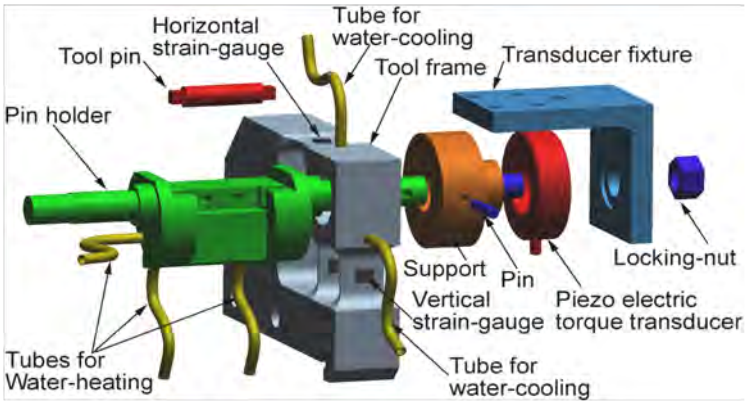

Figure 5.3: *Exploded view of the BUT equipment showing the transducer design and tool preheating system [155].*

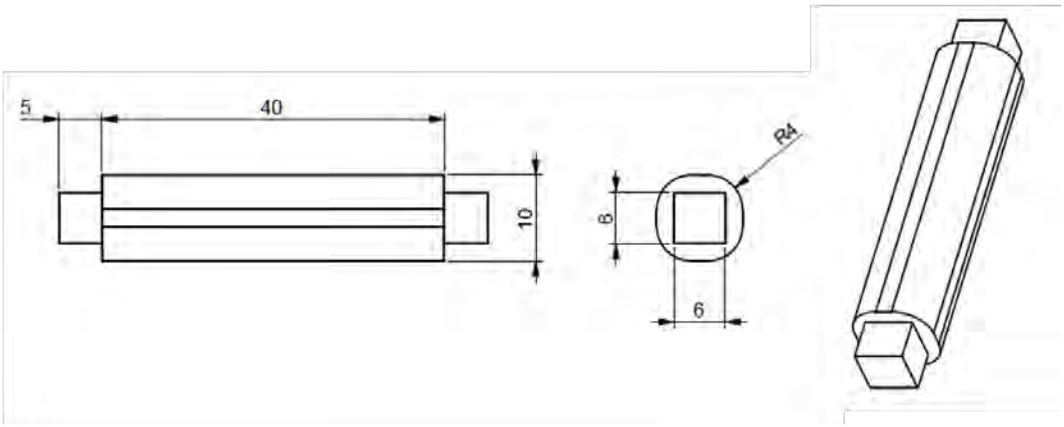

Figure 5.4: *BUT technical drawing.*

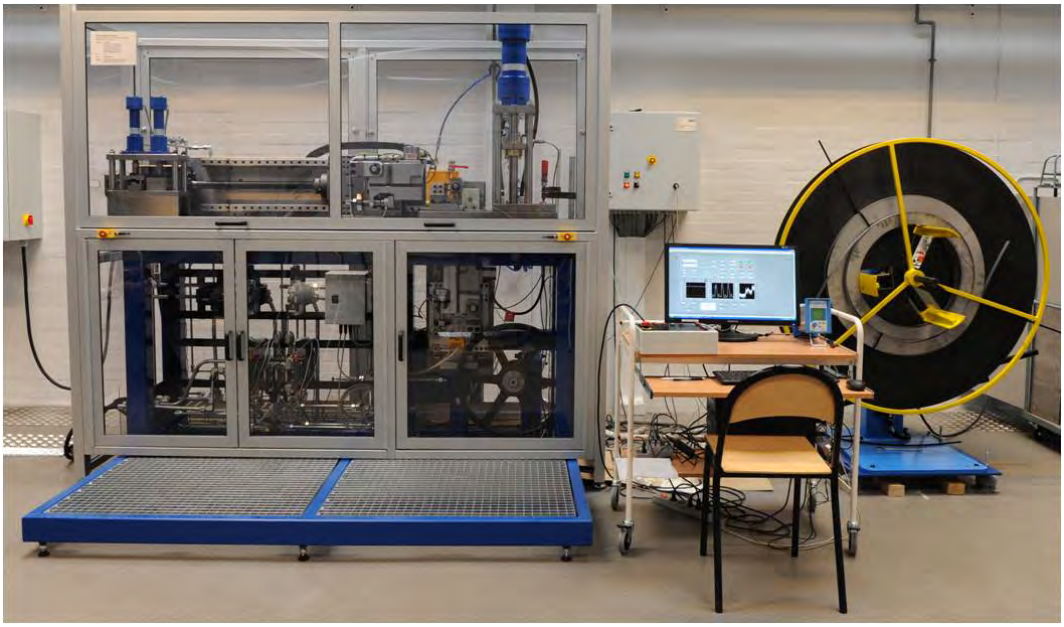

Figure 5.5: *New universal sheet tribo-tester present in DTU tribo-laboloratory [157].*

5.1.2 Strip Reduction Test

Differently from the BUT, the Strip Reduction Test simulates another forming process: *ironing*. As said before, ironing is often applied after deep-drawing and it is especially used when forming, for example, high, thin-walled cans [38, 152]. Compared to the BUT, the SRT represents much more severe tribological conditions with higher normal pressures and expansion of the surface [151]. A schematic of the test is shown in figure 5.6, while in figure 5.7 the test apparatus is exhibited.

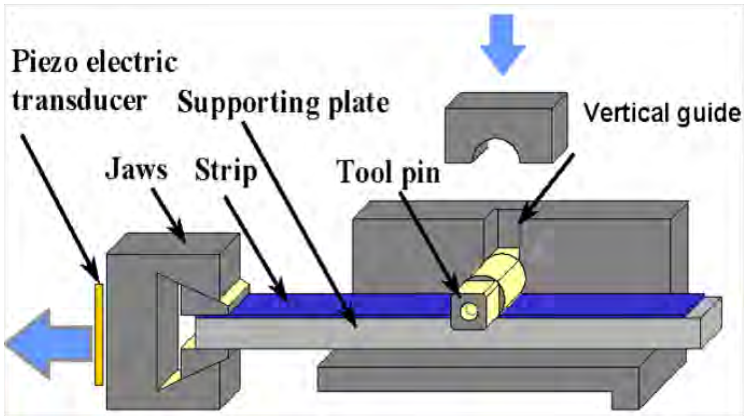

Figure 5.6: *Schematic view of the Strip Reduction Test [151].*

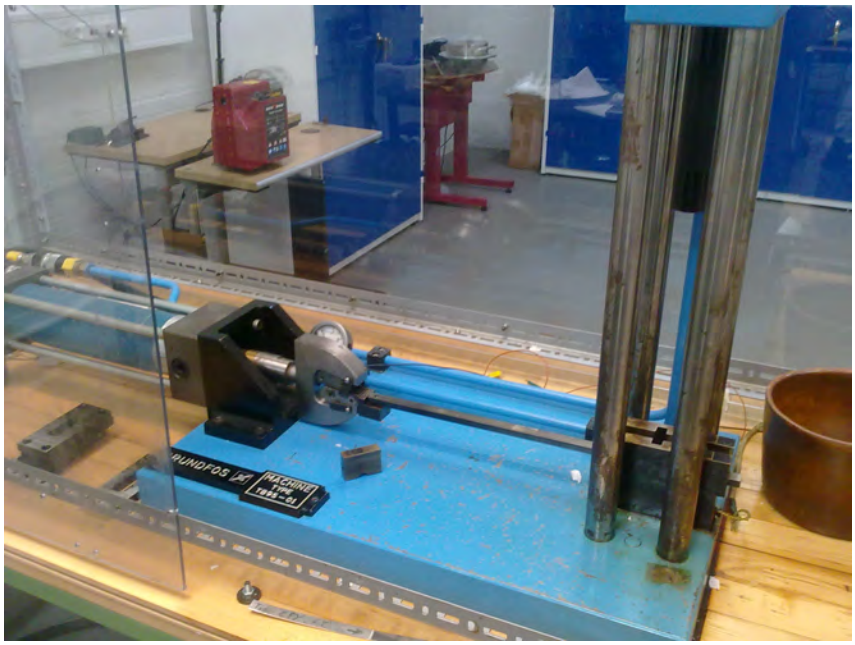

Figure 5.7: *Strip Reduction Test apparatus.*

The thickness of the strip is reduced between a non-rotating, hardened tool pin representing the die and a supporting plate representing the punch [152, 153]. The tool is held in place by vertical guides, while the strip and the plate are clamped together in the front end by some jaws corresponding to the punch nose [152, 153]. The guides constrain the movement of the strip only along the horizontal direction keeping the degrees of freedom along the vertical one: the gap between tool and plate can hence be varied allowing different levels of reduction. The ironing is performed by drawing the stick and strip in the direction of the jaws [152, 153] while the tool is loaded in order to achieve the targeted reduction. The drawing speed is kept constant during the experiments and is equal to 80 mm/s; while the drawing forces are constantly measured by transducers connected to the apparatus (figure 5.6). The normal load is also kept constant during the experiment. The load is given by a small press acting on a upper support or "shoe": the press would always keep the same stroke, therefore by adjusting the shoe height with compensation strips the aimed reduction can be obtained. The amount of adjustment is regulated by a model described in section 5.4. Nominally the tool pin is round with diameter Ø15 mm with square ends (see figure 5.8). These square ends allow four repetitions of the test with the same tool by rotating the tool pin 90° after each test.

During the project though the square ends design was modified creating octagonal ends: the test repetitions with a single tool were therefore

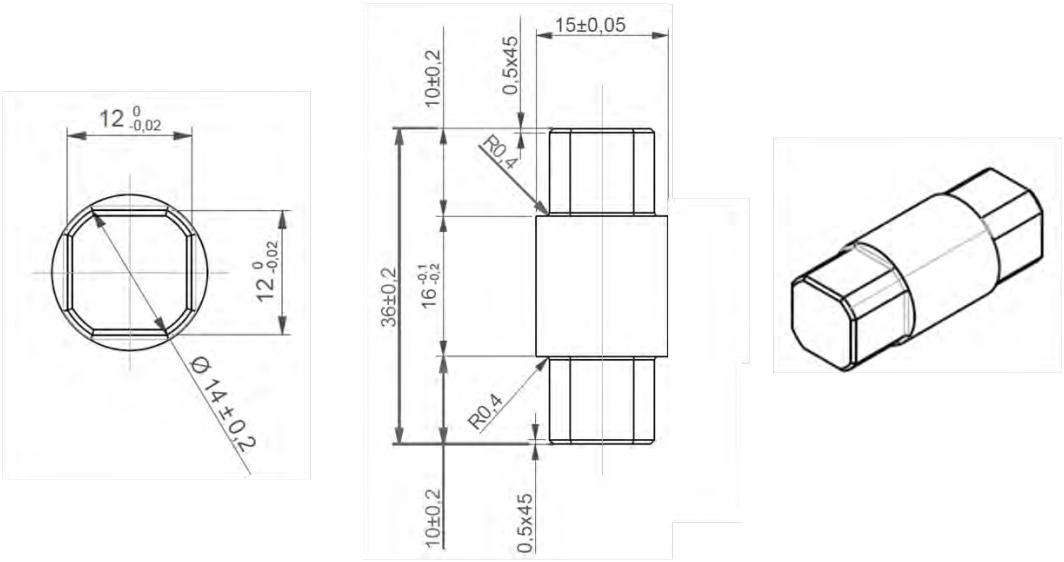

Figure 5.8: *SRT technical drawing.*

doubled. As for the BUT, pre-heating of the tool is possible thanks to electric heaters inserted in the shoe loading the pin tool [151], but not used in this framework. Again, the tests on MUFU surfaces represent a novelty as normally the tool are polished to Ra = 0.02 µm for assessing the lubricant performances. As before, the aim of the test is to detect the point, i.e. the sliding length, at which the lubricant film breaks. This is possible by measuring the strip roughness at regular intervals along the strip length [153, 154]. The procedure will be explained in detail in section 5.4.

5.1.3 Tools manufacturing considerations

The manufacturing of the both BUT and SRT tools is quite different from the one of the AST specimens or of deep-drawing dies. The AST rods or dies with MUFU texture are in fact axisymmetric and can be quite straightforwardly produced using turning as first operation. The resulting valley pattern will be circumferential meaning that the valleys are arranged transversally in relation to the movement of the counter-surface (the sleeve in the case of the AST, the workpiece in the case of dies). While BUT tools are in most cases non axisymmetric, SRT tools instead are, but if turning is used, the valleys lay would be parallel to the strip movement. Previous studies by [67] analysed the effectiveness of textured tools in a metal forming operation in which a strip is drawn through converging dies: a tribological situation similar to the SRT. Their studies showed how transversal grooves could remarkably decrease the friction compared to the smooth case and

how, on the other hand, parallel grooves could instead increase the friction leading to wear. The turning operation, therefore, would not be of much use in the present case. In order to have grooves transversal to the movement, milling should be used instead, see figure 5.9.

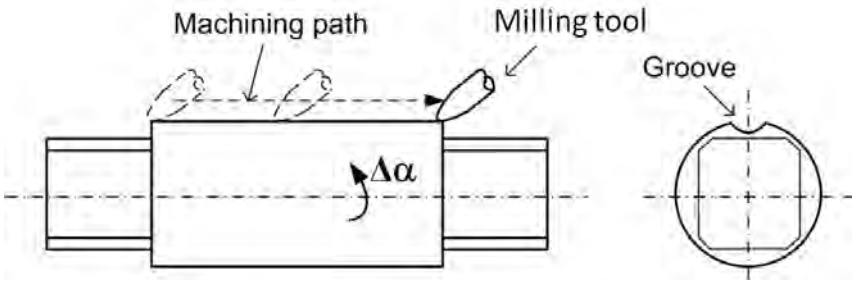

Figure 5.9: *Schematic drawing of milling of axial grooves in SRT tools.*

The manufacturing of the MUFU surface is thus not a continuous process. The grooves are created one-by-one by passing the milling tool. Each groove is made by rotating the fixture that clamps the tool by an angle $\Delta\alpha$. This could lead essentially to two problems. One is that there is not an integer multiple of the feed (or period) chosen in one revolution. The problem was overcome by starting the milling operations where there would be no contact, that is on the rim between two different end faces. The second problem that may happen is the off-centred rotation of the workpiece (the SRT tool) with respect to the milling tool, see figure 5.10. The consequence of this problem is unequal depth of the MUFU grooves. If the grooves depth varies considerably, problems may arise in the specimens characterisation, as the method utilised relies strongly on the deterministic nature of the process.

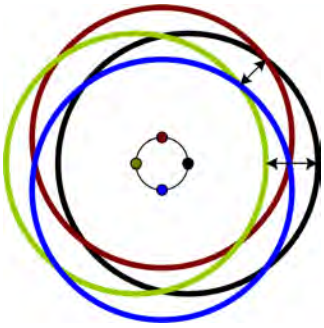

Figure 5.10: *Off-centred rotation of the SRT workpiece.*

5.2 Bending Under Tension tests of MUFU surfaces

In this section the Bending Under Tension tests are presented. As said above, the BUT is the test which simulates a deep-drawing operation, the targeted field of application at the beginning of the project. This section starts with the characterisation of the tools received from Strecon.

5.2.1 BUT tools characterisation

For the BUT test campaign 6 tool pins were manufactured: 4 tools were presenting different MUFU surfaces and 2 were mirror polished and used as a reference. Each tool was made of the same material: Vanadis 4 [158]), which is a chromium-molybdenum-vanadium alloyed steel with a hardness of 63 HRC. Each tool had a shoulder with radius equal to 3.5 mm, the same radius used for the dies in the real deep drawing operation discussed later (section 5.3). Differently from traditional BUT tools, each pin had only 1 radius, meaning that just one test could be performed each pin. The manufacturing was in fact rather complicated as all MUFU tools underwent a primary milling operation in order to achieve a transversal texture.

Measurement settings and results

The four BUT tools with MUFU surfaces were labelled respectively BUT1, BUT2, BUT3 and BUT4. The two polished references were named Ref1 and Ref2. BUT1 and BUT3 were milled with a feed of 0.3 mm, whereas BUT2 and BUT4 were milled with feed equal to 0.2 mm. The FTS was used for the measurement of the parts. Although the focus of the test goes only on the radius of curvature which is the only location where the contact should occur, both the flat zones were measured. These flat zones were called *horizontal* and *vertical* depending on their position on the BUT machine. The set-up of the measurement is illustrated in figure 5.11.
Five profiles were taken each zone for a total of 15 profiles per tool. The stylus speed was set to 0.5 mm/s and a probe with tip radius of 2 µm was chosen. The probing direction was transversal to the surface lay. The profile length was 4 mm on the flat zones, while 3.2 mm on the radius. Due to the large form components present in such profiles which can cause distortions as shown in figure 3.20, a polynomial fitting is done before the λs operation. A modified RGR was employed in all cases: closing operation with disk radius equal to 80 mm, first quartile estimator and threshold reduced to 1σ. The λc value was set to 0.8 mm. Moreover, 1.5 mm x 0.3 mm surface topographies are again taken for visualisation purposes. In figure 5.12 are

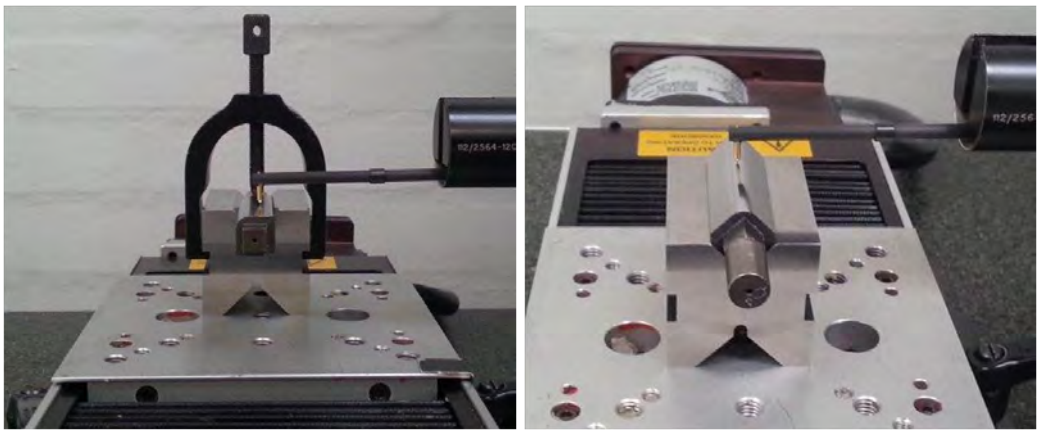

(a) Flat zone. (b) Radius.

Figure 5.11: *Set-ups for measurements on BUT tools.*

displayed the measurements taken on the radii of each tool. The y-axis is fixed to a range of 21 µm for comparing the textures scales.

From figure 5.12 it can be seen that the filters in some cases did not work properly. The polynomial fitting of the large form component has in itself some end effects so that the MUFU ridges at the profile edges were at a much lower level than the others and appear "pulled down" in the roughness profile. Those ridges were not taken into account in the parameter calculation. Another problem affected most of the radii profiles: there occurred some outward peaks and subsequently some areas of depression. This is more evident in BUT2. By looking at the primary profile (figure 5.13), the occurrence is explained by the large waviness components detected. The presence of a large waviness clashes with the basic assumption of small or negligible waviness and leads to filtering errors.

In order to allow the description of only the MUFU texture, a further morphological filtering is performed: a closing operation with disk radius 80 mm. In this way the profiles result aligned and the parameter calculation is permitted. The parameters quantifying the MUFU textures are collected in table 5.1. The high waviness was however detected only on the radii, so that the flat zone are filtered "simply" with the mentioned modified RGR.

Milling errors were detected on the flat zones, especially on BUT1 and BUT2, see figure 5.14. In particular the error of BUT1, a flat area which presumably was originated by very shallow milling marks polished away by the RAP machine, affects the results giving an unnaturally high bearing area. However, these errors are considered of minor importance, because there should not be any tribological contact in the zones where they occur.

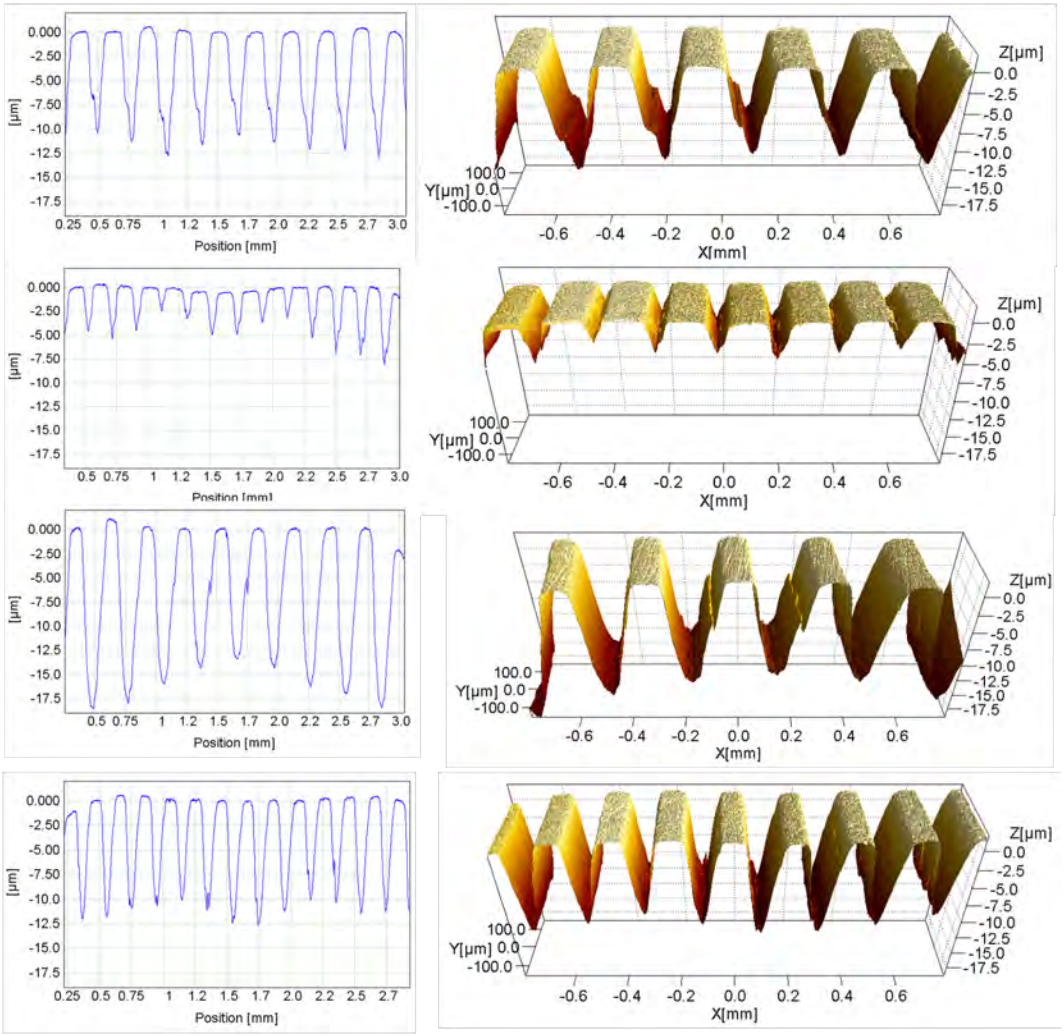

Figure 5.12: *Profiles and areal topographies on the radii of BUT tools. From top down BUT1, BUT2, BUT3 and BUT4.*

The characterisation of the polished references was carried out in a similar way. The only difference with the MUFU tools is the filtering procedure used. A simple Gaussian Regression of the 2nd order without previous polynomial fitting was used. This choice could theoretically have caused problems in the radius zone. If a polynomial filtering of the 2nd order was instead employed no difference with applying the GR2 were noted. When using this fitting, though, a very high waviness is noted, see figure 5.15. A further GR2 operation cannot follow properly the line yielding a distorted profile with two lateral "wings". Two possibilities open up: the first is to trim the profile and evaluate it over 2.4 mm around the center; the second is to use a higher order polynomial fitting.

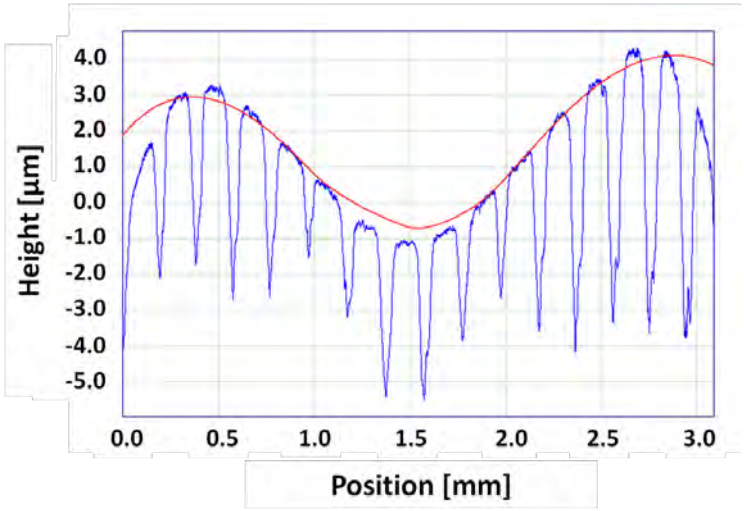

Figure 5.13: *Primary profile and reference line positioning of the radius of BUT2.*

Table 5.1: Characterisation of the BUT tools with MUFU surfaces.

Tool	**Rt [µm]**		**Ra pl. [µm]**		**EQF [µm]**		**BA [%]**	
	Average	**U**	**Average**	**U**	**Average**	**U**	**Average**	σ
BUT1-R	13.292	0.314	0.041	0.010	3.493	0.191	44.2	1.2
-H	8.554	0.503	0.046	0.010	1.559	0.183	70.2	4.8
-V	11.690	0.570	0.043	0.009	1.618	0.275	55.9	0.8
BUT2-R	7.747	0.538	0.045	0.010	0.797	0.149	60.0	4.1
-H	8.137	1.057	0.044	0.010	1.084	0.186	59.4	2.2
-V	12.605	1.000	0.059	0.011	1.803	0.088	48.6	0.9
BUT3-R	18.681	1.057	0.061	0.017	5.947	0.553	32.9	4.1
-H	10.552	0.196	0.038	0.009	2.688	0.076	46.2	0.6
-V	16.784	0.340	0.039	0.010	6.351	0.114	31.6	0.7
BUT4-R	12.241	0.481	0.047	0.010	3.282	0.285	39.1	2.3
-H	9.279	0.249	0.043	0.009	1.856	0.078	49.7	1.5
-V	8.325	0.312	0.039	0.009	1.722	0.085	47.7	1.2

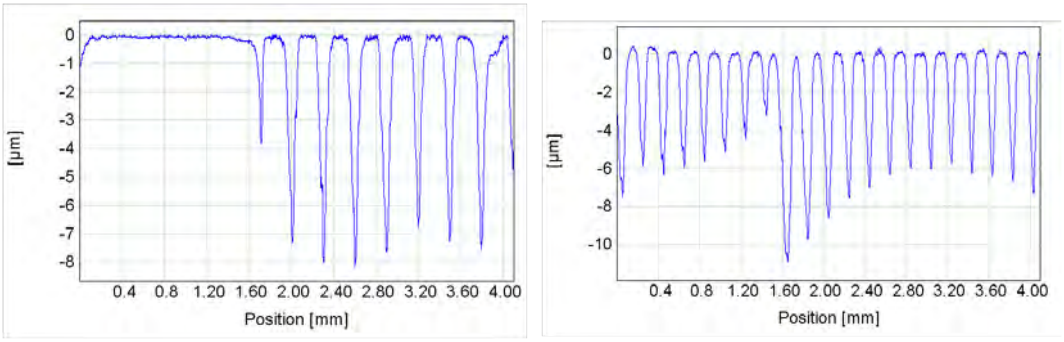

Figure 5.14: *Milling errors on BUT1 (left) and BUT2 (right).*

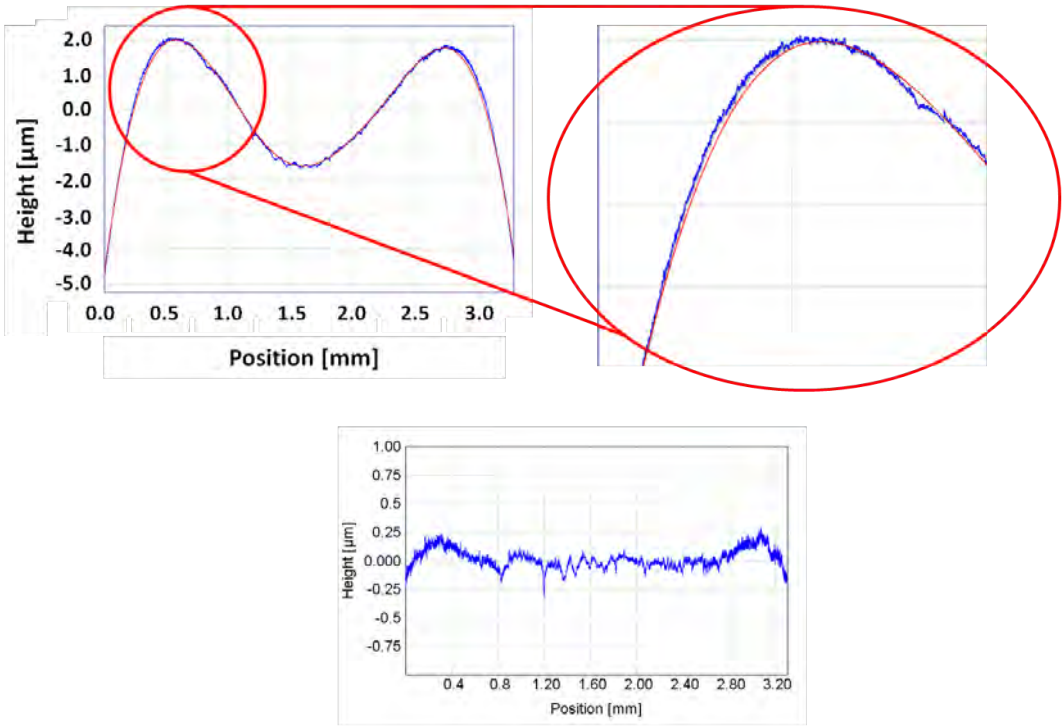

Figure 5.15: *Primary profile on the radius of Ref1 when a 2nd order fitting is employed. Zoom on the fitting error and resulting roughness profile.*

A 9th order polynomial fitting proved following much better the wavy radius profile and the following GR operation yielded nearly no end distortions (figure 5.16). The profile could be analysed along the whole evaluation length. In table 5.2 the results of the measurement are summarized.

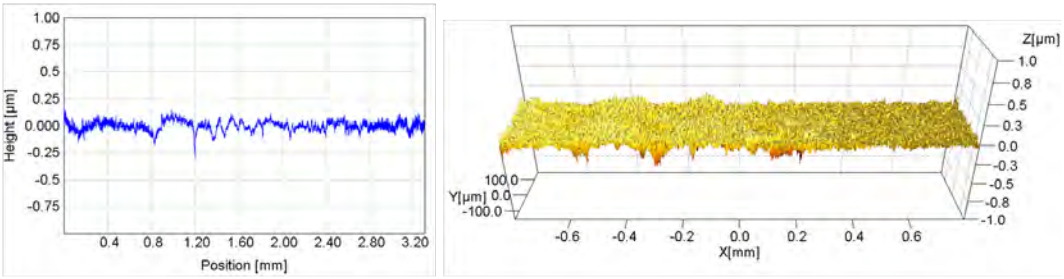

Figure 5.16: *Roughness profile and areal measurement on Ref1.*

Table 5.2: Ra and Rt values on the three sides of Ref1 and Ref2.

	Ra [µm]		**Rt [µm]**	
	Average	**U**	**Average**	**U**
Ref1-R	0.036	0.009	0.470	0.114
-H	0.057	0.010	0.521	0.087
-V	0.073	0.015	0.917	0.167
Ref2-R	0.049	0.012	0.503	0.103
-H	0.068	0.010	0.656	0.113
-V	0.030	0.009	0.246	0.025

Discussion

Besides the already mentioned filtering issues and the solutions adopted, some BUT tools seem affected by quite large waviness components, especially BUT2 and Ref1. The waviness consisted of a central zone of depression, which is located in the macro-scale at 45° from the beginning of the curvature. The maximum height of depression measured on Ref1 is estimated being 3.5 µm, while the highest depressions are present both on BUT2 and BUT3 with approximately 5.5 µm. Relatively to their scale, then BUT2 and Ref1 appeared therefore more evident. The waviness tops are approximately 1 mm away from the central zone of the depression. By using simple trigonometry, it is found that those points correspond at respectively 28° and 62°. Anyhow, this waviness is not thought being particularly problematic since the central zone of depression can be considered as a (relatively) gigantic reservoirs. Moreover, some recent studies such as [159] shows how the normal pressure at 45° in deep drawing operations is nearly zero and almost no contact occurs there. This occurrence is likely to happen also for the present BUT test: a just presented investigation by [160]

demonstrates in fact how in a BUT test run with a special die having a reduced curvature of 45° the contact pressure is zero in the middle of the curvature. If the result can be transferred to a 90° tool, there would not be contact at 45°.
By removing the waviness, the roughness can be studied. BUT1 and BUT3 were milled with the same feed and have the same valley density. BUT2 and BUT4 can be paired as well. BUT1 has higher BA than BUT3 (45% against 33%) and so has BUT2 with respect to BUT4 (60% against 40%). Consequently BUT3 has the highest EQF and BUT2 the lowest. The other two tools have it instead comparable. The plateau roughness is alike for three out of four tools: only BUT4 has higher Ra (0.061 µm against approximately 0.044 µm).
Ref1 and Ref2 were polished to a finer level than the 0.1 µm indicated by Andreasen et al. [155]. The achieved roughness (0.036 µm and 0.049 µm) are anyway more or less in line with the plateau roughness of the MUFU surfaces given the uncertainties of the measurements.

5.2.2 BUT tests set-up and results

The tests were carried out at room temperature (20°C) and the lubricant used was a Rhenus SU 166 A, where 166 represents its viscosity (166 cSt at 40°C) [161]. This is a lubricant whose usage has recently started in industry being it a less hazardous alternative to highly effective chlorinated paraffin oils. The workpiece material was stainless steel EN 1.4307 and the nominal strip thickness was 1 mm. The pulling direction is along the horizontal side, see figure 5.17.
The test parameters were kept constant for all tests: back tension 200 MPa, sliding length 20 mm and sliding speed 50 mm/s. The total number of strokes was set to 1500 each test. During the test transducers would measure the front as well as the back tension and the tool torque as described in [155]. The torque graph is presented (figure 5.18) since the torque is much more sensitive to changes of friction than the drawing force, as already noted by Andreasen et al. [155]. With the "warm" colours are presented the tools with 0.3 mm feed rate (BUT1 and BUT3), while with the "cold" colours are shown the remaining two MUFU tools. The polished references are indicated with the darkest colours.

Discussion

The torque graph shows interesting results to be discussed. Starting from the polished references, they displayed immediately galling. The torque at the beginning had the lowest values, but soon skyrocketed. Heavy galling

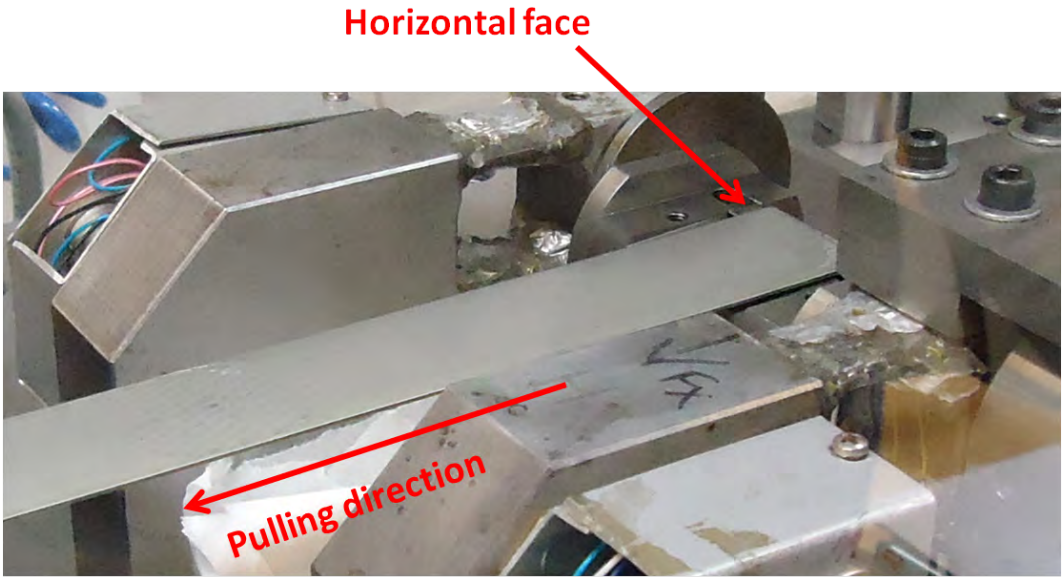

Figure 5.17: *Pulling direction during bending under tension tests.*

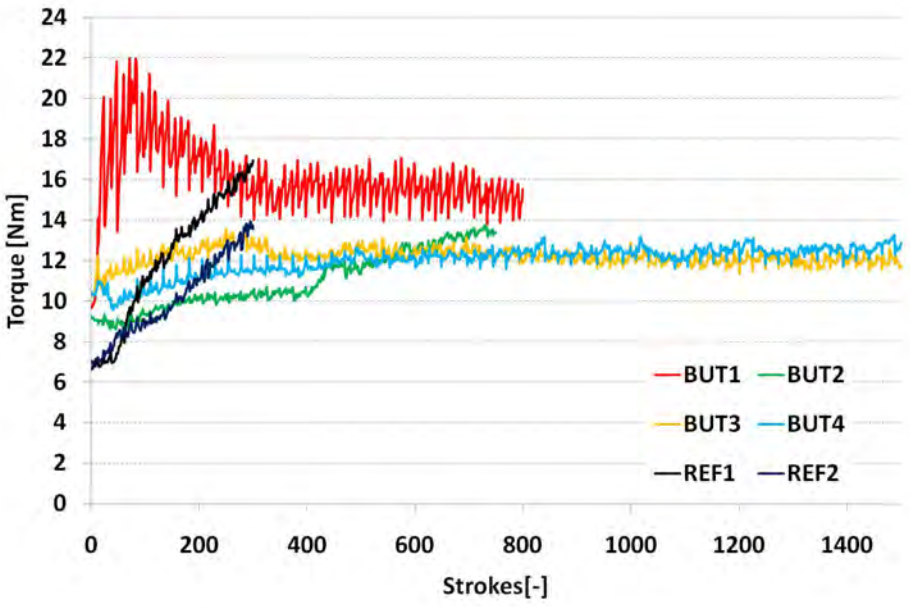

Figure 5.18: *Torque results of all BUT tests.*

was detected on the outcoming strips, so that it was decided to stop the test after 300 strokes in order to save time and strip material. Considering the MUFU tools, instead, the torque was increasing in the first 100 strokes but not at the same pace as the polished tools. The feeling though was that the situation was bound to get worse, but in two cases (BUT3 and BUT4) it

stabilized and the test could be pulled off seemingly without the appearance of galling. BUT1 showed a rapidly increasing trend at the beginning of the test. It was even feared that the strip would break, but, oddly enough, the torque decreased and then stabilized. The detected presence of galling on the strip pushed though to the decision of stopping the test at 800 strokes. BUT2 showed a more "normal" behaviour: it slightly increased, then it stabilized until suddenly, the abrupt breakage of lubricant film caused galling. The test was stopped at 750 strokes.
At a first glance, the results seem opposite than what observed with the SRT. The MUFU tools, this time and for this application, appear to work better than the polished references. Moreover, there are differences among the MUFU tools themselves: BUT2 failed but displayed at the beginning the lowest torque; BUT3 and BUT4 did not show evident signs of galling; BUT1 had quite contradictory results: it seemed to have failed since the very beginning, then "magically" recovers and gets back on track with constant, though high torque. Now, BUT3 and BUT4 have a thing in common: a low BA. In particular BUT3 has an average BA equal to 33%, while BUT4 has 39%. BUT2, the only tool which displayed a clear occurrence of galling and abrupt increase of forces, instead had BA equal to 60%, evidently higher than those two tools. It seems like BUT2 is a half-way between the polished references and the two tools with low bearing area. The hypothesis is that the high bearing area maintained only initially the oil film, but once it broke, galling simply propagated. The later breakage of BUT2 is maybe due to its pockets, absent in the polished references, that provided the contact with extra-lubrication. Moreover and maybe most importantly given that the pockets are not closed, another function seems to be provided, which is the creation of a discontinuity on the surface texture. Imagining that pick-up occurred on a plateau, the presence of a pocket with oil inside would hinder the propagation of the pick-up across the whole surface. The metal-to-metal contact would in fact be initially limited to a reduced area, few plateaus. In order to expand, the pick-up should overtake the obstacle represented by the valley. It should build up across the whole valley section, squeezing the lubricant away before proceeding to the next plateau and there joining, if present, other cold-welded workpiece material. If that was the case and reminding that the valleys are laterally opened, it was easier for the pick-up to build across the shallower valleys of BUT2, while it encountered big difficulties in the cases of BUT3 and BUT4. The low BA combined with much deeper valleys offered very small room for the pick-up propagation hence the better results. Still, from the graph, BUT1's behaviour remains inexplicable. It had higher BA than BUT3 and BUT4, but thanks to its feed rate, the EQF was not significantly different than BUT4's. For having a clearer understanding on what happened during the test, it is therefore of

extreme importance the post-test inspection of both tools and workpieces.

5.2.3 BUT post-test inspection

The post-test inspection started right after each test was completed. Chronologically, the first test to be done was the one with BUT3. Once the strip had been removed, a strange occurrence was noted on the tool: it was covered by a black substance. Immediately, the thought went to huge amounts of pick-up, but surprisingly, the substance was quite easily removed during a primary cleaning operation. Therefore, it was not pick-up, which imply the cold-welding of the material and cannot be removed by hand-cleaning operations. Instead, the substance was a black powder. Fortunately, the powder was not utterly removed from the cleaning, so that the tool could be brought to a Scanning Electron Microscope (SEM) for a closer look and especially a metallographic inspection. The powder was located especially on the horizontal side, which is, as shown in figure 5.17, the exit side of the strip where the pulling takes place. In figure 5.19 the SEM images taken on BUT3 are shown exhibiting clearly the difference between the substance covering the tool and the MUFU texture underneath. The zoomed zone is chosen for the metallographic inspection: 10 points are detected transiting from the substance to the tool.

Figure 5.19: *SEM images of BUT3. Zoom on a cracked zone chosen for the metallographic inspection.*

Points 1-6 showed the presence of chromium in a percentage of approximately 18% and especially the presence of nickel. In points 7-10 the nickel disappeared and, as expected, vanadium and appeared. The results are therefore pretty clear: the substance is without doubt stainless steel, in other words workpiece material. During the forming operation the strip material was scraped off by the tool but did not cold weld to it. The scraped material

was instead depositing and accumulating over the tool creating eventually a layer on the horizontal face of the tool. It is possible that this layer changed the contact conditions in the radius and somehow protected the tool from producing pick-up. The focus variation microscope (hereafter named by its brand, Alicona 2.6(a)) was used with a 10X magnification for investigating the tool radius (figure 5.20). The image showed a great amount of dark workpiece material collected on the valleys and the beginning of pick-up on the plateaus. The presence of the valleys seem to interrupt the propagation process; acting besides as containers for collecting the debris. In the end, what can have happened is that the plateaus wore the workpiece at the beginning of the process, hence the increasing torque trend. Galling was tough not produced at once because the texture hindered its propagation and rather helped the transporting of workpiece material elsewhere. Some deposited in the valleys, some was transferred on the tool flat zone.

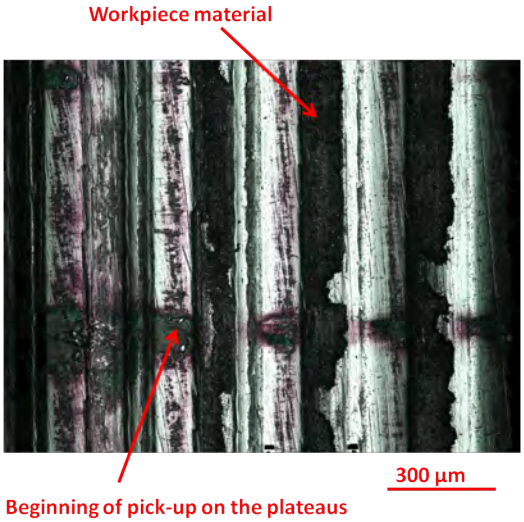

Figure 5.20: *Alicona image of BUT3 radius.*

The scraping off and transporting of workpiece material creating a separation layer helps in clarifying what happened with BUT1. After partly cleaning the sample, the tool was brought to the SEM. Figure 5.21 shows a great amount of pick-up detected on the tool. Hence, the tool actually failed at the beginning of the test building up the pick-up and producing galling on the strip. At the same time though, in other parts along the width of the tool, the scraping phenomenon was occurring. After some time during the test, the pick-up was blocked by the same pulverized strip material and probably covered by it. The result was that the galling was being gradually "buried" and scratching less and less the coming strip.
The final result is quite paradoxical. Looking at figure 5.22, the strip after

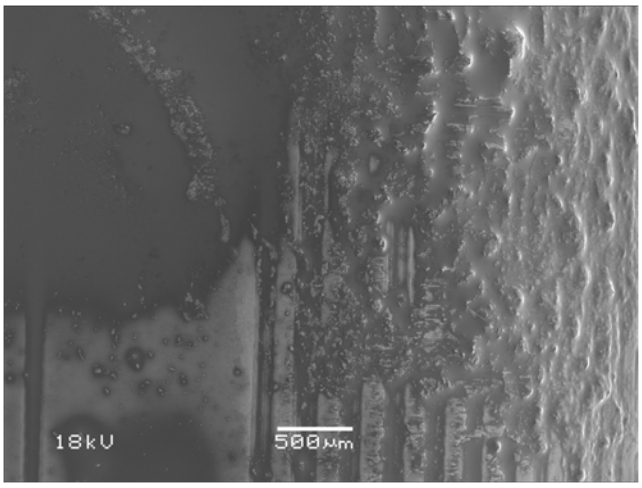

Figure 5.21: *SEM image of BUT1.*

250 strokes appear in worse conditions than the one taken at 750 strokes. The latter exhibited only few isolated scratches, sign that the pick-up was acting but with less efficacy than before.

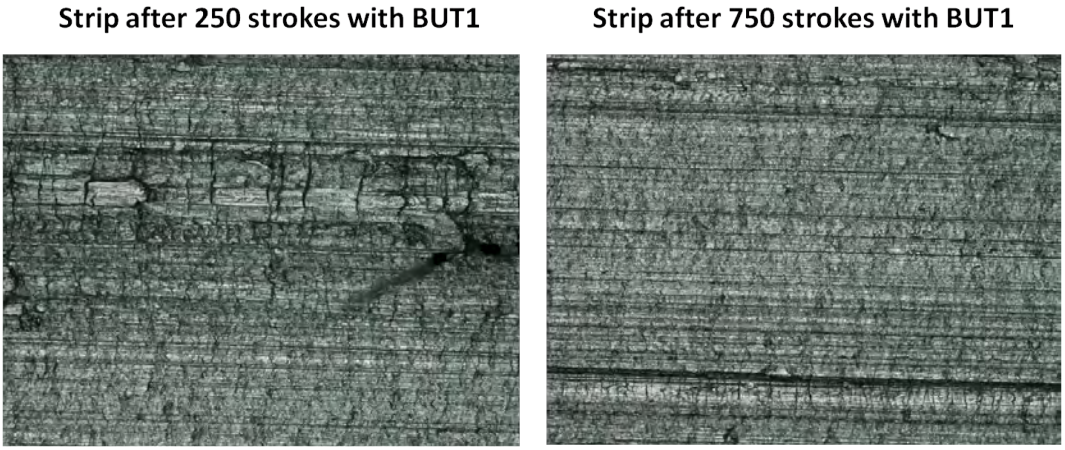

Figure 5.22: *Comparison of strip textures after 250 strokes and 750 strokes with BUT1.*

This could be a support of the hypothesis that the pick-up was getting gradually "submerged" and in the end only few remaining spikes were causing the singular scratches. The initial spiking of the torque means that pick-up was building up, the decrease in torque means that the powder was blocking and submerging the pick-up stabilizing eventually.
Going back with the discussion to BUT3, the difference in terms of pick-up between it and the polished tools is substantial. Alicona was used again with the same magnification on the polished tool radius exhibiting evident

pick up (figure 5.23). A profile taken across the texture (marked in orange in the figure) displayed a height of the pick-up of approximately 30 µm. The same procedure is applied to the BUT3 image and the height of the pick-up appear being 1.2 µm, way lower than the polished tool.

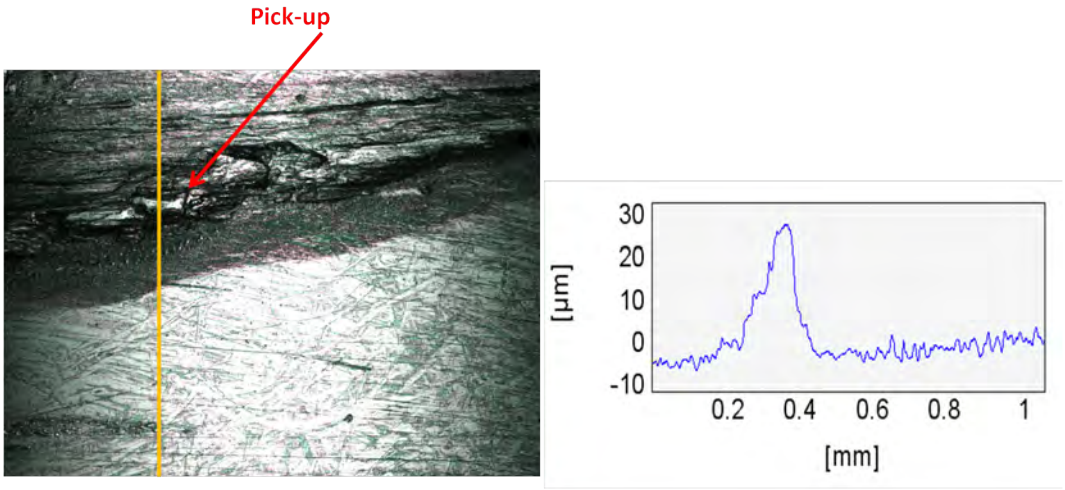

Figure 5.23: *Alicona image of Ref1 radius and pick up height profile.*

What can be concluded from this analysis is that the lubrication film broke in all cases. While with the polished tools the result of the film breaking yielded galling at once, the MUFU tools scraped the strip, but its material did not cold-weld in all cases. In some cases like BUT3 or BUT4 the workpiece material was transported in other places (valleys, flat area, etc.); in other cases like BUT1 or BUT2 a part of it cold welded to the tool producing pick-up and galling. As noted before, it is likely that a big role in this process is played by the valleys which interrupt the pick-up propagation, supply lubricant helping in the transport of the powder and offer a place for debris storage. The depth of galling when using MUFU tools such as BUT3 is much lower than when using polished tools. With reference to figure 5.24, the strips after 1500 strokes with BUT3 and after 250 strokes with Ref1 are compared. The depth of galling of Ref1 (red profile) is evidently much higher than the depth of galling of BUT3 (blue profile). The quality of the surface yielded by Ref1 is certainly not acceptable, while it is questionable, from a manufacturer's point of view, whether the quality given by BUT3 could be accepted. MUFU tools as BUT3, in fact, even though they do not produce clear or huge amount of galling, they however wear the surface producing transversal scratches that are not exactly welcome as production results.
Anyhow, the scope of the test was to compare the functionality of MUFU tools compared to each other and to reference surfaces. In the cases of low

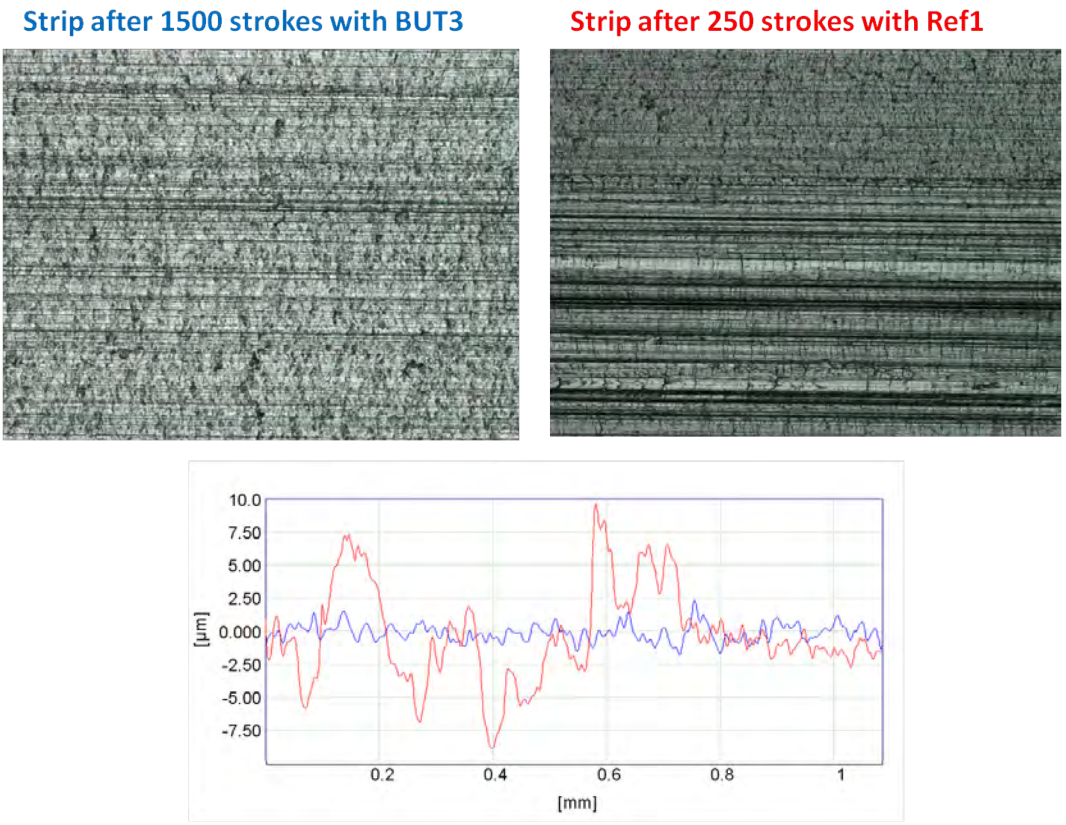

Figure 5.24: *Comparison of strip textures after 1500 strokes with BUT3 and 250 strokes with Ref1.*

bearing areas, the MUFU tools showed better functional results with no drastic occurrence of pick-up and galling unlike the selected references. It is imaginable that changing some test parameters such as the back tension (200 MPa represent the limit of the machine) better results in terms of quality can be achieved but maybe not as interesting in terms of experimental research.

5.3 Deep drawing production tests of MUFU surfaces

For the sake of continuity, before talking about the strip reduction tests which simulate another process, this section is dedicated to a series of tests run in production conditions which represent the real-life application of the BUT. The aim of the tests was in fact to evaluate the performances of MUFU surfaces in a real deep-drawing process and compare them with the tool typology currently utilized in industry. Compared to the BUT tests,

the tool will have a significant geometrical difference besides the many others (production conditions, forces involved, etc.). The BUT tool was a shoulder projected straight along the third dimension; a real deep-drawing die is axisymmetrical. Differently from the BUT tools then, deep- drawing dies have not open valleys and the lubricant cannot escape from the sides. This phenomenon seemed not to have occurred in a significant or clearly detectable manner during the BUT tests but it cannot be excluded. With closed valleys the result might have been better, hence the motivation for the present test campaign.
The experiments were performed at Grundfos A/S [162] utilizing a progressive deep-drawing tool (figure 5.25(a)) producing cable cups. The production of the cable cups consists of 7 consecutive deep-drawing operations, in which a sheet is formed to reach the final shape. Only the first operation (figure 5.25(b)) is a classical deep-drawing, where the un-deformed sheet is drawn by means of a punch into a die generating the cup shape. The following operations modify the cup length and thickness until eventually shearing the bottom away and producing the final cable cup (figure 5.25(c)). Anyhow, the first operation will be the one of interest in these tests.
Two different MUFU dies as well as a reference one were produced for performing the first operation. For the MUFU dies, named A and B, the initial machining operation was hard-turning, made possible thanks to the axisymmetric geometry. The feed rates were 0.2 mm for die A and 0.3 for die B generating different texture densities. The reference die was polished to Ra = 0.06 µm and then PVD-coated with TiAlN, which is known for its wear resistance properties [163]. For the other operations the original dies, also coated, were utilized.

5.3.1 Deep drawing dies characterisation

The characterisation of the deep drawing dies proceeded alike the one of BUT tools. The same instrument (FTS) and settings were used, except for the profile lengths. Again, three zones were detected: horizontal, vertical and radius (figure 5.26), each of them was measured with a profile length of 3.2 mm, 4 mm and 2.4 mm respectively.
Again, the zone of bigger importance is certainly the radius, where [159] has demonstrated undergoing the higher normal pressures. There should not be any contact in the vertical zone, whereas contact should take place in the horizontal one due to the blank holder. This pressure is though much smaller than what takes place on the radius. Anyhow, twelve profiles were taken in each zone, in a way similar to what done for the AST specimens characterisation: each zone was divided in four position 90° apart and three profiles were taken each position. Both MUFU dies were characterised

before and after testing. The reference die was instead not available for characterisation therefore the nominal values are taken as true.
While the horizontal zone showed a pretty clear MUFU structure (figure 5.27) in both dies highlighting an evident difference in valleys density and depth; that is unfortunately not true in the case of the radius (figure 5.28). The CNC lathe machining the surface could in fact not follow the contour of the rounded region as precisely as for the flat regions. This resulted in rather irregular pockets with variable height, which made the

(a)

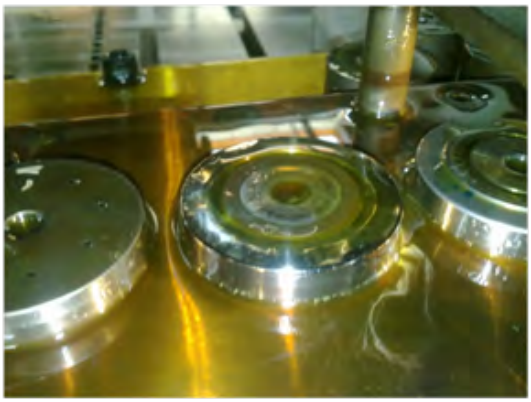

(b)

(c)

Figure 5.25: *Production of cable cups: (a) progressive deep drawing tool; (b) first operation die; (c) final product.*

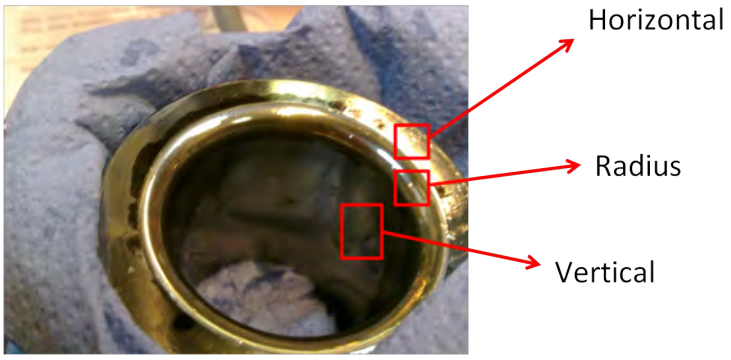

Figure 5.26: *Dies measuring zones.*

characterisation rather challenging.

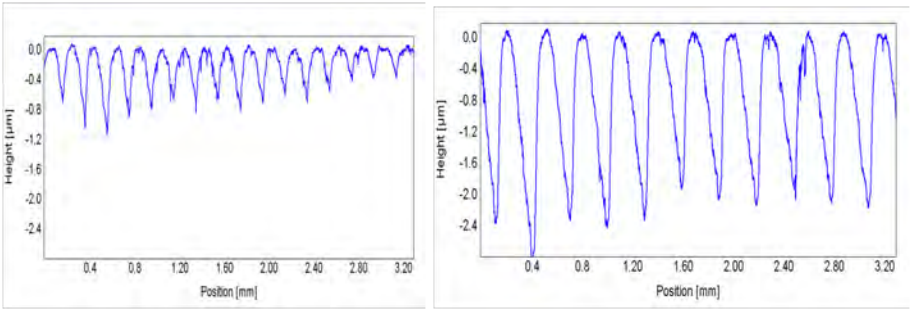

(a) (b)

Figure 5.27: *Profiles of the horizontal positions of the two dies: (a) die A; (b) die B.*

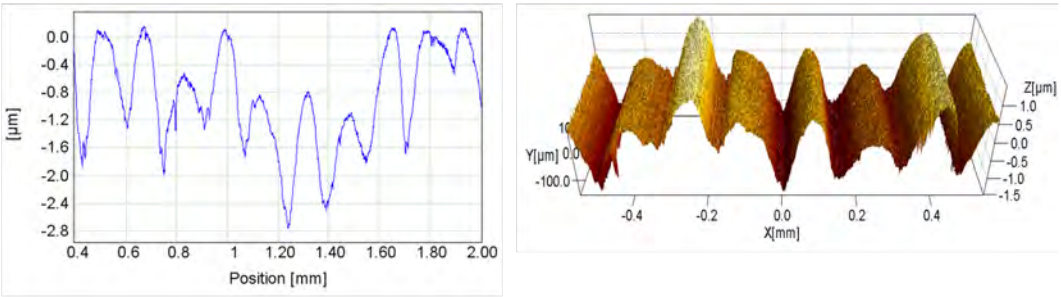

Figure 5.28: *Profile and areal measurement on the radius of die B.*

Therefore, to achieve acceptable results in the die characterisation, a morphological closing operation with high radius (80 mm) followed the modified robust regression filtering applied in the case of the flat zones. The results are collected in table 5.3 with their respective expanded uncertainties.

Table 5.3: Characterisation of the deep-drawing MUFU tools.

Die	**Rt [µm]**		**Ra pl. [µm]**		**EQF [µm]**		**BA [%]**	
	Average	**U**	**Average**	**U**	**Average**	**U**	**Average**	σ
A -R	1.479	0.077	0.013	0.009	0.312	0.039	23.4	7.4
-H	1.308	0.060	0.018	0.009	0.215	0.023	38.6	2.8
-V	1.643	0.085	0.033	0.009	0.185	0.019	55.7	2.7
B -R	2.109	0.074	0.023	0.009	0.492	0.061	26.1	6.4
-H	3.774	0.741	0.022	0.009	0.727	0.028	30.7	3.4
-V	2.930	0.110	0.026	0.009	0.860	0.044	34.2	2.4

Discussion

The Rt values highlight the difference in texture scale of the two dies: as also seen in figure 5.27, die B has deeper and more capacitive pockets. The EQF values confirm the reasoning. The non-ideal texture achieved on the radius zone did fortunately not affect in a decisive manner the parameters calculations except for the BA which showed great statistical variations. Despite that, it is quite safe to conclude that the bearing areas of both dies were just above the value of 20% in the radius zone; whereas higher values were achieved in the less interesting flat zones. Moreover, always speaking about the radius zone the plateaus of die A seem finer. A last remark is made on the high uncertainty related to the Rt of the horizontal side of die B: scratches were detected and some were probed by the stylus biasing therefore the results. These scratches are however considered not affecting the results given the tribological contact conditions.

5.3.2 Test set-up and results

Initially, the progressive tool was mounted on a test-press allowing the operator to accurately control the movement of the punches which form the sheet at the constant speed of 10 mm/s. Load cells and position transducers were installed to monitor forces and displacements during the test. The same sheet material and lubricant were used for every test. The sheet was made of stainless steel EN 1.4301, very similar to the BUT workpiece material, being the latter a low-carbon alternative with overall the same formability properties. The lubricant used was Rhenus SU 166 A.
At the beginning, some repeatability tests were performed (figure 5.29) by

manually activating the press. Seven tests were performed using die A displaying an average max load value of 48.6 kN with a standard deviation of 0.2 kN. The repeatability was therefore very satisfactory.

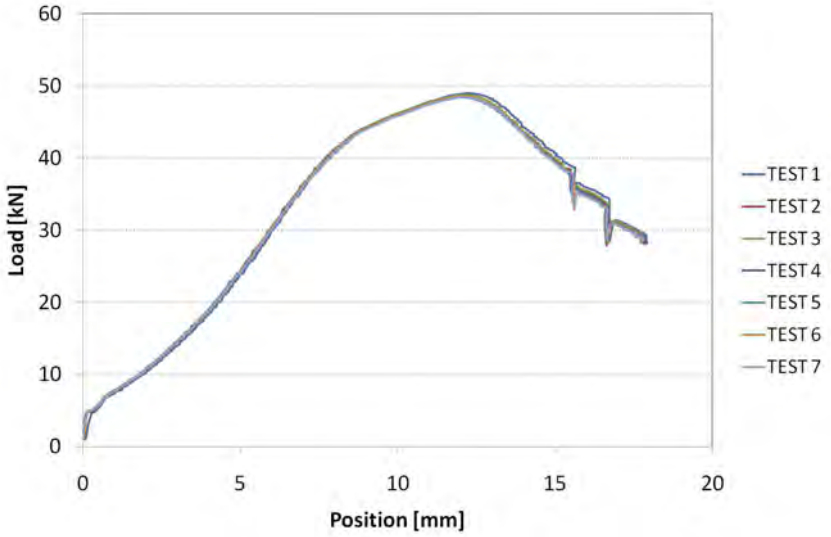

Figure 5.29: *Repeatability of the measured load during a deep-drawing operation.*

Afterwards, the press was made operating automatically and performed 20 operations for each tested die. In figures 5.30 and 5.31 the average curves and maximum values of the 20 operations are calculated and plotted. The error bars of figure 5.31 represent the standard deviations of the 20 maxima. Successively the set-up was dismounted and remounted in a automatic press of the production line. Only die B was employed and 1500 parts were manufactured using the same sheet material and lubricant. For the sake of representation, only the cycles between 200 and 300 seconds are displayed in figure 5.32.

Discussion

With reference to figure 5.30, it is clear that the three curves have alike trends. The forces connected with the reference coated die diverge from the ones related to the two MUFU dies when the load exceeds 35 kN. Above this limit, the load related to the coated die climbs up to over 50 kN, while the one associated to the MUFU dies stays at a lower level not surpassing the 50 kN threshold. The average value of the maxima (figure 5.31) is in fact approximately 50.6 kN for the coated die, while it is respectively 48.6 and 48.5 kN for the two MUFU dies. Standard deviations of 0.2-0.3 kN were observed, confirming the high repeatability of the tests. The test shows evidently how the forces of a deep-drawing process when an un-coated

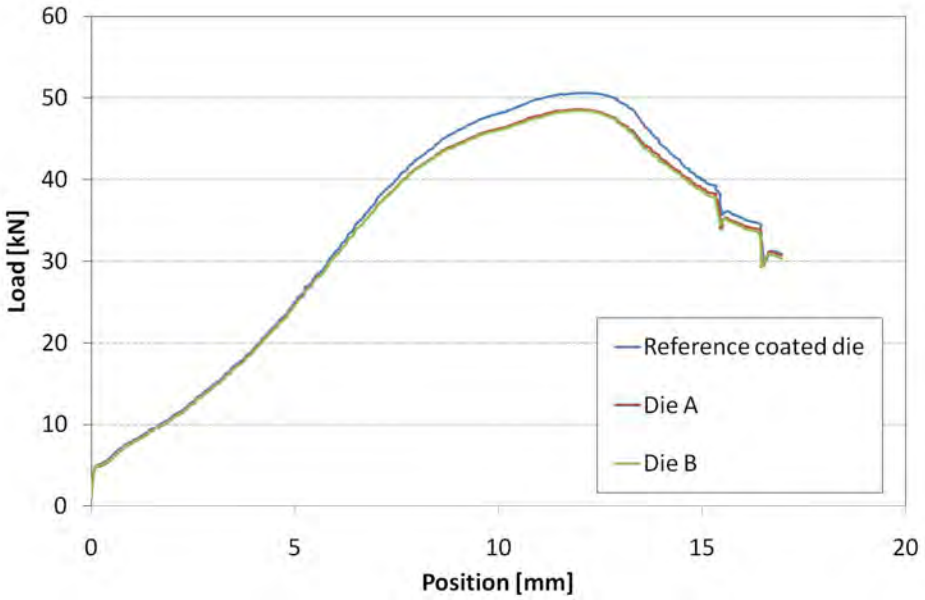

Figure 5.30: *Average force trend of coated and MUFU dies.*

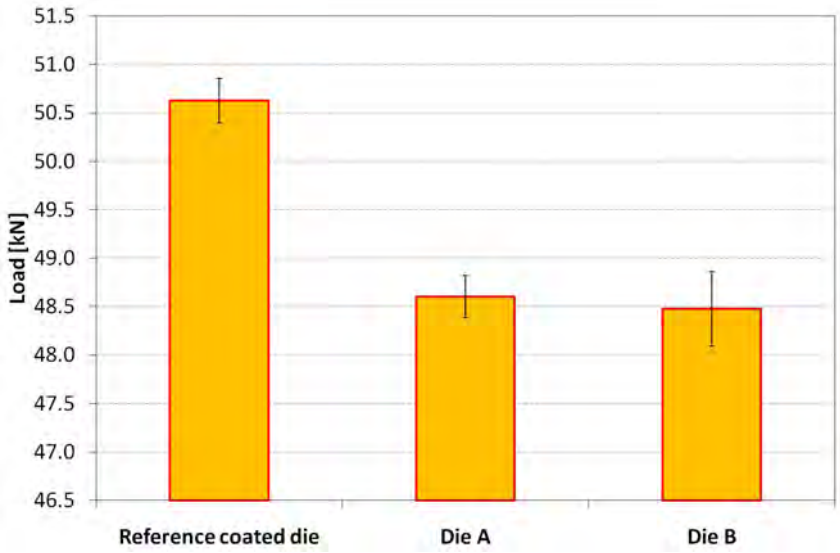

Figure 5.31: *Die comparison: average of max forces and their standard deviations calculated over 20 repetitions each.*

MUFU die is used are comparable and even lower than the ones associated to the usage of a coated die, which is generally acknowledged having good tribological performances. The lower forces recorded by the MUFU dies are an indication of the occurrence of micro-plasto-hydrodynamic lubrication. The pockets are in fact closed now meaning that the lubricant

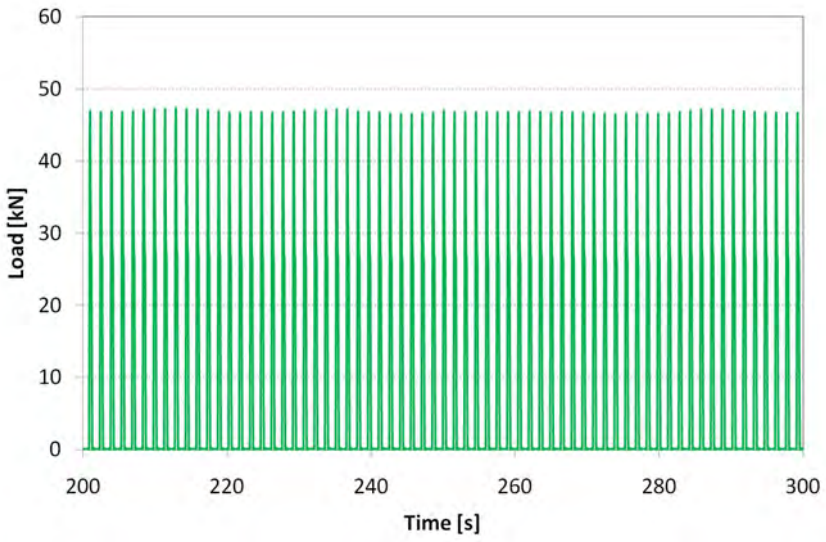

Figure 5.32: *Force trends on first operation during the automatic production of 1500 parts.*

is pressurized and squeezed out adding an extra fluid layer separating tool and workpiece. That resulted in lower friction forces and this can mean less likelihood of wear occurrence, but this cannot be ascertained with only 20 operations. The tests on the automatic press were therefore run. The maximum recorded force of those tests, 47.8 kN, was even lower than the ones measured during the 20 repetitions and no galling could be detected on the final part and no pick-up could be observed by visual inspection on the tool. This is not a definitive assessment, but it is a clue that MUFU surfaces can be an effective alternative to coating in deep drawing operations by lowering the process forces and consequently the likelihood of wear occurrence. The test do not display a significant statistical difference between MUFU textures. This does not imply that all the possible textures will present similar behaviours; but there might be some parameters that weigh more than others. The two textures are very different, but have in common a low plateau BA, which the BUT tests showed being an important factor. Further tests should be run in the future to determine if increasing the bearing area different results are achieved. For other purposes outside the present investigation other workpiece materials were tested, which are not usually used in the specific manufacturing process. Among those materials, which were more challenging due their higher strengths, there were a lean duplex stainless steel (EN 1.4162) and a high strength fully martensitic steel with ultimate tensile strength of approximately 1200 MPa. The two MUFU dies were tested and the results are shown in figure 5.33.
The results exhibited that, when using materials that require higher forming

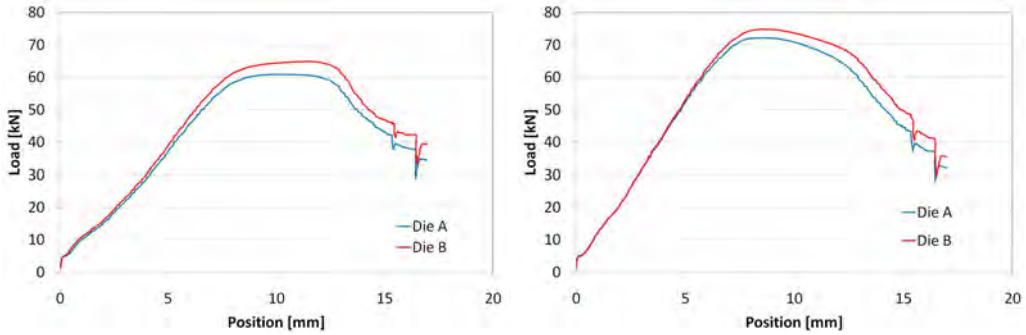

(a) EN 1.4162. (b) Fully martensitic steel.

Figure 5.33: *Force trends of the MUFU dies when testing other workpiece materials.*

forces, the MUFU behaviours finally diverge. In both cases die A is the one that displayed lower forces. This could mean that at the difference in texture become eventually relevant at higher process forces, and that a high number of smaller pockets (lower Rt and EQF) where the pressure build-up is higher (and presumably thus the escape) helps in a better separation of tool and workpiece. Unfortunately there were no tests with the original die on those materials and a comparison cannot be made.
The conclusion and summary of this discussion is that MUFU surfaces are effective in deep-drawing processes and represent an alternative to coating. When using the material normally employed in production, no statistical difference was noted in the results and the reason for that could be found in alike BA. Low BAs seem to be a prerequisite for well functioning MUFU surfaces and a counter proof with tests at higher BA would be of interest. When the process forces increase, the feeling is that the pocket density and depth gain importance, being numerous and shallower pockets better performing due to higher pressures build-ups. Unfortunately, reference tests were not made so that the forces connected to coated dies are in these cases unknown.

5.3.3 Post test inspection

As said before, at a first glance the dies did not suffer any pick-up and the final part fulfilled the quality requirements (figure 5.25(c)) without showing traces of galling. The dies were nevertheless inspected again with the FTS maintaining the previous settings. The filters used were kept. The results are collected in table 5.4.
For die A the results are basically unaltered, further confirmation that the tests ran smoothly. On die B, instead, there was one interesting difference in the measurement before and after testing. The plateau roughness is slightly

Table 5.4: Characterisation of the deep-drawing MUFU tools after testing.

Die	**Rt [µm]**		**Ra pl. [µm]**		**EQF [µm]**		**BA [%]**	
	Average	**U**	**Average**	**U**	**Average**	**U**	**Average**	σ
A -R	1.500	0.078	0.016	0.010	0.350	0.076	22.2	8.0
-H	1.312	0.064	0.018	0.009	0.220	0.027	37.8	5.8
-V	1.577	0.058	0.030	0.009	0.180	0.014	56.4	2.6
B -R	2.334	0.161	0.032	0.010	0.567	0.053	25.2	7.2
-H	3.758	0.643	0.022	0.009	0.756	0.031	31.0	4.4
-V	2.748	0.452	0.026	0.009	0.868	0.041	33.6	2.6

increased. The die was brought under a microscope for a visual inspection of the radius (figure 5.34).

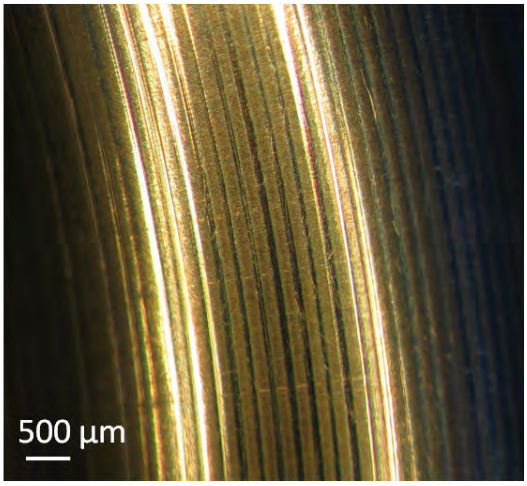

Figure 5.34: *Visual inspection of die B after testing.*

The inspection showed that the MUFU structure was still clearly visible and no evident sign of pick up are present. Nevertheless, the structure displayed a dark "veil" on the plateau zone of the radius. In all likelihood that is a fine layer of workpiece material deposited onto the plateaus. This could be referred to as "nano-pick-up" and could be the cause for the increased plateau roughness. Probably the same occurrence as in the BUT tests happened during the 1500 strokes in production conditions, though at much a lower degree. The closed pockets are deemed playing an important role

in preventing the scraping of material, hence the likelihood of occurrence of galling. The final quality of the product is well within the range of acceptability.

5.4 Strip Reduction Tests of MUFU surfaces

In this section the strip reduction tests run for assessing the performances of MUFU surfaces are presented.

5.4.1 SRT tools characterisation

For the SRT campaign, 6 tool pins were manufactured by Strecon: 4 tools were presenting different MUFU surfaces and 2 were mirror polished and used as a reference. The material was the same the same as for the BUT tests: Vanadis 4 [158].

Measurement settings and results

The four SRT tools with MUFU surface were labelled respectively SRT1, SRT2, SRT3 and SRT4. The two polished references were named Pol1 and Pol2. SRT1 and SRT2 were the tools produced first, before the modifications of the tool ends. They had therefore only 4 sides. All other tools, instead, had 8 sides. SRT1 and SRT4 were milled with a feed of 0.2 mm, whereas SRT2 and SRT3 were milled with feed equal to 0.3 mm. The FTS was used once again for the measurement of the parts. The set-up of the measurement is illustrated in figure 5.35. In the case of the MUFU specimens, three profiles were taken each side for a total of 12 profiles in the case of SRT1 and SRT2 and of 24 profiles in the case of SRT3 and SRT4. The instrument settings were the same as before; the profile length was set equal to 4 mm and the measurement taken transversal to the surface lay.
Again, a form removal by polynomial fitting of the 3rd order is done before the λs operation. The same modified RGR was employed in all cases with the difference that the closing operation was made with disk radius equal to 0.8 mm. Moreover, a 1 mm x 0.3 mm surface topographies are again taken for visualisation purposes. Only one topography was taken each tool pin, on the position marked with number 1. First of all the cases of the tools SRT1 and SRT2 are treated. The profiles and the topographies of the two tools are shown in figure 5.36, using a fixed y-axis range of 10 µm for comparing the textures scales. In table 5.5 the parameters quantifying the surface are listed. The results are presented zone by zone in order to detect the possible occurrence of off-centring problem during the milling operation.

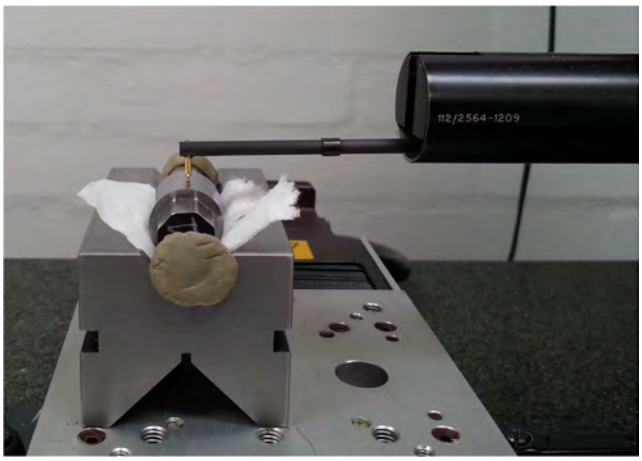

Figure 5.35: *Measurement set-up for the SRT tools.*

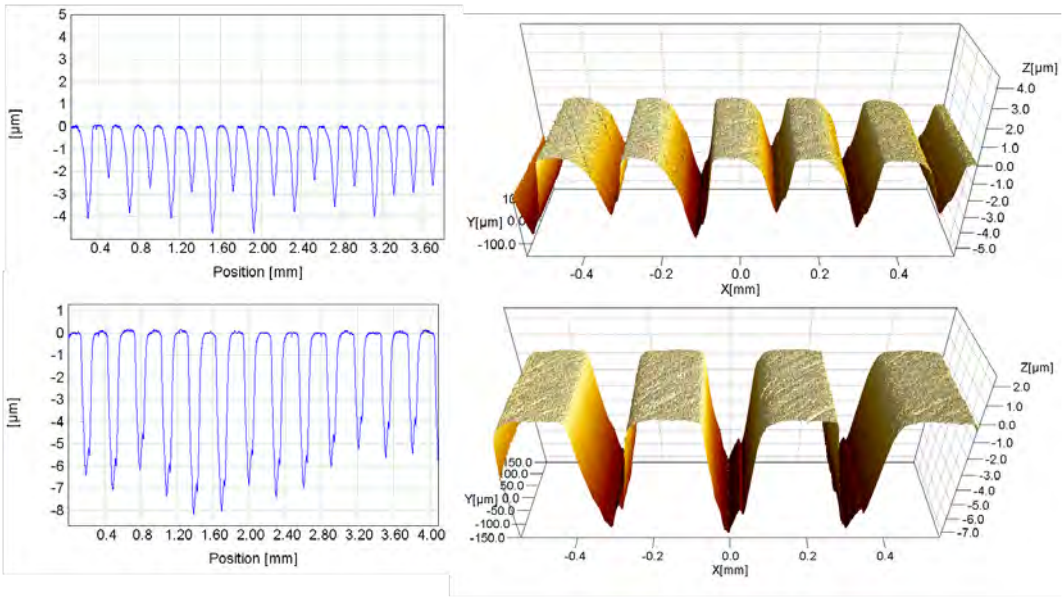

Figure 5.36: *Profiles and 3D topographies of the tools SRT1 (top) and SRT2 (bottom).*

It is evident from the profile and the areal measurement on SRT1 that the milling process did not provide a constant cutting depth, so that some valleys are shallower than others. As explained in section 3.5.2, this occurrence can hinder a good outcome of the separation procedure. This fact actually happened in the measurement of the fourth zone: some valleys were included in the plateaus profile, affecting both plateaus and valley profiles. While in the case of the plateaus the "outliers" could be eliminated by excluding them from the parameters calculation, that was not possible for the valley profile since volumes were missing and could not be

Table 5.5: Characterisation of the tools SRT1 and SRT2.

Tool	**Rt [µm]**		**Ra pl. [µm]**		**EQF [µm]**		**BA [%]**	
	Average	**U**	**Average**	**U**	**Average**	**U**	**Average**	σ
SRT1	4.902	0.119	0.018	0.009	0.923	0.078	43.8	1.1
	3.776	0.107	0.019	0.009	0.624	0.026	50.3	0.5
	3.902	0.166	0.019	0.010	0.757	0.038	41.4	0.2
	4.405	0.116	0.017	0.009	0.668	0.106	45.2	0.1
SRT2	8.969	0.712	0.025	0.009	1.826	0.105	52.8	1.1
	8.972	0.638	0.026	0.009	2.112	0.188	49.1	1.8
	8.568	0.731	0.029	0.009	1.875	0.133	52.4	0.5
	8.051	0.818	0.024	0.009	1.850	0.124	49.6	0.1

reintegrated. The resulting EQF was thus lower than it should be, and it is marked with red in table 5.5. The solution to this problem in the future is to improve the flexibility on the software by allowing the possibility of setting a higher lower threshold.
In the following, the analyses of SRT3 and SRT4 are presented separately due to large differences within the faces of the same tool that must be displayed and discussed. In figure 5.37 two profiles of SRT3 are shown taken on positions 1 and 6 together with an areal measurement again on position 1. In table 5.6 the calculated parameters are listed together with their expanded uncertainties. In figure 5.38, instead, the profiles taken on SRT4 on the same positions as SRT3 and the areal topography are displayed. In table 5.7 the parameters and expanded uncertainties pertaining to SRT4 are listed. Already from the 3D topography of figure 5.38 it can be seen that the valley had very high roughness and that drastically affected the results. SRT4 had not an "ideal" MUFU surface, and at the positions with higher bearing area the valley roughness merged with the plateaus one yielding quite overestimated results. These biased results are marked in red in table 5.7.

Eventually the case of the two polished reference is treated. Differently from the MUFU tools, the measurement strategy chosen was different. Since they were mirror polished to a very low roughness across the whole surface, there is no reason to think the several faces to be different from each other. Therefore only one profile was taken on each face, measured along the axial

direction, which is the easiest and fastest way for measuring such items. In order to prove that there is no substantial difference in measuring profiles

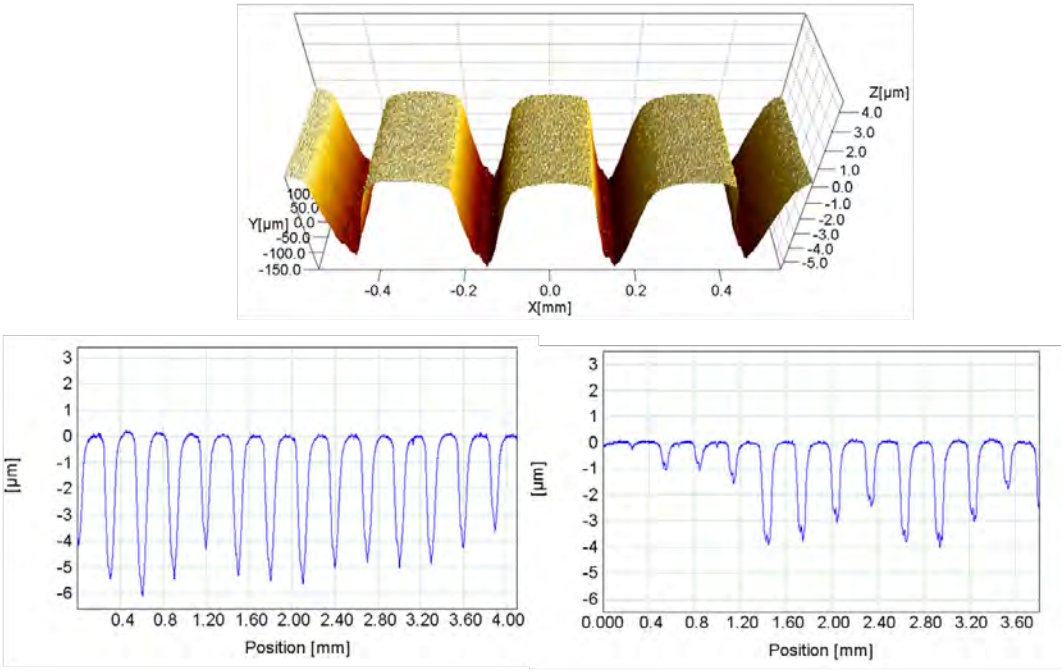

Figure 5.37: *Two Profiles and the 3D topography of the tool SRT3. The profile on the left was taken on position 1, while the one on the right was taken on position 6.*

Table 5.6: Characterisation of tool SRT3.

Tool	**Rt [µm]**		**Ra pl. [µm]**		**EQF [µm]**		**BA [%]**	
	Average	**U**	**Average**	**U**	**Average**	**U**	**Average**	σ
SRT3	6.490	0.261	0.024	0.009	1.251	0.088	50.7	0.5
	7.380	0.420	0.025	0.009	1.278	0.082	52.2	0.2
	5.690	0.189	0.024	0.009	1.048	0.117	53.8	1.6
	6.040	0.197	0.024	0.009	0.864	0.156	56.7	1.1
	5.295	0.552	0.024	0.009	0.866	0.188	54.8	2.1
	4.373	0.200	0.020	0.009	0.700	0.089	61.3	3.2
	5.615	0.379	0.023	0.009	0.970	0.070	52.2	1.4
	5.182	0.187	0.023	0.009	0.886	0.079	54.4	1.6

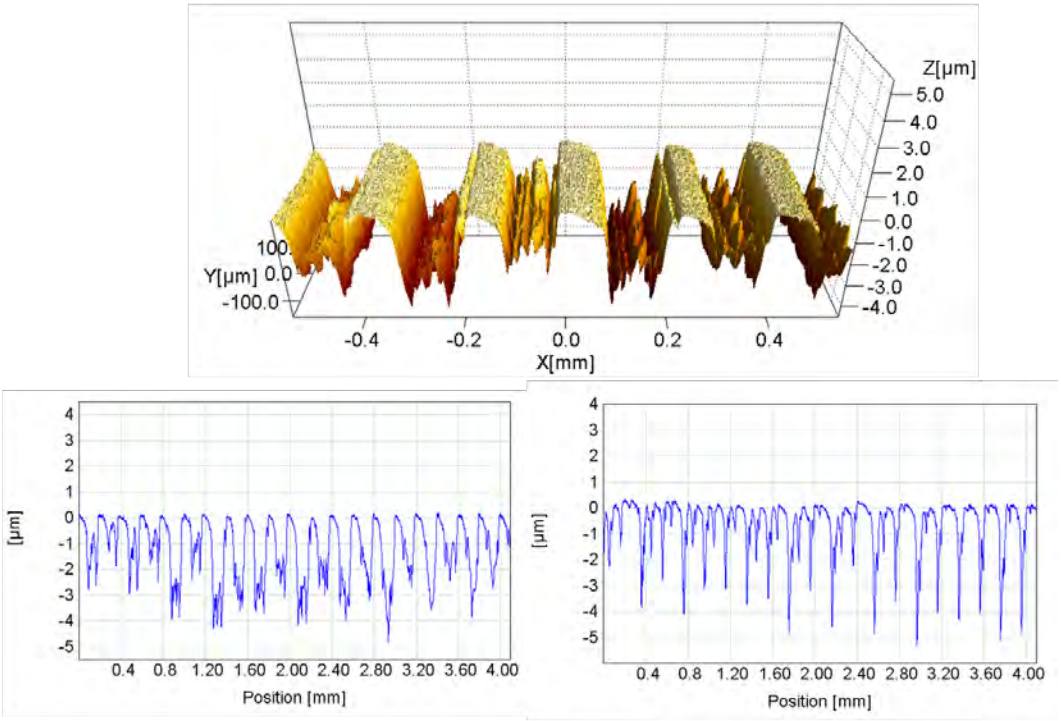

Figure 5.38: *Two Profiles and the 3D topography of the tool SRT4. The profile on the left was taken on position 1, while the one on the right was taken on position 6.*

Table 5.7: Characterisation of tool SRT4.

Tool	**Rt [µm]**		**Ra pl. [µm]**		**EQF [µm]**		**BA [%]**	
	Average	**U**	**Average**	**U**	**Average**	**U**	**Average**	σ
SRT4	4.890	0.192	0.035	0.013	1.072	0.071	29.3	3.1
	5.271	0.289	0.030	0.011	1.189	0.052	30.1	3.3
	5.369	0.195	0.029	0.010	1.212	0.072	30.2	0.9
	8.057	0.978	0.033	0.010	1.779	0.145	33.9	0.4
	3.455	0.651	0.104	0.045	0.333	0.037	52.5	5.0
	5.635	0.220	0.181	0.032	0.390	0.053	63.4	0.8
	8.068	1.287	0.039	0.010	0.726	0.085	61.5	3.4
	6.746	0.513	0.058	0.013	0.890	0.153	44.3	0.4

axially or circumferentially, two areal measurements were taken along the two directions and compared (figure 5.39). Along the axial direction the measured Sa was equal to 0.016 µm, while along the circumferential direction Sa = 0.017 µm, hence very similar. The similarity of the height histograms is remarkable, with a almost perfect Gaussian distribution of the heights slightly skewed to the right. The Ssk values are respectively 0.51 and 0.53, very close indeed to each other. The angular spectra prove that the images are taken along two different directions, since they seem almost mirrored, with a peak jutting out at 15° and 160°.
The instrument settings were the same as before, whereas the characterisation procedure was different. There was obviously no need to use robust filters, thus a "simple" GR2 was used instead. No form removal was applied beforehand.

The two tools were perfectly alike, so just a profile of Pol1 is shown along with a 3D topography (figure 5.40). The profile is shown in two different scales in order to appreciate both its nano-roughness and to compare it with the MUFU tools. In table 5.8, instead, the Ra and Rt average values along with their expanded uncertainties are listed.

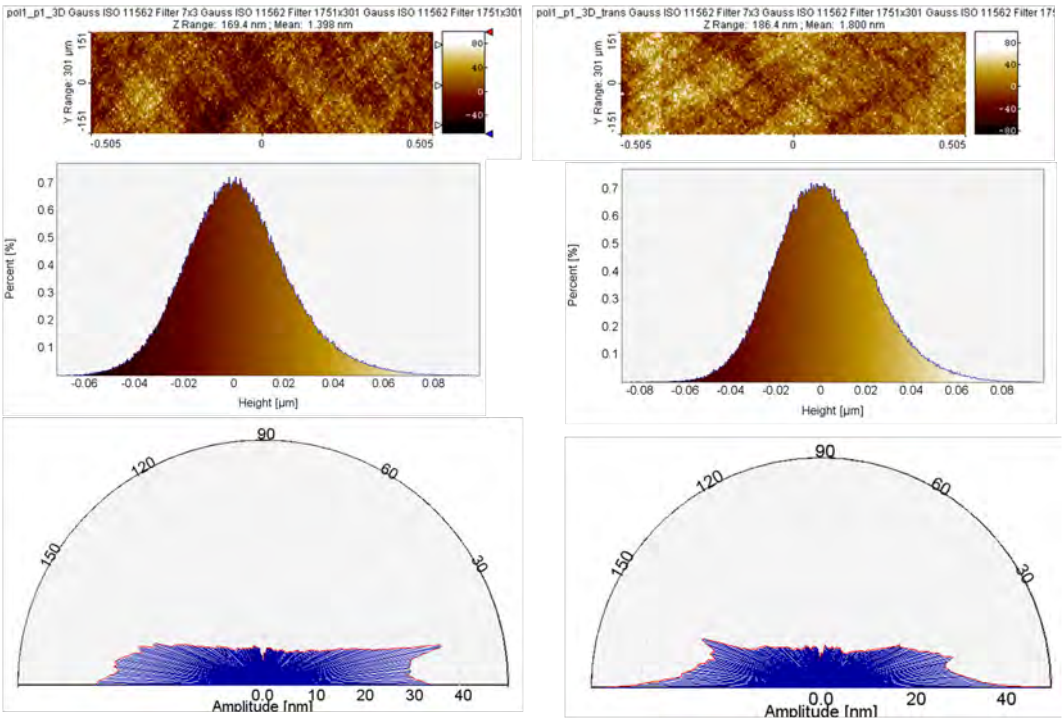

Figure 5.39: *Areal measurements taken on Pol1 along the axial (left) and the circumferential (right) direction along with their histogram and angular spectrum.*

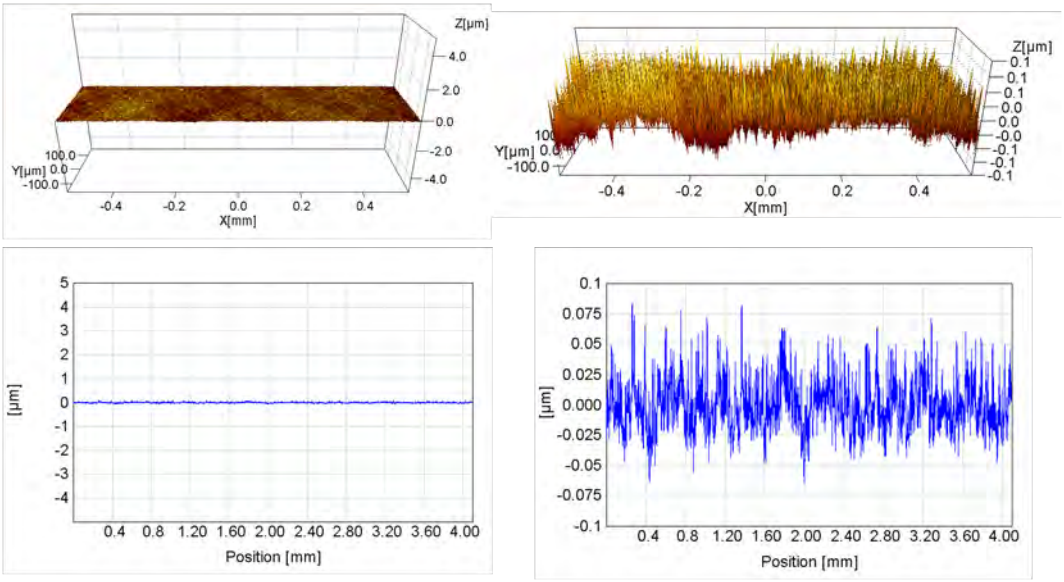

Figure 5.40: *Profile and areal measurement on tool Pol1. Two different scale are displayed.*

Table 5.8: Ra and Rt values of the polished tools.

	Pol1		**Pol2**	
	Average	**U**	**Average**	**U**
Ra [µm]	0.016	0.009	0.016	0.009
Rt [µm]	0.168	0.032	0.156	0.017

Discussion

Starting from the analysis of the polished references, it is outstanding the degree of similarity of these two tools, as the instruments indicates the same average Ra, very close to the mentioned 0.02 µm and even finer. More complicated is instead the discussion of the MUFU tools. Generally speaking the milling operation appeared to be affected by some errors beside the off-centring so that a constant cutting depth was not achieved. It has been already commented that in the case of SRT1 that resulted in characterisation problems on the fourth zone. Anyhow, for SRT1 and SRT2 the plateau roughness was quite consistent, being the former slightly finer. The average Rt value of SRT1 was changing quite a bit in the several zones, while the Rt of SRT2 was more regular, though governed by greater uncertainty. SRT2 has deeper valleys than SRT1, which certainly helped the algorithm to perform a correct separation. To deeper valleys is connected the higher EQF even though SRT2 had slightly higher BA than SRT1. The

bearing area of SRT1 spans between 41% to 50%, while SRT2 had more stable BA comprised between 49% and 52%.
The question regarding SRT3 and SRT4 is even more complicated. The milling errors were quite evident across the eight zones each tool is composed of. SRT3 was varying less than SRT4. Even though the profile height Rt had values ranging from 4.4 µm to 7.3 µm, the Ra of the plateaus was rather stable, being approximately 0.023 µm. The EQF was affected by the Rt variations as well as the BA changes. The bearing area ranges from 50% to 61%, being the highest BA detected on position 6, shown in figure 5.37. As the figure highlights, an almost flat area with valleys nearly erased is detected at the beginning of the measurement causing the high BA at the plateaus threshold. While SRT3 had a rather regular valley distribution, the same cannot be said for SRT4. The considerable roughness of the valleys renders the surface not a true MUFU. Moreover, the changes from side to side are conspicuous. Sides 1-4 had relatively low bearing areas (around 30%), while sides 5-8 had much higher bearing areas up even to 63%. Those sides where most challenging to characterise and the plateaus Ra was much higher due to the inclusion of some valley roughness. The plateaus Ra of the first 4 sides was more reasonable, being it just above 0.030 µm. The EQF of these four sides was above 1 µm, whereas for the last four sides EQF was well lower than that. What it can be concluded from the MUFU tools characterisation is that each side does not represent a repetition of the previous one, but a whole new tribological situation. This is especially true for SRT3 and SRT4.

5.4.2 Strip reduction tests set-up and results

Once the characterisation had been completed, another operation had to take place before testing. The SRT tools were manufactured from a batch of existing ones Strecon had in stock. These tools had a substantial difference with standard ones: their diameter was Ø16.7 mm, quite bigger than the nominal one. These bigger tools required modifications of the SRT machine and a subsequent modification of the model calculating the reduction. The modification to the SRT apparatus was limited to the shoe.

A new shoe

The bigger tool radius meant that the tool pins could not be coupled to the existing shoe properly. A new one was needed. The original shoe had the following dimensions: width 50 mm, height 36 mm, a central rounded cradle for accommodating the tool with radius 7.5 mm and maximum height 6 mm. The cradle is therefore less than half circumference. The

modifications must involve the radius of the cradle (changed to 8.35 mm) as well as the maximum cradle height and the shoe overall height. The maximum cradle height must increase proportionally with the radius in order to achieve the same area of contact, while the shoe height must be reduced accordingly in order to reach the same level as the old shoe. Thanks to geometrical considerations, the new shoe would have overall height of 35 mm (1 mm less than the old one) and a maximum cradle height of 6.7 mm (figure 5.41). The width was kept constant and no holes for the tool heating were bored since the heating was not used. The shoe was manufactured at the department's workshop.

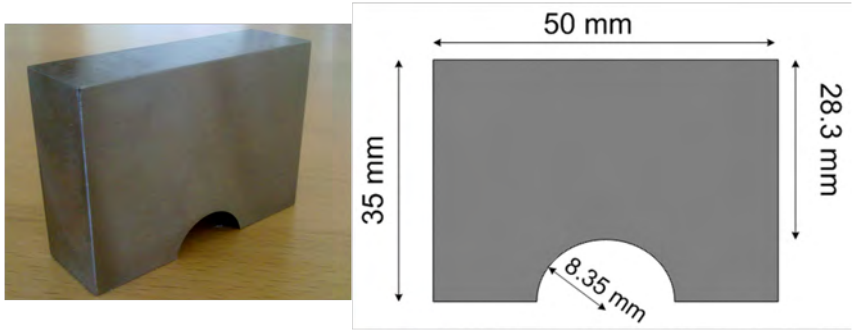

Figure 5.41: *SRT new shoe and dimensions.*

The model calculating the adjustment strips to be applied in order to achieve a wanted reduction must be also modified accordingly. The adjustment J was calculated by the following formula:

$$J = 3.18 + D - E - G \cdot \left(1 - \frac{I}{100}\right) \tag{5.1}$$

where D is the top plate thickness (plate placed above the vertical guides to keep the shoe in place), E is the tool radius, G is the strip thickness, I is the percentage of reduction and 3.18 is a constant value equal to the overall apparatus height minus the supporting plate thickness and the reduced shoe height (shoe height minus the cradle). The modifications at the model involved the radius E and that constant parameter, which was set to 4.88 given the 1.7 mm difference between the old and the new tool.

Running the tests

The tests were carried out at room temperature (20°C) and the same lubricant as before (Rhenus SU 166 A [161]) was used for all tests. The workpiece material was stainless steel EN 1.4401 and the nominal strip thickness was 0.7 mm. The goal reduction was set to 20%. The parameters related to all the tests are collected in figure D.1 present in appendix D

where also the pulling forces measured during the drawing operation are plotted. In this chapter are however presented the plots of Pol2 and SRT3 for visualizing the difference between the MUFU surfaces and the polished references. These plots are shown in figures 5.42 and 5.43.
Due to excellent results obtained by the polished surfaces, it seemed interesting to try higher reductions than 20%, hence explaining the presence of the arrow in figure 5.42. Reductions up even to 38% were successfully attempted. In figure 5.43, the third test on SRT3 is missing due to an acquisition error.

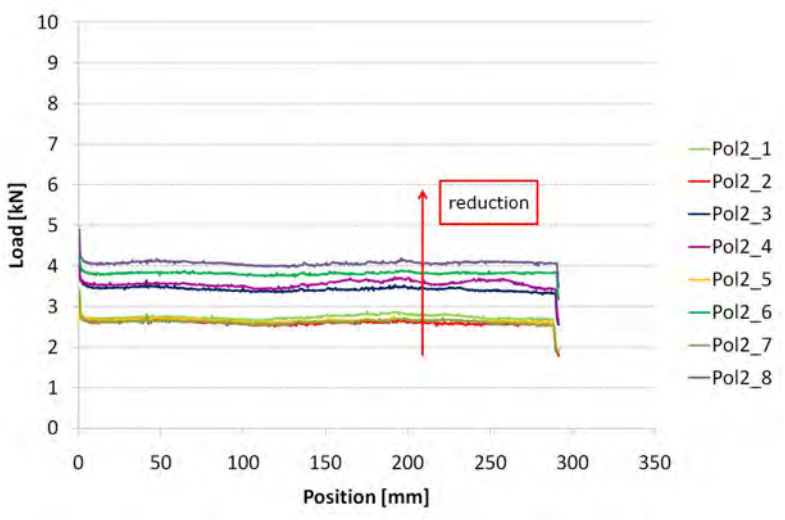

Figure 5.42: *Force results of tool Pol2.*

Galling analysis

After testing the analysis of galling is performed as described by Andreasen et al. [153, 154]. Each strip was divided in equidistant intervals of 30 mm for a total of 9 intervals each unbroken strip. The strip roughness was measured with a skid instrument (Sutronic 4+) with an evaluation length spanning almost the whole length of the strip (12.5 mm). The successive measurements can detect more or less the point of onset of galling if a sudden roughening of the strip surface occurs. The 9 profiles are plotted together forming a "multiplot". As an example in figure 5.44 is shown a multiplot from SRT3 pos 1. Galling occurs almost immediately and propagates drastically. All multiplots are collected in appendix D.
Two non-standard parameters have been defined by Andreasen et al. [153, 154] for the quantification of galling: Nri and $Nri2$ which are respectively the amount of valleys which are deeper than 0.5 µm and 1 µm. Since galling

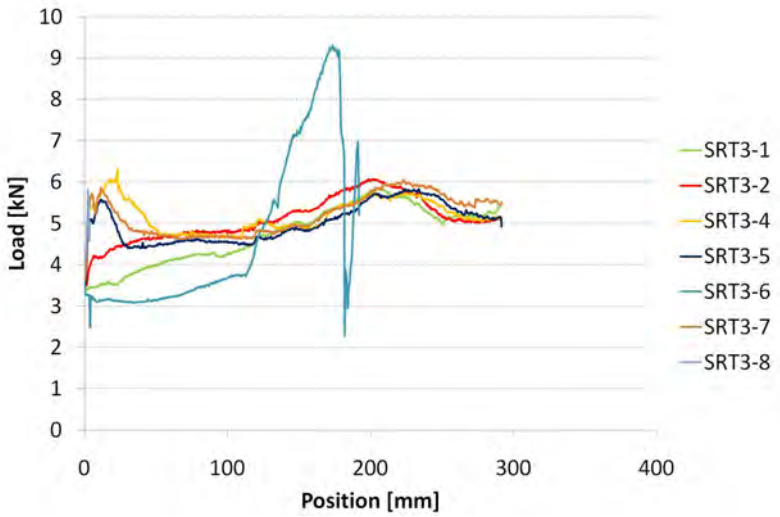

Figure 5.43: *Force results of tool SRT3.*

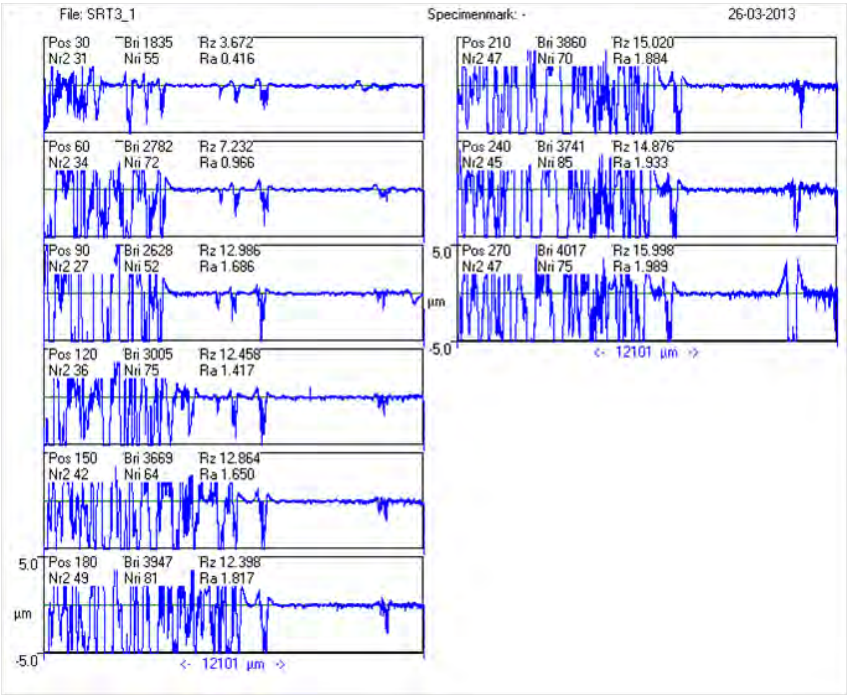

Figure 5.44: *Multiplot of SRT3 position 1.*

was extremely high on the majority of strips, only $Nri2$ was considered. Moreover, since in most cases galling was occurring immediatly, its analysis was associated with Ra in order to estimate its progression. Again, the evolution of the parameters for inspecting galling can be found for each strip in appendix D after the corresponding set of multiplots. In some

cases the results are incomplete or not presented due to strip breakage (figure 5.45). As before, the cases of Pol2 and SRT3 are shown here plotted in the same scale for better understanding the difference between a MUFU surface and a polished reference. Since the polished tools basically did not display any sign of galling, in their case only the plots of $Nri2$ are presented maintaining the same scale as for the MUFU plot (figure 5.46 and 5.47). Only in one case in fact $Nri2$ overcame the number of 10, in the seventh test with Pol2. That (light) galling detected was caused by a transversal scratch. The galling did not propagate and remained constant throughout the length of the strip. That test is regarded as an outlier. Eventually, in figure 5.48 the Ra evolution for the SRT3 test is exhibited.

Figure 5.45: *Broken strip from SRT1.*

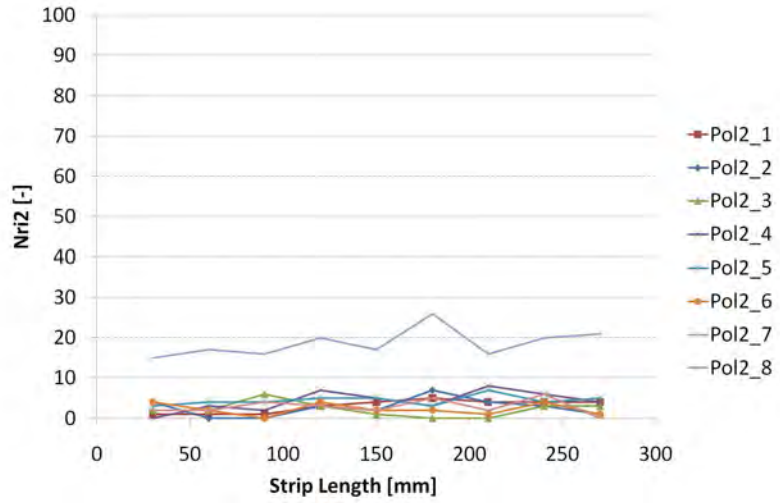

Figure 5.46: *Nri2 plot of Pol2.*

Discussion

From what shown on the tests the conclusion is clear. The reference mirror-polished tools gave a much better functional response than the MUFU tools. The polished tools, in fact, gave outstanding performances in (almost) all

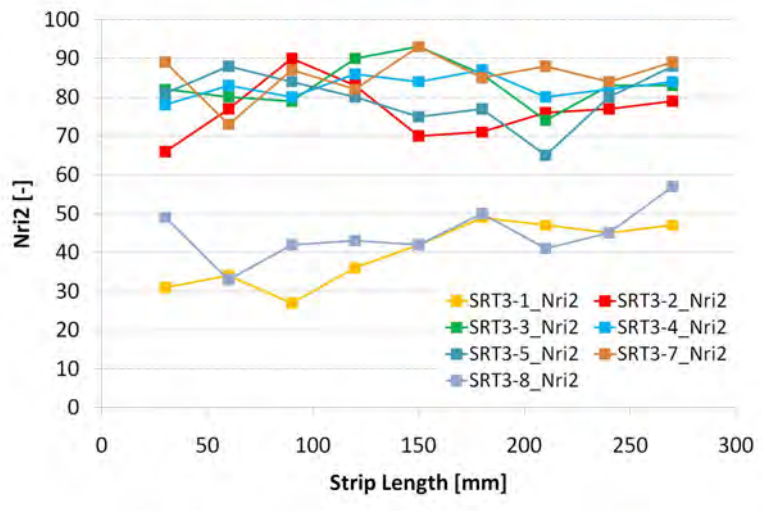

Figure 5.47: *Nri2 plot of SRT3.*

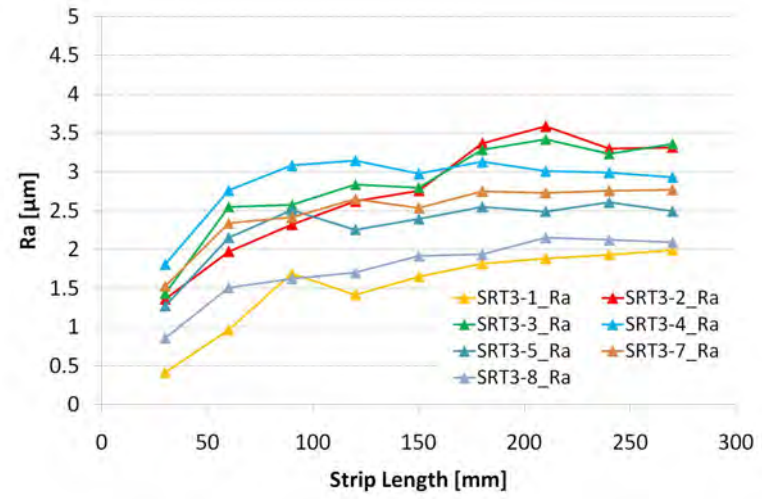

Figure 5.48: *Ra plot of SRT3.*

the tests done, so that insisting on testing with 20% reduction seemed of little use. Higher reductions were attempted, successfully. Generally speaking, $Nri2$ did not surpass the value of 10, meaning that in each test there were less than 10 valleys deeper than 1 µm. An impressive 38% reduction was achieved on the last test without the occurrence of galling on the strip. It means that this lubricant, the usage of which is not recorded in the department's literature regarding SRT, performs excellently at room temperature. Moreover, the extremely low roughness helped in the maintenance of a lubricant film, hence galling was not set off. The pulling

forces were increasing coherently with increased reduction. Compared to these results, the MUFU tools performances were disastrous. Many strips broke and that was demonstrated by abrupt increase of the pulling forces above 8 kN. The ruptures were not neat cuts, but the result of ever increasing forces due to sudden lubricant breakages and the wearing action of the tool onto the strips. The strips manifested galling, twisted and eventually broke (figure 5.49). Sometimes the galling causing the twisting appeared only on the side as shown in figure 5.45 or it was uniformly distributed (figure 5.50).

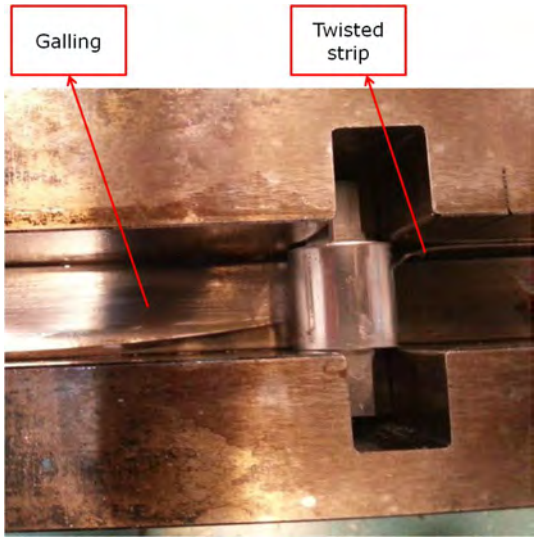

Figure 5.49: *Twisting and breaking of a strip.*

Figure 5.50: *Broken strip from SRT2.*

It is difficult to say whether one typology of texture is more prone to complete failure than others. The parameter that at a first glance appears to have a certain influence is the bearing area. BAs much lower than 50% seem to be a guaranty of complete failure since out of the four with BA approximately equal to 30%, three broke and one was on the verge of fracturing with a huge amount of galling observed on the strip surface. Bearing areas comprised between 40% and 55% showed contrasting, but better outcomes. Some broke, some didn't. Among the strips which broke the strip with highest EQF and Rt (SRT2 pos 2) and a strip with one of the lowest EQF (SRT1 position 2). The only strip which did not present

galling was the one with lowest EQF and had a BA of approximately 52%. The sensation is that with increasing BA the likelihood of better results increases. Unfortunately the three tests made with BA over 60% disprove this hypothesis. In two cases the strip broke, one unfortunately because of a too high reduction level achieved (well above 30%). The second fracture was sudden and without onset of galling: SRT3 position 6, which figure 5.37 showed having an increasing depth of the valleys was seemingly working fine (figure 5.51) when suddenly it cracked in two. The test which could be pulled till the end showed the highest $Nri2$ of all, being them around the value of 100.

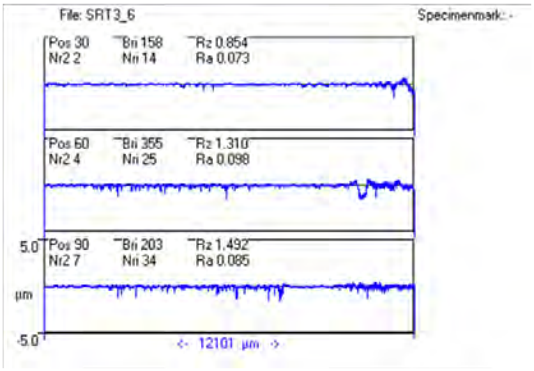

Figure 5.51: *Multiplot of SRT3 position 6.*

A second parameter that seems to have influence is the feed or valleys period. Among the tests that could be completed, the tools with higher feeds had higher pulling forces. So, while SRT1 and SRT4 had drawing forces generally lower than respectively 3 kN and 4 kN with peaks of 4 kN and 5 kN, SRT2 and SRT3 had values comprised between 4 kN and 6 kN. SRT3, especially, the tool that could complete almost all its tests, had the highest drawing forces with an average above 5 kN.
Anyhow, this discussion on which MUFU parameter have provided the better results seems preposterous when there is a texture that clearly performs better: the mirror-polished reference. It is better to veer the reasoning on: *"What went wrong with the MUFU tools?"* The galling analysis is quite clarifying on this point. The $Nri2$ parameter was high (up to 90 valleys deep more than 1 µm) from the very beginning in the almost totality of the tests. Galling occurred at once and in many cases it kept constant, as the number $Nri2$ was not further increasing with the sliding length. In some of these cases $Nri2$ was fairly constant, while the Ra trend was monotonically ascending, meaning that the depth of galling was increasing but not propagating. Most likely, in the cases galling propagated, the strip broke. Hence, in these experiments, the limit of lubrication, i.e. the

length at which galling sets off, could not be studied, since from the very beginning the lubricant film was broken. What happened then? For better understanding the situation it is useful to look at the pick-up occurred on the tools. In figure 5.52 the pick up on side 4 of SRT3 is shown. The picture shows an area with galling covering all the contact (on the left-hand side) and an area with galling covering an area of approximately 0.9 mm (smaller than the total contact) from the strip exit.

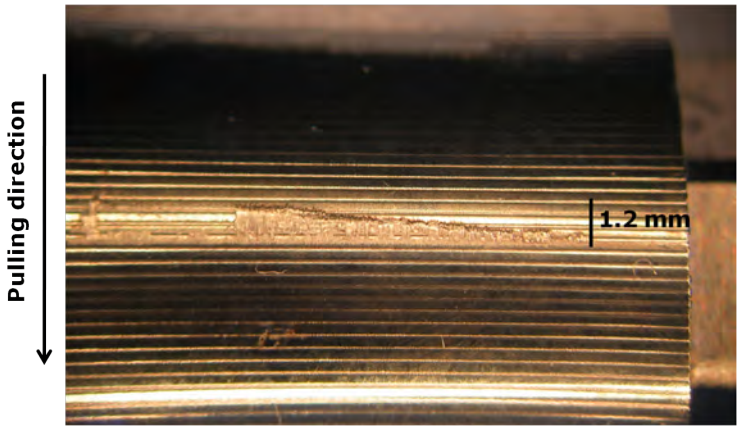

Figure 5.52: *Pick-up on tool SRT3.*

A range of hypotheses can be made. The first one concerns the valleys, which instead of acting as a reservoirs for providing extra-lubrication in the contact, collect the coming lubrication and channel it out from the contact leaving the following plateau without a sufficient film. A reason for this could be the open grooves that can cause the squeezing of the lubricant on the sides, although this occurrence could not be visualized during the test. This hypothesis came to the mind during the tests seeing the poor results, therefore a different trial was attempted in two of the final tests: the change of lubrication. A plain mineral oil CR5 was used instead. This lubricant had already proven bad in previous lubricant testing [153, 154] due to the fact that has no additives unlike the Rhenus oil, but it is characterised by a much higher viscosity (660 cSt). The idea was that the higher viscosity would prevent to some extent the lubricant to escape from the contact and good results with that oil would have been interesting to discuss and justify. Nevertheless, the experiments went bad as well: one strip broke, the other one exhibited heavy galling. This hypothesis could thus not be proven straight away. A second hypothesis puts under investigation the strip entrance. The hypothesis is that the strip enters directly in the valley and encounters a steep changing of slope between the valley flank angle and the following plateau. In there the lubrication finds a "wall": the oil is collected inside that first pocket and accumulates there and in the

surrounding environment since the valley is partly open. The lubricant film would be very thin from the very beginning increasing the likelihood of galling occurrence. A third hypothesis focuses instead its attention on the strip exit. During the loading, the high normal pressures acting locally from the plateaus would "indent" the strip causing it to flow inside the valley and contact the flanks. Galling would have formed there and accumulated gradually during the test across the contact zone reaching in certain cases the strip entrance.This thinking is supported by previous research done by [164]. In their experiments, textured surfaces for deep-drawing tools were obtained by rolling. In one of their test, a strip was drawn between two textured dies featuring transversal grooves (figure 5.53).

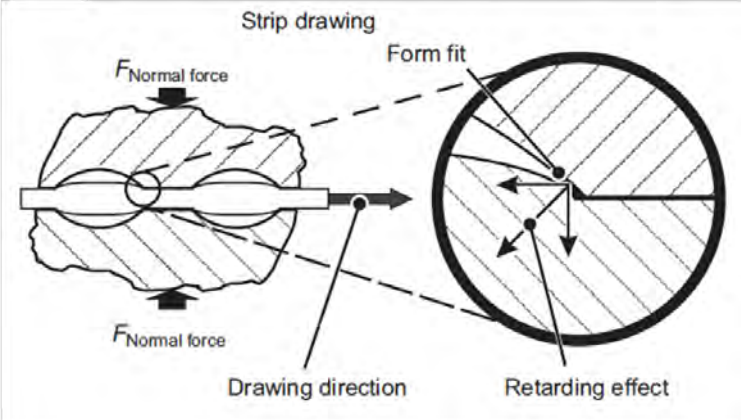

Figure 5.53: *Strip drawing through textured dies with transversal grooves. Picture from [164].*

They observed how the transversal grooves displayed higher friction coefficient due to a retarding effect due to the strip "crashing" on the knee between the flat and the dimple zone on the die. The same occurrence can have happened in the studied strip reduction test, with the further disadvantage that the normal pressures were much higher in the present case than theirs. This third hypothesis questions the utility of the test in the present design when investigating textured surfaces. If the hypothesis was true, a more relevant test would be to start the loading operation concurrently with the pulling of the strip in order to introduce a hydrodynamic component preventing the indentation occurrence. The three hypotheses do not exclude each other. The initial indentation can be accentuated by a insufficient hydrostatic pressure build-up caused by escape from the open channels, while the second hypothesis would cause the thinning of the lubricant film facilitating the galling propagation The conclusion of this discussion is that applying a MUFU surface in ironing operation seems to be quite a risky operation. In real production process the grooves are closed

(axisymmetric tools), so there would not be side escape. The indentation problem would also be reduced since the die would not apply a pre-load. However, the case of the first valley blocking the passage of the lubricant can still occur. Given the brilliant results of the mirror-polished tools at the same conditions, it appears not advisable to use MUFU surfaces in this application. Nevertheless, it would be interesting as future work to run tests closer to production conditions for eliminating the occurrence of (at least) the first and third hypotheses and improving thus the knowledge on the subject.

5.5 Summary and Conclusions

In this chapter the testing of MUFU surfaces for metal forming tools has been presented. Three types of tests were run, two were simulative tests present at DTU's laboratories and one production test. In particular the Bending Under Tension test for simulating deep drawing applications and the Strip Reduction Test for simulating a most severe ironing process were performed. The production test was a real deep-drawing operation carried out in the production department of the Danish company Grundfos A/S. For the simulative tests, milling was the initial machining operation chosen for manufacturing the MUFU tools, which suffered from some technical problems. The final surfaces proved challenging to characterise. Moreover, the problems generated a broad range of surfaces rather than few repetitions of the same surface: the discussion of the results obtained was hence widened. For the production tests, thanks to the axisymmetry of the dies, turning was instead used. Nevertheless, the CNC control of the lathe failed in following precisely the contour yielding an irregular surface particularly difficult to characterise. The tests themselves have shown quite various results.
The Bending Under Tension tests displayed how the MUFU surfaces generated way less galling than the polished references. This was particularly true for the MUFU surfaces with lower bearing area. Although the opened channels did not allow a sufficient fluid pressure build-up and the workpiece material was scraped off, the low bearing area hindered the propagation of galling. Pulverized workpiece material was transported to other places such as the valley bottoms or the exit flat zone instead of cold-welding to the tool. The contact conditions in some cases changed and that could have prevented the formation of further galling. Metal-to-metal contact occurred therefore and, although there was not evident appearance of galling, the quality of the final result is questionable. It must however be remarked once again that the tribological conditions in real deep drawing operations can be different due to open pockets.

The production tests showed how, with closed pockets, the MUFU surfaces can represent an alternative to conventional, coated surfaces. The process forces were lower in the case of MUFU surfaces when employing the workpiece material daily used in production (EN 1.4301). No significant differences were detected between the two textures, difference that could be marked only when using more challenging workpiece materials. Having a low plateau bearing area seems to be an important if not prerequisite factor. When higher forces are involved, the pockets density and depth become important. Generally, lower EQF would lead to higher pressure build-ups and consequently lower forces. Counter-proofs are unfortunately lacking and represent a suggestion for future work. Workpiece scraping-off might have occurred, but at a lower grade thanks to the closed pockets. The quality of the final product was definitely acceptable.
The Strip Reduction Tests, instead, were quite destructive for the MUFU surfaces, while they ran smoothly for the mirror-polished references. Lubricant channelling and film thickness reduction due to the pocket at the strip entrance were investigated as causes of the bad functioning, but the strip indentation was deemed as decisive factor. With the present design, the strip is preloaded before the strip starts its movement. The high load indented the strip causing severe galling since the beginning of the tests. In real production conditions it would not be so with the further advantage of closed pockets. However, problems with the pocket at the entrance may occur and given the brilliant results of the polished reference at the same and at even more severe conditions it seems not advisable to use MUFU surfaces in ironing applications.

Chapter 6

Modelling of MUFU surfaces

In this chapter the geometrical as well the analytical modelling of MUFU surfaces are treated. First the geometrical models are presented, which, based on trigonometrical considerations, can allow the prediction of the MUFU texture obtained from the knowledge of machining parameters. In the following, functional models are presented, which attempt to predict the impact of MUFU geometries on the frictional forces acting on a tribo-system taking into account the trapped lubrication. In order to do so, a brief review on friction models based especially on the department's long experience within the subject is provided which served as a basis for the development of the models. In particular, the models study the situation of a nominally flat hard surface pressing over a MUFU one under the presence of friction stresses trapped lubricant. The normal pressures considered are relatively low, hence the models are confined to the case of asperity deformation. Bulk deformation does not occur. The models are targeted to sliding machine elements with the two bodies (one harder than the other) parallel to each other and under boundary lubrication conditions: it is basically the case of the Axial Sliding Test. Eventually obvious limitations due to the assumptions are discussed with proposals for future improvements and generalizations.

6.1 Geometrical modelling

As mentioned already in Chapter 1, MUFU surfaces are composed by a coarser and deterministic machining operation followed by a finer and random polishing operation. The final texture will therefore have both deterministic (the valleys) and random (the plateaus) components (figure 6.1). Disregarding momentarily the random components and considering the plateaus as perfectly flat, the MUFU basic geometry can be derived directly from a turned one which has been truncated by an horizontal plane, see

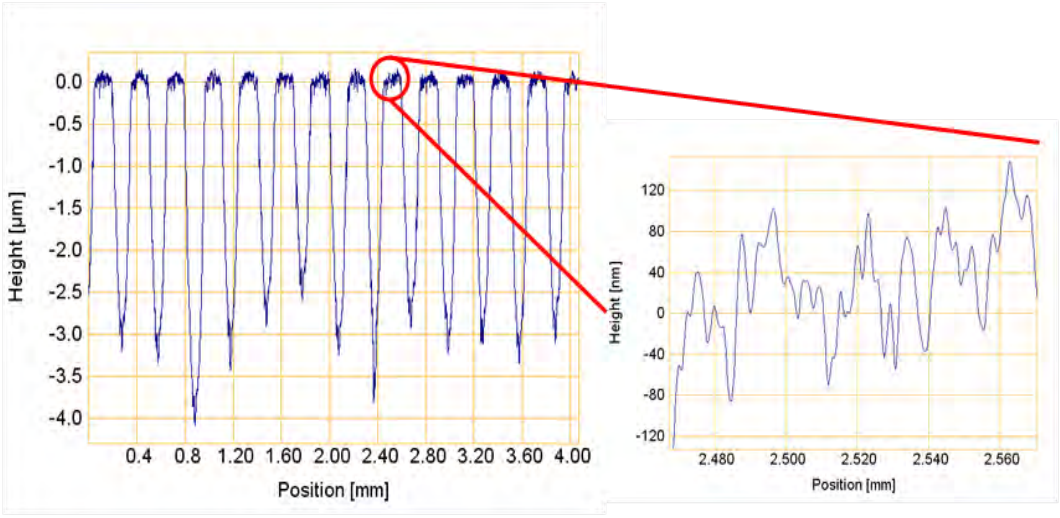

Figure 6.1: *Real MUFU profile: determinstic components at a micro-scale (left) and random components at a nano-scale (right).*

figure 6.2.
The explanation for the parameters indicated in figure 6.2 as well as all other parameters presented in this chapter can be found in the Nomenclature before Chapter 1.

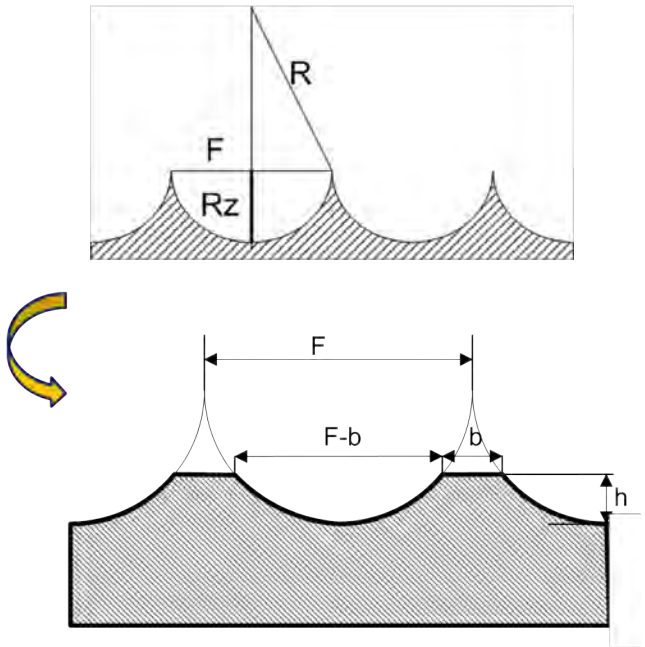

Figure 6.2: *Geometrical modelling of a turned surface (above) and of the derived MUFU surface (below).*

With reference to figure 6.2, a turned surface can be completely described by two parameters: the radius R and the feed rate F. The total height of the turned profile Rz is in fact a variable dependent uniquely by those two parameters, as it can be seen from equation 6.1.

$$Rz = R - \sqrt{R^2 - \frac{F^2}{4}} \tag{6.1}$$

The step for passing from a turned surface to a MUFU one is straightforward and only one parameter more is sufficient for utterly describing an ideal MUFU surface (equation 6.2): the bearing area of the plateaus BA, or, alternatively, the bearing segment b.

$$h = R - \sqrt{R^2 - \frac{F^2}{4}(1 - BA)^2} = R - \sqrt{R^2 - \frac{F^2}{4}\left(1 - \frac{b}{F}\right)^2} \tag{6.2}$$

A notation must be made on the maximum height of a MUFU profile. It is here indicated with h, but it is, of course, a Rz on its turn: in order to do not generate confusions, for the present chapter the word Rz refers only to the maximum height of a turned profile.
A real MUFU surface does not obviously have a completely flat bearing area no matter how finely the plateaus are polished. As already observed in Chapter 1, an abrasive process as polishing will generate a surface with height distribution close to Gaussian [5]. This aspect is also confirmed by the height distributions displayed in figure 5.39. Now, the standard deviation of such a distribution is the root mean square height, or in other words, the Rq of the plateaus [5, 37]. Therefore, for obtaining the geometry of a "real" MUFU surface by means of an algorithm, only four parameters are needed as input: R, F, BA and Rq. This is implemented in Matlab and shown in figure 6.3. In real production, instead, only the first two parameters are input of the process (an operator chooses tool nose radius and feed rate beforehand), while the BA is an output which is to some extent controllable by carefully proceeding with iterative polishing operations. The fourth parameter, instead, cannot be decided precisely beforehand. It is an output of the process which can be modified by changing properly the polishing parameters. It is therefore a control parameter, thus field parameter such as Ra can be used for the scope.

6.2 Friction models

This section is a very brief review of friction models with the focus set on the models taken as basis for the present investigation. Modelling

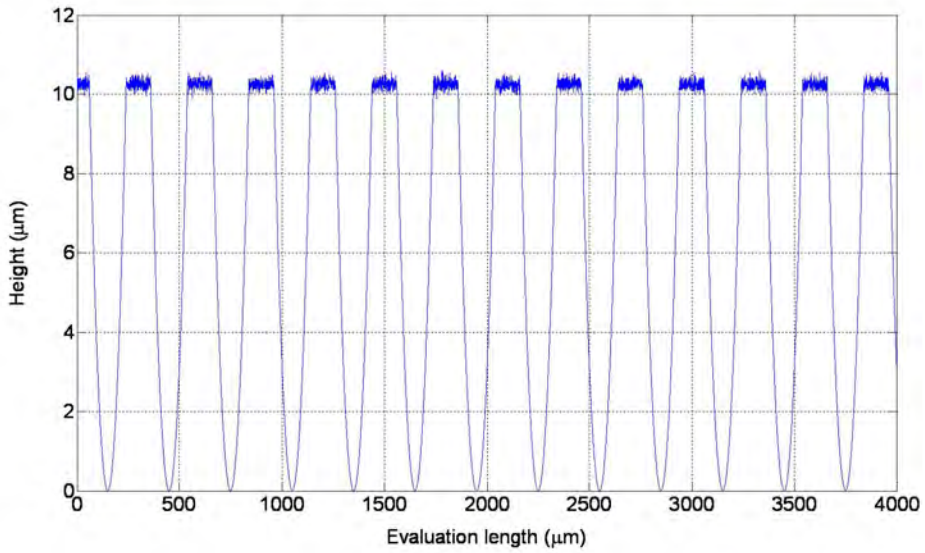

Figure 6.3: *MUFU profile generated using an algorithm. The parameters chosen are R=0.4 mm, F=0.3 mm,BA= 0.4 and Rq=0.1 µm.*

of friction has been subject of scientific research since the 18th century, when Coulomb [165] formulated his well-renown and still broadly accepted and utilized hypotheses upon dry friction occurring on contacting moving bodies. Numerous models or theories trying to extend and generalize Coulomb's studies have been proposed since then taking into account the asperity contact [166–169], the effect of normal pressure [167–170], contaminant films [166, 168, 169] and eventually the presence of trapped lubrication building up a hydrostatic pressure [171].
A simple way to look into friction phenomena is to consider the friction force as composed by two components: adhesion and deformation [37].

$$F_f = F_a + F_d \tag{6.3}$$

The *adhesive* contribution is the force necessary to break the cold welded junctions formed when, under load, the asperities come into contact (left-hand side of figure 6.4). If the two asperities are in oblique contact, after breaking the weld, an additional force is necessary for displacing the newly formed "wall" of the softer material. The *deformation* component describes indeed this ploughing action that the harder material exercises. However, especially in the case of hard contacting metals and remembering that the surface roughness is only a gentle undulation of the surface, the deformation contribution is normally much smaller than the adhesive one [37]. Therefore henceforward when talking about friction force, it will

be implicitly intended the adhesive contribution of friction.

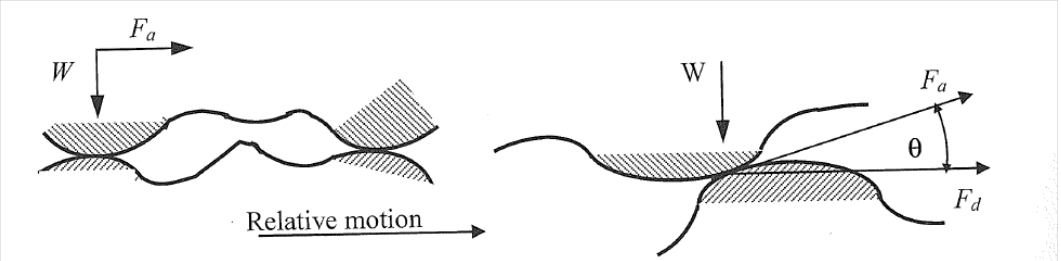

Figure 6.4: *Adhesion and deformation friction components, image taken from [37].*

6.2.1 Adhesive friction models

All models of adhesive friction convene with Coulomb's hypothesis that the friction force is independent on the size of the contact area (nominal contact area), but it depends solely on the load, the normal force applied to the sliding body, and is directly proportional to it (equation 6.4). As the normal load increases, the *real* area of contact increases as well, so that more force is necessary to break the welded bonds.

$$F_a = \mu W \tag{6.4}$$

The loads can be divided by the nominal area of contact and thus be rewritten in terms of pressure.

$$\tau_n = \frac{F_a}{A_N} = \mu \frac{W}{A_N} = \mu q \tag{6.5}$$

Coulomb's law of friction, though, is valid for a limited range of normal pressures: the load and the friction cannot increase together infinitely. In fact, when the normal pressure becomes particularly high, all the asperities tend to flatten and the real area of contact tends to the apparent area. It is then necessary a pressure equal to the very shear stress of the material in order to break the bonds and the friction force cannot overcome it, as the material will start to flow in the inner layers. Modern friction models take this aspect into account [167, 170]. In particular, work at DTU by Wanheim and Bay [168, 169] resulted in the devising of a "general friction model", which, inspired by Bowden and Tabor's adhesive theory [166], is based on the development of slip-line fields for describing the asperity deformation at both high and low normal pressures. The model, expressed in term of friction stresses, is given in equation 6.6 and proves to be well

in agreement with Coulomb's one at low pressures while diverges from it at high pressures. The friction factor f is a coefficient that represents the amount of adhesion at the contact points [171] and can vary between 0 and 1. This factor is influenced by metal combination, type of lubricant, contaminating film, etc. [168].

$$\tau_n = f\frac{A_R}{A_N}k = f\alpha k \tag{6.6}$$

Graphically the Wanheim and Bay's general friction law is represented in figure 6.5. In the calculation of the real area of contact, the hypothesis of *junction growth* suggested by Bowden and Tabor [166] is adopted: at increasing friction conditions, the plastic flow will be higher thus the real area of contact increases. Hence the explanation of the higher contact area ratios for higher friction factors at the same normal pressure (figure 6.5(b)). Moreover, it can be seen that for normal pressures below 1.5 times the yield strength of the material Coulomb's law applies, while when the normal pressures overcome this limit, the friction stresses tends to $f \cdot k$, i.e. the contact area ratio tends to 1. In case of dry friction without contaminating film the passage from the proportionality to the constancy is abrupt; but if a contaminating film is present the passage is smoother and the contact area ratio tends slower to 1.

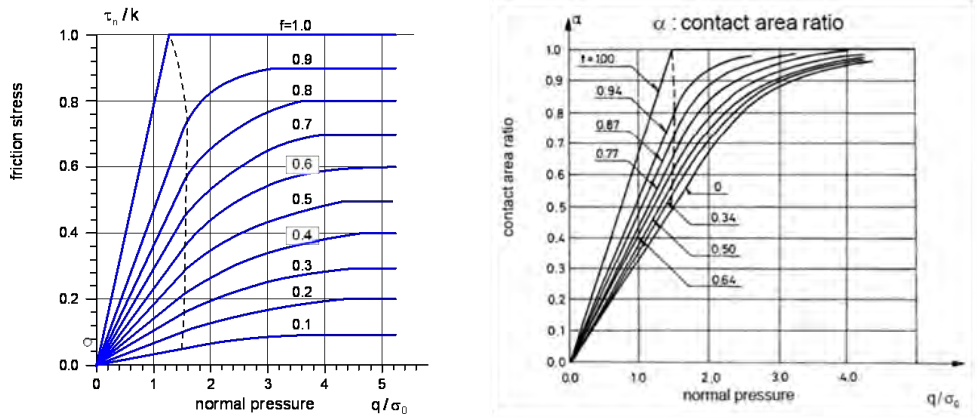

(a) Friction stress vs. normal pressure (b) Contact area ratio vs. normal pressure

Figure 6.5: *Wanheim and Bay's general friction model, adapted from [168, 169].*

The passage from the proportionality to the constancy is called "limit of proportionality". It is possible to find the limit analytically [172]. For the curves shown in figure 6.5(a), the limit is given by equations 6.7 and 6.8.

$$\frac{q'}{\sigma_0} = \frac{1 + \frac{\pi}{2} + \arccos f + \sqrt{1 - f^2}}{\sqrt{3}(1 + \sqrt{1 - f})} \tag{6.7}$$

$$\frac{\tau_n'}{k} = 1 - \sqrt{1 - f} \tag{6.8}$$

From those equations the relation between the friction factor and Coulomb's friction coefficient can be calculated by dividing equations 6.7 and 6.8.

$$\mu = \frac{f}{1 + \frac{\pi}{2} + \arccos f + \sqrt{1 - f^2}} \tag{6.9}$$

Effect of trapped lubrication

It has been explained how the general friction model expand Coulomb's model by taking into account the influence of normal pressure and the possible presence of a contaminant film. The model can be further extended by now considering the effect of trapped lubrication which contributes in a decisive manner in the reduction of friction stresses. In fact, as the tool presses down the asperities, a hydrostatic pressure builds-up inside the valleys, helping the asperities in contrasting the tool advancement. Therefore there would be less real area of contact at equal normal pressure and thus lower friction stresses. Wanheim and Bay, together with Nellemann [171] quantified this phenomenon. In order to understand their procedure, it must be first pointed out that for performing their slip-line analysis Wanheim and Bay [168, 169] considered an infinitely deep workpiece (plain strain condition) having a triangular cross section (triangular profile), see figure 6.6. It can be said that the considered workpiece has the cross section as it was turned with a triangular tool.

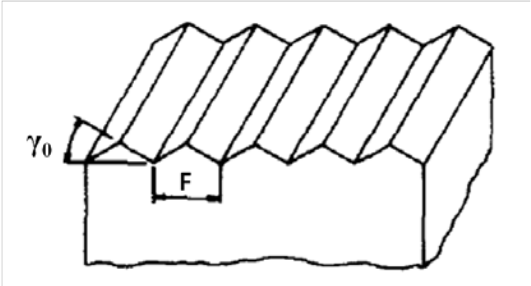

Figure 6.6: *Workpiece topography in Wanheim and Bay's analysis, adapted from [172].*

The initial volume of this pocket is given by the expression:

$$V_0 = Rz_{tri}\frac{F}{2} \tag{6.10}$$

Now, following the calculation procedure given in [171]:

$$V = V_0 - F\delta = F\Big(\frac{Rz_{tri}}{2} - \delta\Big) \tag{6.11}$$

$$\frac{\mathrm{d}V}{\mathrm{d}\delta} = -F \tag{6.12}$$

Introducing the expression for the lubricant bulk modulus:

$$K = -V\frac{\mathrm{d}p}{\mathrm{d}V} \tag{6.13}$$

$$\frac{\mathrm{d}p}{K} = -\frac{\mathrm{d}V}{V} = \frac{2\mathrm{d}\delta}{Rz_{tri} - 2\delta} \tag{6.14}$$

$$\int_0^{p_f}\frac{\mathrm{d}p}{K} = 2\int_0^{\delta}\frac{\mathrm{d}\delta}{Rz_{tri} - 2\delta} = \ln\Big(1 - \frac{2\delta}{Rz_{tri}}\Big) \tag{6.15}$$

According to [171] the lubricant bulk modulus can be divided in two components $K = K_0 + K_1 p$ yielding therefore:

$$\frac{p_f}{K_0} = \frac{1}{K_1}\Big[\Big(1 - 2\frac{\delta}{Rz_{tri}}\Big)^{-K_1} - 1\Big] \tag{6.16}$$

The normal pressure for obtaining the same real area of contact as in the case without trapped lubricant is:

$$q = p_f + q_{dry} \tag{6.17}$$

The contact area in the lubricated case is:

$$\alpha = \frac{\delta}{Rz_{tri}} \cdot \frac{2(2 + C)}{3 + C} \tag{6.18}$$

where:

$$C = \frac{3\tan\gamma - 4 + 2\sqrt{3\tan\gamma + 4}}{4 - \tan\gamma} \tag{6.19}$$

The difference between considering the presence of trapped lubricant or not is evident when looking at the accordingly modified curves (figure 6.7). At

the same normal pressure, say 3.5 times the yield stress, with lubrication the contact area ratio is barely 7.5%, while without lubrication is above 90%.

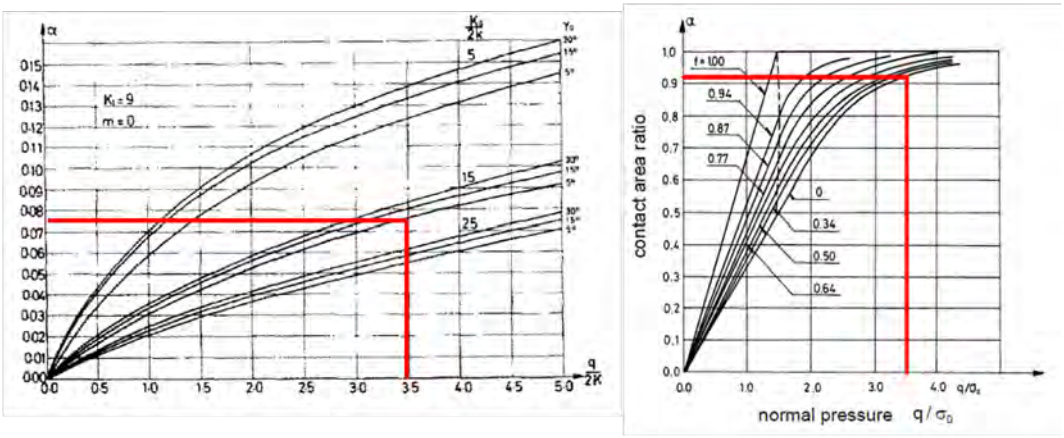

Figure 6.7: *Contact area ratio curves with lubrication (left) and without (right), adapted from [171] and [168].*

In the following this very method is applied directly in the case of a real turned surface (with round tool nose radius) for eventually considering the case of a MUFU surface.

6.3 General friction model applied to turned and MUFU surfaces

6.3.1 Turned surfaces

It has been said how the workpiece structure considered by Wanheim and Bay resembles the texture yielded by a turning operation with a triangular tool nose. The asperity angle in their model is constant and equal to γ. For turning, though, it is usually used a rounded tool nose. The slopes are then ever varying starting from a zero angle at the bottom of the valleys and reaching a γ_{max} at the top of the cusps. The equation for the maximum asperity angle is the following:

$$\gamma_{max} = \arctan \left[\frac{\sqrt{R^2 - \frac{F^2}{4}}}{R^2 - \frac{F^2}{4}} \cdot \frac{F}{2} \right] \tag{6.20}$$

Now, the asperity angle is usually considered small (5° - 10°) [172], but it is not always the case. Higher asperity angles can actually change the slope of

the friction curves and equations 6.7 and 6.8 would not be valid anymore. The case presented in figure 6.5 refers in fact to the case of extremely small asperity angle ($\gamma \approx 0°$), and subsequent studies [169, 172] investigate higher asperity angles ($\gamma = 15°$ and $30°$) tracing the slip-line fields for that cases. The studies observed steeper curves at higher asperity angles, and the offset between the $\gamma = 0°$ and $\gamma = 15°$ cases is particularly relevant for normal pressures close to the yield strength of the material and high friction factors. Unfortunately, the development of the slip-line fields was made before the worldwide spread of computers, so that neither algorithms for their calculation nor databases with recorded values are available. Furthermore, even mastering the technique, the manual development of slip-line fields in an environment with variable slopes would be an extremely challenging task to achieve.
Fortunately in turned surfaces, the asperity angles are in most cases quite small. If the feed is half the radius, for example, γ_{max} = 14.5° with mean asperity angle equal to 7.2°. Therefore, from now on, it is made the fundamental assumption that the presented friction curves are valid for all turned surface and equations 6.7 and 6.8 apply. It must though be kept in mind that for $F > 0.5R$, the error due to this assumption can become relevant and the derived friction curves would be underestimated.
With this assumption, in dry conditions, different turned textures behave alike. This is not true in lubricated conditions, where the hydrostatic pressure increase depends on the texture geometry. The procedure to calculate the hydrostatic pressure increase is similar to what done in section 6.2.1. With reference to figure 6.8, equation 6.21 is modified accordingly.

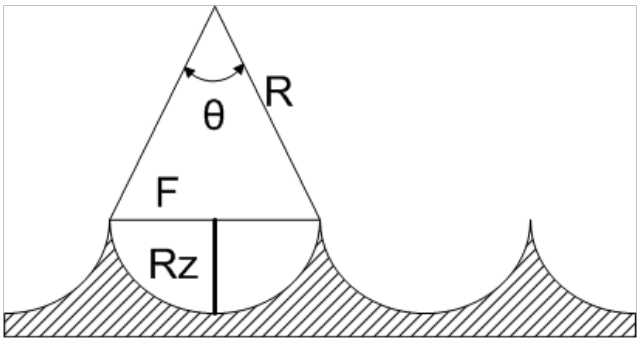

Figure 6.8: *Geometrical model of a turned surface with focus on the central angle.*

$$V_0 = \pi R^2 \cdot \frac{\theta}{2\pi} - \frac{F}{2}(R - Rz) = R^2 \arccos\left[\frac{R - Rz}{R}\right] - \frac{F}{2}(R - Rz) \quad (6.21)$$

The volume calculation proceeds as before. The integral of equation 6.15 becomes:

$$\int_0^{p_f} \frac{\mathrm{d}p}{K} = F \int_0^{\delta} \frac{\mathrm{d}\delta}{R^2 \arccos\left[\frac{R-Rz}{R}\right] - \frac{F}{2}(R-Rz) - F\delta} = \\ = -\ln\left(1 - \frac{2F\delta}{2R^2 \arccos\left[\frac{R-Rz}{R}\right] - F(R-Rz)}\right) \tag{6.22}$$

The solution of this integral is:

$$\frac{p_f}{K_0} = \frac{1}{K_1}\left[\left(1 - \frac{2F\delta}{2R^2 \arccos\left[\frac{R-Rz}{R}\right] - F(R-Rz)}\right)^{-K_1} - 1\right] \tag{6.23}$$

Knowing p_f, the total normal pressure can be calculated from equation 6.17. Equations 6.18 and 6.19 are still valid if another assumption is made: depending on the tool travel δ, the turned profile is "locally" approximated to a triangular one (figure 6.9). The asperity slope to be put into equation 6.19 is then a function of the tool travel: the more the tool is chosen to advance, the lower is the initial slope to be considered.

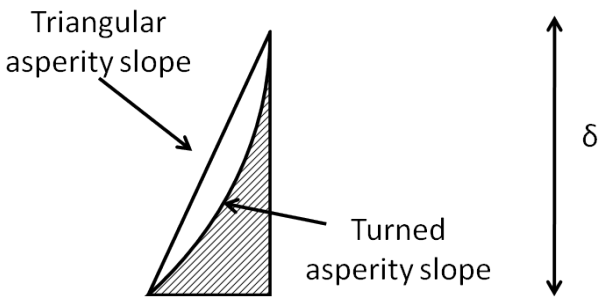

Figure 6.9: *Local triangular approximation of a turned asperity.*

All the information for calculating the friction stresses in turned surfaces under lubricated conditions are now available. The following step is to expand the model to MUFU surfaces.

6.3.2 MUFU surfaces

Ideal MUFU surfaces

The first case under examination is the case of perfectly flat plateaus pressed by a flat tool. This is obviously an unrealistic situation, because

when the plateau roughness becomes particularly small it can be compared to the tool one and the case of rough plateaus treated in the following applies. Imagining however that situation, it is supposed that the tool, as it contacts the plateaus adheres to them giving at once α equal to BA. The hypothesis is that the contact area ratio will not increase together with the normal load until the correspondent curve of figure 6.5(b) is met. No hydrostatic pressure increase will be observed until the tool begins to advance. When that finally happens, the new contact area ratio will be BA plus the one calculated using equation 6.18 substituting Rz with h. The term C will be calculated according to the assumption of section 6.3.1 and thus dependent on δ. The hydrostatic pressure increase is calculated according to equation 6.23 utilizing $F - b$ instead of F and h instead of Rz. Again the total normal pressure will be estimated using equation 6.17.
Since only low normal pressures are considered in this analysis, the likelihood of tool advancement in these conditions is very low. On the other hand, the complete flatness assumption means that even for very low normal pressures $\alpha = BA$ extremely high friction stresses are observed. Bonding at a molecular or atomic level can certainly occur, but in this case it is the premise that is faulty. The plateaus and the tool are not flat, they are of small but same scale roughness, thus they must be treated as rough contacting surfaces. This is the subject of the next two paragraphs.

Rough plateaus: asperities on asperites

One possibility for treating the case of rough plateaus is following the analysis made by Steffensen and Wanheim [173], in a study derived directly from [168]. In [173] it is observed that a roughness profile is composed by higher peaks superimposed by a roughness of a smaller scale (figure 6.10). The smaller scale roughness is of the same nature as the bigger one, a deterministic pattern of triangular asperities. Knowing the smaller scale asperity angle and period (feed), the total area of contact can be calculated taking into account that the smaller scale asperities undergo a normal pressure $q_{pl} = q/BA$ higher than q. The contact area ratio will be $\alpha = BA \cdot \alpha_1$.

Figure 6.10: *Asperities on asperities model, adatped from [173].*

This method has the advantage of being relatively simple. The analysis can be carried out as previously explained (triangular asperities) and the hydrostatic pressure due to fluid retention can be calculated as well. On the other hand, the method has some disadvantages. Practically speaking the knowledge of the small scale γ_1 and feed are not straightforward. While the feed can be somehow found looking at the Rsm of the plateau region, the estimation of γ_1 is less direct. In another work by Bay and Wanheim [174] the period and the Ra value of the surface are linked in an expression (equation 6.25) comprising the asperity angle as well.

$$Ra = \frac{F \cdot \tan \gamma_1}{8} \tag{6.24}$$

The equation can be reversed to find the angle:

$$\gamma_1 = \arctan\left(\frac{8Ra}{F}\right) \tag{6.25}$$

With the estimation of F and γ_1 the calculation can now take place.
However, there are other two main problems connected with this method. First of all, the tool is still considered nominally flat, which is a quite faulty assumption since the plateau and tool roughness are in most cases of the same magnitude. The second problem is that the plateau texture is here considered deterministic, which is untrue as remarked many times during this work. In order to take care of these problems, the case of the contact of two rough surfaces with a Gaussian distribution of heights must be considered, which is the topic of the next section.

Rough plateaus with a random distribution of heights

A quite remarkable and renowned work studying the contact of rough surfaces with random distribution of heights is made by Greenwood et al. back in the 1960s and 1970s [175, 176]. In their studies, laws for determining the real area of contact of two random surfaces loaded against each other in dry conditions are proposed considering in [176] also the cases of different deformation typologies (elastic rather than plastic), asperity shapes and height distributions. An important conclusion given by [176] is that "any model of contact between surfaces, both of which are assumed to be rough, can be simulated by a model in which only one surface is rough". That means that the considered case of rough tool against rough plateau can be substituted by the equivalent case of flat tool against rough(er) plateau. In the equivalent case the rougher plateau will be characterised by a Gaussian height distribution having standard deviation Rq_{eq} equal to:

$$Rq_{eq} = \sqrt{Rq_t^2 + Rq_{wp}^2} \tag{6.26}$$

Following the analysis in [175, 176] and with reference to figure 6.11, if there are N peaks within the nominal area of contact, then the number of penetrated peaks n is:

$$n = N \cdot \int_d^\infty \phi(z_s)\mathrm{d}z_s \tag{6.27}$$

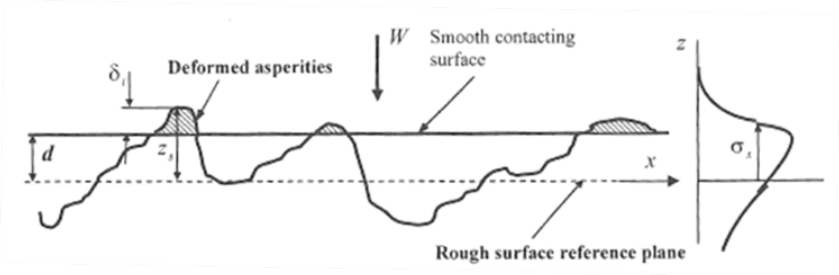

Figure 6.11: *Rough surface penetrated by a rigid smooth surface, from [37].*

Considering the function $m(\cdot)$ defining the area of a singular deformed peak, the real area of contact becomes:

$$A_R = N \cdot \int_d^\infty m(\delta_i) \cdot \phi(z_s)\mathrm{d}z_s \tag{6.28}$$

Similarly, if g is a function describing the load on a singular asperity:

$$W = q_{dry} \cdot A_N = N \cdot \int_d^\infty g(\delta_i) \cdot \phi(z_s)\mathrm{d}z_s \tag{6.29}$$

The analysis proceeds with the definition of $\phi(\cdot)$, $m(\cdot)$ and $g(\cdot)$. Starting from $\phi(\cdot)$, although some authors [37, 175] choose an exponential distribution for easing the integral calculation, the assumption of Gaussian distribution is maintained. It is useful to scale the equations with Rq_{eq} to make them non-dimensional. Therefore, $z_s' = z_s/Rq_{eq}$; $d' = d/Rq_{eq}$ and $\delta_i' = \delta_i/Rq_{eq} = z_s' - d'$. The formula will be:

$$\phi(z_s')^* = \frac{1}{\sqrt{2\pi}} \cdot e^{\frac{-z_s'^2}{2}} \tag{6.30}$$

For the definition of $m(\cdot)$ and $g(\cdot)$ some assumptions must be made. Greenwood and Williamson [175] as well as [37] consider spherical asperities, which is a plausible assumption in case of Robot Assisted Polished surfaces since the pulse module combined with the rotational movement of the spindle provide at once both circumferential and axial cutting directions. In the case of ground surfaces, instead, the grinding wheel operates in only one direction. Ground surfaces are therefore constituted by long ridges and the texture directionality is much more evident than in RAP surfaces (figure 6.12).

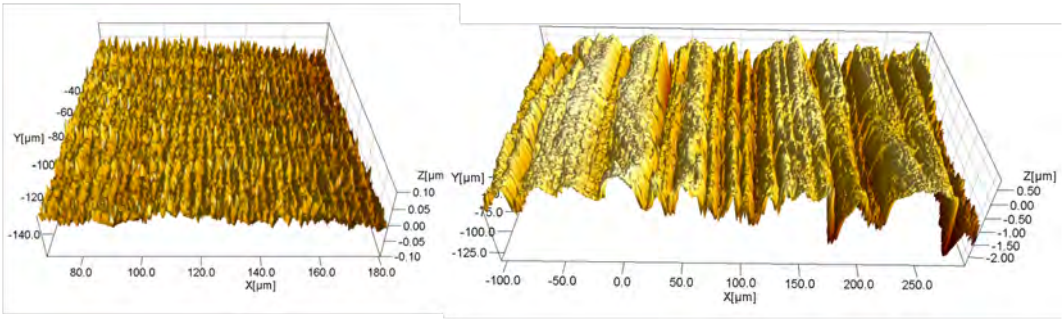

Figure 6.12: *Surface texture of a Polished surface (left) and Ground surface (right).*

The definition of $m(\cdot)$ and $g(\cdot)$ is here provided in both cases: spherical asperities and long cylindrical ridges.
In the case of spherical asperities, the asperity radius is considered the same for all asperities [37, 175]:

$$m(\delta_i) = \pi\beta\delta_i \tag{6.31}$$

$$g(\delta_i) = \frac{4}{3}E^*\beta^{1/2}\delta_i^{3/2} = \frac{4}{3}E^*\beta^{1/2}\delta_i'^{3/2}Rq_{eq}^{3/2} \tag{6.32}$$

where E^* is the equivalent elastic module given by:

$$\frac{1}{E^*} = \frac{1-\nu_1^2}{E_1} + \frac{1-\nu_2^2}{E_2} \tag{6.33}$$

Inserting equations 6.30, 6.31, 6.32 into equations 6.28, 6.29 and taking into account that $\phi(z_s')^*\mathrm{d}z_s' = \phi(z_s)\mathrm{d}z_s$ [176], the equations become:

$$A_R = N \cdot \frac{\pi\beta Rq_{eq}}{\sqrt{2\pi}} \int_{d'}^{\infty} (z_s' - d')e^{\frac{-z_s'^2}{2}}\mathrm{d}z_s' = N\pi\beta Rq_{eq} \cdot S_1(d') \tag{6.34}$$

$$W = N \cdot \frac{1}{\sqrt{2\pi}} \cdot \frac{4}{3} E^* \beta^{1/2} R q_{eq}^{3/2} \int_{d'}^{\infty} (z_s' - d')^{\frac{3}{2}} e^{\frac{-z_s'^2}{2}} \mathrm{d}z_s' = \\ = \frac{4}{3} N E^* \beta^{1/2} R q_{eq}^{3/2} \cdot S_{3/2}(d') \tag{6.35}$$

Where $S_i(\cdot)$ is the integral of the Gaussian distribution as defined by Greenwood and Tripp [176].
The normal pressure on the asperities is given by ratio for equations 6.35 and 6.34:

$$p = \frac{W}{A_R} = \frac{4}{3\pi} R q_{eq}^{1/2} E^* \beta^{-1/2} \cdot \frac{S_{3/2}(d')}{S_1(d')} \tag{6.36}$$

As it can be noticed by equation 6.31, this is a three-dimensional analysis and the area of contact in each asperity is represented by a circular section obtained by pressing a plane over a sphere. The number N is the number of asperity within a nominal surface A_N. However, this work has so far dealt only with profiles. It is useful to translate A_N and A_R in terms of linear areas of contact A_{Nl} and A_{Rl} under the following condition:

$$\alpha = \frac{A_R}{A_N} = \frac{A_{Rl}}{A_{Nl}} \tag{6.37}$$

A_{Nl} can be intended as the evaluation length of the profile in case of polished surface or, alternatively, b in case of MUFU plateau. For calculating A_{Rl} equations 6.31 and 6.34 must be modified accordingly:

$$a_i(\delta_i) = 2\sqrt{\beta \delta_i} \tag{6.38}$$

$$A_{Rl} = N \cdot \frac{2\beta^{1/2} R q_{eq}^{1/2}}{\sqrt{2\pi}} \int_{d'}^{\infty} (z_s' - d')^{1/2} e^{\frac{-z_s'^2}{2}} \mathrm{d}z_s' = 2N\beta^{1/2} R q_{eq}^{1/2} \cdot S_{1/2}(d') \tag{6.39}$$

With the knowledge of the formulas for p, A_{Nl} and A_{Rl}, the calculation of friction stresses with spherical asperities is made possible. This is done in section 6.4, after the case of infinitely long cylindrical ridges is addressed.
The Hertzian (elastic) contact between a flat surface and an infinitely long cylinder is treated by Hamrock et al. [177] already in terms of load and area per unit length. The total area of contact is therefore represented by a segment. Now, the case of many cylinders (the ridges) at different heights is treated. First of all the non-dimensional load on an asperity is defined according to [177]:

$$W_i' = \frac{W_i}{E^* \beta} \tag{6.40}$$

Then, the local area of contact and local tool travel are given by the equations 6.41 and 6.42:

$$a_i = 2\beta \sqrt{\frac{8W_i'}{\pi}} \tag{6.41}$$

$$\delta_i = \frac{2\beta W_i'}{\pi} \left[\ln\left(\frac{2\pi}{W_i'}\right) - 1 \right] \tag{6.42}$$

Because of the natural logarithm, it is not possible to analytically determine the equations for $a_i(\delta_i)$ and $g_l(\delta_i)$. It is therefore necessary to empirically determine them by calculating an array of a_i and δ_i using different load values and then plotting the loads and the areas as a function of the tool travel. The area and load equations can thus be estimated:

$$a_i(\delta_i) = \xi \delta_i^t \tag{6.43}$$

$$g_l(\delta_i) = E^* \beta \left(\kappa \delta_i^2 + \zeta \delta_i \right) \tag{6.44}$$

Inserting them now in equations 6.28 and 6.29 it will result in the final equations of this section:

$$A_{Rl} = \frac{N R q_{eq}^t \xi}{\sqrt{2\pi}} \int_{d'}^{\infty} (z_s' - d')^t e^{\frac{-z_s'^2}{2}} \mathrm{d}z_s' = N R q_{eq}^t \xi \cdot S_t(d') \tag{6.45}$$

$$\begin{aligned} W_l &= \frac{N \kappa E^* \beta R q_{eq}^2}{\sqrt{2\pi}} \int_{d'}^{\infty} (z_s' - d')^2 e^{\frac{-z_s'^2}{2}} \mathrm{d}z_s' + \frac{N \zeta E^* \beta R q_{eq}}{\sqrt{2\pi}} \int_{d'}^{\infty} (z_s' - d') e^{\frac{-z_s'^2}{2}} \mathrm{d}z_s' = \\ &= N E^* \beta R q_{eq} \left(\kappa R q_{eq} \cdot S_2(d') + \zeta \cdot S_1(d') \right) \end{aligned} \tag{6.46}$$

The normal pressure p can be calculated dividing equation 6.46 by equation 6.45, while the contact area ratio is the ratio between equation 6.45 and the profile evaluation length in case of ground surfaces.

6.4 Application of the models

In this section, the models above discussed are applied to the practical case of the Axial Sliding Test. The results obtained using these theoretical models are compared to what shown by the experiments. The models are implemented in Excel, except for the calculation of the integral of the Gaussian distribution which was particularly challenging and required a mathematical software (Maple 16) for carrying out such an operation. Different sheets were realized depending on the approach adopted for describing the plateau roughness, namely "asperities on asperities" or "randomly distributed". The parameters needed are inserted as input and the calculation procedure for determining friction stresses and contact area ratios follows the flowchart of figure 6.13.

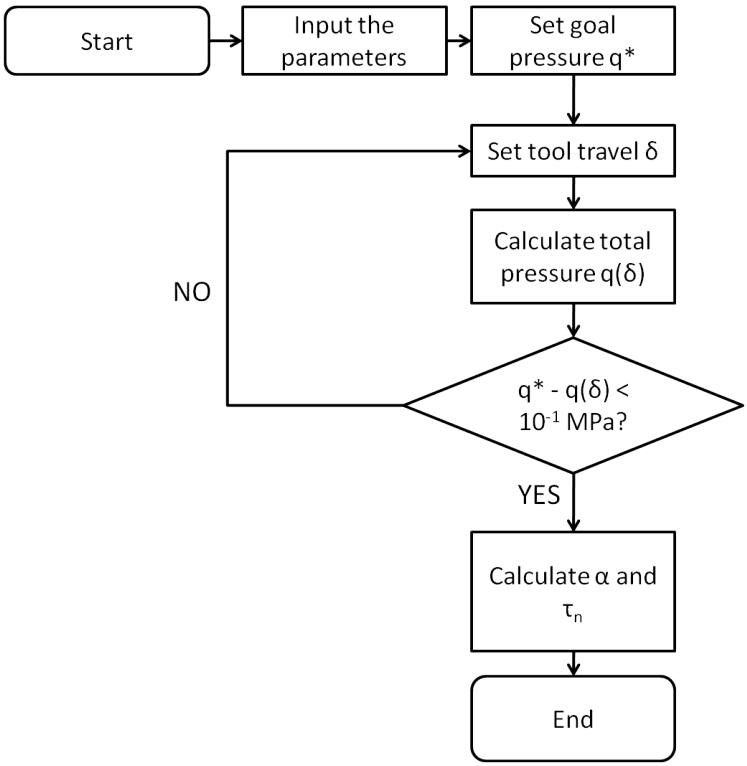

Figure 6.13: *Algorithm for calculating friction stresses and contact area ratios.*

After inputting the values, a goal pressure is set, typically 34 MPa, which is the AST incremental pressure per mm. Afterwards the tool advancement δ is guessed and the corresponding q_{dry} and p_f are determined as well as α. If the calculated total pressure $q(\delta)$ is very close to the goal (less than 0.1 MPa difference), the iterations end and the correct contact area ratio is found. From the knowledge of α, f and k, the friction stresses can be calculated. k

is a material property and therefore is known, while f must be determined calibrating the models with the experimental results. More precisely, one surface (for example the turned one) is taken as a reference and the model is calibrated by selecting a f that pairs well the experimental and simulated friction curves. The same f will be used afterwards for determining the simulated friction curves of the MUFU surfaces.

6.4.1 Asperities on asperities

The first approach adopted is the so-called "asperities on asperities". The turned surface is taken as a reference and the plateau roughness is intended as regularly patterned with a triangular cross section. The ground and polished surface are not taken into account for this analysis. The input values are listed in table 6.1.

Table 6.1: Input values for "asperities on asperities" simulation.

	Fine-Turned	**MUFU20%**	**MUFU40%**	**MUFU55%**
R [µm]	400	400	400	400
F [µm]	100	300	300	300
BA [-]	-	0.2	0.4	0.55
Ra [µm]	-	0.028	0.058	0.046
Rsm [µm]	-	15	15	15
σ_0 [MPa]	2530	2530	2530	2530
K_0 [MPa]	2000	2000	2000	2000
K_1 [-]	9.25	9.25	9.25	9.25

The first three lines pertains to known geometrical parameters of the surfaces. The fourth line, the Ra, is an estimated value combining the roughness of the mirror-polished sleeve and the plateaus roughness. Now, the combination can be done only in terms of Rq as shown in equation 6.26. The Rq values are therefore combined and from those the Ra is estimated using a formula found in [5]:

$$Ra = \sqrt{\frac{2}{\pi}} \cdot Rq \tag{6.47}$$

The Rsm value, or feed of the small asperities cannot unfortunately be calculated by means of SPIP™. It is then measured manually on asperities

and the value of 15 µm is considered a sound estimation.
The shear stress k is derived by the yield stress σ_0 according to the von Mises yield criterion:

$$k = \frac{\sigma_0}{\sqrt{3}} \tag{6.48}$$

The calculation of the bulk modulus parameters, instead, was challenging because the lubricant bulk modulus was not given for the used oil. Therefore, the values used by [171] were taken. They were of course referring to another oil with respect to the ones used in the test, but, as long as these parameters were kept constant, this aspect did not affect the final result. The models are calibrated on the turned surface and the friction factor used for the simulations is $f = 0.64$ corresponding to a friction coefficient of $\mu = 0.152$ without trapped lubrication. The results are plotted in figure 6.14, where the lines represent the experimental values and the dots represent the theoretical values. Since the focus goes on the slope of the curves (which is indeed the friction coefficient) and the turned reference follows a linear increase after 6.8 MPa (figure 4.21), the curves are aligned and only the relative pressure increase from 6.8 MPa is considered. This explains the difference between figures 6.14 and 4.21.

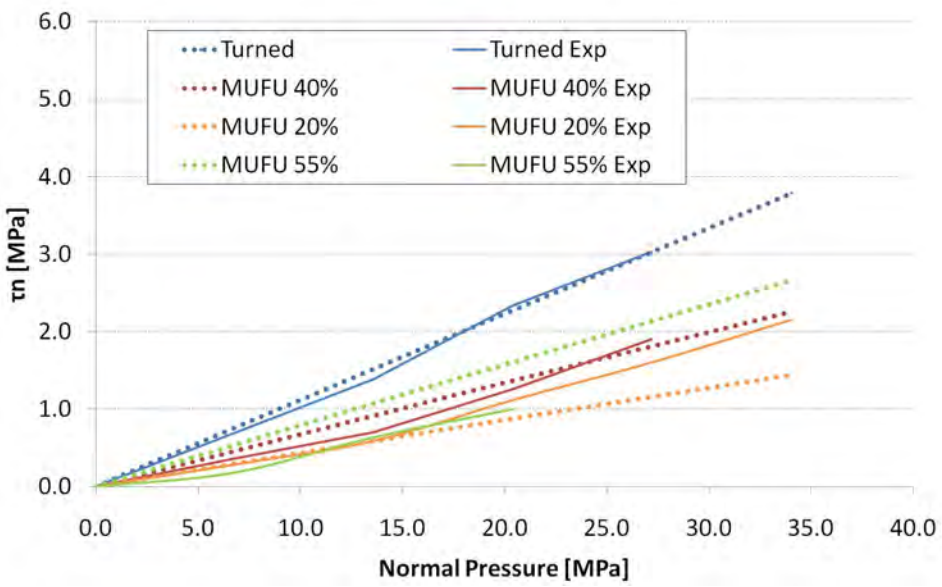

Figure 6.14: *Application of theoretical models with asperities on asperities approach and experimental results of AST test.*

In figure 6.15, instead, the experimental friction coefficients are plotted together with the theoretical friction coefficient. Differently from figure 4.22,

the experimental coefficients are here calculated only in the considered range of normal pressures and using a linear fit. Moreover, the graph of figure 6.15 shows also the hydrostatic pressure built up by the trapped lubricant at 34 MPa.

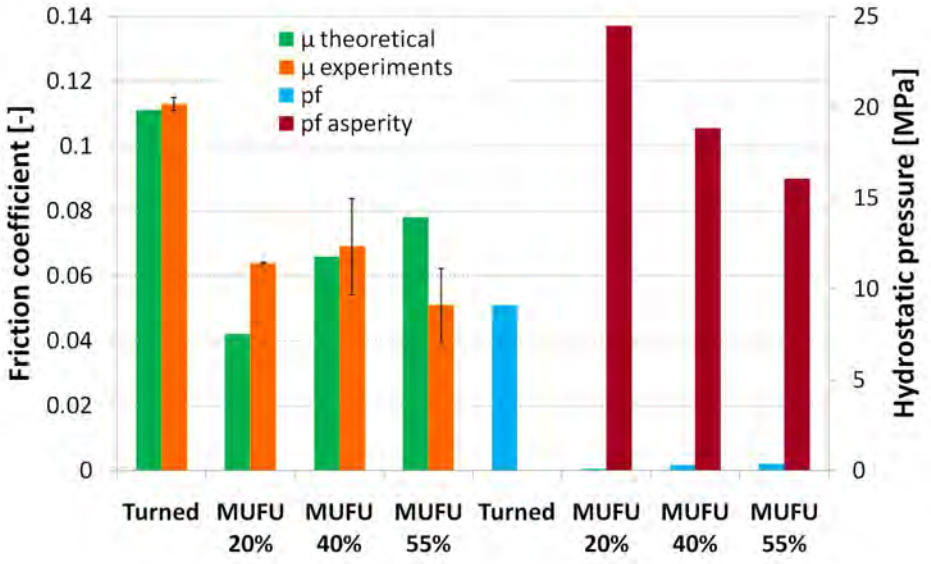

Figure 6.15: *Friction coefficients comparison between models and experiments together with the hydrostatic pressure of the trapped lubricant.*

Discussion

At a first glance the values resulting from the models do not follow what shown in the experiments. While the MUFU40% texture shows good agreement between theoretical and experimental results, the same cannot be said for the other two MUFU textures. The simulated values, in fact, gave a strong underestimation of the MUFU20% friction coefficients and, on the other hand, a overestimation of the MUFU40% coefficient. Moreover it appears that there is a clear trend: higher bearing areas means higher friction coefficients. Nevertheless, the turned surface, which has nominally zero bearing area, displayed the highest friction coefficient, aspect that is in line with what experimentally observed. In order to understand this behaviour, the hydrostatic pressure built up by the trapped lubricant is analysed. From figure 6.15, it can be noticed that the lubricant trapped in the nano-scale roughness of the plateaus has a strong contribution in helping the surface bearing the imposed load and hindering the advancement of the tool. In particular, when a low bearing area is involved, the pressure on the

plateau q_{pl} is higher than the case of high bearing area. The fluid trapped in the nano-roughness will then build-up a higher hydrostatic pressure impeding the tool to advance and thus to form a high real area of contact. Figure 6.15 demonstrates that the highest pressure build-up is formed on MUFU20%. The turned surface, which does not have a plateau and cannot build up localized pressures, does not have that contribution, hence the highest friction stresses and coefficients.
The pressure build-up in the big pockets, instead, was not as relevant as for the small-scale asperities. It was noted, though, that smaller pockets imply higher pressure build-ups. That was the case of the turned surface (the 0.1 mm feed utilized generated small valley features) which had the highest hydrostatic pressure build-up at a texture scale (not nano-scale), and MUFU 55% which had the highest valleys build-up among the MUFU textures.
Concluding, it appears that this approach, while correctly takes into account the hydrostatic pressure build-up, it somehow overestimates its impact at a nano-scale. This and other problems or limitations connected with this approach are discussed in section 6.5.

6.4.2 Randomly distributed plateau heights

Rather than considering the plateau roughness a regular pattern of triangular asperities, more correctly, the second approach consider the asperities as randomly distributed following a spherical or cylindrical shape. The cylindrical shape is applied to the ground surface while the spherical shape is applied to the MUFU plateaus and the polished surface. The ground surface is taken as reference. Many input values are taken from table 6.1, as for example the feed F which represents now the evaluation length for the ground and the polished surface. In table 6.2 are presented the other parameters required for the present analysis.
While the material properties or the Rq_{eq} were quantities easily retrievable, the other parameters presented quite a challenge. The total number of peaks N can be calculated as the inverse of the density of summits, a parameter yielded by SPIP™. The asperity radius was calculated manually on some asperities and the numbers provided in the table represent what is believed a reasonable estimate. The last four parameters related only to the ground surface were calculated as explained above when devising equations 6.43 and 6.44.
After creating a little database containing the several $S_i(\cdot)$, the calculation of the parameters took place. The models were calibrated on the ground surface resulting in an estimated friction factor $f = 0.175$. The low value for the friction factor is the only indicator of the presence of the lubricant, which is not considered trapped and therefore does not superimpose a hydrostatic

Table 6.2: Input values for the simulation with random asperities.

	Ground	**Polished**	**MUFU20%**	**MUFU40%**	**MUFU55%**
E [GPa]	225	225	225	225	225
ν [-]	0.3	0.3	0.3	0.3	0.3
Rq_{eq} [µm]	0.665	0.081	0.036	0.073	0.058
N [-]	45	90	7	16	45
β [µm]	30	35	35	35	25
ξ [(µm)$^{1-t}$]	8.275	-	-	-	-
t [-]	0.532	-	-	-	-
κ [(µm)$^{-2}$]	0.011	-	-	-	-
ζ [(µm)$^{-1}$]	0.004	-	-	-	-

pressure. The results are plotted in figure 6.16.

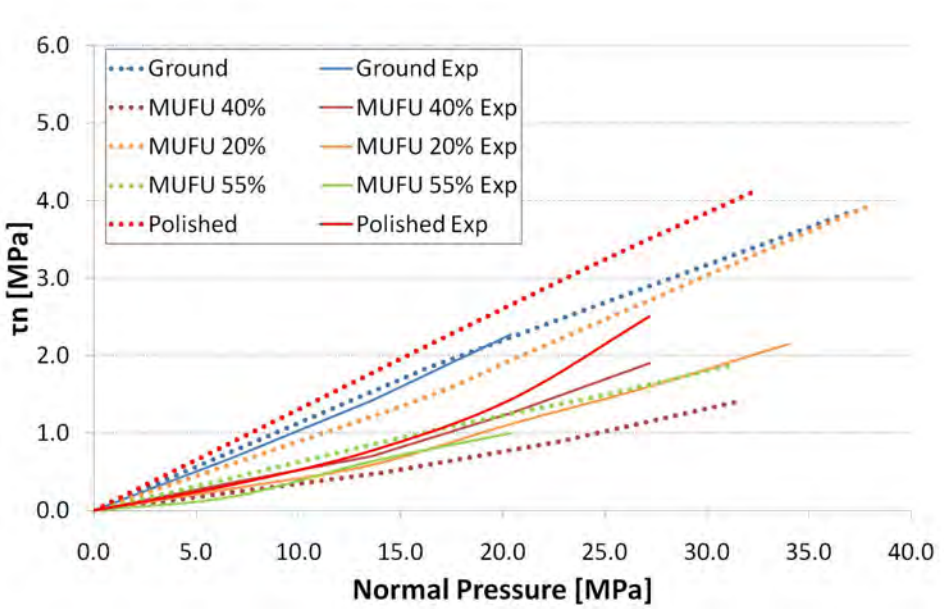

Figure 6.16: *Application of theoretical models with randomly distributed heights and experimental results of AST test.*

As before, the friction coefficients are found fitting a line through each data series. The comparison between theoretical models and experiments is displayed in figure 6.17. The hydrostatic pressure increase displayed

regards only the MUFU surfaces. The pressure of the lubricant trapped in the large valleys is in fact calculated as a function of the tool travel. The point of the first contact becomes important in this calculation. It is assumed that the highest peak with height Rp is located at the plateaus edge. The deformation of the MUFU ridge for calculating the hydrostatic pressure increase follows the one of an ideal MUFU surface with total height $h + Rp$. The bearing area of this ideal surface will be slightly lower than the real one. The case of MUFU40% is taken as an example. At a height h the bearing area is indeed 40%. Now if a Rp = 0.185 µm is considered the ideal MUFU surface for the hydrostatic pressure calculation will have height $h + 0.185$ and an initial bearing area $BA(h + Rp)$ = 39.5 %. The pressure increments are calculated at q = 24 MPa.

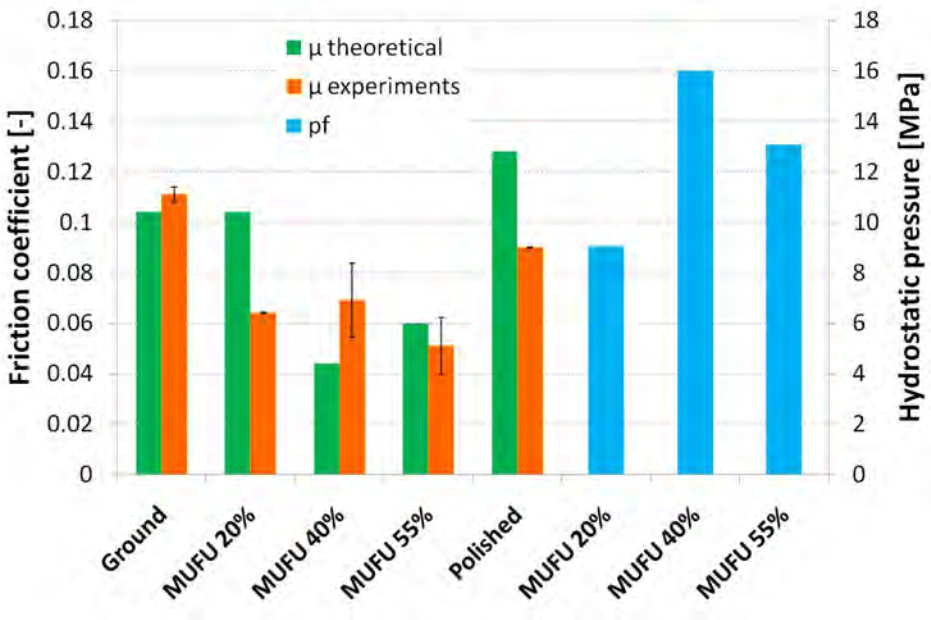

Figure 6.17: *Friction coefficients comparison between models with randomly distributed heights and experiments. The pressure increase in the MUFU pockets is also displayed.*

Discussion

Before going into the details of the results obtained, it must be remarked that the calibration of the model was not straightforward since the contact area was in this case not increasing with a perfect linearity. It is thus explained the small difference between theoretical and experimental value. As for the "asperities on asperities" case, there are discrepancies between theory and experiments, but these seem to go towards another direction. The results of MUFU20% are greatly overestimated while the friction coefficient

of MUFU40% is underestimated. MUFU55% is instead in line with what observed experimentally. The polished rod, despite its overestimation, confirmed to be associated with higher coefficients than the MUFU rods. As said, no lubricant was thought being trapped into the random texture, therefore no superimposed hydrostatic pressure was observed neither for the ground surface, nor for the polished one, nor for the plateaus nano-scale roughness. A pressure increase was however calculated in the MUFU valleys, which played a big role in relieving the asperities from the pressure and therefore to reduce the friction stresses and coefficients. It is observed that the highest pressure increase is associated with MUFU40% although the smallest pockets belong to MUFU55%. The explanation for this behaviour lies on the maximum asperity height Rp, highest in MUFU40%, and the tool travel. With a high Rp the tool was allowed to travel more before encountering other asperities and the hydrostatic pressure was increasing accordingly. The point of the first contact represents a weakness of this method and will be discussed in section 6.5. The large tool travel allowed by the high first point of contact caused the hydrostatic pressure on MUFU40% increase much more than the other cases. MUFU20%, on the other side, beside having larger valleys, had the lowest first point of contact, hence the small pressure increase.

6.5 Models limitations and suggestions for improvements and extensions

It has been shown by the application of the models that both approaches suffer different types of limitations which provided contradictory results. The experimental truth lies in between, sign that some aspects are overlooked and others overestimated in both models. A point of divergence between theory and experiment is the original assumption of the model: the rod is considered soft and the tool hard, so that only the rod can deform. In reality the rod is softer, but its nominal hardness is very similar to the sleeve one. It may be possible that on the workpiece surface are present local hardnesses higher than the sleeve one. The original assumption will in that case fall and it would be the workpiece which indents the tool. This might have actually happened when the observed scratches were created. The other limitations of both models are here treated separately.

Asperities on asperities

This approach has both philosophical and practical weaknesses, but in the end, proved to give the results closest to the experimental observations. The

philosophical flaw in the approach is to consider the plateaus as composed by a deterministic structure of triangular long ridges. This assumption eased significantly the calculation allowing the consideration of the trapped lubricant even at a plateau level. In reality, as illustrated, the plateaus are composed rather by sphere-like asperities through which the lubricant can flow rather than being trapped into long channels. Therefore, the assumption led automatically to the practical problem of overestimating the pressure trapped in the small plateau dips. The finer a plateau was polished, the smaller were their valleys, the higher the hydrostatic pressure increases. Another practical question arises: does the lubricant behave uniformly at all scales? In this model it is supposed so, but this is a rather questionable point that should be investigated further. Anyhow, the lubricant trapped at a nano-scale biases excessively the results and it is the prominent cause of the results obtained. Another point lies with the other assumption of independence from the slope in dry conditions. All turned surfaces behave alike in dry conditions. A solution is to present a new set of friction stresses-normal pressure and area ratio-normal pressure curves at different asperity angle and select the most suitable ones depending on the case.

Plateaus with a random distribution of heights

Philosophically speaking, this approach is more correct than the previous one. The surfaces considered are in fact "real" ones, with the asperities following a certain distribution and having a well-defined shape (spherical or cylindrical). However, it suffers from some major practical limitations. First of all, the parameter definitions. The asperity radius and number are information which are almost impossible to retrieve precisely. While the method adopted for the asperity number gives a rather good estimate, the asperity radius is no more than a guess. Initially the inverse of the parameter Rsc indicating the curvature of the maxima was considered, but this methodology was providing unlikely (too high) values. Therefore the radius was measured manually with some SPIP^{TM} tools, but the radii were spanning from 20 µm and 50 µm. Summarizing, methods for properly determining the input parameters are needed so that more reliable results will therefore be obtained. Another practical issue is that the Gaussian distribution spans from plus to minus infinity. Obviously there are no peaks infinitely high and the rightful distribution is only Gaussian-like with all the values comprised between the highest peak and deepest valley. The integrals, however, provides non-zero values of contact area even for d higher than the highest peak. The initial point issue was acknowledged already by [176] and its solution is debated.
There are a number of other limitations. First of all the method does

not consider the *junction growth*, hence the area of contact is somewhat underestimated, or at least exact only when the tool is simply pressing over the surface and no tangential forces are present. Another problem lies with the trapping of lubricant. No trapping was considered, hence the low friction factor. One way to consider the trapping is by viewing the profile valleys as a unique big pocket. The void volume Vv at the beginning and at the end of the tool travel should be then measured and subtracted. Another, probably more correct way is to assess at each tool advancement which pockets are closed and determine separately the hydrostatic pressures. Practically this is an extremely complicated solution. Spatial information and the knowledge of local volumes are needed making it quite an impervious path to tread. Another problem noted by [176] is that at negative d' the contact may merge since the asperities are not bounded by the neighbouring ones. This however never occurs in the present case.

6.5.1 Extending the models

A possible way to extend the model is to increase the importance of the lubricant in the calculation. Besides the hydrostatic pressure increase, the relative velocity of the rod during its sliding movement can in principle cause the lubricant to build a *hydrodynamic pressure*.

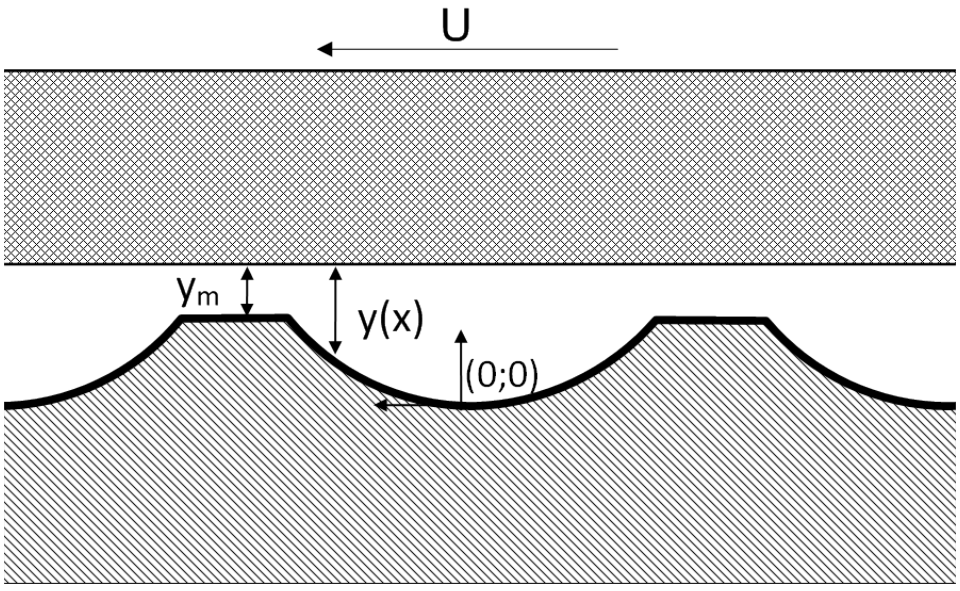

Figure 6.18: *MUFU surface and moving tool. Highlight on the lubricant film thickness.*

With reference to figure 6.18, the valleys slope can be intended as micro-wedges where the Reynolds equation applies:

$$\frac{\mathrm{d}p_f}{\mathrm{d}x} = 6\eta U \frac{(y - y_m)}{y^3} \tag{6.49}$$

The lubricant film thickness can be rewritten as a function of the horizontal distance x from the bottom of the valleys (origin shown in figure 6.18):

$$y(x) = \sqrt{R^2 - x^2} - R + h + y_m \tag{6.50}$$

with $0 \leq x \leq \frac{F-b}{2}$. The calculation of y_m when the tool approaches the plateaus is not straightforward due to the rough nature of the plateaus themselves. One option is to proceed as Bech, Bay et al. [62–64] did in their already mentioned experiments. In their studies the upper die was smooth and theoretically flat, while the strip presented triangular pockets separated each other. Between the pockets, the strip was characterised by rough plateau regions: the profile looks very similar to the one in figure 6.18, with triangular shapes of the valleys instead of circular. They use the Reynolds equation too, which applies to any pocket shape: y_m is defined as the Ra of the plateaus, or alternatively the combined plateau-tool Ra. After determining the minimum film thickness, the increase in fluid pressure can be quantified through equation 6.49. If the fluid pressure overtakes the normal pressure applied on the top of the MUFU asperity, then the lubricant escapes from the valleys backwards with respect to the workpiece relative movement [62–64]. The escaping of lubricant forms an additional film between tool and workpiece. This occurrence is however not likely to happen during the axial sliding tests due to the low rod speed.

6.6 Summary and conclusions

In this chapter theoretical models trying to explain the functionality of MUFU surfaces have been presented. Initially, models describing the geometry of turned as well as MUFU surfaces as a function of tool nose radius, feed rate and plateau bearing area were shown. These geometrical models were used in the following when devising and applying the functionality models. These were in practice adhesive friction models thought for simulating the AST experimental results and clarifying them. A literature review was performed taking up the case of a flat hard tool pressing over a textured soft workpiece. The contact area of the deformed workpiece asperities increases together with the normal pressure, but its quantification depends on the approach chosen. Two main approaches for assessing the contact area were presented. The difference between them depends on how the workpiece texture is assumed. In the first approach, a deterministic texture is assumed at all times, thus both at a micro-

and nano-level. This assumption eased greatly the area calculation and allowed the consideration of trapped lubricant superimposing a hydrostatic pressure. Unfortunately, having a deterministic texture at nano-scale does not reflect reality and the hydrostatic pressure building up at a plateau level was having a great impact in the calculation. Therefore, the results obtained by the application of the theoretical models were biased by that occurrence. While the friction coefficient of MUFU40% was in agreement to what observed experimentally, the coefficients of MUFU20% and MUFU55% were respectively underestimated and overestimated. The second approach was instead rightly considering the plateaus roughness to be random, following a Gaussian height distribution. This introduced substantial difficulties in the application of the models and the impossibility of considering the trapping of lubricant (in the MUFU surfaces the trapping of lubricant was considered at a micro-level, still deterministic, but not at a nano-level). Other problems or limitations biasing on their turn the results were discussed. The main limitation involved the first point of contact. The MUFU surfaces had in fact lubricant trapping at a "big" valley level, and, with a high plateau peak, the tool was allowed to travel more before finding other oppositions. This implied higher hydrostatic pressure build-ups when a plateau was rougher. For this reason MUFU20% rod was underestimated and MUFU40% overestimated. Concluding, the proposed models, devised entirely from literature studies and geometrical considerations, present different kinds of limitations yielding contrasting results. The experimental truth lay in between. The limitations were however acknowledged and discussed. Moreover an extension of the model based on the hydrodynamic pressure increase was also proposed.

Chapter 7

Towards numerical modelling

As it can be already intended from the title, this chapter casts a look at the future. In this chapter the work done in the last period of the project is collected and pertains the initial development of numerical models for simulating the functional behaviour of MUFU surfaces in metal forming applications. The models presented in Chapter 6 consider in fact just the case of a flat hard tool pressing upon a softer, textured workpiece. This is however not the case of MUFU surfaces for metal forming applications, where the texturing process involves the tool side. It is the opposite situation: a textured hard surface in tribological contact with a flat soft workpiece. The tool asperities are not supposed to deform, rather it is thought that the workpiece, while plastically deforming because of the manufacturing process, will tend to flow inside the tool cavities. This will result in a pressing action that increases the pressure of the lubricant stored in the valleys and eventually causes its escape. The outward flow will feed the contact with fresh lubricant creating therefore an extra-layer separating tool and workpiece. The study of this phenomenon is however impossible to be done analytically: the material behaviour of the workpiece (plastic flow) and the lubricant behaviour must be taken into account concurrently while the whole situation varies over time. Only through numerical modelling calculations and assessments can be made possible. Numerical models studying rough surfaces in mixed lubrication conditions do exist. In [33] patterns of defined geometric features constitute the surface texture and their impact on the film thickness is analysed in rolling/sliding contacts. A novel study by [178] introduced real, measured rough surfaces into a numerical code for studying their impact on the friction of two sliding and lubricated bodies. Though extremely advanced, these models are not apt for the present case. They are in fact aimed to machine elements and solid deformation is not taken into account. Here, a coupled fluid-structure model is needed: the workpiece must deform according to the process it is

undergoing and at the same time the fluid escape from the MUFU valley must be assessed. The introduction of a fully-coupled model for MUFU surfaces is the topic of this chapter. An existing model was adopted and adapted in order to conform with the case in exam. Preliminary numerical computations were carried out simulating the Strip Reduction Test and Bending Under Tension test. The preliminary results are discussed stressing particularly on current limitations. Proposal for future improvements are furthermore addressed.

7.1 Fully-coupled fluid-structure models

A finite element (FE) model for metal forming operations coupling the workpiece deformation and the hystrostatic pressure increase of a lubricant trapped in one of the workpiece cavities was proposed by [179]. It is a 2 dimensional model under the plain strain assumption composed by four parts (figure 7.1(a)): an oil cavity, a rigid tool, an elasto-plastic workpiece and oil leakage via the interface between the tool and workpiece [179]. The tool moves at a constant downward speed pressing over the workpiece that is allowed to deform and to flow on the sides. The workpiece material work-hardens as it deforms. The oil builds-up a hydrostatic pressure that is supposed constant inside the pocket. The pressure value is stored as information in a reference node shown in figure 7.1(b). The oil leakage calculated by [179] is directly proportional to this hydrostatic pressure and a set reference pressure. No hydrodynamic contributions are taken into account in this model due to the extremely low speed of the process [179].
This very approach is taken up some years later by [180, 181] and applied to the case of mixed-lubrication in cold rolling operations. In [180, 181] a fully-coupled FE model was developed for the cold rolling process with the ultimate goal of predicting the workpiece texture after the forming operation. The initial texture workpiece is determined by a shot blasting [181] operation providing lubricant pockets for oil retention. Although the texture resulting from the shot blasting is not regularly patterned, in the model by [180, 181] it is considered so. The pockets have a trapezoidal section with well-defined slopes and heights (figure 7.2). The plain strain assumption is maintained. Material properties such as strain-hardening and fluid properties such as lubricant piezo-viscosity act concurrently during the simulated operation determining the final volume and height of the pocket.
A part of fundamental importance in that model is the handling of the lubricant escape from the pockets. According to [180, 181] the lubricant is supposed to flow from a cavity to another, see figure 7.3. Each i^{th} cavity experiences therefore a fluid escape and supply.

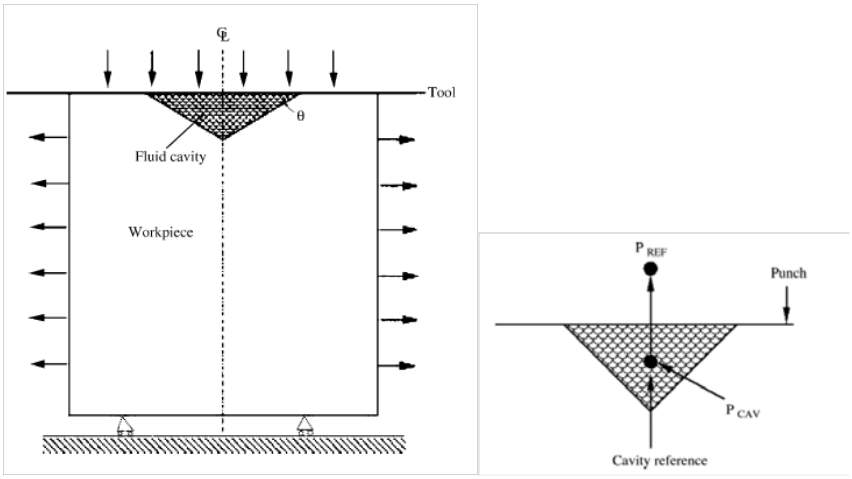

(a) FE model components.

(b) Schematic of a hydrostatic fluid element.

Figure 7.1: *Schematic of the coupled FE model introduced by [179].*

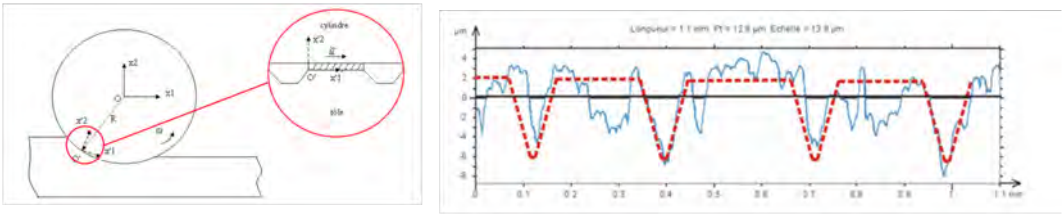

Figure 7.2: *Schematic of cold rolling process and workpiece texture [180].*

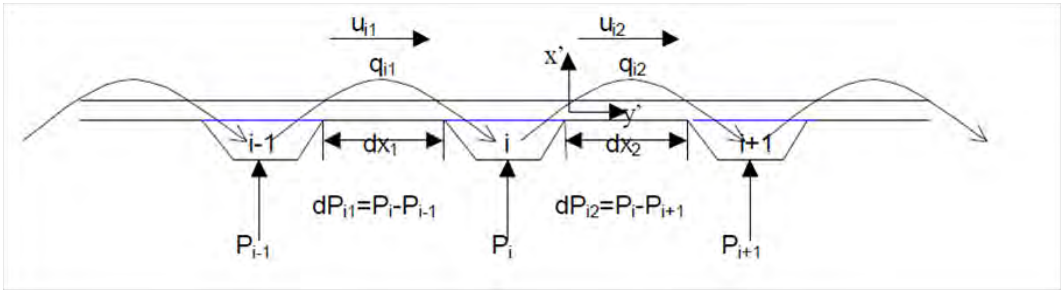

Figure 7.3: *Fluid exchange between lubricant pockets [180].*

In order to quantify the fluid flow, [181] solved the 2D Navier-Stokes equations using the Reynolds approximation and the flow rate conservation [180, 181] arriving to the following system of equations:

$$\begin{cases} q_{i1} = -\dfrac{h^3}{12\eta}\dfrac{\mathrm{d}P_{i1}}{\mathrm{d}x_{i1}} + \dfrac{(u_r - u_{i1})h}{2} \\ q_{i2} = -\dfrac{h^3}{12\eta}\dfrac{\mathrm{d}P_{i2}}{\mathrm{d}x_{i2}} - \dfrac{(u_r - u_{i2})h}{2} \\ q_i = q_{i1} + q_{i2} \end{cases} \tag{7.1}$$

where q_i, q_{i1} and q_{i2} are respectively the total flow rate of the i^{th} cavity and the singular flow rates from the neighbouring cavities; h is the lubricant film thickness; η is the oil viscosity; $\mathrm{d}P$ is the fluid pressure gradient between a cavity and the neighbouring one; $\mathrm{d}x$ is the plateau length; u_r is the roller tangential speed and u_{ij} is the velocity of the j^{th} plateau.
Later, this model was adopted by Hubert et al. [182, 183] and targeted to another application: strip drawing of a textured workpiece through converging dies. The numerical model (figure 7.4) was validated by using the same experimental set-up as [61–64] (figure 7.5).

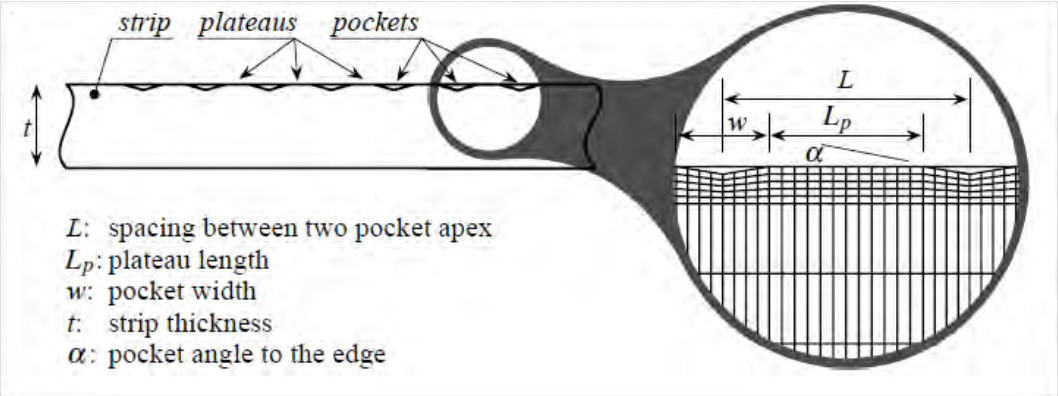

Figure 7.4: *FE model configuration for strip drawing through converging dies [182].*

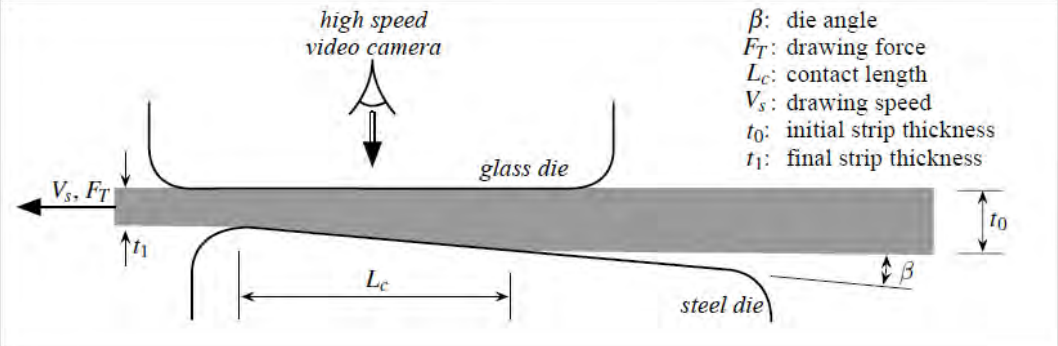

Figure 7.5: *Experimental device used by [182].*

The model required a little adjustment from the previous case. There is no roller speed as the dies are stationary. With reference to figure 7.6, the system of equations 7.2 becomes:

$$\begin{cases} q_{i1} = -\dfrac{h^3}{12\eta}\dfrac{\mathrm{d}P_{i1}}{\mathrm{d}x_{i1}} + \dfrac{u_1 h}{2} \\ q_{i2} = -\dfrac{h^3}{12\eta}\dfrac{\mathrm{d}P_{i2}}{\mathrm{d}x_{i2}} - \dfrac{u_2 h}{2} \\ q_i = q_{i1} + q_{i2} \\ V_i^* = q_i \Delta t \end{cases} \tag{7.2}$$

where u_1 and u_2 are the tool-plateau relative velocities, V_i^* the volume of escaped/entered lubricant in the i^{th} cavity during a time increment Δt.

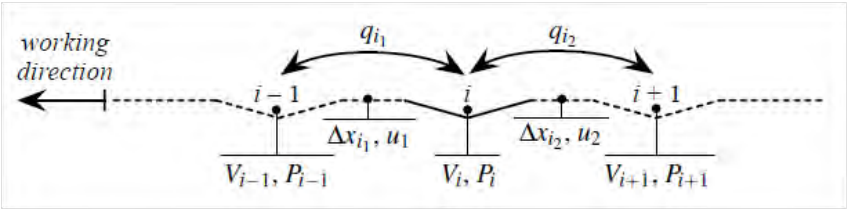

Figure 7.6: *Lubricant exchange case considered by [182].*

7.2 Implementation of the fully-coupled model for MUFU surfaces

The numerical models discussed in the previous section consider, as all the models presented so far, the workpiece to be the textured part. This is, of course, not the desired situation. Nevertheless, the model by [182, 183] was adopted and adjusted in order to suit with the case of a hard and textured tool. The adjustments did not regard the general philosophy of the model, rather they pertained geometrical considerations, material definitions and meshing strategy. Every single piece of the model including parts geometries, material and fluid properties, fluid flows and steps definitions was coded using a programming language named Python. The Python code is read by the commercial FE software Abaqus/CAE which performs the fluid flow computations.

7.2.1 New geometrical model

The models want to simulate the SRT and BUT processes, so that the model from flat parts must be modified considering a round tool. As a consequence, the equations of section 6.1 have to be changed taking into account the tool roundness. The formulas for calculating the geometries refer to figure 7.7.

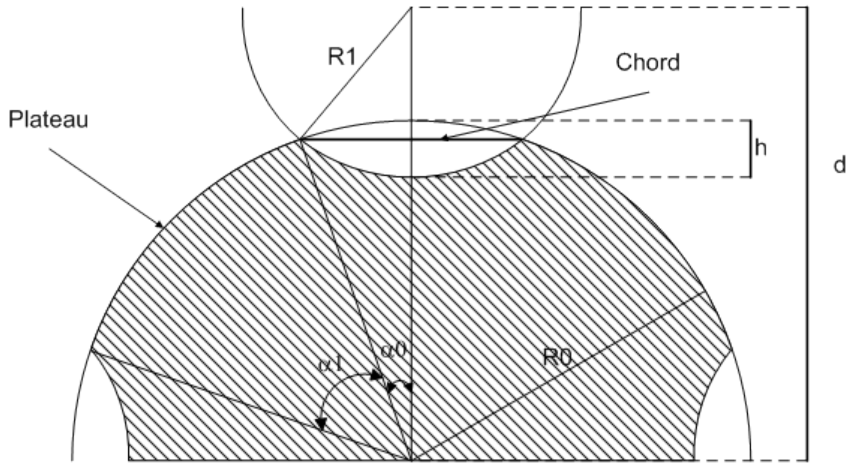

Figure 7.7: *Geometry of a MUFU round tool.*

The MUFU surface height is not anymore calculated as a function of F, BA and R (which becomes now $R1$), but also as a function of the tool radius $R0$. Keeping the definition of the bearing segment $b = BA \cdot F$ the angles α_1 and α_0 useful in the script for building the model are defined by the equations:

$$\alpha_1 = \frac{b}{R0} \tag{7.3}$$

$$\alpha_0 = \frac{1}{2}\left(\frac{F}{R0} - \alpha_1\right) \tag{7.4}$$

From the knowledge of those angles the cavity height h according to figure 7.7 is given by the expression:

$$h = R0 \cdot (1 - \cos\alpha_0) + R1 - \sqrt{R1^2 - (R0\sin\alpha_0)^2} \tag{7.5}$$

After knowing the radii, the angles and the cavity height, only two pieces of information more are necessary to build the model: the number of elements per plateau (Nel_{pl}) and per valley (Nel_v). From these the elements dimensions Lel_{pl} and Lel_v can be extrapolated (equations 7.6 and 7.7)and the model built.

$$Lel_{pl} = \frac{b}{Nel_{pl}} \tag{7.6}$$

$$Lel_{v} = \frac{2\alpha_0 R0}{Nel_{v}} \tag{7.7}$$

An Abaqus plug-in was developed, which, by inserting the input values, will create the assembly. The model, 2-dimensional and under the plain strain assumption, is built node by node, which are placed in a fashion to form quadrangular elements.The following step is to mesh the model.

7.2.2 Meshing the model

There are several meshing strategies that can be chosen for the model. One option is to mesh the model as done by Hubert et al. [182, 183]. Their strategy can be seen in figure 7.4: they chose rectangular elements with constant length but varying height. In the proximity of the cavities the height is small, so that the elements have nearly square shapes; in the inner layers of the workpiece the height is higher and the elements are purely rectangular. In the present case this choice does not seem to be the most appropriate. Hubert et al. focus entirely on the textured workpiece and the flat tool could be treated as a rigid body which did not require any mesh. Here, the model was basically reversed and the textured workpiece became the textured tool. On the other hand, the rigid tool could not become a rigid workpiece: the workpiece should be able to deform during the forming process! Therefore, both tool and workpiece are meshed, and, since the attention goes particularly on the cavities zone, the mesh should be denser (finer) in that area and coarser far from the cavities. Choosing rectangular elements would result in an unnecessarily dense mesh along the horizontal direction throughout the entire part area for both tool and workpiece. In turn this would automatically lead to longer calculation times and computational requirements. A new meshing strategy was therefore chosen, sketched in figure 7.8. After a transition zone with trapezoidal elements, the inner layers will have element sizes thrice the outer layers. There can be a sequence of inner zones, each of them will enlarge the element size by three times.
In figure 7.9, the application of the new meshing strategy on a SRT model is displayed. For this case, a total of two zones (inner and outer) are chosen for the tool and three zones (outer, central and inner) are selected for the workpiece. It can be noted that for having a suitable amount of strip elements per tool cavity, an extremely fine mesh on the outer zone is required. Having a rectangular mesh would result in an unacceptable

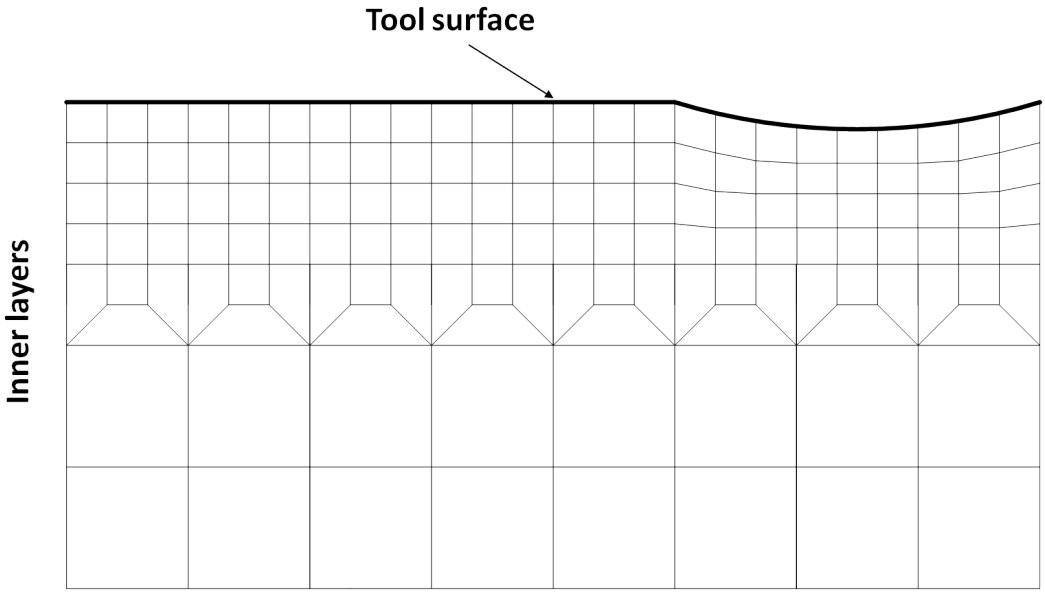

Figure 7.8: *New meshing strategy.*

number of elements (especially on the strip side) with consequent long times spent in model building and simulation running.

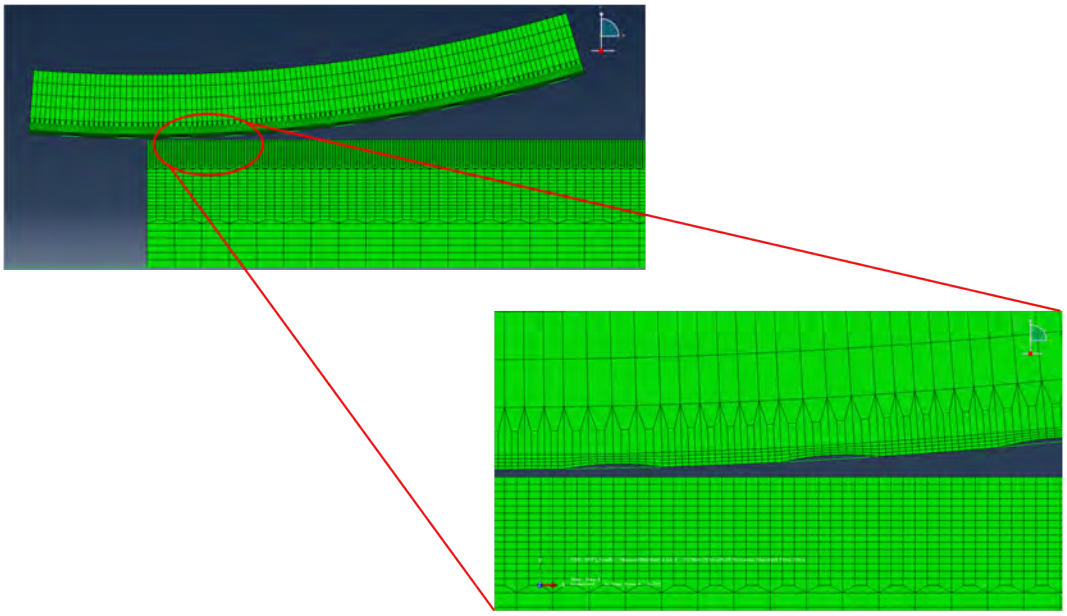

Figure 7.9: *New meshing strategy.*

Figure 7.9 introduces a topic of fundamental importance for the computation: the definition of the fluid elements. In the figure in fact green segments

appear to close the lubricant pockets. It is actually the case: the pockets are sealed. The fluid elements considered in the model require to be contained in a closed environment, thus the model present from the very beginning filled pockets. The pockets are closed by a fictional segment (truss element) having negligible material properties. It will be seen later that this artifice, though necessary, will constitute the biggest limitation of the actual model for the sought applications.

7.2.3 Defining the materials

The meshing is followed by the materials definitions. The tools were considered purely elastic with modulus of elasticity equal to 225 GPa [158]. The strips were instead considered of elastic-plastic materials subject to strain-hardening, whose stress-strain curves (figure 7.10) were found by means of material tests carried out at the department. The strip materials correspond to the ones tested during the experimental campaign (the EN 1.4404 considered for the SRT simulation is very similar to EN 1.4401, being the former a low carbon version of the latter).

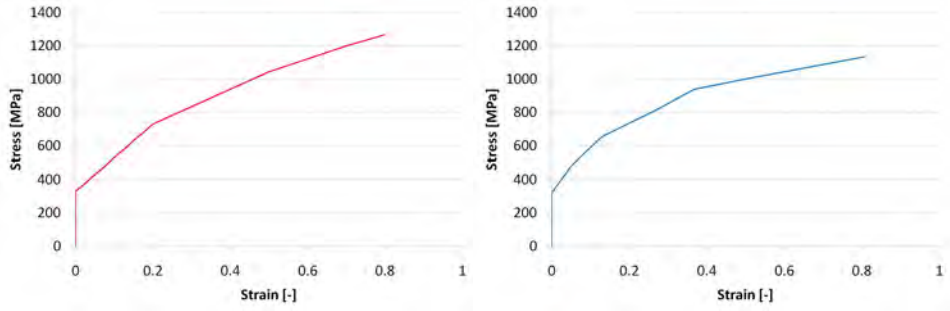

(a) SRT material: EN 1.4404. (b) BUT material: EN 1.4307.

Figure 7.10: *Strip material models.*

The fluid properties were also assigned. The fluid under consideration has, as said, a kinematic viscosity of 160 cSt, which, combined with a fluid density of 1028 kg/m^3, gives a dynamic viscosity of 0.164 Pa·s. Moreover, the *piezoviscous* property of the lubricant was added. The lubricant viscosity changes in fact with the pressure. Here the Barus law [184] was applied for considering this aspect:

$$\eta = \eta_0 \exp(\alpha p) \tag{7.8}$$

where η_0 is the viscosity at environmental pressure, p is the pressure and α is a constant. The determination of α can be quite challenging but, for the preliminary investigations discussed in section 7.3 a value of 20·10^{-9} Pa^{-1}

was chosen.
The last operation to be performed is to define the analysis step. An analysis step comprises the loading and boundary conditions of the model and governs the interaction among the several components according to the definitions previously given. Since each analysis step differs based on the model of interest, their discussion is provided on the following section when discussing separately each application.

7.3 Applications and practical problems of numerical models when analysing MUFU surfaces

In this section, the models are applied namely to the SRT and BUT cases. These calculations represent the first attempt in the investigation of the functional behaviour of MUFU surfaces for metal forming applications through numerical simulations. The results obtained with the simulations must therefore not be intended as definitive, but they should be looked at as the first steps of a long and probably tortuous path towards a comprehensive and reliable modelling of the lubricant escape in presence of MUFU surfaces and hence their functionality. The work initiated here could in fact constitute the starting point of a future project focused particularly on numerical modelling of fluid behaviour upon employment of functional surfaces. The ultimate goal would be the prediction of a texture that would cause the highest fluid escape, thus providing more lubricant in the contact and as a result lower friction forces and less likelihood of wear occurrence. In that direction the first steps are here trodden.

7.3.1 Strip Reduction Test simulation

The SRT simulation consists of two main operations. In the first operation the SRT tool is loaded against the strip following a set downward movement until a targeted reduction is achieved. This is done in an unique analysis step, the result of which is shown in figure 7.11.
The second operation consists in pulling the strip along the horizontal direction at a constant speed of 80 mm/s. This is done in many small steps (increments) with a very short simulation time to ensure the stability of the procedure. At the end of each increment the lubricant flows are computed according to system 7.2. Once this operation is completed, the procedure restarts until the global simulation time is reached. For these preliminary investigations the number of increments is set to 5000 which, considering a

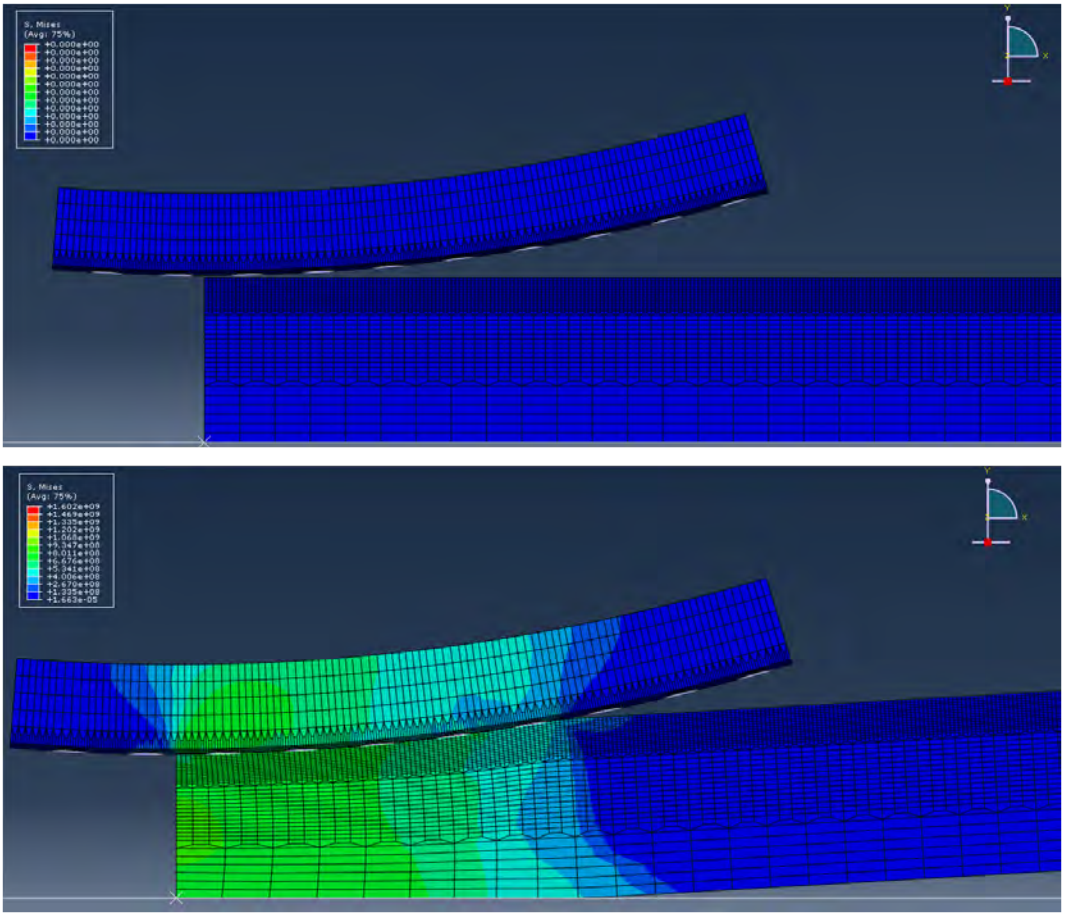

Figure 7.11: *Loading operation in SRT simulation. The von Mises stresses are displayed.*

time increment of 10^{-5}s each step, corresponds to 4 mm pulling of the strip. This, of course, is a much lower value than the original process, but because of the long simulation time and the high memory requirements longer simulations were not practicable. The simulation of the SRT of figure 7.11 is now displayed at 2500 and 5000 increments, see figure 7.12.

Five SRT simulations are run, each representing one of the MUFU tools tested in reality. Given the high differences in bearing area of SRT4, this tool is analysed twice, one with low bearing area and one with high. The tools and strip dimensions reproduces the real test ones: tool radius 8.35 mm and strip thickness 0.7 mm. What changes, instead, are the input parameters characterising the tool texture. The parameters are collected in table 7.1, remarking that h, the lubricant film thickness between the workpiece and the plateau, is calculated following the assumption given by [64] and estimated being the combined plateau-tool Ra.

The fluid flows of the simulation shown in figure 7.12 are plotted in the

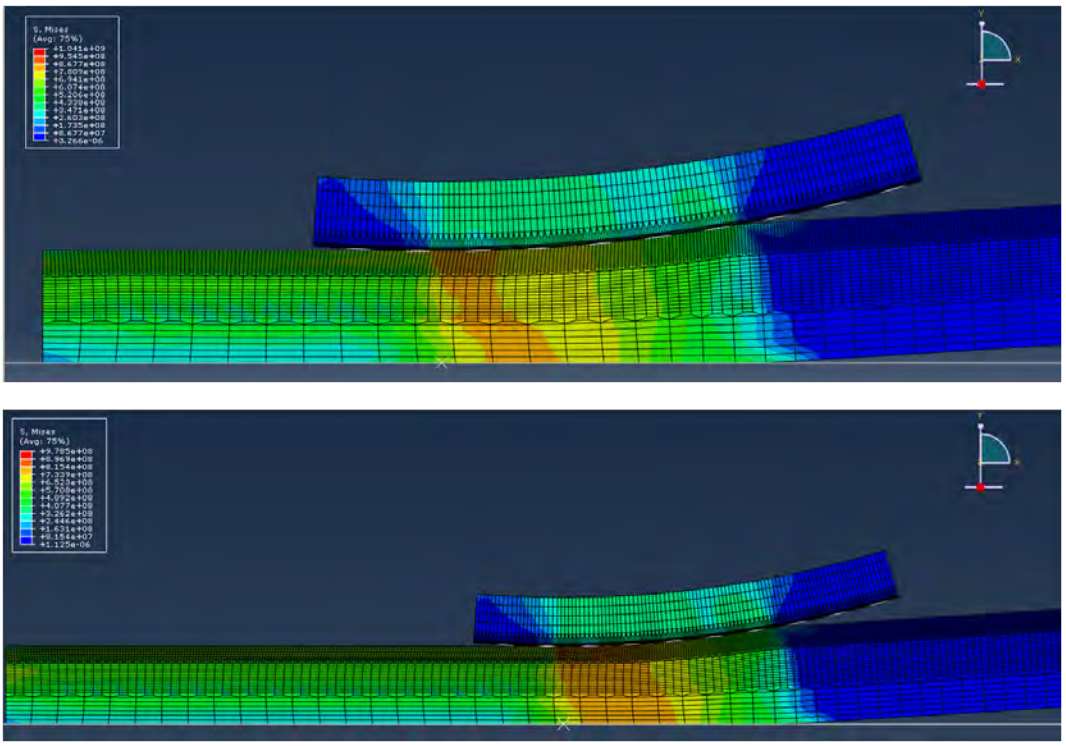

Figure 7.12: *Simulation of a SRT test. Increment number 2500 (above) and 5000 (below).*

Table 7.1: Input values for the SRT numerical simulations.

	SRT1	**SRT2**	**SRT3**	**SRT4low**	**SRT4high**
R1 [mm]	0.4	0.4	0.4	0.8	0.8
F [mm]	0.2	0.3	0.3	0.2	0.2
BA [%]	45	50	55	30	60
h [µm]	0.08	0.08	0.08	0.08	0.08

graph of figure 7.13. This graph regards tool SRT3 and the flows considered pertain to the cavities inside the contact. The time scale starts from 1 s since the first second was dedicated to the loading operation and no fluid exchange is calculated there. As it can be seen, the first cavity inside the contact undergoes an extremely high lubricant flow. The reason is that the algorithm has been slightly modified allowing the entrance of lubricant as the strip enters the contact. This decision was made for reflecting more the real process, where the lubricant is smeared on the strip and enters gradually the contact zone. Furthermore, a fluid exit was associated to the

last pocket into contact presuming that a low film thickness was retained onto the exiting strip.

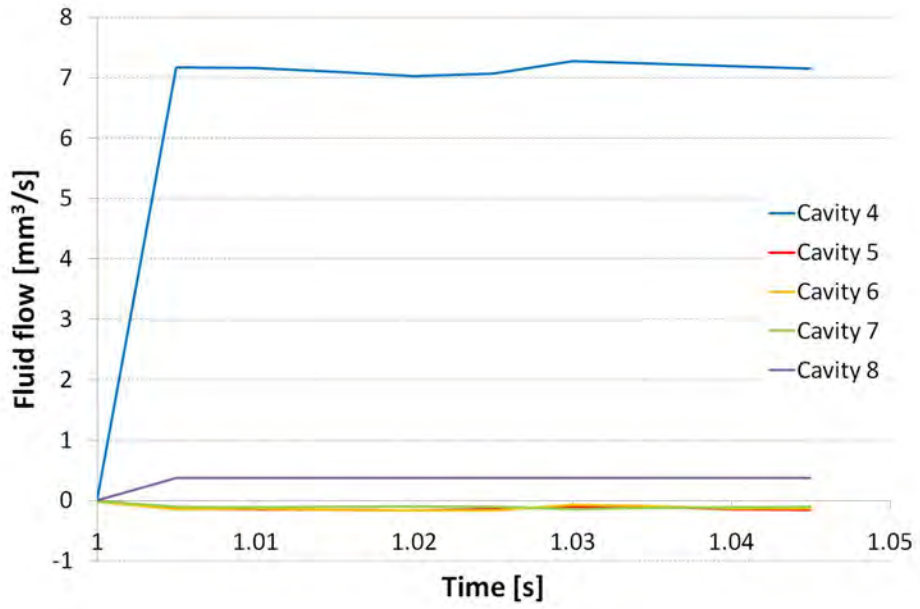

Figure 7.13: *Fluid flows of the cavities inside the contact during the SRT3 simulation.*

In figure 7.14 the graph of figure 7.13 is zoomed focusing on the three innermost cavities, where the fluid flows of interest take place. The fluid flows are negative, meaning that the fluid was escaping from the cavities. In particular, the escaping flow of each cavity was entering the following cavity and so on explaining the positive flow inside the last cavity into the contact.
For each tool, an average fluid escape from the inner cavities is calculated and plotted in figure 7.15. The standard deviation is chosen as a measure of variability.

Discussion

The outcome of the simulations is pretty clear. The inner pockets of SRT1 and SRT4 both with high and low bearing area undergo very similar fluid escapes, being them slightly above 0.08 mm^3/s. SRT2 and SRT3 experience on their turn similar fluid escapes, but at a higher level (approximately 0.125 mm^3/s). There is one parameter that in particular differentiate the two pairs: the feed rate. SRT1 and SRT4 have lower F (0.2 mm) while SRT2 and SRT3 have higher F (0.3 mm). According to the simulation results, the other parameters did not play any major role. The bearing area, which at the beginning was thought being a likely factor of importance, does not

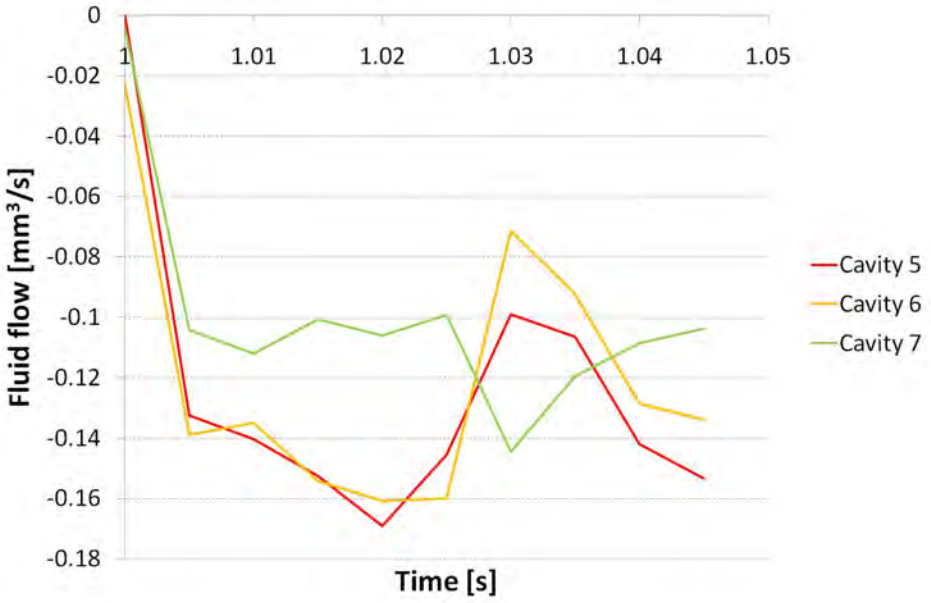

Figure 7.14: *Fluid flows of the innermost cavities during the SRT3 simulation.*

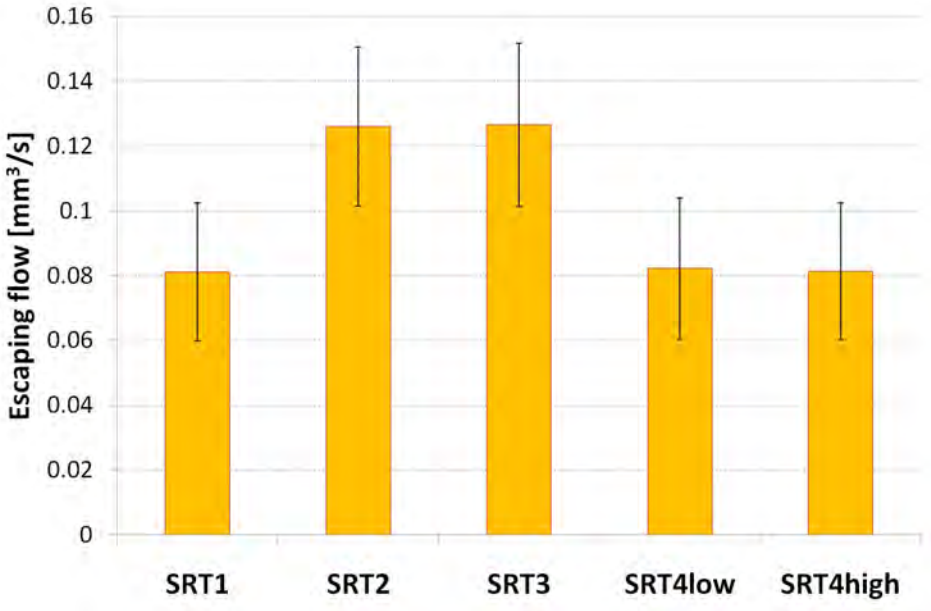

Figure 7.15: *Comparison of average fluid escapes from the inner cavities.*

affect in a significant way the calculation. SRT4low and SRT4high, whose only difference lies in the value of BA, yield in fact coinciding results, demonstrating the statement. According to this model then, at higher feeds are associated higher escapes, which is in theory a positive factor for the

functionality of the surface. Higher fluid escapes imply that fresh lubricant comes at all times feeding the contact and rescuing the plateaus from the menace of lubricant breakage, the asperity contact and the consequent galling. The drawing forces should be therefore lower as there is less risk of mixed lubrication regime. Going back to the discussion of the SRT results in section 5.4.2 it was noted that the feed is a parameter that can have a certain influence. In particular, SRT1 and SRT4 had drawing forces lower that SRT2 and SRT3. The simulation results and the drawing forces measured during the experiments seem therefore to contradict each other. It means that the simulation does not reproduce well what happens during the test. As it can be seen from figure 7.16, the tool cannot in fact indent the strip because of the presence of the truss elements. If the indentations are on one hand unwanted occurrences eased by the fact that the lubricant can escape from the sides, on the other hand the truss elements preclude any possibility for the strip to flow inside the pockets.

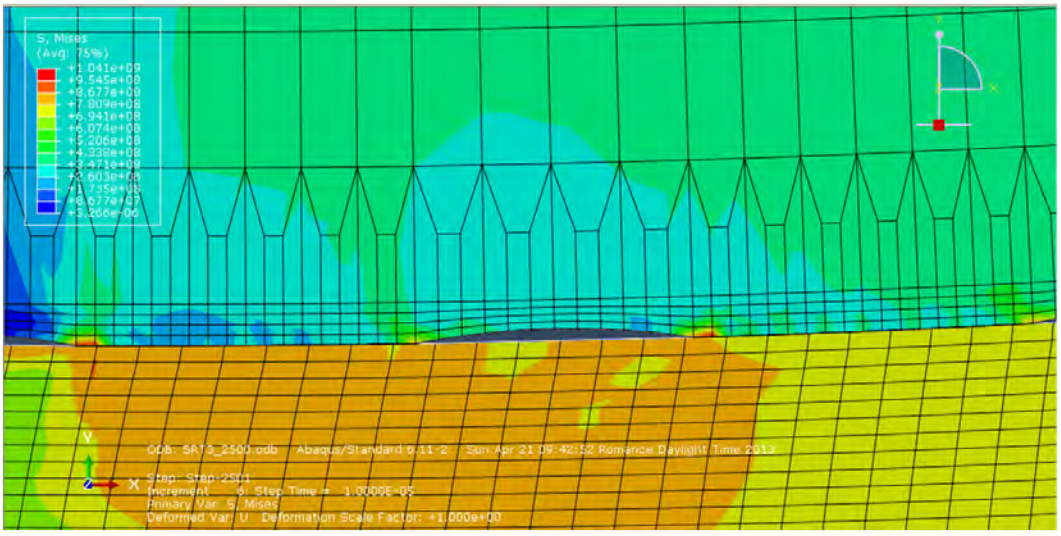

Figure 7.16: *Zoom on the contact between the tool and the workpiece in proximity of a cavity.*

If the truss and the fluid elements are removed, the tool clearly indents the strip (figure 7.17). No hydrostatic pressure is opposing the strip inward movement and the cavities are all filled with workpiece material. This occurrence together with the strip crashing on the pockets edges during the pulling operation (figure 7.18) make the elements on the outermost layer of the strip bend backwards due to the high stresses they are subjected. This is a clear signal towards pick-up and galling formation hence the outcome of the experimental tests.
Unfortunately the actual model cannot be promptly improved for permit-

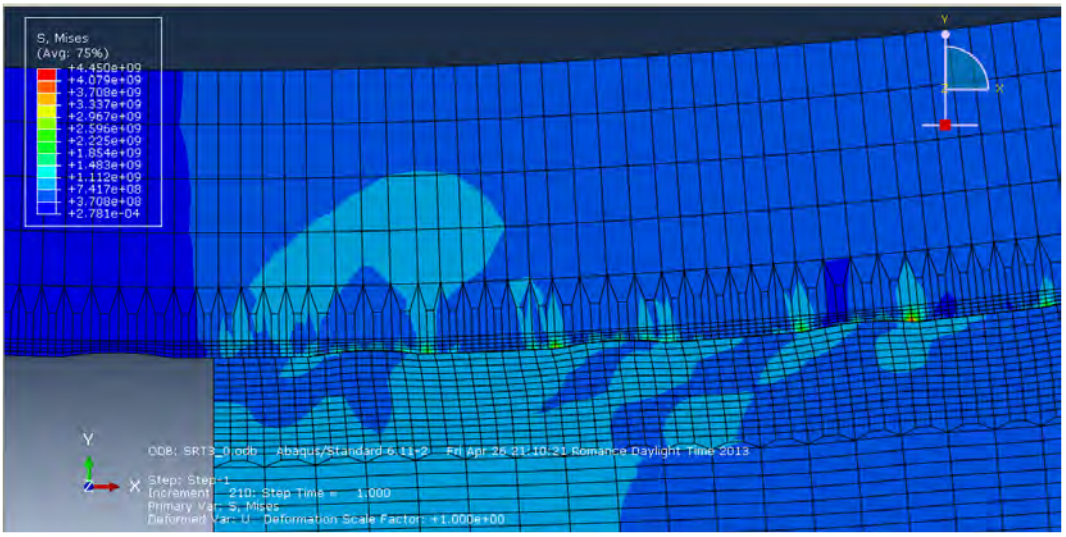

Figure 7.17: *Tool indentation of the strip after the loading operation.*

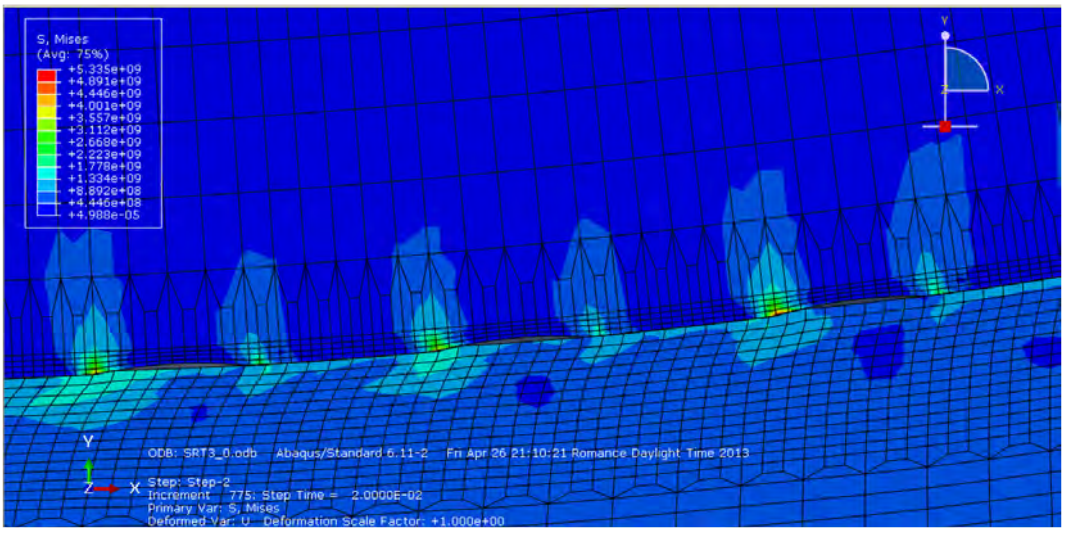

Figure 7.18: *Crashing of the strip on pockets edges. The outermost elements bend backwards.*

ting the strip entrance with concurrent lubricant pressure increase. The truss elements, which are indispensable for permitting the presence of trapped lubrication, are singular segments connecting the nodes at the pockets edges. These elements are inflexible, meaning that they do not allow any rotation around the nodes at their ends but just translations. A possible solution to this problem involves finding other elements than trusses for closing the pockets allowing rotation around the nodes. Unfortunately the fluid elements inside the pockets do not permit any rotation either, therefore

this path is not practicable. Another solution consists in "discretising" the covers substituting the singular truss element with a multitude of trusses. This is certainly a more accessible way and the ongoing and future research should focus on its successful implementation and codification. The cover rigidity constitutes in fact the biggest limitation and the first obstacle to be overcome in the development of reliable numerical models for assessing the functionality of MUFU surfaces applied to metal forming tools.

7.3.2 Bending Under Test simulation

Although the SRT simulation indicates that the direct adoption of the models suffers of some evident practical problems, the model was further adapted to simulate the BUT case and another dedicate plug-in was created. The parts and texture geometrical models did not require any modifications except from their spatial arrangement. Also in this case there are two main operations. In the first operation the strip, now above the round tool, is bended over the tool radius by means of a rigid punch (figure 7.19).

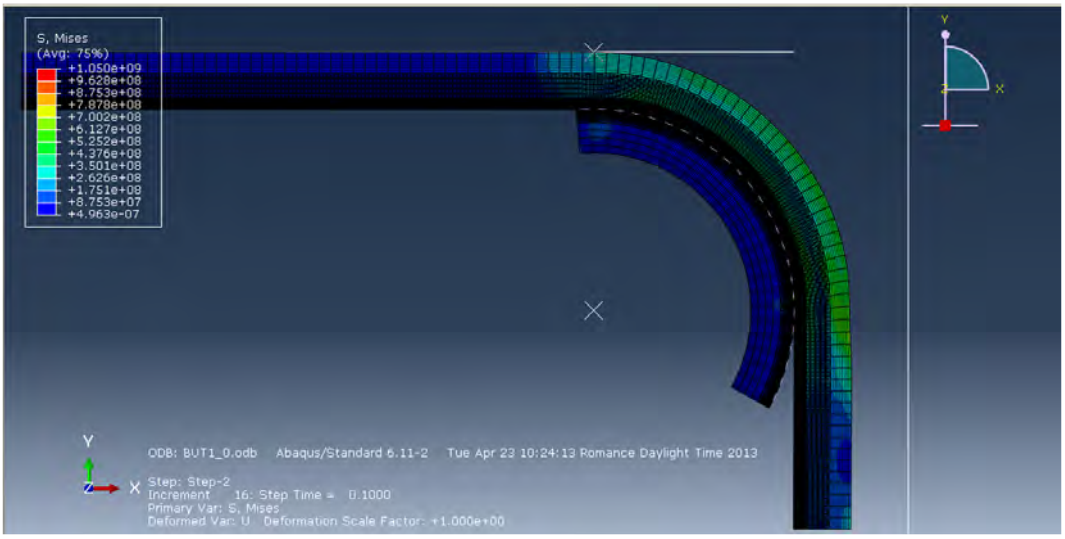

Figure 7.19: *Bending of the strip over the tool shoulder.*

In the second operation the strip is pulled drawing its bended end downwards at a speed of 50 mm/s. In the meantime a back tension of 200 MPa is applied to the other end of the strip. Four simulations are run, each representing the geometry of the tools tested in reality. The new tool radius is set equal to 3.5 mm and the strip thickness is equal to 1 mm. The parameters are collected in table 7.2.
The simulations soon crash. In order to understand the reason of this occurrence, the contact between tool and strip after the first operation is

Table 7.2: Input values for the BUT numerical simulations.

	BUT1	**BUT2**	**BUT3**	**BUT4**
$R1$ [mm]	0.3	0.2	0.3	0.2
F [mm]	0.3	0.2	0.3	0.2
BA [%]	45	60	35	40
h [µm]	0.08	0.08	0.08	0.08

looked at in detail (figure 7.20). The contact is much more complicated to describe than the SRT case. The strip does not contact the entire tool shoulder, but only small areas at the beginning and at the end of the curvature. In a large area of the shoulder, especially in its center (i.e. at 45°), there is a clear clearance between tool and strip, see figure 7.20.

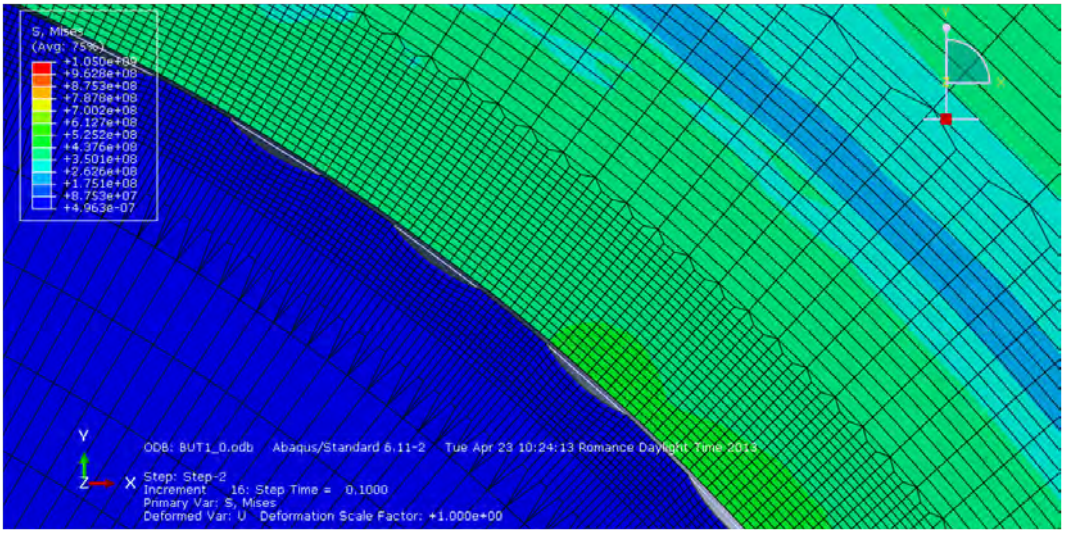

Figure 7.20: *Clearance between tool and strip at 45°.*

Along the whole radius of curvature there is therefore an alternation of closed and open pockets. There is a significant difference compared to the case analysed by Hubert et al. [182, 183]. They detect six possible contact cases (figure 7.21) particular instances of the system 7.2. The cavity can in fact be completely open and no lubricant flow takes place; can be partly open on one side or the other and there is some fluid escape towards the environment; or it can be completely closed with surrounding pockets closed too or one of them open. In their tests they had only two cavities partly open: one at the entrance and one at the exit. All other cavities were

closed. The SRT simulation resembles very much this situation, but the BUT doesn't.

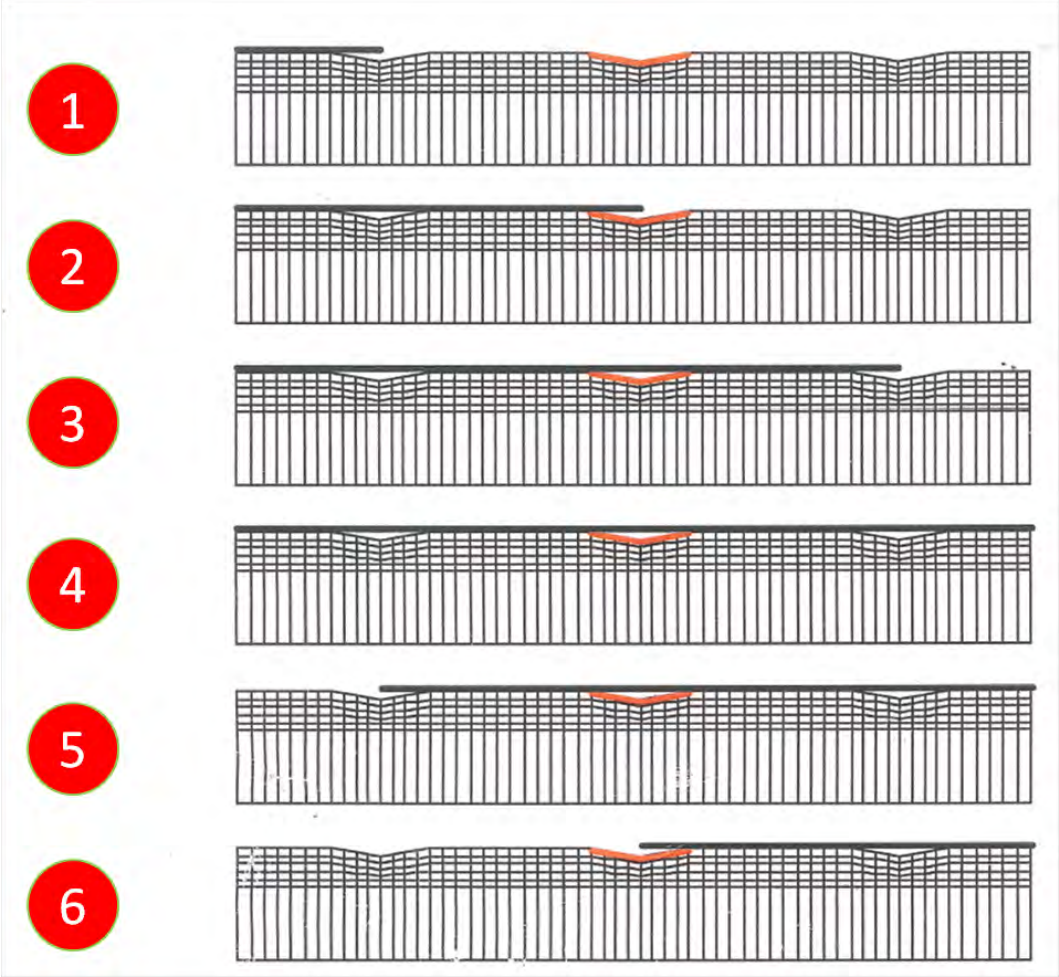

Figure 7.21: *Six possible contact cases in strip drawing through converging dies.*

The cases of half-open pockets happen also in the middle of the contact complicating the study. There happened the unexpected case of a completely closed cavity surrounded by open pockets issue handled by merging cases 3 and 5. Once a front and a back tension are applied, the connection between tool and strip tightens and new pockets are closed. During the drawing process the contact conditions modify continuously. The same pocket opens and closes over time. As a demonstration of that the flows of the first 11 cavities of BUT2 are plotted in graph of figure 7.22. The graph is rather confused due to the ever changing situation. Cavity 8, for example, normally open, closes all of a sudden and undergoes a lubricant escape; other cavities change from a completely open situation to a partly open one and experience large intakes of lubricant.

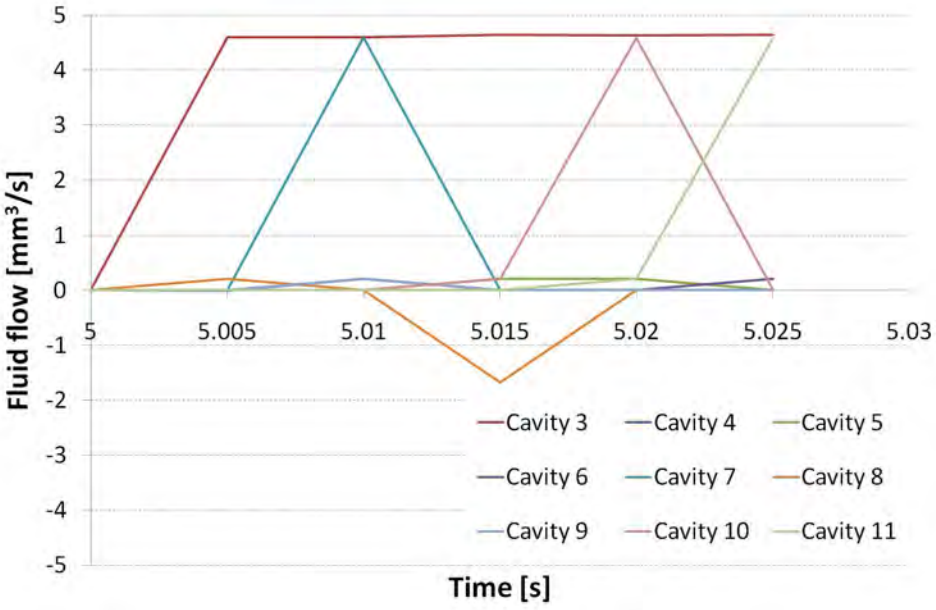

Figure 7.22: *Flows of the first 11 cavities (1 and 2 not displayed) of BUT2.*

The ever changing situation does not represent a problem *per se* as long as there are non-zero flows. Unfortunately after some loops, the simulations were stopped due to the unusual case of all cavities apparently open. This is not likely to happen in practice and, looking at the simulation result of the last iteration, it does not happen in the simulation either (figure 7.23). Evidently there is a flaw in the algorithm which causes an incorrect

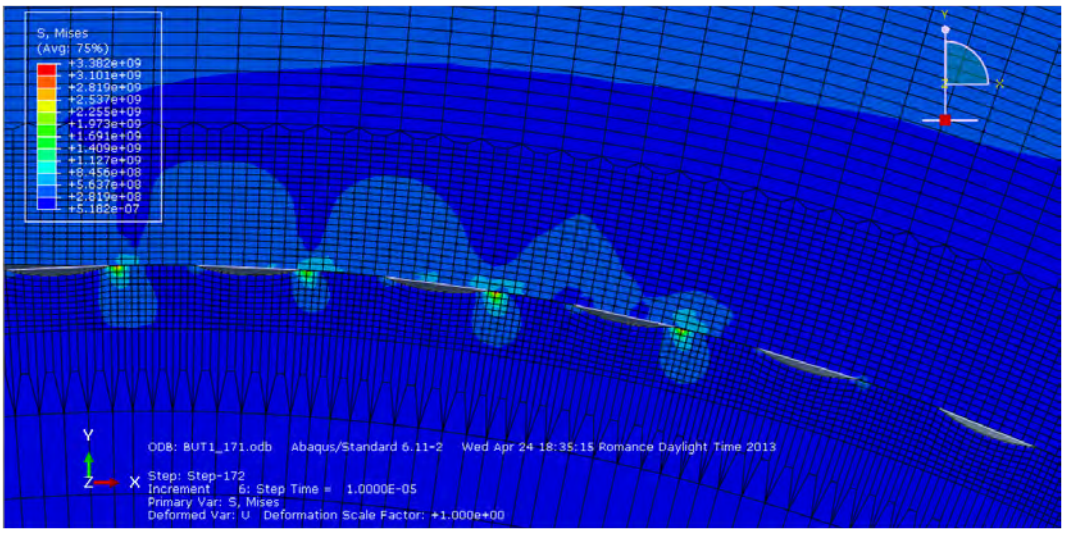

Figure 7.23: *Plateaus contacts on the last iteration of BUT1 simulation before failure.*

recognition of the plateau-strip contact. Some of the pockets that the model considers fully open are instead at least partly closed and should be treated as such. This defect outlines a certain inflexibility of the model which cannot be readily adapted to new tribological situations. The model suffers of the same issues as the SRT one, with in addition the contact problems. The solution to be implemented in the near future is to improve the contact recognition and to study thoroughly the new contact cases. Only after these necessary ameliorations the issue related to the covers should be handled.

7.4 Extension and redefinition of the models

The practical problems that the models presently suffer have been addressed in the previous section. In this section some suggestions for extending or improving the current models are proposed. The extension that is here suggested, if implementable, will automatically lead to a redefinition of the models themselves. It has been said and discussed how it is essential to make the covers bendable in order to allow the workpiece to flow into the pockets. Once that issue has been solved, the implementation of the extension can be studied. This is basically the one proposed in the previous chapter in section 6.5.1: the consideration of the texture micro-wedges. The models currently utilized adopt in fact the same assumption made originally by [179]: the fluid pressure is considered constant inside the whole pocket. While this hypothesis is valid for low speed processes, already in [179] it is envisaged the utilization of a dynamic approach in case the forming speed was higher. During the Strip Reduction Test and the Bending Under Tension test the speed are respectively 80 mm/s and 50 mm/s, not exactly negligible. The hydrodynamic pressure increase due to the wedge becomes therefore important, so that the pressure distribution inside the pocket cannot be considered uniform. In [62–64] the micro-wedge is considered, so that the formula they apply for the hydrodynamic pressure increase (equation 6.49) can be utilised in the actual case as well. The situation is though much more complicated since the workpiece flows inside the pocket (see figure 7.24); the simple knowledge of the pocket geometry is therefore not anymore sufficient. The instantaneous distance between tool and workpiece for each point constituting the two parts should be calculated and the corresponding pressure devised.
By aiming at having pressure differentials inside a single pockets, the whole philosophy behind the models developed by [180–183] falls and a whole new model should be defined. The model treated so far can be ultimately summarized as the description of the fluid exchange between communicating vessels. The two vessels are the pockets which experience a constant pressure P_i and are separated by a tube of height h and length

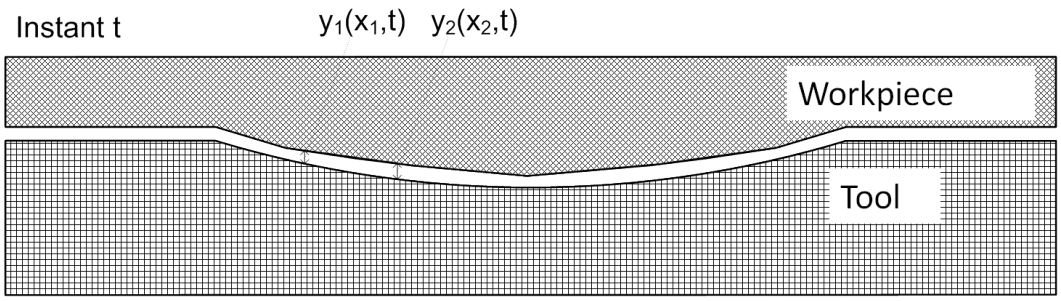

Figure 7.24: *Tool-workpiece distance in case of the workpiece enters a tool pocket.*

Δx. The fluid exchange occurs as soon as there is a difference of pressure between the two pockets. With the new assumption this model cannot be applied. Rather, the new model will "unbind" the pockets: in accordance with the assumptions made by Bech, Bay et al. [62–64] lubricant escape takes place when the maximum fluid pressure overcomes the one of the surrounding plateau. Given the speed of the process it is likely that the escape would occur backwards. A further possibility is to merge the two models and assume that the escaped lubricant will travel completely to the following pocket releasing the pressure the pocket is experiencing and reducing the overall escaping flow. These observations are at the moment simply at the level of speculations, but they represent a basis for future work within the subject.

7.5 Summary and conclusions

In this chapter the first steps towards numerical modelling assessing MUFU surfaces functionality in metal forming applications have been made. Numerical methods are necessary since the models should consider the workpiece material flow inside and outside the tool pockets concurrently with the lubricant behaviour during the forming operation. Existing numerical methods analysing the lubricant escape from a textured workpiece undergoing plastic deformation have been listed. In particular, the model developed recently by Hubert et al. [182, 183] has been adopted and adapted to the actual case. The adaptation consisted in "reversing" the models: from a textured workpiece to a textured die. The results of the initial investigations displayed higher escape for the tools with higher radius, but, most importantly, the principal practical issue was discovered and highlighted: the strip cannot flow inside the pockets during the drawing operation. This occurrence is due to the unavoidable presence of truss elements sealing the pockets. The next operation that must be done in

the future development of reliable numerical models is to handle this problem allowing the workpiece penetration inside the lubricant reservoirs. The BUT simulation outlines the models rigidity in adapting to new conditions: the contact recognition is rather poor in lower normal pressure conditions. Generally speaking, the development of numerical models is a lengthy process which need to be tackled step by step. All the problems detected with the initial simulation here presented must be addressed and solved before further proceeding with models improvement. The biggest improvement that can be made once the issues are managed is to include fluid pressure differentials due to the process dynamics and the the pocket geometry. This is a non-trivial extension which can lead to the complete redefinition of the considered model. The bases that are here laid suggest that the path towards a reliable implementation of numerical models for textured tools is not free from difficulties, but, if successfully undertaken, can lead to the prediction of the texture that guarantees the highest fluid escape and thus best functionality.

Chapter 8

Summary, conclusions and outlook

Friction losses and wear occurrence are issues of worldwide interest. In the striving for their reduction, surface texturing represents one possible solution. A surface can be in fact artificially engineered in order to introduce features that can pursue a certain function. The recently developed MUFU surfaces lie among them and their name originates from the word **mu**lti**fu**nctional. They present a regular pattern of valley features apt for storing the oil and eventually providing extra-lubrication when the tribological contact occur. Moreover they exhibit a uppermost flat layer suitable for bearing the normal load the part featuring them undergoes during the tribological contact. Their introduction represents in the mind of their inventors a big opportunity for improving the performances of tools and machine elements to which the surfaces are applied, including the possible utilization of greener or less hazardous lubricants in industry. Despite the good premise, the introduction of MUFU surfaces is bound with a series of challenges constituting the core of this Ph.D. dissertation.
In this thesis the exploration has touched different fields and disciplines but maintaining a unique common ground: surface texture. The two questions made in Chapter 1 *"Do MUFU surfaces improve the tribological performances of the mechanical systems employing them?"* and *"How can MUFU surfaces be described?"* made the research spanning over the fields of metrology, tribology including test design and running of experimental tests, theoretical as well as numerical modelling. The work is divided in a way that each chapter covers one of the topic covered. The second question was addressed first because no test can take place before knowing what is going to be tested. The metrological investigation represents under a certain point of view the "soul" of the work, no further investigations were possible without first developing methods for a comprehensive description of the surfaces under exam. Two chapters of the thesis have been dedicated to the metrological aspect of the problem. In particular:

- The current approach in the study of surface texture has been illustrated stressing particularly on the principal actions of measuring, visualising, filtering and quantifying. Depending on the needs, the most suitable instrument must be chosen for the surface data capturing. Afterwards, by means of surface visualisation the most suitable analysis procedures and techniques must be selected. Typically, filtering is the next step. A number of standardised filtering techniques have been reviewed from the most classically utilised methods to new developments. The choice of a correct filtering procedure is of paramount importance, as some filters are more useful than others for a certain scope and some filters are more prone than others to yield distortions. Once the data have been filtered, a parameter quantifying the surface in analysis must be selected always keeping in mind its relevance in relation to the surface function. Eventually the question of the traceability of a measurement has been addressed, fundamental issue for accepting a measurement result worldwide.

- The usage of current practice standards has demonstrated being not suitable for characterising MUFU surfaces. Advanced filtering methods involving mainly Robust Gaussian Regression (RGR) filters are deemed being the correct path towards an acceptable characterisation of MUFU surfaces. The filters equations have been coded and Robust filters implemented in the software SPIP^{TM}. Modifications were though needed comprising the utilisation of tighter thresholds for recognising the outliers and the employment of a morphological first guess during the robust filter iterations. The "modified" RGR allows the attainment of an undistorted roughness profile. Moreover, existing parameters were neither meaningful nor satisfactory in the surface description, so that a method recognising profile features has been developed. The features can be separated in independent profiles that can be analysed thoroughly according to the features functions. Two feature typologies have been identified, namely plateaus and valleys. One field parameters is deemed enough for the former and another parameter (EQF) has been defined for the latter. These parameters have demonstrated traceable as it was a regular roughness measurement.

The tribological tests are collected in two chapters depending on the aimed application: machine elements and metal forming tools.

- Concerning machine elements, a new test rig, named Axial Sliding Test (AST), has been devised, designed and built for simulating pure sliding conditions between two counterparts. The test makes use of

the stripwinding technique for keeping the normal pressure constant and requires two machines: a press to load the system and a tensile test machine for performing the sliding. The test is calibrated so that the normal pressure increase is known each mm of advancement of the stripwound container (34 MPa/mm). Before the experimental campaign preliminary tests as well as repeatability tests had been carried out for improving the test knowledge and refining the test procedures. Six rods with different textures were selected for the experimental campaign. The specimens were characterised making use of the newly developed methods. The major outcome of the tests has revealed how MUFU surfaces shows friction forces and coefficients clearly lower than regularly machined surfaces such as turned or ground surfaces. The improvement in friction conditions is up to 50%. It is believed that at relatively high normal pressures the role of the trapped lubricant building up a hydrostatic pressure becomes decisive for relieving the contacting asperities.

- Concerning metal forming tools, simulative tests present at DTU's laboratories as well as production tests were run. The simulative tests performed were respectively the Bending Under Tension (BUT) test for simulating deep drawing applications and the Strip Reduction Test (SRT) for simulating the ironing process. The production tests consisted in a a real deep-drawing operation. For the characterisation, the newly developed methods were again utilised despite some problems due to imperfect manufacturing. The outcome of the tests has revealed that the MUFU surfaces generates less galling than the polished references in BUT applications. In particular the low bearing area does not give room to galling propagation and the scraped off material is transported elsewhere, for example it accumulates in the MUFU valleys. The deep-drawing process, similar to the BUT has shown the same results: low bearing area dies does not cause any sign of galling, occurrence helped in this case by the closed lubricant pockets. The result is seemingly independent from the pockets density and size when the common EN 1.4301 is used as workpiece material. Only with more challenging materials a difference can be detected: smaller and denser pockets are associated with lower process forces. The strip reduction tests have instead resulted being quite destructive for the MUFU surfaces, while the mirror-polished references work smoothly. The high loads of this severe process make the pockets indenting the strip causing severe galling and breakages from the beginning of the tests. It is not known whether in production conditions, with closed channels and without pre-loading these surfaces can perform better. At the moment though they seem not advisable for ironing

applications.

The last two chapters pertain the functional modelling of MUFU surfaces in an attempt to explain theoretically what observed during the experiments and to permit the future drawing of more general conclusions.

- The first chapter has concerned analytical models trying to explain the functionality of MUFU surfaces at relatively low normal pressure and sliding speed, practically the AST case. The AST was simulated considering a flat hard tool pressing over a soft workpiece with a geometrically defined texture. Adhesive friction models found in literature were adopted to evaluate the functionality of the surfaces. The real area of contact between tool and workpiece is calculated based on asperity deformation taking into account the asperity geometry, the height distribution and the presence of lubrication. Two approaches were followed treating differently the height distribution of the plateau nano roughness: the first one considered it as deterministic, the second one as random. Following the first approach, the plateau nano roughness has a great impact in the calculation, so that particularly smooth plateaus are associated with a great increase of lubricant pressure increase and consequently the underestimation of friction coefficients. The second approach, instead, although being theoretically more correct, does not consider the hydrostatic pressure of the trapped lubricant and suffers the problem of determining in a sound manner the first point of contact. The first and second approach yield contrasting results, while the experimental truth lay in between.

- The second chapter has concerned the first steps towards numerical modelling of MUFU surfaces functionality in metal forming applications. A number of existing numerical methods were studied and the one most similar to the processes studied were adopted. The models were adapted for simulating the laboratory metal forming tests. The models suffer of some practical problems presently impeding a reliable simulation of the actual process. These problems have been addressed and solving them represent now the foremost objective towards the development of trustful numerical models. This is a lengthy and difficult process, but if successfully undertaken, it can lead to the prediction of the texture that guarantees the best functionality.

The conclusions of this thesis work can be thus summarized:

1. Robust metrological methods have been developed for the characterisation of MUFU surfaces. The great majority of MUFU surfaces can be now characterised in a sound manner without incurring in distortions;

2. Tests for machine elements in pure sliding conditions have shown how the employment of MUFU surfaces can determine the reduction of friction forces and coefficients up to 50%;

3. Tests for metal forming tools have shown how the employment of MUFU surfaces with low bearing area can prevent the occurrence of galling phenomena thanks to the interrupted contact. Having a high number of small pockets seems also to be beneficial, especially when challenging materials are used in real deep-drawing operations;

4. Analytical models based on literature underestimate or overestimate the calculated values and are therefore not reliable taken as they are;

5. Numerical modelling seems to be a promising path for simulating MUFU surfaces for metal forming tools. Ultimately they can predict a texture with improved functionality. Their implementation is though not an easy task and represents and interesting ground for future studies.

8.1 Proposals for future work

This rather broad work in terms of tackled topics leaves a number of suggestions for future work, as listed below:

- The most important future work related to the characterisation methodologies concerns the areal implementation of the profile methods here discussed, aspect that gains importance with the growing utilization of areal measurements. As said, the methods are utterly extendible to the third dimension. Moreover more efficient and rapid algorithms can be implemented substituting the naive approach here utilised for the morphological first guess. This latter improvement can be particularly important for speeding the areal filtering up.

- A second improvement in the characterisation method is the removal of the plateau roundness. Presently done with local polynomial fitting, it is not always satisfactory and can be improved by using for example wavelet filters at a plateau scale.

- Further tests can be done with the AST, for example texturing the sleeve rather than the rod. It can be imagined that, if the sleeve is MUFU-textured and the rod flat (polished), the results obtained should be comparable to the reverse situation. Nonetheless, in [185] is observed that, when a surface with transversal texture is moving, the valleys will act as carrier of lubricant; whereas when this surface

is stationary the asperities can act as barriers for the lubricant flow. The results can therefore be different and it would be interesting to study them. Moreover, it has not been studied the case MUFU against MUFU, which is quite intriguing since the outcome of such tests is at the moment rather unpredictable. It can be guessed that this is an unfavourable situation since asperity interlocking might occur, but this can be determined only by testing.

- Another suggestion of industrial interest is to perform production tests for components presenting tribological conditions similar to the ones observed during AST for having a confirmation of the MUFU surfaces goodness when full-scale parts are involved.

- Regarding the tests for metal forming tools, other MUFU textures would be interesting to explore especially in real deep drawing processes. For example, in order to definitely assess the influence of the bearing area, dies turned with the same feed and tool nose radius but polished to different BA should be experimented.

- It would be interesting to run new BUT tests using textured surfaces aside from MUFU surfaces. A texture having transversal channels of limited length (therefore closed) is certainly a relevant candidate for providing good tribological results, but not the only possibility. Similarly to what experimented by Holmberg [57] in rolling contacts, dimpled surfaces or herringbone patterned can be other candidates. The employment of textured surfaces in simulative metal forming tools is, as said, a novelty for the DTU laboratories and therefore the field of exploration can be quite broad.

- Testing MUFU surfaces for ironing applications in real production conditions would give a definitive idea on the potentiality of the surfaces. This would eliminate the doubt on whether it was solely the surfaces or also the test design that contributed in achieving destructive results.

- Surface modelling should definitely go towards the numerical approach. Problems and potentialities of numerical modelling for metal forming tools have been discussed highlighting also possible extensions such as considering the micro-wedge between tool and workpiece forming a pressure differential. Numerical modelling should not be confined to metal forming tools. The model recently presented by [178], for example, regards a case very similar to the AST, so that that process can also be studied numerically overcoming eventually the limitations of the analytical approaches.

References

[1] L. De Chiffre, H. Kunzmann, G. N. Peggs, D. A. Lucca, Surfaces in precision engineering, microengineering and nanotechnology, CIRP Annals Manufacturing Technology 52 (2) (2003) 561–577.

[2] A. A. G. Bruzzone, H. L. Costa, P. M. Lonardo, D. A. Lucca, Advances in engineered surfaces for functional performance, CIRP Annals Manufacturing Technology 57 (2008) 750–769.

[3] L. Blunt, X. Jiang, Advanced Techniques for Assessment Surface Topography, Kogan Page Science, London, UK, 2003.

[4] ISO 25178-2, Geometrical Product Specifications (GPS)- Surface texture: Areal - terms, definitions and surface texture parameters, internation Organization for Standardization (2012).

[5] T. R. Thomas, Rough Surfaces, 2nd Edition, Imperial College Press, 1999.

[6] C. J. Evans, J. B. Bryan, "Structured", "Textured" or "Engineered" surfaces, CIRP Annals Manufacturing Technology 48 (2) (1999) 541–556.

[7] X. J. Jiang, D. J. Whitehouse, Technological shifts in surface metrology, CIRP Annals Manufacturing Technology 61 (2012) 815–836.

[8] G. Schmalz, Technische Oberflächenkunde, Springer-Verlag, Berlin, 1936.

[9] J. Abbot, A. Firestone, A new profilograph measures roughness of finely finished and ground surfaces, Automotive Industry (1933) 204.

[10] L. De Chiffre, P. Lonardo, H. Trumplod, D. A. Lucca, G. Goch, C. A. Brown, J. Raja, H. N. Hansen, Quantitative characterization of surface texture, CIRP Annals Manufacturing Technology 49 (2) (2000) 635–652.

[11] K. J. Stout, P. J. Sullivan, W. P. Dong, E. Mainsah, N. Luo, T. Mathia, H. Zahouani, The development of methods for the characterisation of roughness in three dimensions, Commission of the European Communities, 1993.

[12] R. P. Feynman, There's plenty of room at the bottom, Engineering and Science 23 (1960) 22–36.

[13] L. Alting, F. Kilmura, H. N. Hansen, G. Bissacco, Micro engineering, CIRP Annals Manufacturing Technology 52 (2) (2003) 635–657.

[14] P. M. Lonardo, D. A. Lucca, A. A. G. Bruzzone, Emerging trends in surface metrology, CIRP Annals Manufacturing Technology 51 (2) (2002) 701–723.

[15] T. R. Thomas, Trends in surface roughness, International Journal of Machine Tools and Manufacture 38 (5-6) (1998) 405–411.

[16] L. De Chiffre, Geometrical Metrology and Machine Testing, DTU Mekanik - CGM, 2011.

[17] D. J. Whitehouse, Handbook of Surface Metrology, 2nd Edition, CRC Press Taylor & Francis Group, Boca Raton, FL, 2011.

[18] K. Autumn, Properties, principles, and parameters of the gecko adhesive system, in: M. A. Smith, J. A. Callow (Eds.), Biological Adhesives, Springer Berlin Heidelberg, 2006, pp. 225–256.

[19] W. Barthlott, C. Neinhuis, Purity of the sacred lotus, or escape from contamination in biological surfaces, Planta 202 (1) (1997) 1–8.

[20] J. Canning, K. Sommer, S. Huntigton, A. Carter, Silica-based fibre fresnel lens, Optics Communications 199 (2001) 375–381.

[21] P. Butler-Smith, D. Axinte, M. Daine, Ordered diamond micro-arrays for ultra-precision grinding - an evaluation in Ti–6Al–4V, International Journal of Machine Tools and Manufacture 51 (2011) 54–66.

[22] E. Stratakis, V. Zorba, M. Barberoglou, E. Spanakis, S. Rhizopoulou, P. Tzanetakis, S. Anastasiadis, C. Fotakis, Laser structuring of water-repellent biomimetic surfaces, `http://s3.amazonaws.com/publicationslist.org/data/sophia.rhizopoulou/ref-99/LOTUS%20EFFECT%20%201441_5423_0_2009-01-16.pdf`, accessed 13th January 2013.

[23] X. Jiang, Robust solution for the evaluation of stratified functional surfaces, CIRP Annals Manufacturing Technology 59 (2010) 573–576.

[24] K. J. Stout, Engineered surfaces part 1. - a philosophy of manufacture, KSME International Journal 14 (1) (2000) 72–83.

[25] K. J. Stout, L. Blunt, A contribution to the debate on surface classifications- random systematic, unstructured, structured and engineered, International Journal of Machine Tools and Manufacturing 41 (2001) 2039–2044.

[26] K. J. Stout, E. J. Davis, P. J. Sullivan, Atlas of machined surfaces, Chapman and Hall, Cambridge, UK, 1990.

[27] S. Kalpakjian, S. R. Schmid, Manufacturing processes for Engineering Materials, 4th Edition, Paerson Education Inc., Upper Saddle river, NJ, 2003.

[28] U. Pettersson, S. Jacobson, Textured surfaces for improved lubrication at high pressure and low sliding speed of roller/piston in hydraulic motors, Tribology International 40 (2007) 355–359.

[29] W. Koszela, P. Pawlus, L. Galda, The effect of oil pockets size and distribution on wear in lubricated sliding, Wear 263 (2007) 1585–1592.

[30] H. L. Costa, I. M. Hutchings, Hydrodynamic lubrication of textured steel surfaces under reciprocating sliding conditions, Tribology International 40 (2007) 1227–1238.

[31] M. Nakano, A. Korenaga, A. Korenaga, K. Miyake, T. Murakami, Y. Ando, H. Usami, S. Sasaki, Applying micro-texture to cast iron surfaces to reduce the friction coefficient under lubricated conditions, Tribology Letters 28 (2007) 131–137.

[32] M. Vrbka, O. Šamànek, P. Šperka, T. Nàvrat, I. Křupka, M. Hartl, Effect of surface texturing on rolling contact fatigue within mixed lubricated non-conformal rolling/sliding contacts, Tribology International 43 (2010) 1457–1465.

[33] N. Ren, T. Nanbu, Y. Yasuda, D. Zhu, Q. Wang, Micro textures in concentrated-conformal-contact lubrication: Effect of distribution patterns, Tribology Letters 28 (2007) 275–285.

[34] G. Stachowiak, P. Podsialdo, 3-d characterization, optimization, and classification of textured surfaces, Tribology Letters 32 (2008) 13–21.

[35] M. Zou, L. Cai, H. Wang, D. Yang, T. Wyrobeck, Adhesion and friction studies of a selectively micro/nano-textured surface produced by UV assisted crystallization of amorphous silicon, Tribology Letters 20 (2005) 43–52.

[36] Beckman Coulter Biomedical GmbH, https://www.beckmancoulter.com/wsrportal/wsr/company/about-us/corporate-overview/index.htm, accessed 7th February 2013.

[37] R. Gohar, H. Rahnejat, Fundamentals of Tribology, Imperial College Press, London, UK, 2008.

[38] J. A. Schey, Tribology in Metalworking, American Society for Metals, Metals Park, Ohio, 1984.

[39] J. A. Williams, Engineering Tribology, Oxford University Press, Oxford, UK, 1994.

[40] H. P. Jost, Lubrication (Tribology)- A Report on the Present Position and Industry's Needs, Great Britain Department of Education and Science, H.M. Stationery Office, London, UK, 1966, pp. 1–17.

[41] H. P. Jost, Tribology- origin and future, Wear 136 (1) (1990) 1–17.

[42] I. Hutchings, Tribology – friction and wear of engineering materials, Wear 136 (1) (1990) 703–707.

[43] N. Bay, A. Azushima, P. Groche, I. Ishibashi, M. Merklein, M. Morishita, T. Nakamura, S. Schmid, M. Yoshida, Environmentally benign tribo-systems for metal forming, CIRP Annals Manufacturing Technology 59 (2010) 760–780.

[44] R. Stribeck, Die wesentliechen ichen eigenschaften gleit und rollen lager, Transaction of ASME 29 (1907) 420–463.

[45] M. Santochi, M. Vignale, A study on the functional properties of a honed surface, CIRP Annals Manufacturing Technology 31 (1) (1982) 431–434.

[46] M. C. Malburg, J. Raja, D. J. Whitehouse, Characterization of surface texture generated by plateau-honing process, CIRP Annals Manufacturing Technology 42 (1) (1993) 637–639.

[47] D. J. Whitehouse, Some theoretical aspects of a practical measurement problem in plateau honing, International Journal of Production Research 21 (2) (1983) 215–221.

[48] M. C. Malburg, Cylinder bore surface texture analysis, http://www.digitalmetrology.com/Papers/CylinderBoreNoBkgd.pdf, accessed 18th January 2013 (2002).

[49] K. J. Stout, T. A. Spedding, The characterization of internal combustion engine bores, Wear 83 (1982) 311–326.

[50] ISO 13565-1, Geometrical Product Specifications (GPS)- Surface texture: Profile method - surfaces having stratified functional properties - part 1: Filtering and general measurement conditions, internation Organization for Standardization (1996).

[51] ISO 13565-2, Geometrical Product Specifications (GPS)- Surface texture: Profile method - surfaces having stratified functional properties - part 2: Height characterization using the linear material ratio curve, internation Organization for Standardization (1998).

[52] ISO 13565-3, Geometrical Product Specifications (GPS)- Surface texture: Profile method - surfaces having stratified functional properties - part 3: Height characterization using the material probability curve, internation Organization for Standardization (1998).

[53] B. G. Rosén, Towards surface engineering, Ph.D. thesis, Chalmers University of Technology, Göteborg, Sweden (1994).

[54] B. G. Rosén, R. Crafoord, Interactive surface modelling: model of a function-oriented expert system for specification of surface properties, Industrial Metrology 2 (1992) 107–119.

[55] B. G. Rosén, R. Ohlsson, J. Westberg, Interactive surface modelling, an implementation of an expert system for specification of surface roughness and topography, International Journal of Machine Tools & Manufacture 35 (2) (1992) 317–324.

[56] R. Ohlsson, B. G. Rosén, Surface texture knowledge support – ISM, in: L. Blunt, X. Jiang (Eds.), Advanced Techniques for Assessment Surface Topography, Kogan Page Science, London, UK, 2003, pp. 325–337.

[57] K. Holmberg, The mechanism of lubrication in low speed rolling contacts, Journal of Tribology 111 (1989) 703–707.

[58] A. Erdemir, Review of engineered tribological interfaces for improved boundary lubrication, Tribology International 38 (2005) 249–256.

[59] A. Ramesh, W. Akram, S. P. Mishra, A. H. Cannon, A. A. Polycarpou, K. W. P., Friction characteristics of microtextured surfaces under mixed and hydrodynamic lubrication, Tribology International 57 (2013) 170–176.

[60] T. Mizuno, M. Okamoto, Effects of lubricant viscosity at pressure and sliding velocity on lubricating conditions in the compression-friction test on sheet metals, Journal of Lubrication Technology 104 (1982) 53–59.

[61] A. Azushima, S. Yoneyamas, T. Yamaguchi, H. Kudo, Direct observation of microcontact behavior at the interface between tool and workpiece in lubricated upsetting, CIRP Annals Manufacturing Technology 45 (1996) 205–210.

[62] J. I. Bech, N. Bay, M. Eriksen, A study of mechanisms of liquid lubrication in metal forming, CIRP Annals Manufacturing Technology 47 (1) (1998) 221–226.

[63] J. I. Bech, N. Bay, M. Eriksen, Entrapment and escape of liquid lubricant in metal forming, Wear 232 (1999) 134–139.

[64] C. G. Sørensen, J. I. Bech, J. L. Andreasen, N. Bay, U. Engel, T. Neudecker, A basic study of the influence of surface topography on mechanisms of liquid lubrication in metal forming, CIRP Annals Manufacturing Technology 48 (1) (1999) 203–208.

[65] U. Wagner, U. Engel, Microtexturing of cold-forging tools – influence on tool life, Proceedings of the Institution of Mechanical Engineers, part B: Journal of Engineering Manufacture 220 (2004) 27–33.

[66] K. Wagner, R. Volkl, U. Engel, Tool life enhancement in cold forging by locally optimized surfaces, Journal of Material Process Technology 201 (2008) 2–8.

[67] H. L. Costa, I. M. Hutchings, Effects of die surface patterning on lubrication in strip drawing, Journal of Material Process Technology 209 (2009) 1175–1180.

[68] Strecon A/S, `http://www.strecon.com/`, accessed 10th February 2013.

[69] J. Grønbæk, Rap - robot assisted polishing - roboterunterstütztes polieren von umformwerkzeugen., in: Jahresteffen der Kaltmassivumformer, VDI, Düsseldorf, Germany, 2008.

[70] S. Rebeggiani, B. G. Rosén, Evaluation of a robot assisted polishing equipment, in: Proceedings of the 2nd Swedish Production Symposium, Stockholm, Sweden, 2008, pp. 1–6.

[71] R. S. Eriksen, M. Arentoft, J. Grønbæk, N. Bay, Manufacture of functional surfaces through combined application of tool manufacturing processes and robot assisted polishing, CIRP Annals Manufacturing Technology 61 (2012) 563–566.

[72] AB Sandvik Coromant, Sweden, Modern Metal Cutting - a practical handbook (1994).

[73] A. Godi, K. S. Friis, L. De Chiffre, Characterization of multifunctional surfaces during fabrication, in: Proceedings of the 11th eu**spen** International Conference, Como, Italy, 2011, pp. 92–95.

[74] Image Metrology A/S, `http://www.imagemet.com/`, accessed 13th February 2013.

[75] L. De Chiffre, Surface topography analysis, in: H. Czichos, T. Saito, L. Smith (Eds.), Springer Handbook of metrology and testing, Springer, New York, 2000, pp. 308–326.

[76] ISO 3274, Geometrical Product Specifications (GPS)- Surface texture: Profile method - nominal characteristics of contact (stylus) instruments, internation Organization for Standardization (1996).

[77] V. Radhakrishnan, Effect of stylus radius on the roughness values measured with tracing stylus instruments, Wear 16 (1970) 325–335.

[78] R. Leach, Optical Measurements of Surface Topography, Springer, Berlin, Germany, 2011.

[79] P. M. Lonardo, L. De Chiffre, U. Sjoblom, Characterisation of functional surfaces, in: Proceedings of the 2nd International Conference of Tribology in Manufacturing Processes, Nyborg, Denmark, 2004, pp. 39–62.

[80] R. Leach, Fundamentals principles of engineering nanometrology, Elsevier Inc., Oxford, UK, 2010.

[81] F. Helmli, Focus variation instruments, in: R. Leach (Ed.), Optical Measurements of Surface Topography, Springer, Berlin, Germany, 2011, pp. 131–166.

[82] Alicona Imaging GmbH, `http://www.alicona.at/home/`, accessed 19th February 2013.

[83] G. Häusler, E. Svenja, Limitations of optical 3d sensors, in: R. Leach (Ed.), Optical Measurements of Surface Topography, Springer, Berlin, Germany, 2011, pp. 23–48.

[84] F. Marinello, Atomic force microscopy in nanometrology: Modeling and enhancement of the instrument, Ph.D. thesis, Università degli Studi di Padova, Padova, Italy (2006).

[85] I. Davì, Characterization of a deep, nanometer, scale diffraction grating with atomic force microscope, Master's thesis, DFM, DTU, Kgs. Lyngby, Denmark (2005).

[86] G. Dai, F. Pohlenz, H. U. Danzebrink, M. Xu, K. Hasche, G. Wilkening, Metrological large range scanning probe microscope, Review of Scientific Instruments 75 (4) (2004) 962–968.

[87] M. Stedman, Basis for comparing the performance of surface measuring machines, Precision Engineering 9 (1987) 149–152.

[88] ISO 4287, Geometrical Product Specifications (GPS)- Surface texture: Profile method - Terms, definitions and surface texture parameters, Internation Organization for Standardization (1997).

[89] ISO 4288, Geometrical Product Specifications (GPS)- Surface texture: Profile method - rules and procedures for the assessment of surface texture, internation Organization for Standardization (1996).

[90] J. Raja, B. Muralikrishnan, S. Fu, Recent advances in separation of roughness, waviness and form, Precision Engineering 26 (2002) 222–235.

[91] D. J. Whitehouse, Improved type of wavefilter for use in surface-finish measurement, Proceedings of the Institution of Mechanical Engineers 182 (11) (1968) 306–318.

[92] ISO 16610-21, Geometrical Product Specifications (GPS)- Filtration - part 21: Linear profile filters: Gaussian filters, internation Organization for Standardization (2011).

[93] W. Zeng, X. Jiang, P. J. Scott, Fast algorithm of the robust gaussian regression filter for areal surface analysis, Measurement Science and Technology 21 (2010) 055108.

[94] ISO 16610-22, Geometrical Product Specifications (GPS)- Filtration - part 22: Linear profile filters: Spline filters, internation Organization for Standardization (2006).

[95] ISO 16610-29, Geometrical Product Specifications (GPS)- Filtration - part 29: Linear profile filters: Spline wavelets, internation Organization for Standardization (2006).

[96] ISO 16610-31, Geometrical Product Specifications (GPS)- Filtration - part 31: Robust profile filters - gaussian regression filters, internation Organization for Standardization (2010).

[97] ISO 16610-32, Geometrical Product Specifications (GPS)- Filtration - part 32: Robust profile filters - spline filters, internation Organization for Standardization (2009).

[98] ISO 16610-40, Geometrical Product Specifications (GPS)- Filtration-part 40: Morphological profile filters - basic concepts, internation Organization for Standardization (2006).

[99] ISO 16610-41, Geometrical Product Specifications (GPS)- Filtration-part 41: Morphological profile filters - disk and horizontal line-segment filters, internation Organization for Standardization (2007).

[100] S. Brinkmann, H. Bodschwinna, H. W. Lemke, Accessing roughness in three-dimensions using gaussina regression filtering, International Journal of Machine Tools & Manufacture 41 (2001) 2153–2161.

[101] S. Brinkmann, H. Bodschwinna, Advanced gaussian filters, in: L. Blunt, X. Jiang (Eds.), Advanced Techniques for Assessment Surface Topography, Kogan Page Science, London, UK, 2003, pp. 62–89.

[102] W. Zeng, X. Jiang, P. J. Scott, S. Xiao, L. Blunt, A fast algorithm for the high order linear and nonlinear gaussian regression filter, in: Proceedings of the 9th eu**spen** International Conference, San Sebastian, Spain, 2009, pp. 51–53.

[103] J. Seewig, Linear and robust gaussian regression filters, Journal of Physics: Conference Series 13 (2005) 254–257.

[104] M. Krystek, Form filtering by splines, Measurement 18 (1996) 9–15.

[105] M. Krystek, Discrete l-spline filtering in roundness measurements, Measurement 18 (1996) 129–138.

[106] X. J. Jiang, L. Blunt, Third generation wavelet for the extraction of morphological features from micro and nano scalar surfaces, Wear 257 (2004) 1235–1340.

[107] X. J. Jiang, P. Scott, D. J. Whitehouse, Wavelets and their applications for surface metrology, CIRP Annals Manufacturing Technology 57 (2008) 555–558.

[108] H. Von Weingraber, Zur definition der oberflächenrauheit, Werkstattstechnik Masch. Bass. 46.

[109] S. Lou, X. Jiang, P. J. Scott, Fast algorithm for morphological filters, Journal of Physics: Conference Series 311 (2011) 012001.

[110] M. Krystek, Spline filters for surface texture analysis, Key Engineering Materials 295–296 (2005) 441–446.

[111] M. Krystek, Morphological filters in surface texture analysis, in: Proceedings of the XI International Colloquium on Surfaces ICS, Chemnitz, Germany, 2005, pp. 43–55.

[112] X. J. Jiang, L. Blunt, K. J. Stout, Three-dimensional surface characterization for orthopaedic joint prostheses, Proceedings of the Institution of Mechanical Engineers 213 (H) (1999) 49–68.

[113] ISO 12085, Geometrical Product Specifications (GPS)- Surface texture: Profile method - motif parameters, internation Organization for Standardization (1996).

[114] P. J. Scott, Foundation of topological characterization of surface texture, International Journal of Machine Tools and Manufacture 38 (5–6) (1998) 559–566.

[115] A. Bleau, L. J. Leon, Watershed-based segmentation and region merging, Computer Vision and Image Understanding 77 (2000) 317–370.

[116] F. Barré, J. Lopez, Watershed lines and catchment basins: a new 3d-motif method, International Journal of Machine Tools & Manufacture 40 (2000) 1171–1184.

[117] J. Maxwell, On hills and dales, The London, Edinburgh and Dublin Philosophy Magazine and Journal Science Series 4 40 (1870) 421–425.

[118] JCGM Joint Committee for Guides in Metrology, International vocabulary of metrology - Basic and general concepts and associated terms (VIM) (2012).

[119] ISO 5436-1, Geometrical Product Specifications (GPS)- Surface texture: Profile method - measurement standards, internation Organization for Standardization (2000).

[120] ISO 25178-701, Geometrical Product Specifications (GPS)- Surface texture: Areal - calibration and measurement standards for contact (stylus) instruments, internation Organization for Standardization (2010).

[121] JCGM Joint Committee for Guides in Metrology, Evaluation of measurement data - Guide to the expression of uncertainty in measurement (2008).

[122] S. Gasparin, Verification of tolerance chains in micro manufacturing, Ph.D. thesis, Technical University of Denmark, Kongens Lyngby, Denmark (2012).

[123] K. S. Friis, A. Godi, L. De Chiffre, Characterization and robust filtering of multifunctional surfaces using iso standards, Measurement Science and Technology 22 (2011) 125101.

[124] A. Godi, A. Kühle, L. De Chiffre, A plateau- valley separation method for multifunctional surfaces characterization, in: Proceedings of the 12th eu**spen** International Conference, Stockholm, Sweden, 2012, pp. 190–193.

[125] A. Godi, A. Kühle, L. De Chiffre, A plateau- valley separation method for textured surfaces with a deterministic pattern, Precision Engineering. Currently under review.

[126] A. Godi, A. Kühle, L. De Chiffre, A new procedure for characterizing textured surfaces with a deterministic pattern of valley features, Measurement Science and Technology. Currently under review.

[127] R. G. Staudte, S. J. Sheather, Robust Estimation and Testing, Wiley, New York, 1990.

[128] Digital Surf, `http://www.digitalsurf.fr/en/index.html`, accessed 8th March 2013.

[129] W. Grabon, P. Pawlus, L. Galda, A. Dzierwa, P. Podulka, Problems of surface topography with oil pockets analysis, Journal of Physics: Conference Series 311 (2011) 012023.

[130] S. Lou, X. Jiang, P. J. Scott, Algorithms for morphological profile filters and their comparison, Precision Engineering 36 (2012) 414–423.

[131] A. Godi, J. Grønbæk, K. Mohaghegh, P. Klit, L. De Chiffre, An axial sliding test for machine elements surfaces, in: Proceedings of the 15th NordTrib, Trondheim, Norway, 2012, ISBN 978–82–14–05270–1.

[132] A. Godi, J. Grønbæk, K. Mohaghegh, P. Klit, L. De Chiffre, A new rig for testing textured surfaces in pure sliding conditions, Tribology Letters 50 (3) (2013) 397–405.

[133] A. Godi, K. Mohaghegh, J. Grønbæk, P. Klit, L. De Chiffre, Testing of newly developed functional surfaces under pure sliding conditions, Tribology Letters. DOI 10.1007/s11249-013-0162-6.

[134] F. Sadeghi, B. Jalalahmadi, T. S. Slack, N. Raje, N. K. Arakere, A review of rolling contact fatigue, Journal of Tribology 131 (2009) 0141403:1–15.

[135] A. V. Olver, The mechanism of rolling contact fatigue: an update, Proceedings of the Institution of Mechanical Engineers: Journal of Engineering Tribology 219 (2005) 313–330.

[136] J. J. C. Hoo, Rolling contact fatigue testings of bearing steels, American Society for Testing and Materials, Baltimore, MD, 1982.

[137] Standard ASTM G99-04a, Standard test method for wear testing with a pin-on-disk apparatus, http://lopezva.files.wordpress.com/2011/09/g99.pdf, accessed 15th March 2013.

[138] Phoenix Tribology Ltd, http://www.phoenix-tribology.com/, accessed 15th March 2013.

[139] A. G. Plint, M. A. Plint, Test procedure for rapid assessment of frictional properties of engine oils at elevated temperatures, Tribology International 17 (4) (1984) 209–213.

[140] Uddeholms AB, Uddeholm Vanadis 6®, http://www.uddeholm.com/files/vanadis_6-english.pdf, accessed 15th March 2013.

[141] J. Grønbæk, Stripwinding of tool for bulk metal forming, Ph.D. thesis, Technical University of Denmark, Kongens Lyngby, Denmark, in Danish (1981).

[142] J. Grønbæk, Application of stripwinding tool to large reduction cold forging processes, in: Proceedings of the North American Manufacturing Research Conference (NAMRC-X), Hamilton, Canada, 1982, pp. 225–232.

[143] J. Grønbæk, Stripwound cold-forging tools - a technical and economical alternative, Journal of Materials Processing Technology 35 (1992) 483–493.

[144] I. Sidenius, Aksler. Kiler, fedre og splines. Krympning og roterende skiver, Kompendium til maskinelementer KP4, Polyteknisk Forlag, Denmark, 1971, in Danish.

[145] Klüber Lubrication, BARRIERTA® L55 series, http://www.klubersolutions.com/pdfs/Barrierta%20L%2055.pdf, accessed 30th November 2012.

[146] Texaco, Multifak® EP0,1,2, http://www.rolandjrobertdistributor.com/files/Multifak_ep.pdf, accessed 29th November 2012.

[147] K. Guo, X. Zhang, H. Li, G. Meng, Non-reversible friction modeling and identification, Archive of Applied Mechanics 78 (2008) 795–809.

[148] J. Wojewoda, A. Stefański, M. Wiercigroch, T. Kapitaniak, Hysteretic effects of dry friction: modeling and experimental studies, Philosophical Transactions of the Royal Society A 366 (2008) 747–765.

[149] Tritech Forensics, AccuTrans® automix casting silicone material, http://tritechforensics.com/, accessed 22th March 2013.

[150] S. Christiansen, L. De Chiffre, Topographic characterization of progressive wear on deep drawing dies, Tribology Transactions 40 (2) (1997) 346–352.

[151] N. Bay, D. D. Olsson, J. L. Andreasen, Lubricant test methods for sheet metal forming, Tribology International 41 (2008) 844–853.

[152] J. L. Andreasen, N. Bay, M. Andersen, E. Christensen, N. Bjerrum, Screening the performance of lubricants for the ironing of stainless steel with a strip reduction test, Wear 207 (1997) 1–5.

[153] J. L. Andreasen, K. Krebs, G. Kann, N. Bay, Quantitative evaluation of lubricants and tool surfaces for ironing of stainless steel, in: Proceedings of the 1th International Conference on Tribology in Manufacturing Processes, 1997, pp. 358–363.

[154] J. L. Andreasen, N. Bay, L. De Chiffre, Quantification of galling in sheet metal forming by surface topography characterisation, International Journal of Machine Tools and Manufacture 38 (5–6) (1998) 503–510.

[155] J. L. Andreasen, D. D. Olsson, K. Chodnikiewicz, N. Bay, Bending under tension test with direct friction measurement, Proceedings of the Institution of Mechanical Engineers 220 (B) (2006) 73–79.

[156] D. D. Olsson, N. Bay, J. L. Andreasen, Direct friction measurement in draw bead testing, in: P. Bariani (Ed.), Proceedings of the 8th ICTP International Conference on Techonology of Plasticity, Verona, Italy, 2005.

[157] E. Ceron, N. Bay, A methodology for off-line evaluation of new environmentally friendly tribo-systems for sheet metal forming, CIRP Annals Manufacturing Technology.In press.

[158] Uddeholms AB, Uddeholm Vanadis 4-Superclean™, http://www.uddeholm.com.br/br/files/vanadis_4_english_04.pdf, accessed 30th March 2013.

[159] P. Groche, N. Möller, Tribological investigation of deep-drawing processes using servo presses, in: Proceedings of the ASME–International Manufacturing Science and Engineering Conference, no. MSEC2012–7292, Notre Dame, Indiana, 2012.

[160] E. Ceron, N. Bay, Determination of friction in sheet metal forming by means of simulative tribo-tests, Key Engineering Materials 549 (2013) 415–422.

[161] Rhenus Lub, Rhenus SU 166 A, http://www.rhenuslub.de/en//, accessed 28th March 2013.

[162] Grundfos A/S, http://www.grundfos.com/, accessed 07th April 2013.

[163] S. PalDey, S. C. Deevi, Single layer and multilayer wear resistant coatings of (Ti,Al)N: a review, Material Science and Engineering A342 (2003) 58–79.

[164] V. Franzen, J. Witulski, A. Brosius, M. Trompeter, A. E. Tekkaya, Textured surfaces for deep drawing tools by rolling, International Journal of Machine Tools & Manufacture 50 (2010) 969–976.

[165] C. A. Coulomb, Théorie des machines simples, Mémoires de Mathématique et de Physique de l'Academie des Sciences 10 (1785) 161–331.

[166] F. P. Bowden, D. Tabor, Friction and Lubrication of Solids, Clarendon Press, Oxford, UK, 1950.

[167] M. C. Shaw, A. Ber, P. A. Mamin, Friction characteristics of sliding surfaces undergoing subsurface plastic flow, Journal of Basic Engineering 82 (1960) 342–345.

[168] T. Wanheim, N. Bay, A. S. Petersen, A theoretically determined model for friction in metal working processes, Wear 28 (1974) 251–258.

[169] T. Wanheim, N. Bay, A model for friction in metal forming processes, CIRP Annals Manufacturing technology 27 (1) (1978) 189–194.

[170] E. Orowan, The calculation of roll pressure in hot and cold flat rolling, Proceedings of the Institution of Mechanical Engineers: 150 (1943) 140–167.

[171] T. Nellemann, N. Bay, T. Wanheim, Real area of contact and friction stresses - the role of trapped lubricant, Wear 43 (1977) 45–53.

[172] N. Bay, Friction stress and normal stress in bulk metal-forming processes, Journal of Mechanical Working Technology 14 (2) (1987) 203–223.

[173] H. Steffensen, T. Wanheim, Asperities on asperities, Wear 43 (1977) 89–98.

[174] N. Bay, T. Wanheim, A. S. Petersen, Ra and the average effective strain of surface asperities deformed in metal working processes, Wear 34 (1975) 77–84.

[175] J. A. Greenwood, J. B. P. Williamson, Contact of nominally flat surfaces, Proceedings of the Royal Society A295 (1966) 300–319.

[176] J. A. Greenwood, J. H. Tripp, The contact of two nominally flat rough surfaces, Proceedings of the Institution of Mechanical Engineers 185 (1971) 625–633.

[177] B. J. Hamrock, S. R. Schmid, B. O. Jacobson, Fundamentals of Fluid Film Lubrication, 2nd Edition, Marcel Dekker Inc., New York, NY, 2004.

[178] B. Lorentz, A. Albers, A numerical model for mixed lubrication taking into account surface topography, tangential adhesion effects and plastic deformations, Tribology International 59 (2013) 259–266.

[179] A. Stephany, H. R. Le, M. P. F. Sutcliffe, An efficient finite element model of surface pit reduction on stainless steel in metal forming processes, Journal of Materials Processing Technology 170 (2005) 310–316.

[180] A. Belotserkovets, Vers une prediction du profil de rugosite a l'echelle mesoscopique lors de l'operation de laminage a froid, Ph.D. thesis, Université de Valenciennes, Valenciennes, France, in French (2009).

[181] R. Deltombe, A. Belotserkovets, M. Dubar, M. Dubois, L. Dubar, Local approach strategy to predicting final roughness in cold rolling of stainless steel strips, Proceedings of the Institution of Mechanical Engineers Part J: Journal of Engineering Tribology 225 (9) (2011) 887–893.

[182] C. Hubert, N. Bay, P. Christiansen, R. Deltombe, L. Dubar, M. Dubar, A. Dubois, Numerical simulation of lubrication mechanisms at mesoscopic scale, in: Proceedings of the 14th International ESAFORM Conference, Belfast, N. Ireland, 978–0–7354–0911–81729–1734.

[183] L. Dubar, C. Hubert, P. Christiansen, N. Bay, A. Dubois, Analysis of fluid lubrication mechanisms in metal forming at mesoscopic scale, CIRP Annals Manufacturing Technology 61 (2012) 271–274.

[184] C. Barus, Isothermal, isopietics and isometrics in relation to viscosity, American Journal of Science 3rd Series 45 (1893) 87–96.

[185] N. Patir, H. S. Cheng, Application of average flow model to lubrication between rough sliding surfaces, Transaction of ASME 101 (1979) 220–230.

Appendix A

Calibration certificate for FTS50 inductive

CGM
CENTER FOR GEOMETRISK METROLOGI

ilac-MRA

DANAK
CAL Reg.Nr. 273

Kalibreringscertifikat
Calibration Certificate

Antal Bilag **2**
No of Enclosures **2**
Rum11011

Certifikat nr.
Certificate No. **Rum11011**

Objekt
Object **Ruhedsmåler / Roughness measuring instrument**

Fabrikant
Manufacturer **Taylor Hobson**

Type
Type **Form Talysurf Series 2 50 i**

Serienummer
Serial number **2593S3C-09 /Stylus 2 µm standard 112/2564-1209**

Rekvirent
Customer **DTU Mekanik**
Produktionstorvet
2800 Kgs. Lyngby

Dato for modtagelse
Date of reciept **13.12.11**

Dato for certifikatets udstedelse
Date of issue of certificate **31.12.11**

Dato for kalibrering
Date of calibration **13.12.11**

Underskrift
Signature

Jan L. Andreasen
Fagligt ansvarlig
Signatory, Surface Roughness Calibration

Center for Geometrisk Metrologi, Bygning 425
DTU Mekanik, Danmarks Tekniske Universitet
2800 Kgs. Lyngby, CVR-nr. 30 06 09 46
Telefon 45 25 47 60 – Telefax 45 93 01 90 – Email cgm@cgm.dk

Kalibreringens omfang.

Inden kalibreringen er tastspidserne undersøgt for skader og slid og tasttrykket er evalueret. Baggrundsstøjen på ruhedsmåleren er bestemt ud fra 10 aftastninger på et planglas udtrykt som Ra med cut-off 0.8 mm. I hvert kalibreret forstærkningstrin e er der foretaget 5 aftastninger på relevante forstærkningsnormaler til kalibrering af forstærkning. I det størstforstærkningstrin er der foretaget 12 aftastninger på relevante parameternormaler til kalibrering af Ra.

Extent of calibration.

Before the calibration the stylus tips have been checked for damage and wear and the measuring force has been evaluated. The background noise of the roughness measuring instrument has been determined from 10 traces on an optical flat expressed as Ra using cut-off 0.8 mm. In each calibrated magnification range 5 traces has been made on relevant magnification standards for calibration of magnification. In the highest magnification range 12 traces has been made on relevant roughness standards for calibration of Ra.

Kalibreringsresultater og –usikkerheder.

Nedenfor er baggrundsstøjen på ruhedsmåleren og kalibreringsfaktorerne for de kalibrerede forstærkningstrin angivet. Kalibreringsfaktorerne er kun gyldige for den kombination af forstærkning og tast, som er anvendt ved kalibreringen. For forstærkningstrin, hvor kalibreringen er foretaget med flere normaler er der ligeledes givet en kalibreringstabel, som dækker hele måleområdet. Usikkerheden er angivet med faktor k=2 ≈ 95 % konfidensniveau.

Calibration results and uncertainties.

Below the background noise and the calibration factors for the calibrated magnification ranges are given. The calibration factors are only valid for the combination of magnification range and stylus used during the calibration. In measuring ranges where the calibration has been carried with more than one standard a calibration table covering the whole measuring range is also given. The uncertainties refer to the factor k=2 ≈ 95 % confidence level.

Forstærkningstrin Magnification range	Filter cut-off mm Filtre cut-off mm	Baggrundsstøj Ra µm Background noise Ra µm
210 µm, Ultra software	0.80	0.008
210 µm, Sursam74 software	0.80	0.008

Kalibreret Forstærkning / Calibrated Magnification				
Forstærkningstrin Magnification	Referenceværdi Reference value	Filter cut-off mm Filtre cut-off mm	Kalibreringsfaktor Calibration factor	Usikkerhed µm Uncertainty µm
210 µm, Sursam74 software	d = 9.292 µm	Ufiltreret/unfiltered	1.002	0.112

Kalibreret Ra-beregning / Calibrated Ra calculation				
Forstærkningstrin Magnification	Referenceværdi Reference value	Filter cut-off mm Filtre cut-off mm	Kalibreringsfaktor Calibration factor	Usikkerhed µm Uncertainty µm
210 µm, Ultra software	Ra=0.229 µm	0.80	1.009	0.010
210 µm,Ultra software	Ra=0.604 µm	0.80	1.008	0.024
210 µm, Ultra software	Ra=1.706 µm	0.80	1.016	0.068
210 µm, Sursam74 software	Ra=0.229 µm	0.80	0.996	0.009
210 µm, Sursam74 software	Ra=0.604 µm	0.80	1.002	0.024
210 µm, Sursam74 software	Ra=1.706 µm	0.80	1.006	0.068

Måledata.

Parameternormalerne er aftastet i 12 snit fordelt over målefladen. Den følgende tabel giver de beregnede Ra-værdier. Ruhedsmåleren er ikke blevet justeret.

Measuring data.

The parameter standards have been measured in 12 traces distributed over the measuring surface. The table below gives the calculated Ra values. No adjustment has been performed.

Referenceværdi Ra, cut-off 0.80 mm Reference value Ra, cut-off 0.80 mm	0.229 µm	0.604 µm	1.706 µm	0.229 µm	0.604 µm	1.706 µm
Software	Ultra			Sursam74		
Måling nummer Measurement number						
1	0.2279	0.5670	1.6831	0.229	0.601	1.689
2	0.2340	0.6077	1.6733	0.233	0.600	1.692
3	0.2166	0.6181	1.6733	0.231	0.599	1.683
4	0.2288	0.6187	1.6750	0.232	0.601	1.678
5	0.2264	0.5997	1.7008	0.232	0.600	1.694
6	0.2260	0.5882	1.6532	0.227	0.601	1.697
7	0.2272	0.5785	1.6651	0.228	0.604	1.689
8	0.2271	0.5870	1.6682	0.231	0.606	1.691
9	0.2261	0.6145	1.6701	0.229	0.602	1.715
10	0.2343	0.6153	1.6753	0.231	0.606	1.708
11	0.2316	0.5898	1.6990	0.230	0.609	1.709
12	0.2186	0.6053	1.7177	0.226	0.602	1.702

Måledata.

Forstærknings normalen er aftastet i 5 snit fordelt over målefladen. Den følgende tabel giver de målte rilledybder i form af d. Ingen justering er foretaget.

Measuring data.

The magnification standard has been measured in 5 traces distributed over the measuring surface. The table below gives the measured groove depths in term of d. No adjustment has been performed.

Reference rilledybde / Reference groove depth	9.292 µm		
Forstærkning / Magnification Måling nummer Measurement number	210 µm [µm]		
1	9.262		
2	9.285		
3	9.280		
4	9.262		
5	9.293		

Målebetingelser.

Målingerne er udført ifølge procedurerne RU-522 og RU-541. Kalibreringen af profil diagram er foretaget mod ISO type A2 normal med nominelle rille dybde på 9.3 µm. Kalibreringen af parameterberegningen er foretaget mod ISO type D parameternormaler med nominelle Ra-værdier på 0.2 µm, 0.5 µm og 1.7 µm. Målingerne er foretaget med cut-off 0.8 mm (fasekorrekt filter). Ingen kort bølge Ls filter er anvendt. Målingerne er foretaget ved en temperatur på 20 ± 2°C.

Measuring conditions.

The measurements were carried out in accordance with procedures RU-522 and RU-541. The calibration of the profile diagram has been performed using ISO type A 2 roughness standard with nominal groove depth of 9.3 µm. The calibration of the parameter calculation has been performed using ISO type D roughness standards with nominal Ra values of 0.2 µm, 0.5 µm and 1.7 µm. The measurements have been carried out using cut-off 0.8 mm (Gaussian filter). No short wave Ls cut-off was used. The measurements have been carried out at a temperature of 20 ± 2°C.

Kalibreringen er sporbar via normalen:
The calibration is traceable through the standard: **PTB/Halle RN1171 (ISO type D)**

Med certifikatet:
With the certificate: **Rou11004**

Certifikatet er dateret:
The certificate is dated: **02.03.11**

Og
And

Kalibreringen er sporbar via normalen:
The calibration is traceable through the standard: **PTB/Halle RN1261 (ISO type D)**

Med certifikatet:
With the certificate: **Rou11003**

Certifikatet er dateret:
The certificate is dated: **28.02.11**

Og
And

Kalibreringen er sporbar via normalen:
The calibration is traceable through the standard: **PTB/Halle RN1246 (ISO type D)**

Med certifikatet:
With the certificate: **Rou11002**

Certifikatet er dateret:
The certificate is dated: **28.02.11**

Og
And

Kalibreringen er sporbar til:
The calibration is traceable to: **PTB**

Kalibreringen er sporbar via normalen:
The calibration is traceable through the standard: **HALLE no. 826**

Med certifikatet:
With the certificate: **091 PTB 08**

Certifikatet er dateret:
The certificate is dated: **07.11.08**

Bilag til certifikat nr.
Annex to certificate No. **Rum11011**

Baggrundsstøjens betydning for de udførte målinger.

Baggrundsstøjen stammer fra de elektriske og de mekaniske dele i ruhedsmåleren. Der er tale om systematiske fejl på instrumentet - d.v.s. fejl som altid er til stede og som i princippet kan elimineres ved justering og/eller kompensation. Alle profiler vil således være overlejret denne baggrundsstøj, hvilket betyder, at de beregnede ruhedsværdier vil være større end de reelle ruhedsværdier. Som en hovedregel bør ruhedsmåleren ikke anvendes til målinger, af emner med Ra-værdi, der er mindre end 5 gange baggrundsstøjen, da bidraget fra denne ellers bliver uforholdsmæssigt stort.

The influence from the background noise on the measurement results.

The background noise has its origin in the electrical and mechanical components of the roughness instrument – that is, errors who are always present and which it is possible to eliminate by either adjustment or compensation. The measured roughness profiles will in that way be superimposed with this background noise. This means that the calculated roughness parameter values will be greater than the reel ones. As a general rule the roughness instrument should not be used for measurements of surfaces having a Ra-value less than 5 times the background noise, otherwise this contribution to the measurement result will become to large.

Vilkår for certifikatet
Conditions for the certificate

DANAK

Den Danske Akkrediterings- og Metrologifond -DANAK- administrerer den danske akkrediteringsordning på grundlag af en aftale med Sikkerhedsstyrelsen under Økonomi- og Erhvervsministeriet, som er ansvarlig for lovgivningen om akkreditering i Danmark.

De grundlæggende akkrediteringskriterier er beskrevet i henholdsvis DS/EN ISO/IEC 17025 "Generelle krav til prøvnings- og ka1ibreringslaboratoners kompetence" og i DS/EN ISO 15189 "Medicinske laboratorier- Særlige krav til kva1itet og kompetence". DANAK anvender fortolkningsdokumenter til de enkelte krav i standarderne, hvor det skønnes nødvendigt. Disse vil hovedsageligt være udarbejdet af "European co-operation for Accreditation (EA)" eller "Internationa1 Laboratory Accreditation Co-operation (ILAC)" med det formå1 at opnå ensartede kriterier for akkreditering på verdensplan. Sikkerhedsstyrelsen udsteder desuden tekniske forskrifter udarbejdet af DANAK vedr. specifikke krav til akkreditering, som ikke er indeholdt i standarderne.

For at et laboratorium kan være akkrediteret kræves blandt andet:

- at laboratoriet og dets personale skal være fri for enhver kommerciel, økonomisk eller anden form for pression, som kan påvirke deres uvildighed,
- at laboratoriet har et dokumenteret ledelsessystem og en ledelse, der kan sikre, at dette følges og vedligeholdes,
- at laboratoriet råder over teknisk udstyr og lokaler af en tilstrækkelig standard til at kunne udføre den ydelse, som laboratoriet er akkrediteret til,
- at laboratoriet råder over personale med såvel faglig kompetence som praktisk erfaring i udførelsen af de ydelser, som laboratoriet er akkrediteret til,
- at der er indarbejdet faste rutiner for sporbarhed og usikkerhedsbestemmelse,
- at akkrediteret prøvning, kalibrering eller medicinsk undersøgelse udføres efter fuldt validerede og dokumenterede metoder,
- at akkrediterede ydelser udføres og rapporteres i fortrolighed med rekvirenten og i overensstemmelse med dennes behov,
- at laboratoriet skal registrere forløbet af akkrediteret prøvning, kalibrering eller medicinsk undersøgelse således, at dette kan rekonstrueres,
- at laboratoriet er underkastet regelmæssigt tilsyn af DANAK,
- at laboratoriet skal have en forsikring, som kan dække laboratoriets ansvar i forbindelse med udførelsen af akkrediterede ydelser.

Rapporter, der bærer DANAK's akkrediteringsmærke, anvendes ved rapportering af akkrediterede ydelser og viser, at disse er foretaget i henhold til akkrediteringsreglerne.

DANAK

The Danish Accreditation and Metrology Fund -DANAK -is managing the Danish accreditation scheme based on a contract with the Danish Safety Technology Authority under the Danish Ministry of Economics and Business Affairs who is responsible for the legislation on accreditation in Denmark.

The fundamental criteria for accreditation are described in DS/EN ISO/IEC 17025: "General requirements for the competence of testing and calibration laboratories", and in DS/EN ISO/IEC 15189 "Medical laboratories -Particular requirements for quality and competence" respectively. DANAK uses guidance documents to clarify the requirements in the standards, where this is considered to be necessary.. These will mainly be drawn up by the "European co-operation for Accreditation (EA)" or the "International Laboratory Accreditation Co-operation (ILAC)" with a view to obtaining uniform criteria for accreditation worldwide. In addition, the Danish Safety Technology Authority issues Technical Regulations prepared by DANAK with specific requirements for accreditation that are not contained in the standards.

In order for a laboratory to be accredited it is, among other things, required:

- that the laboratory and its personnel are free from any commercial, financial or other pressures, which might influence their impartiality;
- that the laboratory operates a documented management system, and has a management that ensures that the system is followed and maintained;
- that the laboratory has at its disposal all items of equipment, facilities and premises required for correct performance of the service that it is accredited to perform;
- that the laboratory has at its disposal personnel with technical competence and practical experience in performing the services that they are accredited to perform;
- that the laboratory has procedures for traceability and uncertainty calculations;
- that accredited testing, calibration or medical examination are performed in accordance with fully validated and documented methods;
- that accredited services are performed and reported in confidentiality with the customer and in compliance with the customer’s request;
- that the laboratory keeps records which contain sufficient information to permit repetition of the accredited test, calibration or medical examination;
- that the laboratory is subject to surveillance by DANAK on a regular basis;
- that the laboratory shall take out an insurance, which covers liability in connection with the performance of accredited services.

Reports carrying DANAK' s accreditation mark are used when reporting accredited services and show that these have been performed in accordance with the rules for accreditation.

Appendix B

Filters Matlab codes

In this appendix are attached the Matlab codes for the Robust Gaussian Regression filter and for the morphological filter. The case of the RGR filter of the 2nd order with the fast Fourier transform is here presented.

```
function [wp,rp,its,cb0] = RGR2(data,dx,wl,ffconst,eps,no1,cbtype,deltatype)
% Robust Gaussian regression algorithm
% ffconst = filter constant
% its = array saving no of iterations for each profile
% wp = the calculated reference profile = long wave component
% rp = the roughness profile = z-wp
% The convergence criteria eps = 0.0001;

[profiles,n] = size(data);
[no1s,nn] = size(no1);

if profiles ~= no1s
    disp('Number of guesses not equal to no of profiles');
    disp('- setting guesses euqal to []');
    no1 = [];
end

its = zeros(profiles,1);
wp = zeros(profiles,n);
rp = zeros(profiles,n);

for i=1:profiles  % Perform Regression for each profiles
    disp(['Performing Robust GR2 for profile: ',sprintf('%d',i)]);

    its(i) = 0;     % Set iteration to 0
    delta = ones(1,n); % Set initial additional weight function to 1
    cb0(i) = 1;         % Set initial cb threshold to 1

    % Calc initial guess if needed
    if isempty(no1)
```

```
        [first,rfirst] = GR2fft(data(i,:),dx,wl,ffconst,delta);
    else
        disp('Initial "guess" used for iteration 0');
        first = no1(i,:);
    end

    % Calc residuals / residual profile
    res = data(i,:) - first;
    cb1(i) = CalcCB(res,cbtype);

    % Perform the iterations if condition is not meet!
    while abs((cb0(i)-cb1(i))/(cb0(i)+10^(-10))) > eps
        its(i) = its(i)+1;      % Increase iteration number
        cb0(i) = cb1(i);              % Set new "initial" cb
        delta = CalcDelta(res,cb0(i),deltatype);
        [wp(i,:),rp(i,:)] = GR2fft(data(i,:),dx,wl,ffconst,delta);
        res = data(i,:) - wp(i,:);
        cb1(i) = CalcCB(res,cbtype);
        disp([sprintf('Iteration %d complet. Updated cb from %f to %f',...
            its(i),cb0(i),cb1(i))]);
    end
    disp([sprintf('Robust GR2 finished')]);
    first = [];
end

end
```

Three functions not defined in Matlab are present in this script, namely **GR2fft**, **CalcDelta** and **CalcCB**. CalcDelta gives the opportunity of choosing a re-weighing function and CalcCB calculates the threshold. The code for GR2fft is hereby presented:

```
function [longwl, shortwl] = GR2fft(z, dx, lambda, ffconst, wf)

n = length(z);          % Number of profile points

if isempty(wf)
    wf = ones(1,n);
    disp('Additional Weighing Function set to all ones');
end

longwl = zeros(1,n);
shortwl = zeros(1,n);

A = zeros(3,3);
B = zeros(3,1);

% Use maximum of 6*sigma...
sigma = sqrt(log(2)/2/pi^2)*lambda;
q = ceil(6*sigma/dx/2)*2;   % Making sure q is even
```

```
% Construct filter function
p=(1:1:q);
S1 = 1/(sqrt(2*pi)*lambda*ffconst)*...
        exp(-0.5*(p*dx/lambda/ffconst).^2);
S2 = flipdim(S1,2);
S0 = 1/(sqrt(2*pi)*lambda*ffconst);
S = cat(2,S2,S0,S1);


x1 = p*dx;
x2 = -flipdim(x1,2);
x0 = 0;
x = cat(2,x2,x0,x1);
    % Proceed with regression - find constants
    M{1,1} = fftconv(wf,S.*x.^4);
    M{1,2} = fftconv(wf,S.*x.^3);
    M{1,3} = fftconv(wf,S.*x.^2);
    M{2,1} = M{1,2};
    M{2,2} = M{1,3};
    M{2,3} = fftconv(wf,S.*x);
    M{3,1} = M{1,3};
    M{3,2} = M{2,3};
    M{3,3} = fftconv(wf,S);
    Q{1,1} = fftconv(wf.*z , S.*x.^2);
    Q{2,1} = fftconv(wf.*z , S.*x);
    Q{3,1} = fftconv(wf.*z , S);

for k=1:n
    % Solve the linear systems AP = B
    for i=1:3
        for j=1:3
            A(i,j) = M{i,j}(k);
        end
        B(i) = Q{i,1}(k);
    end

    P = A\B;

    longwl(1,k) = P(3);
    shortwl(1,k) = z(1,k) - longwl(1,k);
end
```

A verification of the filter performances against the ones of the commercial software MountainsMap® 6.1 Premium is given in figure B.1.
The code for the morphological closing operation is presented in the following:

```
function [wp] = morphological(z,dx,R)
% This function apllies a morphological filtering to a profile
```

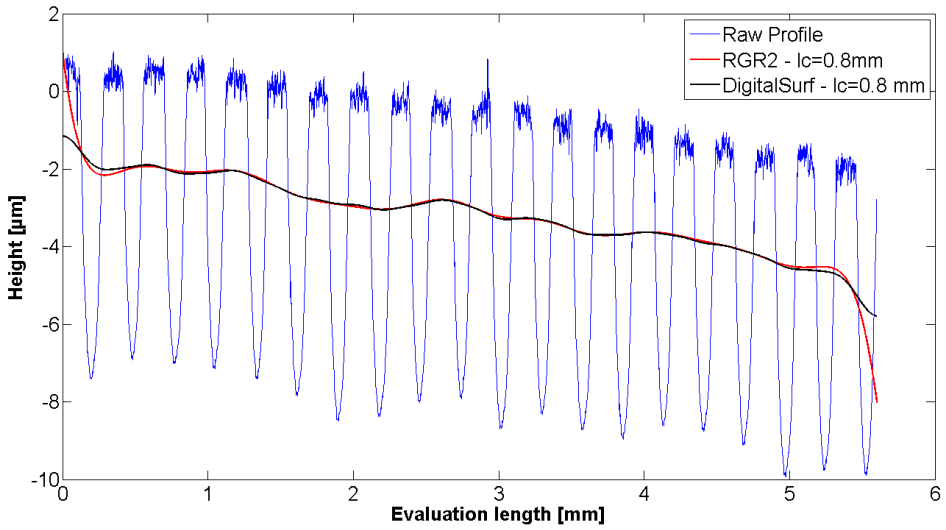

Figure B.1: *Comparison of the filtering reference lines calculated with the Matlab scripts and with MountainsMap® 6.1 Premium.*

```
% dx= spacing in mm!!!
% R= radius of the element in mm!!!
% CLOSING operation

[w1]=dilation(z,dx,R);
[wp]=erosion(w1,dx,R);
end
```

where **dilation** and **erosion** are morphological functions described by the codes:

```
function [wp] = dilation(z,dx,R)
% This function apllies the dilation operation to a profile

% dx= spacing in mm!!!
% R= radius of the element in mm!!!

n = length(z);

R=R*1000; %now in microns
dx=dx*1000; %now in microns

%allocate memory for wp, line resulting from the dilation
wp = zeros(n,1);

%calculate how many points are needed for a half circle and allocate space
%for the circle coordinates
```

```
m = 2*R/dx;
y= zeros(m+n,n);
minz= min(z);

for i=1:n
    z(i)=z(i)-minz; %minimum of profile set to ZERO, create an offset
end;

for j=1:n
    for i=j:j+m
        y(i,j)=i*dx - R; %for each point of the profile calculate the abscissas cov
        y(i,j)=z(j)+sqrt(R^2-(y(i,j)-j*dx)^2); %calculates half circles
    end;
end;

%calculate the wp vector

for i=1:n
    wp(i,1)=max(y(i+m/2,:),[],2);
end;

for i=1:n
    wp(i)=wp(i)+minz; %eliminate the offset
end;

%arrange the vector on a line
wp=wp';

end



function [wp] = erosion(z,dx,R)
% This function apllies the erosion operation to a profile

% dx= spacing in mm!!!
% R= radius of the element in mm!!!

n = length(z);

R=R*1000; %now in microns
dx=dx*1000; %now in microns

%allocate memory for wp, line resulting from the dilation
wp = zeros(n,1);

%calculate how many points are needed for a half circle and allocate space
%for the circle coordinates
m = 2*R/dx;
y= zeros(m+n,n);
maxz= max(z);
```

```
for i=1:n
    z(i)=z(i)-maxz; %minimum of profile set to ZERO
end;

for j=1:n
    for i=j:j+m
        y(i,j)=i*dx - R; %for each point of the profile calculate the abscissas cov
        y(i,j)=z(j)-sqrt(R^2-(y(i,j)-j*dx)^2); %calculates half circles
    end;
end;

%calculate the wp vector

for i=1:n
    wp(i,1)=min(y(i+m/2,:),[],2);
end;

for i=1:n
    wp(i)=wp(i)+maxz; %eliminate the offset
end;

%arrange the vector on a line
wp=wp';

end
```

The last code is a pseudocode for performing a three dimensional feature separation:

```
for j=1:m
    for i:1=n
        if z(x(i,j)+1,j)>z(x(i,j),j)
        %x(i,j) abscissa of the first point above the lower threshold
            p=0;
            while  z(x(i,j)+p,j)<z(x(i,j)+k,j)
            %z(x(i,j)+k,j) first point above upper threshold
                erase(z(x(i,j)+p,j));
                p=p+1;
            end
        else
            p=0;
            while  z(x(i,j)-p,j)<z(x(i,j)-k,j)
            %z(x(i,j)-k,j) first point above upper threshold
                erase(z(x(i,j)-p,j));
                p=p+1;
            end
        end
    end
end
```

The *erase* function is not defined, but, like for the 2D case, it should substitute the height value with a void value keeping allocated the memory for the X-Y position. Therefore at a certain (x, y) position would correspond a null or void value.

Appendix C

Calculation of AST normal pressure

In this appendix the verification and calibration procedure for calculating the AST pressures by means of the Strecon model is presented. The model is written in Excel and only the part of interest is here displayed.
The first step is to insert the input data in the case when no rod is present:
From figure C.1 it can be seen that, given the geometry, by selecting a proper shrinkage goal of the conical housing (sleeve outer diameter d1) a shrinkage of 0.013 mm is obtained corresponding to a container advancement of 1 mm. The model is verified if the shrinkage will be equal to the experimentally determined 0.009 mm if the inner diameter do is set to 26 mm, corresponding to the case of the hollow rod:
The model has thus been verified. The following step is to calibrate it by relating the outer diameter to the sleeve and not to the housing outer diameter. This is done by replacing d1 with 38 and re-calculating the shrinkage goal. The shrinkage should be 0.013 mm when no rod is inside. Therefore the goal, which follows the formula $\text{Shrinkage goal} = (\text{Shrinkage/d1}) \cdot 1000$, is set to 0.3421 (figure C.3).
The advance calculated in figure C.3 corresponds to 1 mm advance at a outer diameter Ø80 mm, teh housing outer diameter. It can be noticed that with new settings, the shrinkage in the case of hollow rod ($\text{do} = 26mm$) is equal to 0.009 mm as experimentally demonstrated. Finally, the normal pressure on a full rod is calculated by substituting do with an extremely low value (if zero is set, the model gives an error). The normal pressure on a full rod is estimated being **34 MPa** every mm of advancement of the stripwound contaienr (figure C.3).

STRECON Beregningsprogram			Input	
Client	MUFU AST	SBA nr	A4017	
Matrice			Material	
Inner diameter	do	38	E-modul	210
Outer diameter	d1	80	Poisson	0.3
Sleeve height	h	58		
Cone angle	v	1	Friction	0.05
Internal pressure from the process	Pi	1		
Kerne				
Inner diameter	d1	80	E-modul	210
Outer diameter	d2	100	Poisson	0.3
STRECON	6			
Inner diameter	d2	100	E-modul	205
Udv. STRECON diameter	d4	160	Poisson	0.3
Shrinkage goal at d1	‰	0.4365		
Resultater fra HM Kerne u/kærvfaktorer				
Pressure d1		[MPa]	28	
Tangential prestressing do			-72	
Diameter reduction do		[mm]	-0.013	
Diameter expansion d4		[mm]	0.014	
Fvalue matrice		[-]	0.178	
Delta tan/delta rad		[-]	1.123	
Diameter springing internal pressure pi= 1		[mm]	0.000	
E-modul Pseudo		[GPa]	207	
Resultater fra Koef1 (I-presse / Udpresse)				
I-presse		[ton]	2.8	
Udpresse		[ton]	1.3	
Advance		[mm]	1.000	

Figure C.1: *Calculating the shrinkage when no rod is present in the assembly. The height is set to 58 mm that is the 60 mm minus 2 mm of chamfers.*

STRECON Beregningsprogram			Input	
Client	MUFU AST	SBA nr	A4017	
Matrice			Material	
Inner diameter	do	26	E-modul	210
Outer diameter	d1	80	Poisson	0.3
Sleeve height	h	58		
Cone angle	v	1	Friction	0.05
Internal pressure from the process	Pi	1		
Kerne				
Inner diameter	d1	80	E-modul	210
Outer diameter	d2	100	Poisson	0.3
STRECON	6			
Inner diameter	d2	100	E-modul	205
Udv. STRECON diameter	d4	160	Poisson	0.3
Shrinkage goal at d1	‰	0.4365		
Resultater fra HM Kerne u/kærvfaktorer				
Pressure d1		[MPa]	31	
Tangential prestressing do			-70	
Diameter reduction do		[mm]	-0.009	
Diameter expansion d4		[mm]	0.016	
Fvalue matrice		[-]	0.081	
Delta tan/delta rad		[-]	1.056	
Diameter springing internal pressure pi= 1		[mm]	0.000	
E-modul Pseudo		[GPa]	207	
Resultater fra Koef1 (I-presse / Udpresse)				
I-presse		[ton]	3.1	
Udpresse		[ton]	1.5	
Advance		[mm]	1.000	

Figure C.2: *Verification of the shrinkage when a hollow rod is present.*

STRECON Beregningsprogram			Input	
Client	MUFU AST	SBA nr	A4017	
Matrice			Material	
Inner diameter	do	26	E-modul	210
Outer diameter	d1	38	Poisson	0.3
Sleeve height	h	58		
Cone angle	v	1	Friction	0.05
Internal pressure from the process	Pi	1		
Kerne				
Inner diameter	d1	38	E-modul	210
Outer diameter	d2	100	Poisson	0.3
STRECON	6			
Inner diameter	d2	100	E-modul	205
Udv. STRECON diameter	d4	160	Poisson	0.3
Shrinkage goal at d1	‰	0.3421		
Resultater fra HM Kerne u/kærvfaktorer				
Pressure d1		[MPa]	18	
Tangential prestressing do			-70	
Diameter reduction do		[mm]	-0.009	
Diameter expansion d4		[mm]	0.002	
Fvalue matrice		[-]	0.453	
Delta tan/delta rad		[-]	1.056	
Diameter springing internal pressure pi= 1		[mm]	0.000	
E-modul Pseudo		[GPa]	209	
Resultater fra Koef1 (I-presse / Udpresse)				
I-presse		[ton]	0.9	
Udpresse		[ton]	0.4	
Advance		[mm]	0.372	

Figure C.3: *Shrinkage related to the sleeve inner diameter.*

STRECON Beregningsprogram				Input
Client	MUFU AST	SBA nr	A4017	
Matrice			Material	
Inner diameter	do	0.000001	E-modul	210
Outer diameter	d1	38	Poisson	0.3
Sleeve height	h	58		
Cone angle	v	1	Friction	0.05
Internal pressure from the process	Pi	1		
Kerne				
Inner diameter	d1	38	E-modul	210
Outer diameter	d2	100	Poisson	0.3
STRECON	6			
Inner diameter	d2	100	E-modul	205
Udv. STRECON diameter	d4	160	Poisson	0.3
Shrinkage goal at d1	‰	0.3421		
Resultater fra HM Kerne u/kærvfaktorer				
Pressure d1		[MPa]	34	
Tangential prestressing do			-68	
Diameter reduction do		[mm]	0.000	
Diameter expansion d4		[mm]	0.003	
Fvalue matrice		[-]	0.000	
Delta tan/delta rad		[-]	1.000	
Diameter springing internal pressure pi= 1		[mm]	0.000	
E-modul Pseudo		[GPa]	209	
Resultater fra Koef1 (I-presse / Udpresse)				
I-presse		[ton]	1.6	
Udpresse		[ton]	0.8	
Advance		[mm]	0.372	

Figure C.4: *Calculation of normal pressure on a full rod.*

Appendix D

SRT parameters, force curves and galling analyses

In this appendix are collected all the parameters, the force curves and the multiplots from the strip reduction tests.

Tool ID	Top plate Thickness	Tool Diameter	Strip Thickness	Strip Width	Reduction %	Adjustement	Comments		
	mm	mm	mm	mm	%	mm		Redt	Red %
SRT1_1	12.680	16.640	0.710	15.00	20	0.35	Change coeff to 4.74	0.47	33.80
SRT1_2	12.680	16.630	0.707	15.00	20	0.22	Twisted and broken		
SRT1_3	12.680	16.640	0.712	15.00	20	0.21		0.579	18.68
SRT1_4	12.680	16.640	0.715	15.00	20	0.21		0.575	19.58
SRT2_1	12.680	16.680	0.711	15.00	20	0.17	Starting breakage	0.583	18.00
SRT2_2	12.680	16.676	0.708	15.00	20	0.18	Twisted and broken	0.577	18.50
SRT2_3	12.680	16.680	0.712	15.00	20	0.17	Twisted and broken	0.585	17.84
SRT2_4	12.680	16.676	0.706	15.00	20	0.18		0.573	18.84
Pol1_1	12.680	16.697	0.703	15.00	20	0.16		0.59	16.07
Pol1_2	12.680	16.697	0.706	15.00	20	0.18	Change coeff to 4.76	0.583	17.42
Pol1_3	12.680	16.697	0.706	15.00	20	0.18		0.583	17.42
Pol1_4	12.680	16.697	0.703	15.00	20	0.22	Change coeff to 4.8	0.545	22.48
Pol1_5	12.680	16.697	0.706	15.00	20	0.22		0.571	19.12
Pol1_6	12.680	16.697	0.708	15.00	20	0.22		0.546	22.88
Pol1_7	12.680	16.697	0.708	15.00	28	0.27		0.511	27.82
Pol1_8	12.680	16.697	0.704	15.00	28	0.28		0.498	29.26
Pol2_1	12.680	16.685	0.705	15.00	20	0.23		0.545	22.70
Pol2_2	12.680	16.685	0.703	15.00	20	0.23		0.55	21.76
Pol2_3	12.680	16.685	0.704	15.00	28	0.29		0.55	21.88
Pol2_4	12.680	16.685	0.706	15.00	28	0.29		0.49	30.59
Pol2_5	12.680	16.685	0.701	15.00	20	0.23		0.495	29.39
Pol2_6	12.680	16.685	0.705	15.00	33	0.32		0.462	34.47
Pol2_7	12.680	16.685	0.708	15.00	20	0.23	Scratch on tool	0.552	22.03
Pol2_8	12.680	16.685	0.703	15.00	35	0.34		0.438	37.70
SRT3_1	12.564	16.552	0.706	15.00	20	0.25		0.55	22.10
SRT3_2	12.564	16.558	0.705	15.00	20	0.24		0.547	22.41
SRT3_3	12.564	16.560	0.705	15.00	20	0.24		0.536	23.97
SRT3_4	12.564	16.554	0.704	15.00	20	0.25		0.533	24.29
SRT3_5	12.564	16.549	0.700	15.00	20	0.26		0.537	23.29
SRT3_6	12.564	16.562	0.706	15.00	20	0.24		0.545	22.80
SRT3_7	12.564	16.563	0.704	15.00	20	0.24		0.525	25.43
SRT3_8	12.564	16.560	0.706	15.00	20	0.24		0.545	22.80
SRT4_1	12.564	16.606	0.700	15.00	20	0.20	Twisted and broken	0.552	21.14
SRT4_2	12.564	16.599	0.701	15.00	20	0.20	Tried oil CR5	0.51	27.25
SRT4_3	12.564	16.607	0.707	15.00	20	0.19	Twisted and broken	0.563	20.37
SRT4_4	12.564	16.595	0.708	15.00	20	0.20	Tried oil CR5	0.55	22.32
SRT4_5	12.564	16.605	0.707	15.00	20	0.19		0.57	19.38
SRT4_6	12.564	16.604	0.703	15.00	20	0.20	High reduction	0.485	31.01
SRT4_7	12.564	16.600	0.705	15.00	20	0.20		0.548	22.27
SRT4_8	12.564	16.565	0.702	15.00	20	0.24	High reduction	0.466	33.62

Figure D.1: *Test parameters for the SRT tools.*

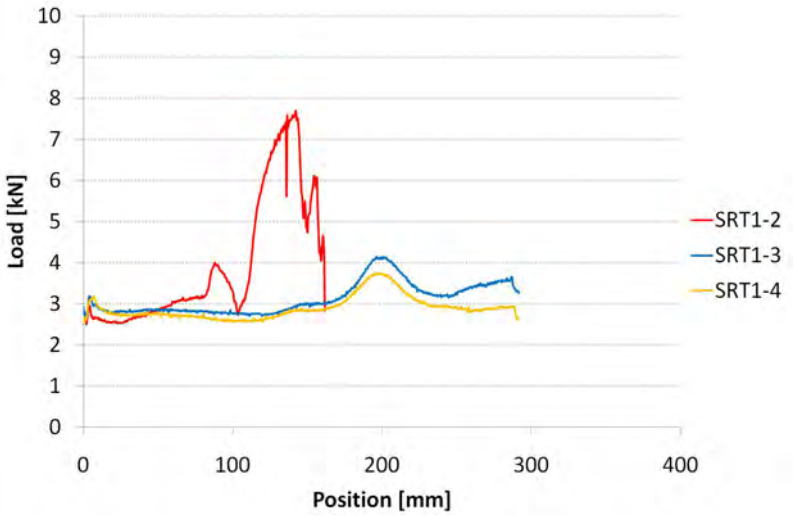

Figure D.2: *Force results of tool SRT1.*

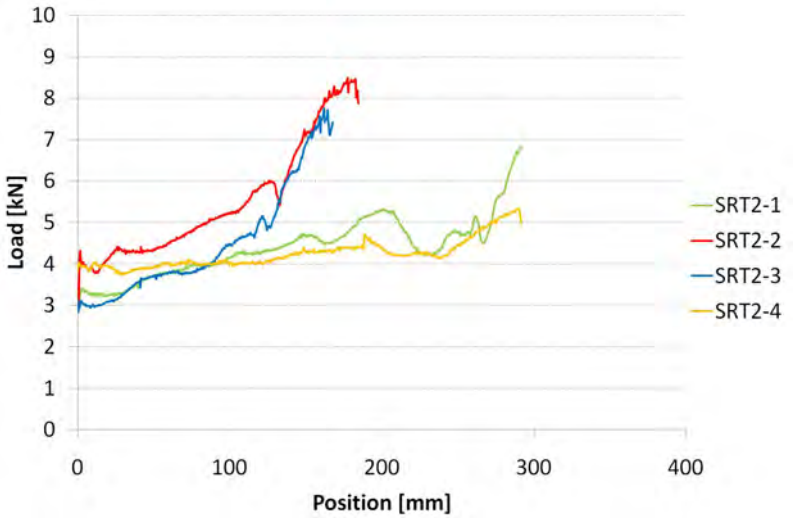

Figure D.3: *Force results of tool SRT2.*

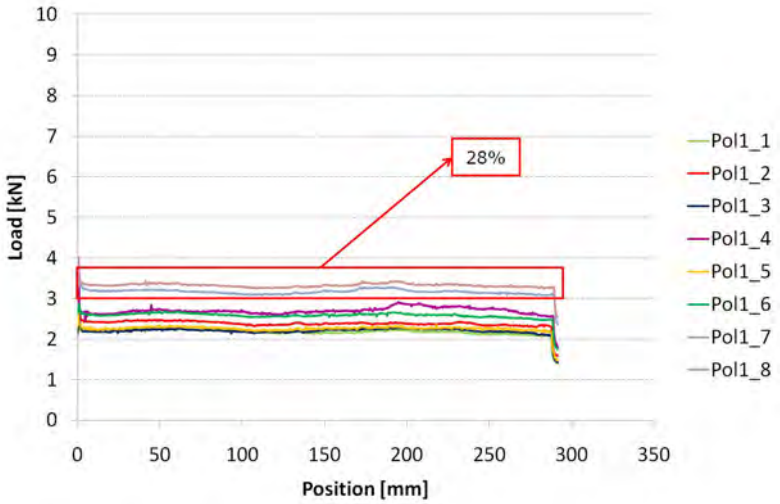

Figure D.4: *Force results of tool Pol1.*

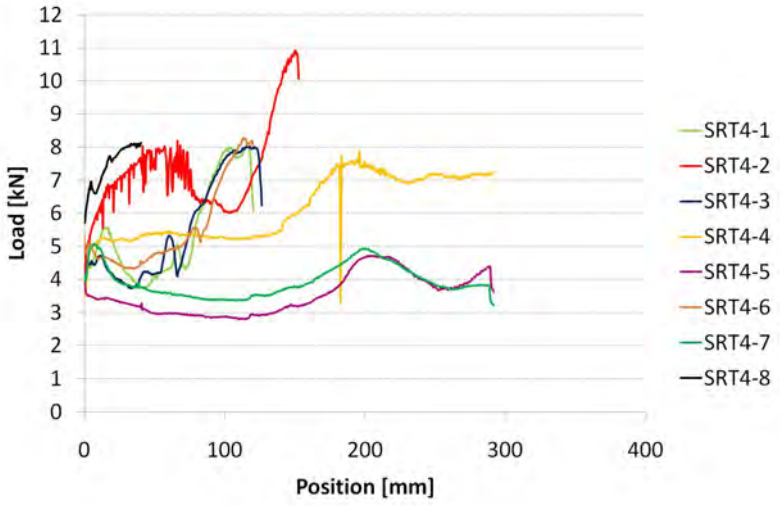

Figure D.5: *Force results of tool SRT4.*

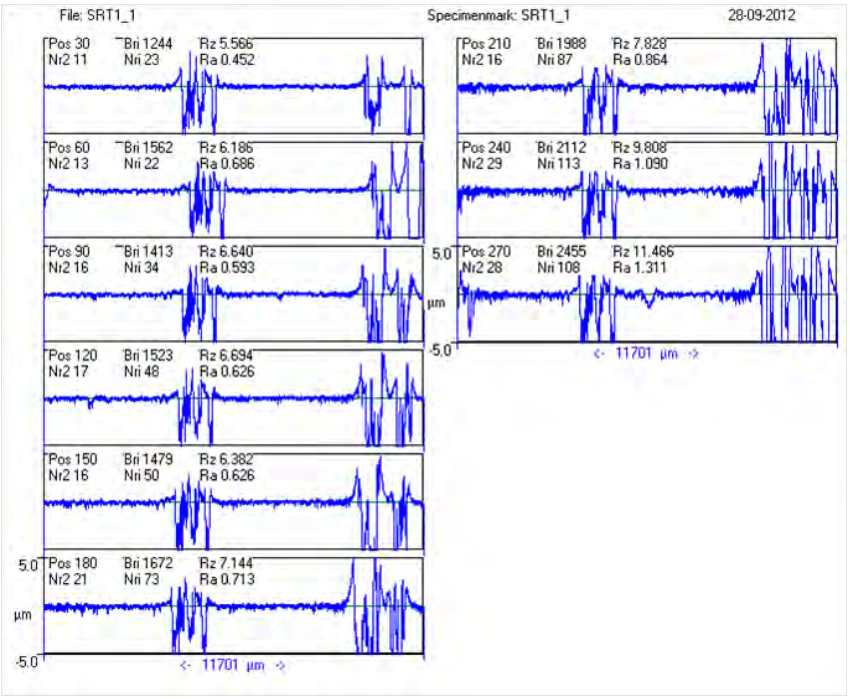

Figure D.6: *Multiplot of SRT1 position 1.*

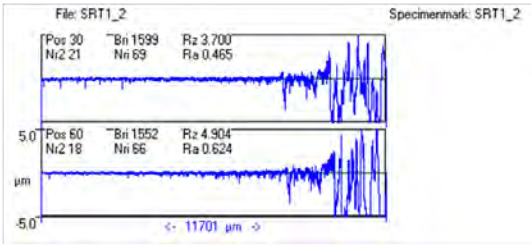

Figure D.7: *Multiplot of SRT1 position 2.*

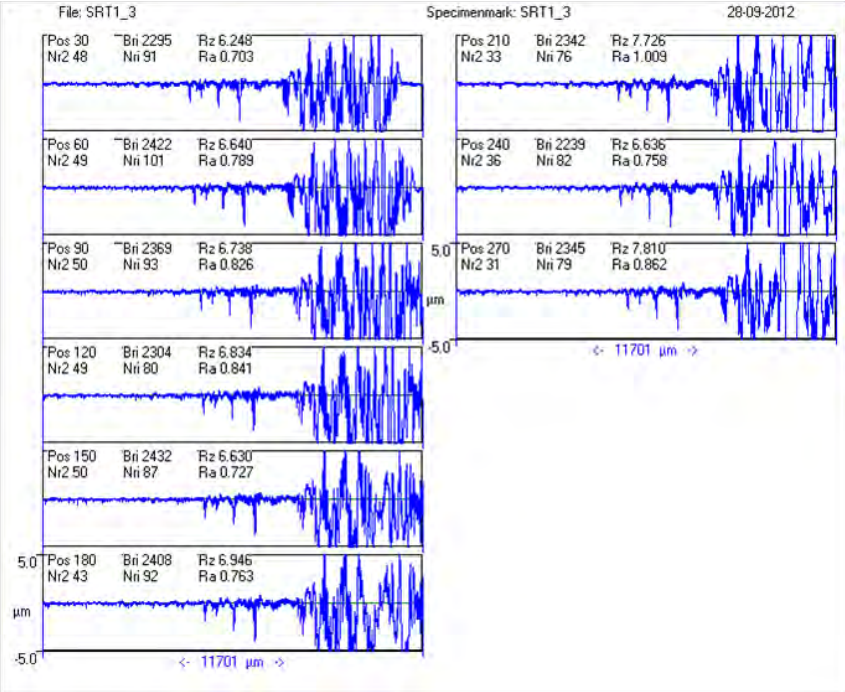

Figure D.8: *Multiplot of SRT1 position 3.*

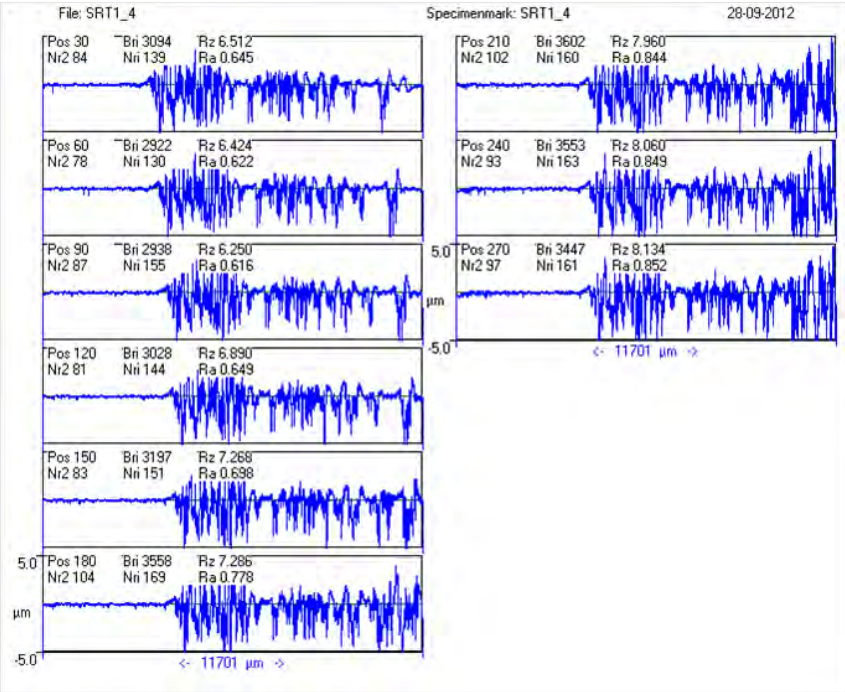

Figure D.9: *Multiplot of SRT1 position 4.*

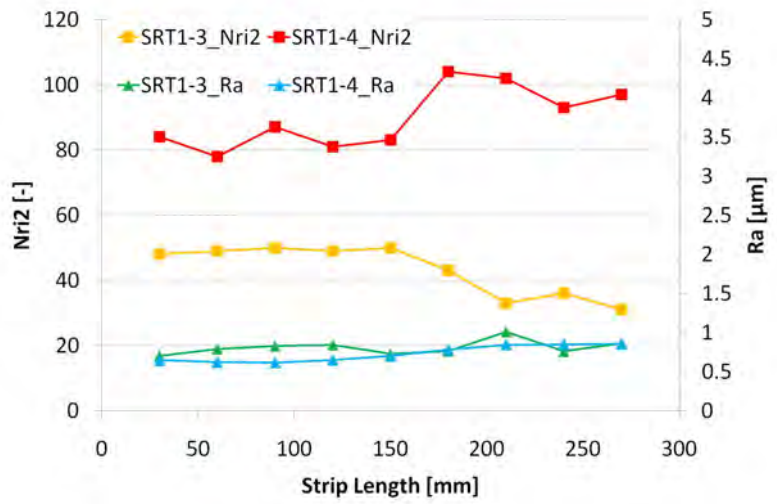

Figure D.10: *Parameters for galling inspection of SRT1.*

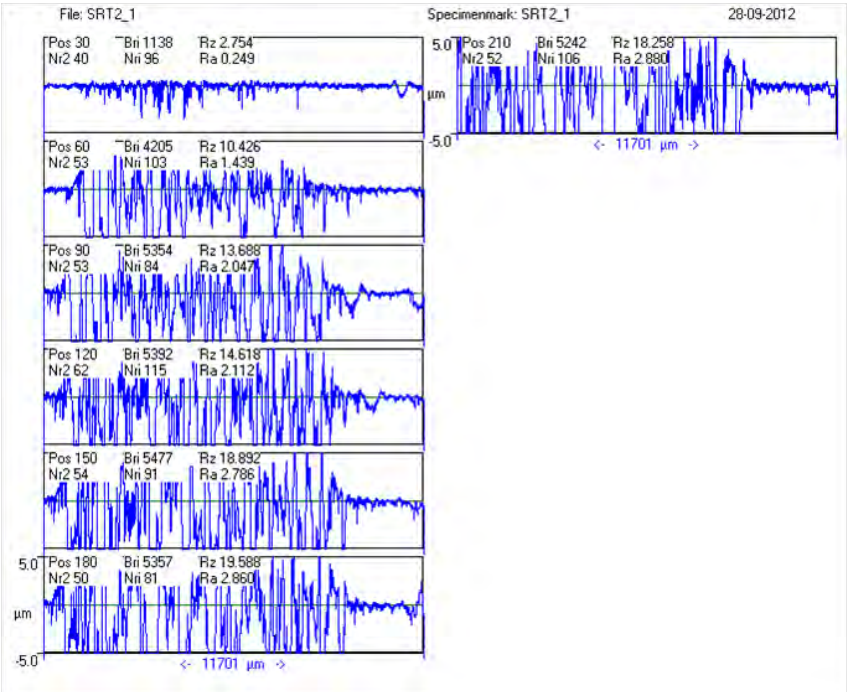

Figure D.11: *Multiplot of SRT2 position 1.*

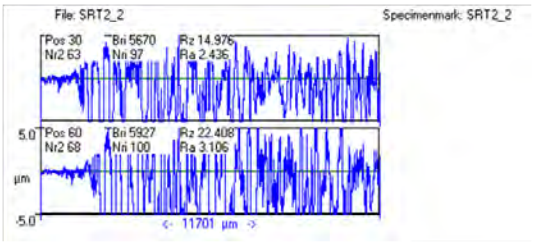

Figure D.12: *Multiplot of SRT2 position 2.*

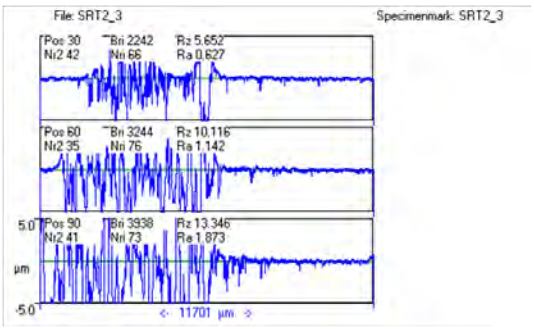

Figure D.13: *Multiplot of SRT2 position 3.*

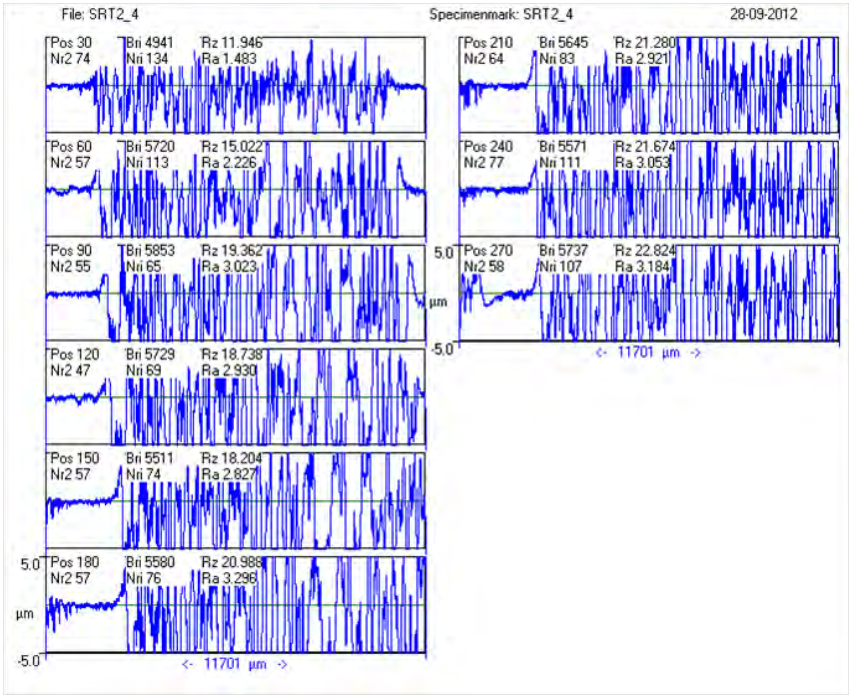

Figure D.14: *Multiplot of SRT2 position 4.*

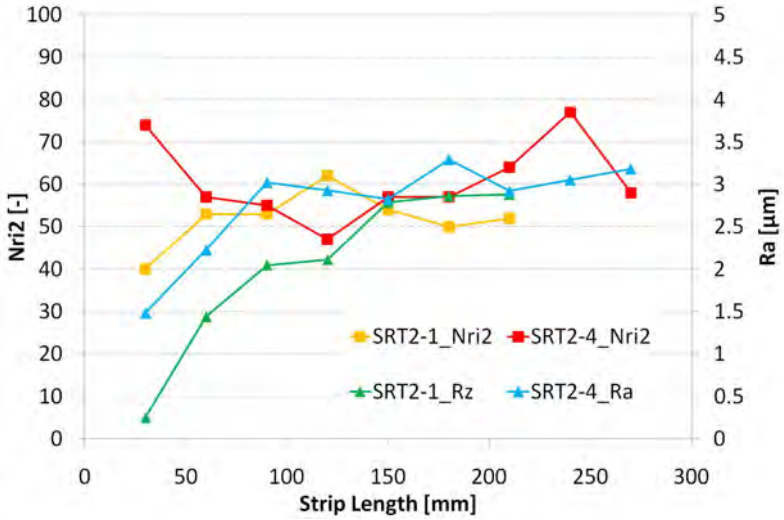

Figure D.15: *Parameters for galling inspection of SRT2.*

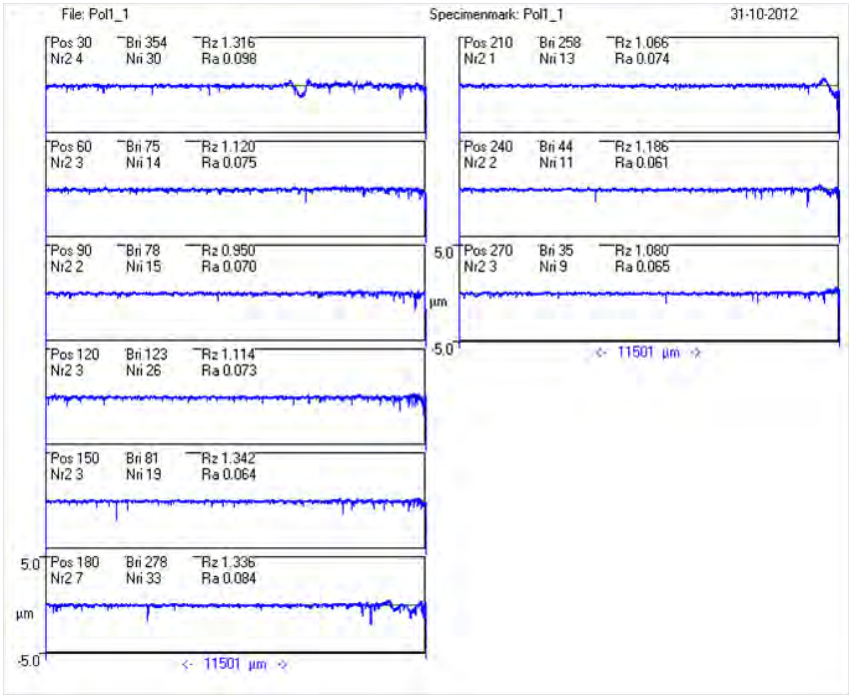

Figure D.16: *Multiplot of Pol1 position 1.*

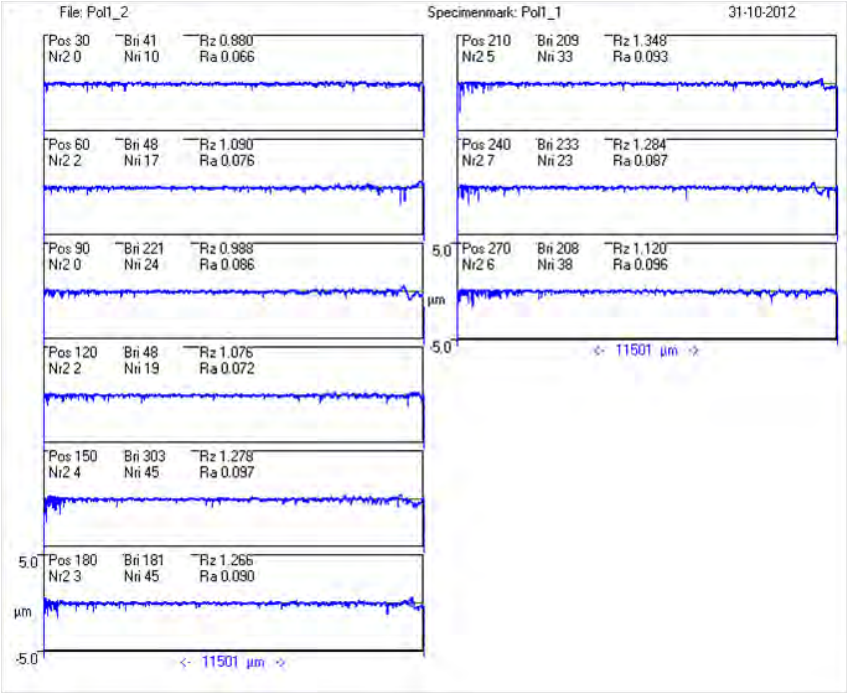

Figure D.17: *Multiplot of Pol1 position 2.*

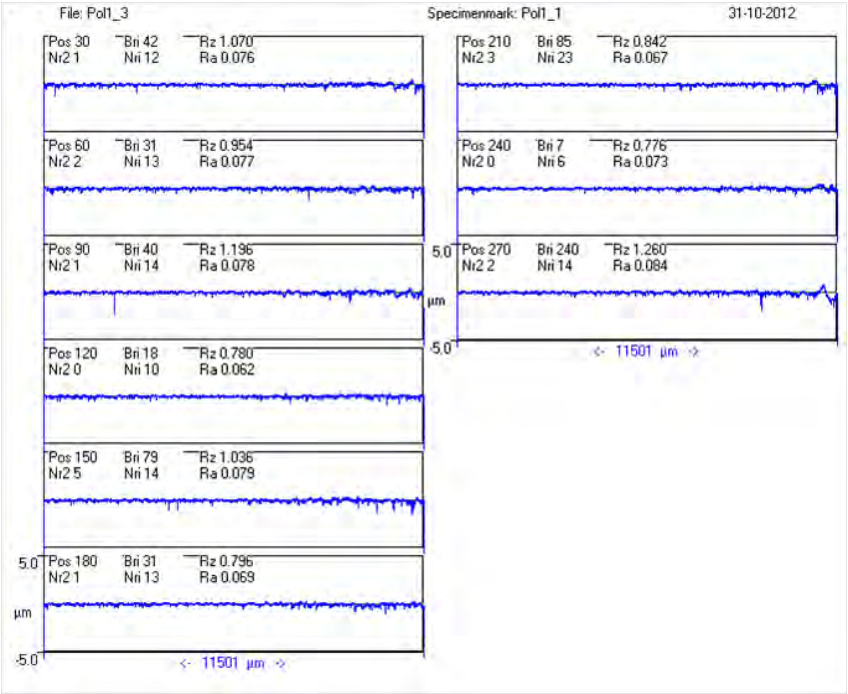

Figure D.18: *Multiplot of Pol1 position 3.*

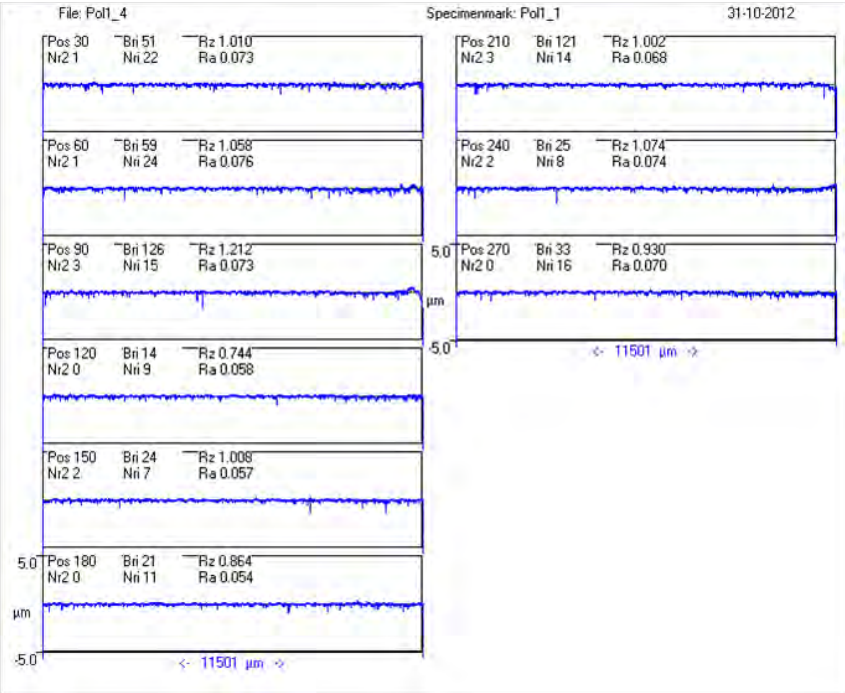

Figure D.19: *Multiplot of Pol1 position 4.*

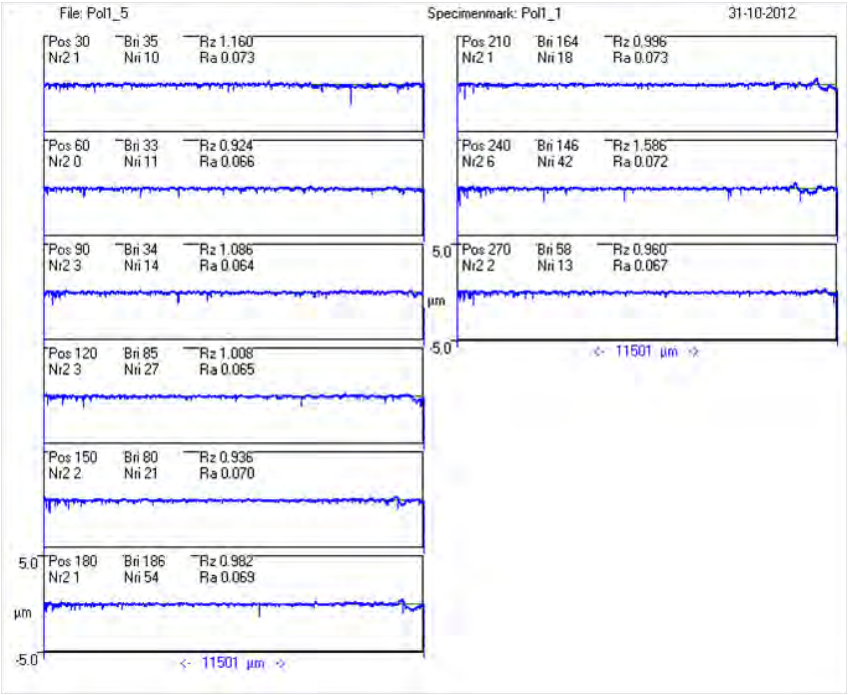

Figure D.20: *Multiplot of Pol1 position 5.*

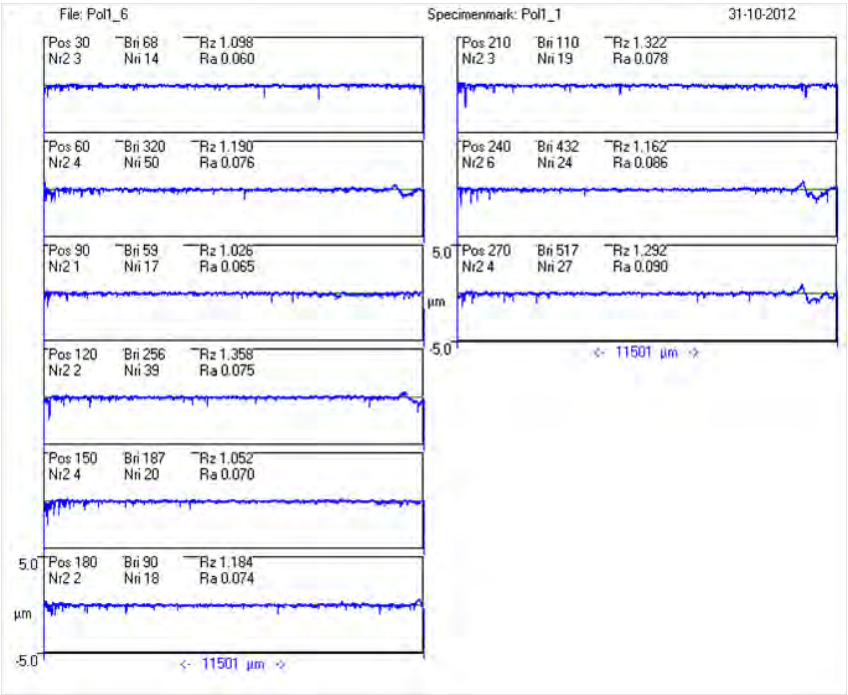

Figure D.21: *Multiplot of Pol1 position 6.*

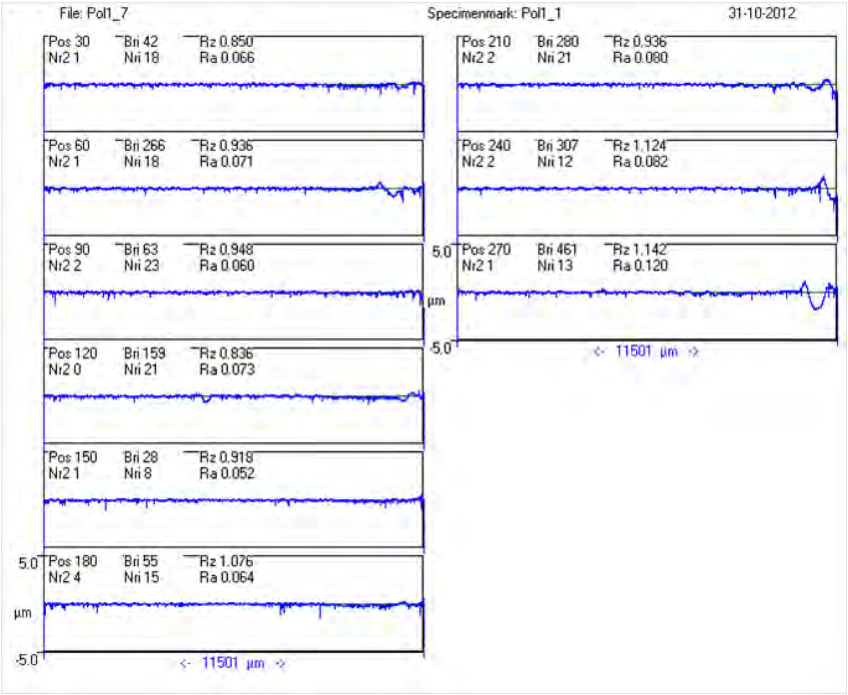

Figure D.22: *Multiplot of Pol1 position 7.*

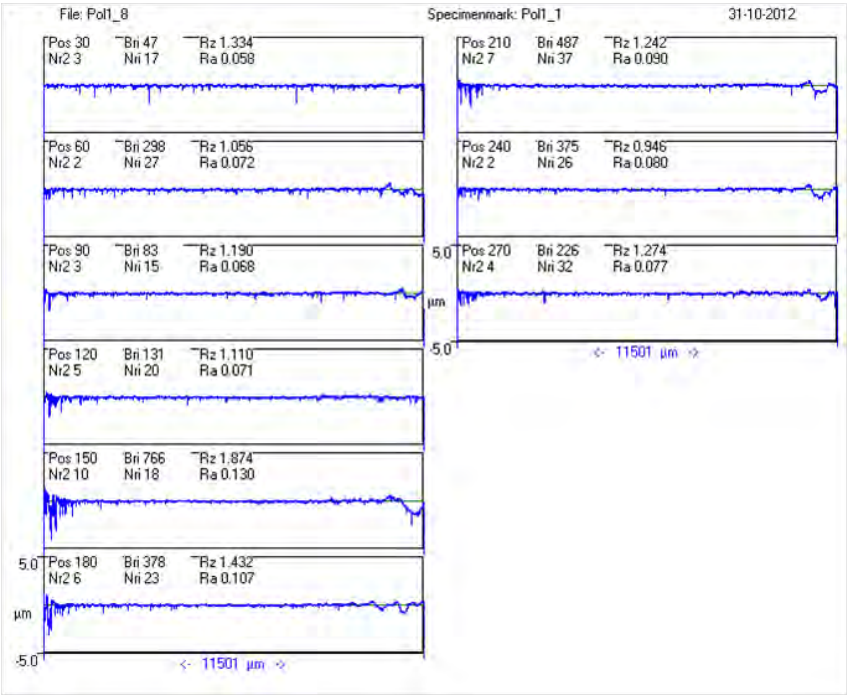

Figure D.23: *Multiplot of Pol1 position 8.*

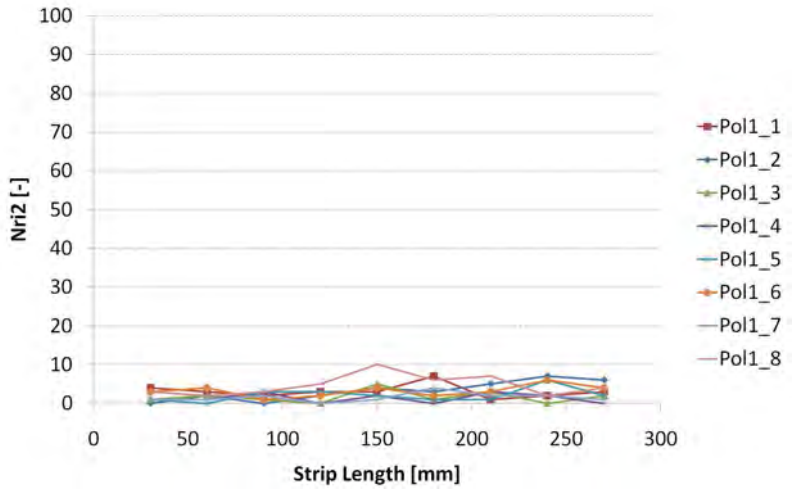

Figure D.24: *Nri2 plot of Pol1.*

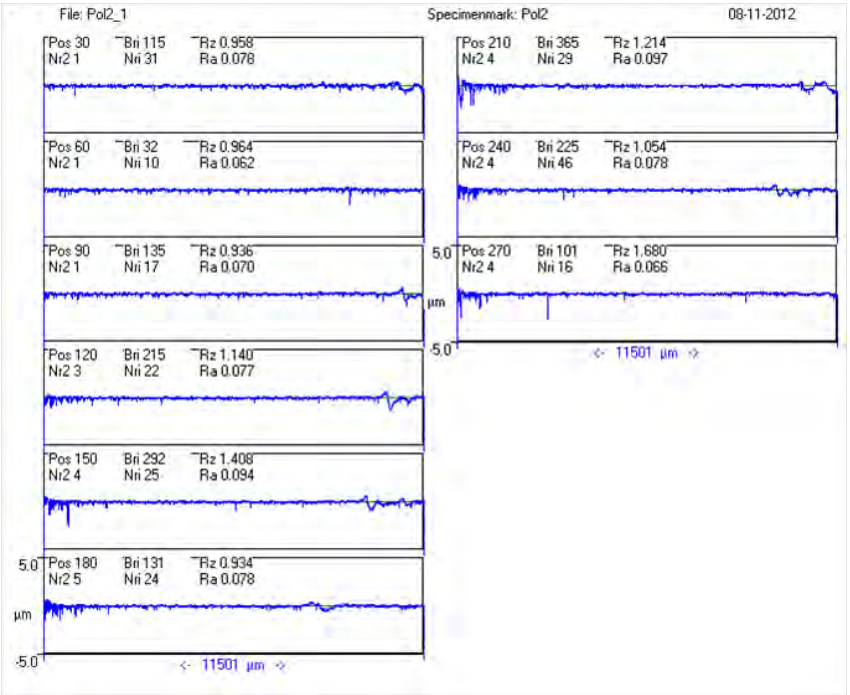

Figure D.25: *Multiplot of Pol2 position 1.*

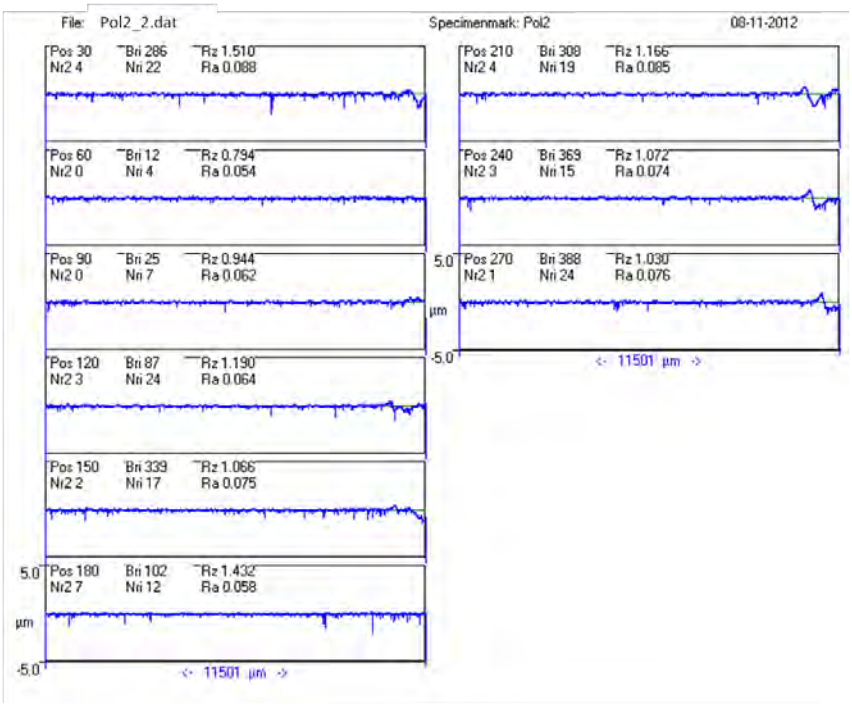

Figure D.26: *Multiplot of Pol2 position 2.*

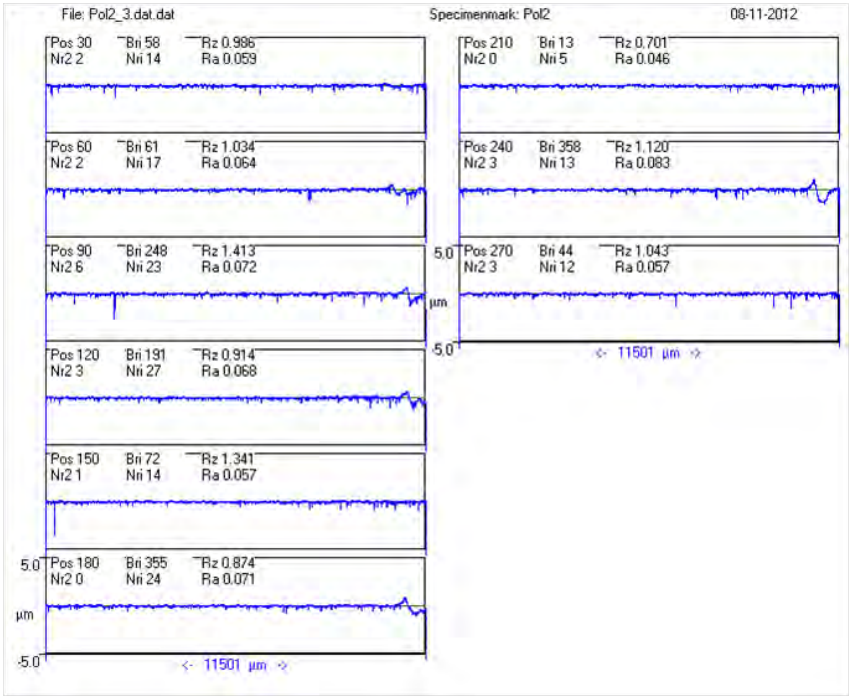

Figure D.27: *Multiplot of Pol2 position 3.*

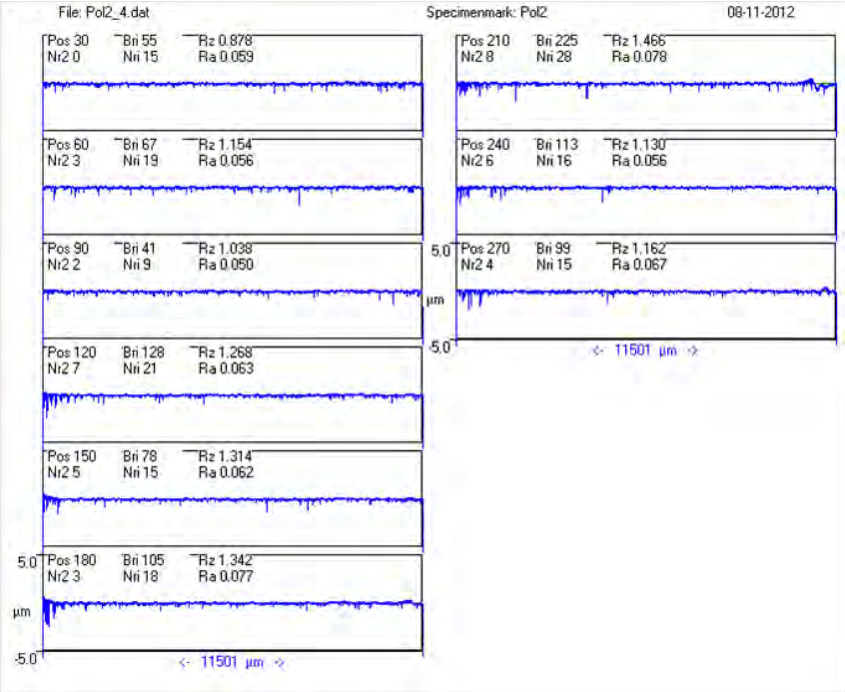

Figure D.28: *Multiplot of Pol2 position 4.*

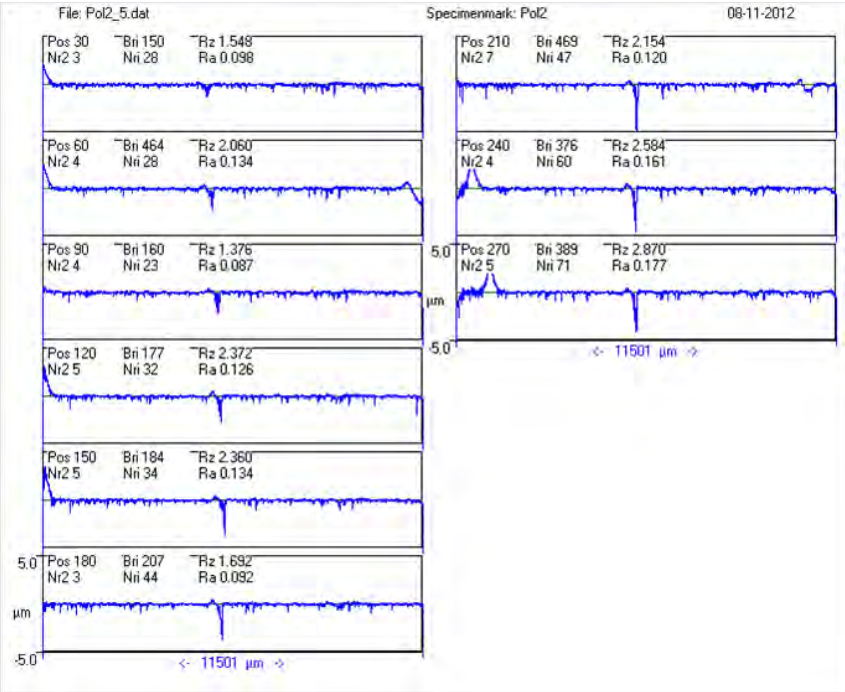

Figure D.29: *Multiplot of Pol2 position 5.*

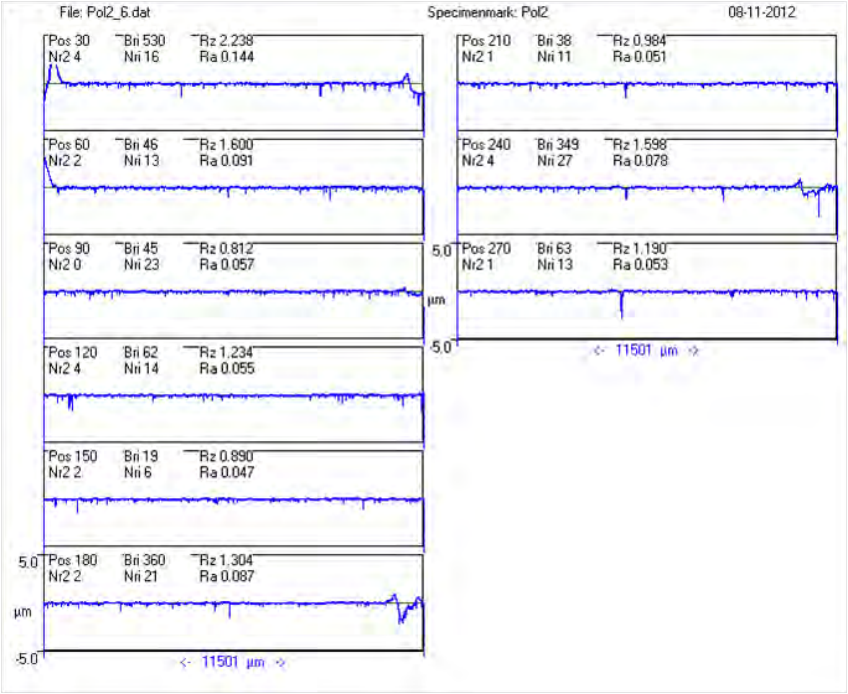

Figure D.30: *Multiplot of Pol2 position 6.*

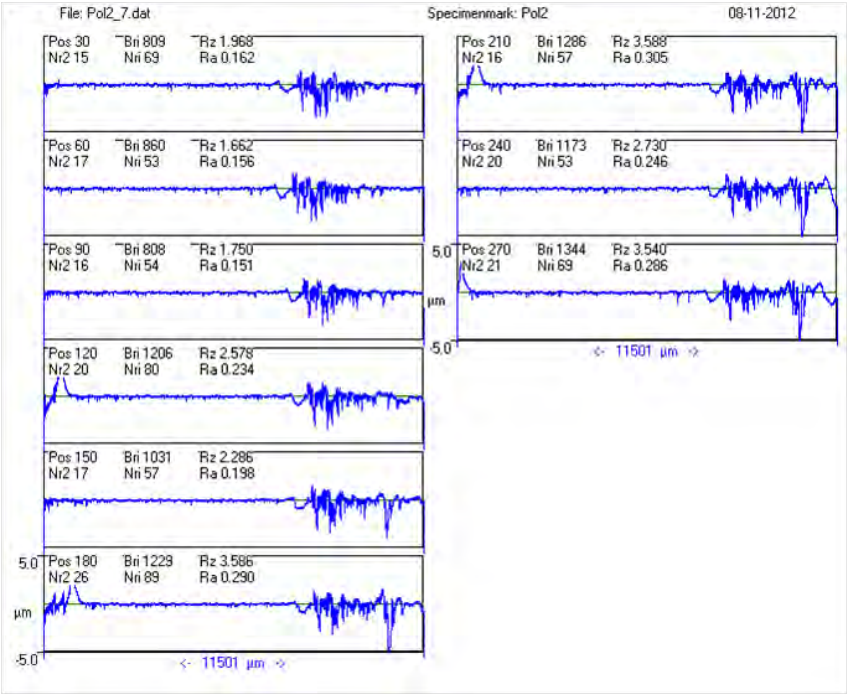

Figure D.31: *Multiplot of Pol2 position 7.*

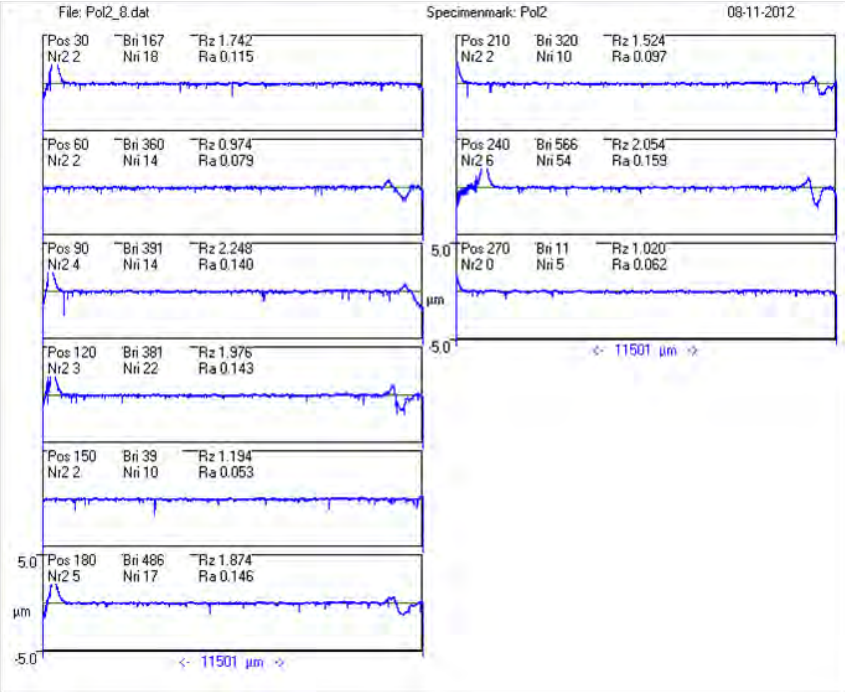

Figure D.32: *Multiplot of Pol2 position 8.*

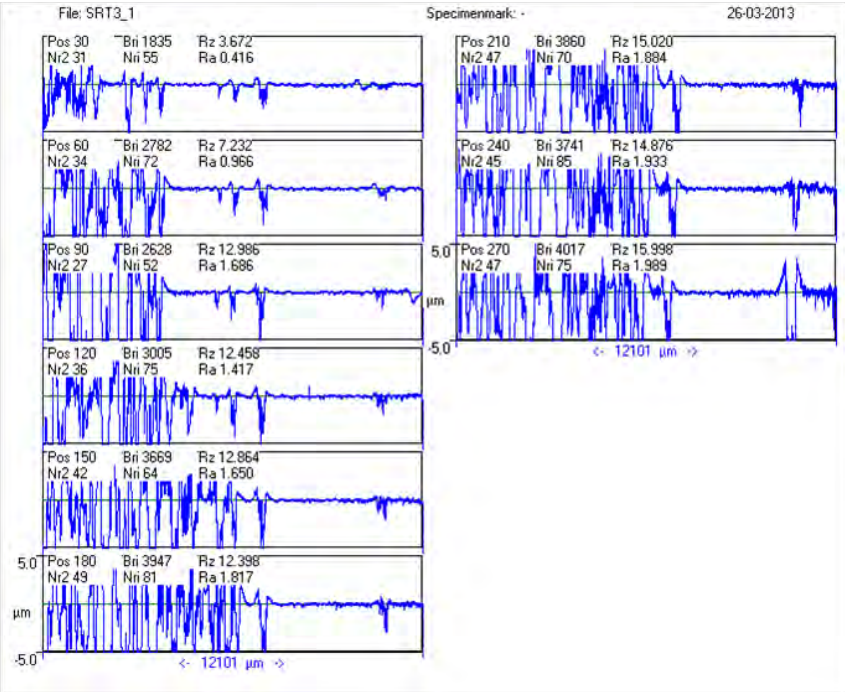

Figure D.33: *Multiplot of SRT3 position 1.*

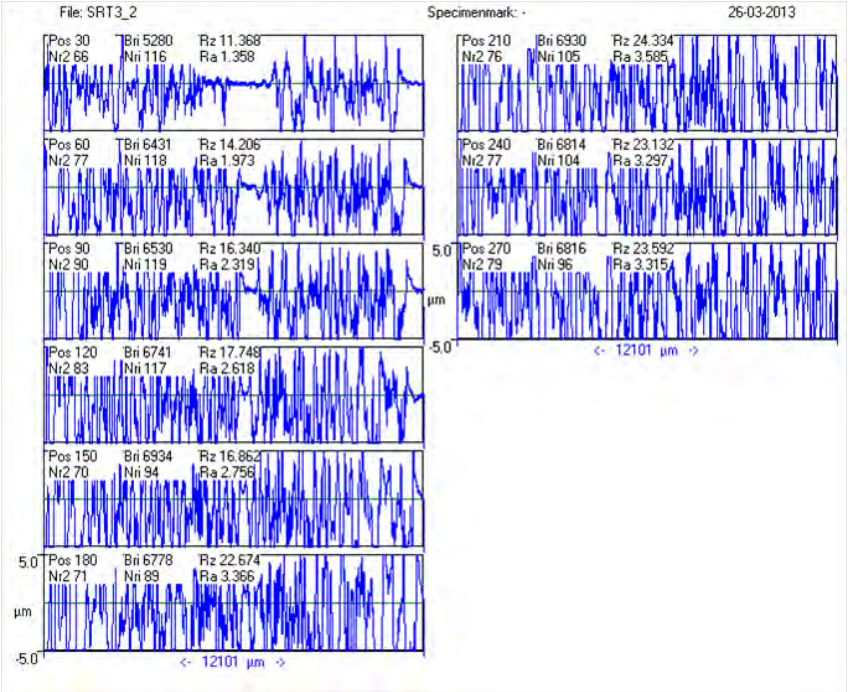

Figure D.34: *Multiplot of SRT3 position 2.*

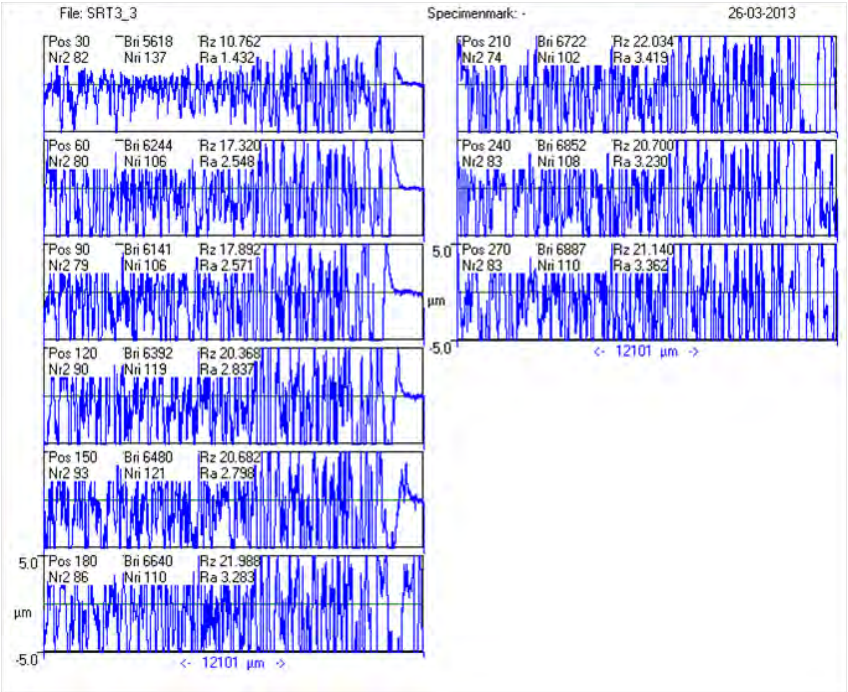

Figure D.35: *Multiplot of SRT3 position 3.*

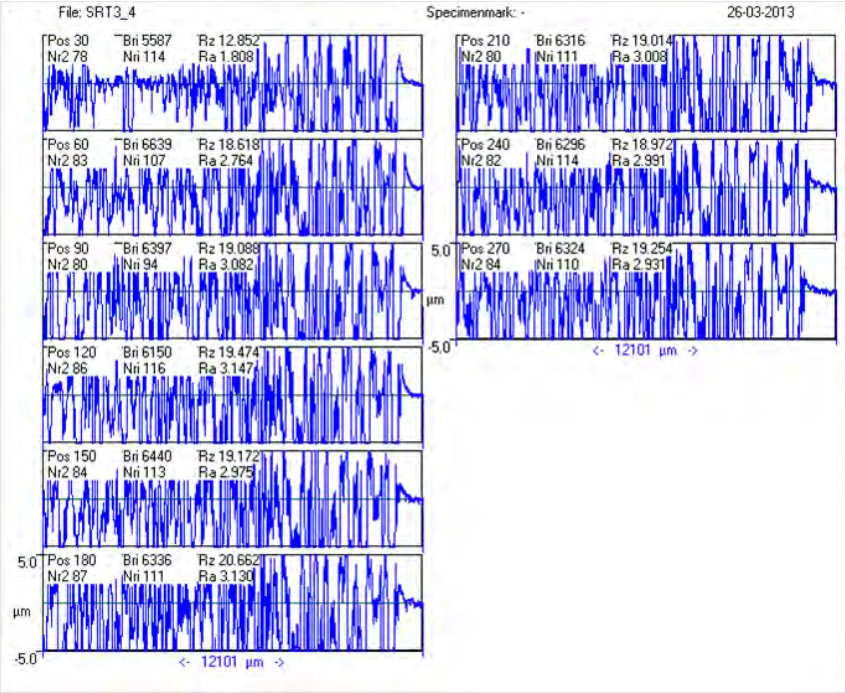

Figure D.36: *Multiplot of SRT3 position 4.*

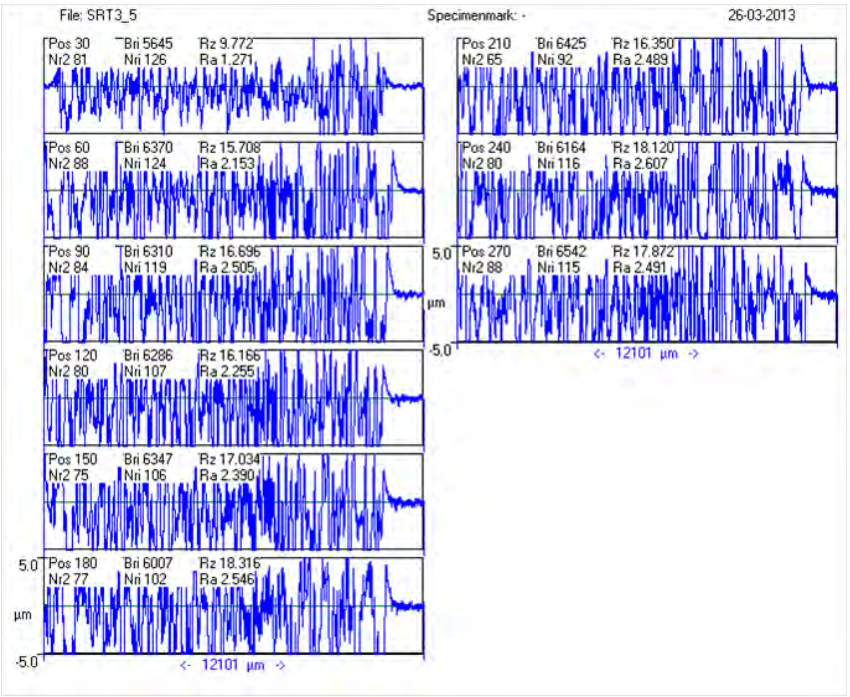

Figure D.37: *Multiplot of SRT3 position 5.*

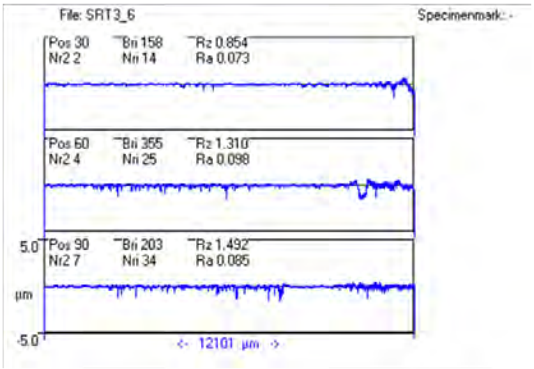

Figure D.38: *Multiplot of SRT3 position 6.*

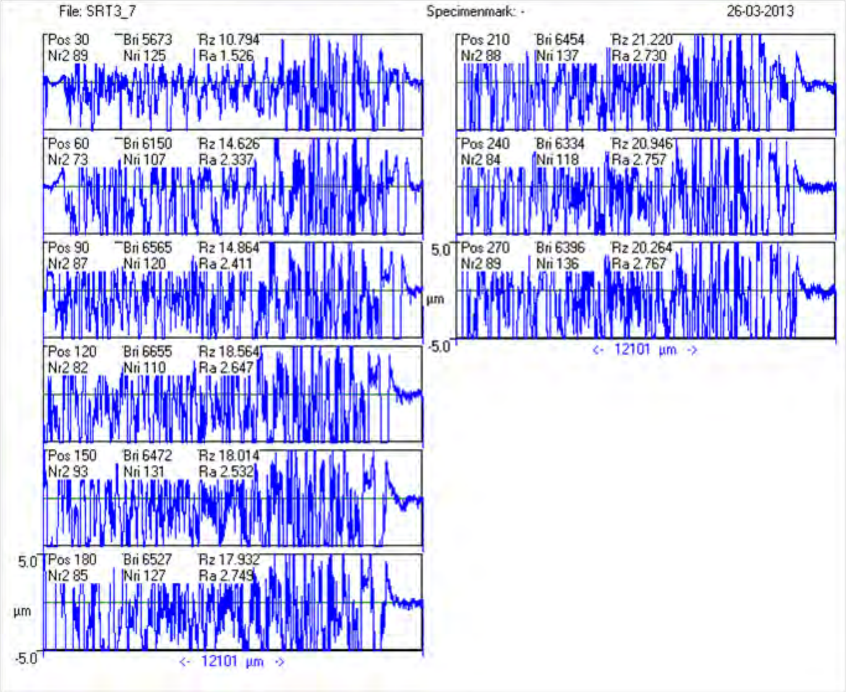

Figure D.39: *Multiplot of SRT3 position 7.*

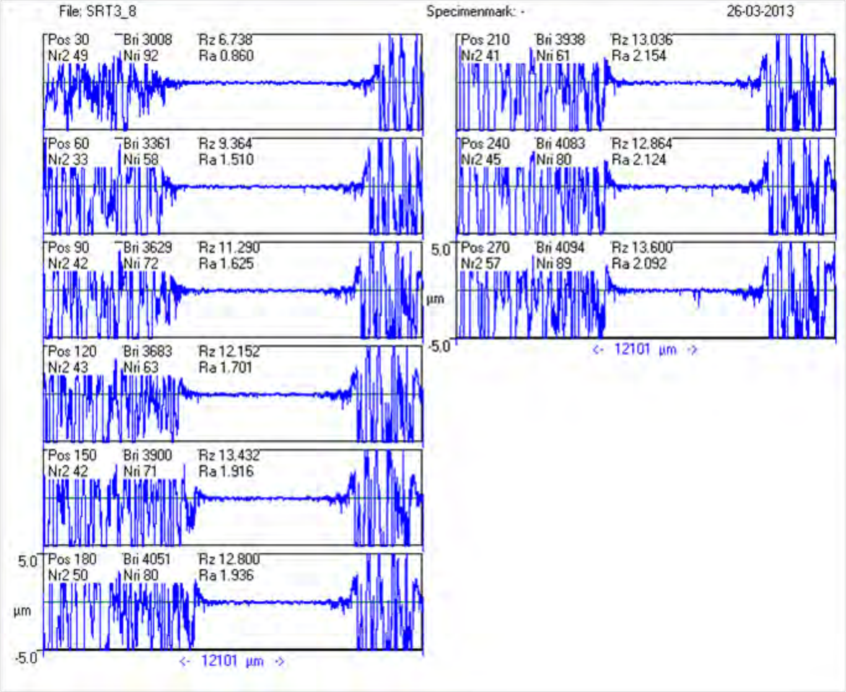

Figure D.40: *Multiplot of SRT3 position 8.*

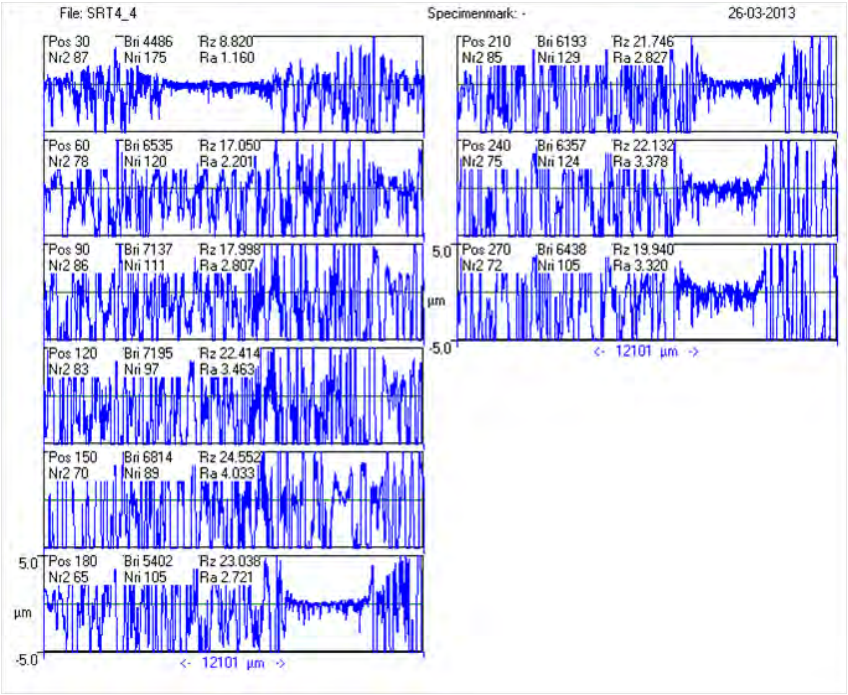

Figure D.41: *Multiplot of SRT4 position 4.*

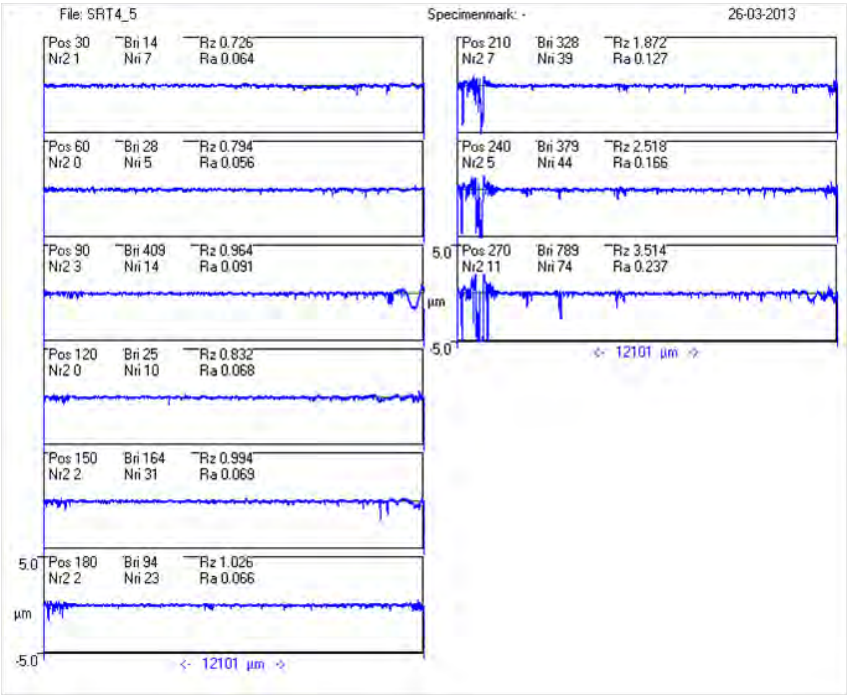

Figure D.42: *Multiplot of SRT4 position 5.*

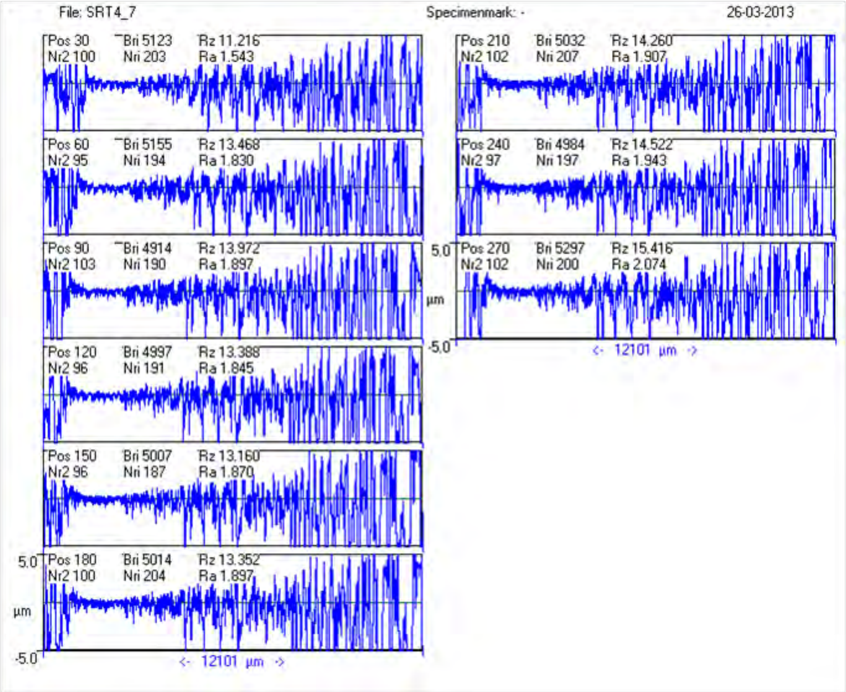

Figure D.43: *Multiplot of SRT4 position 7.*

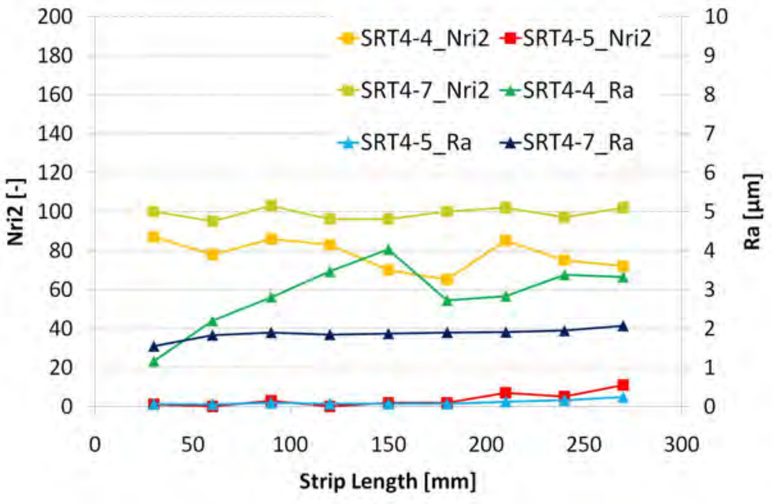

Figure D.44: *Parameters for galling inspection of SRT4.*